IMPACT OF AGING IN THE PRESENCE OF REACTIVE GASES ON CEMENTITIOUS WASTE FORMS AND BARRIERS

By

Janelle Lee Branch

Dissertation

Submitted to the Faculty of the

Graduate School of Vanderbilt University

in partial fulfillment of the requirements

for the degree of

DOCTOR OF PHILOSOPHY
in

Environmental Engineering
February 28, 2018
Nashville, Tennessee

Approved:

David S. Kosson, Ph.D.

Kevin G. Brown, Ph.D.

Andrew C. Garrabrants, Ph.D.

Florence Sanchez, Ph.D.

Hans A. van der Sloot, Ph.D.

Wooyong Um, Ph.D.

To Evelyn, for filling my heart with so much joy.

ACKNOWLEDGEMENTS

This work would not have been possible without the support of my advisor, Dr. David Kosson. Thank you for your invaluable insights and guidance along the way. I also must thank my entire committee for their direction and support. Without them, this work would not have been nearly as complete.

I am deeply grateful to everyone I worked with at Vanderbilt University over the years. First, thank you Dr. Josh Arnold and Dr. Lesa Brown for mentoring me during my first year in the research group. I also must thank Dr. Kevin Brown, Dr. Andrew Garrabrants, and Rossane DeLapp for going above and beyond the call of duty in helping me through countless technical tasks. I am similarly indebted to Rich Teising for always finding creative solutions to implement any type of project and Darlene Weaver for her help with all types of administrative tasks. I was equally lucky to have the support of all other Civil & Environmental Engineering staff members along the way. Finally, to all my fellow graduate students: Thank you for the laughs and camaraderie.

I must also acknowledge the financial support I received from the U. S. Department of Energy, under Cooperative Agreement Number DE-FC01-06EW07053, entitled ‘The Consortium for Risk Evaluation with Stakeholder Participation III’ awarded to Vanderbilt University, David S. Kosson, principal investigator. In addition, thank you to the U.S. National Science Foundation for funding an incredible program that allowed graduate students to conduct research in foreign countries. Specifically, a portion of my work was supported through the National Science Foundation East Asia Pacific Summer Institute Program under award number 1515263. Thank you to the Graduate School at Vanderbilt University for funding travel grants that allow graduate students to have additional opportunities to present their research. I am also especially thankful for Dr. Doug Adams and the Environmental Engineering program for their parental leave policy that allowed me to spend the first few precious weeks of my daughter’s life at home with her.

I also owe an enormous thanks to my family members. Mom and Dad, thank you for encouraging my love of learning from a very early age and for the opportunities you provided to help me achieve my goals. Thank you Jamie, for being my confidant and for providing some much needed laughs along the way.

Fletcher, thank you for being my best friend and the best father to our little girl. I could not have made it through this process without you.

And most importantly, thank you to Evelyn for filling my life with so much love and joy. At the time of this writing you are barely a year old and I can't help but think of the book "The Wonderful Things You Will Be". Darling, please first know you are already so many wonderful things and I can't wait to see what life has in store for you. I hope as you continue explore and experience life you will always stay a sweet, confident, and happy girl.

TABLE OF CONTENTS

Page

DEDICATION ... ii
ACKNOWLEDGEMENTS ... iii
LIST OF TABLES ... ix
LIST OF FIGURES ... xi
NOMENCLATURE ... xv

Chapter

1. INTRODUCTION ... 1
  1.1. Motivation ... 1
  1.2. Objectives and Approach ... 2
  1.3. Structure of the Dissertation ... 3
2. IMPACT OF CARBONATION ON THE MICROSTRUCTURE AND SOLUBILITY OF MAJOR CONSTITUENTS IN MICROCONCRETE MATERIALS WITH VARYING ALKALINITIES DUE TO FLY ASH REPLACEMENT ... 5
  2.1. Abstract ... 5
  2.2. Introduction ... 5
  2.3. Carbonation in cementitious media ... 7
  2.4. Materials and methods ... 8
    2.4.1. Microconcretes ... 8
    2.4.2. Major constituent solubility as a function of pH ... 10
    2.4.3. Thermogravimetric analysis ... 12
    2.4.4. Total inorganic carbon ... 14
    2.4.5. Scanning electron microscopy-energy dispersive x-ray spectrometry ... 14
  2.5. Results ... 15
    2.5.1. Material properties ... 15
    2.5.2. Carbonation depth by pH using phenolphthalein indicator ... 20
    2.5.3. Liquid-solid portioning of major constituents as a function of pH ... 20
    2.5.4. Microstructural analysis ... 22
  2.6. Discussion ... 29
    2.6.1. The role of alkalinity in carbonation ... 29
    2.6.2. Carbonation depth ... 30

2.6.3. Microstructure 31

2.6.4. Extent of reaction 32

2.6.5. pH 33

2.6.6. Solubility of major constituents in carbonated matrices 34

2.6.7. Aggregates 35

2.7. Conclusions 36

2.8. Acknowledgements 37

3. IMPACT OF CARBONATION ON BULK AND ITZ POROSITY IN MICROCONCRETE MATERIALS 38

3.1. Abstract 38

3.2. Introduction 38

3.2.1. Backscattered scanning electron microscopy to detect pore space 39

3.2.2. Carbonation and the interfacial transition zone 40

3.2.3. Impact of fly ash on the microstructure 41

3.3. Materials and methods 42

3.3.1. Microconcrete properties 42

3.3.2. SEM scanning conditions 43

3.3.3. SEM data processing scripts 44

3.3.3.1. EDS segmentation 44

3.3.3.2. Pore space detection 45

3.3.3.3. Interfacial transition zone evaluation 45

3.3.3.4. Overall pore space estimates 46

3.3.3.5. Pore space heat mapping of the bulk paste 47

3.3.3.6. Porosity as a function of distance from the carbonation front 47

3.4. Results 47

3.4.1. Overall bulk and ITZ porosity in non-carbonated and carbonated microconcretes 47

3.4.2. Porosity gradient in carbonated samples 50

3.4.3. Interfacial transition zone porosity gradient 53

3.5. Discussion 54

3.5.1. Impact of fly ash addition on bulk porosity 54

3.5.2. Non-carbonated and uncarbonated porosity comparison 54

3.5.3. Carbonation in the bulk cement paste ... 55
3.5.4. Interfacial transition zone porosity ... 57
3.5.5. Application of BSE segmentation to carbonated microconcretes with fly ash ... 58
3.6. Conclusions ... 59
3.7. Acknowledgements ... 60
4. MICROSTRUCTURAL CHARACTERISTICS AND LEACHING BEHAVIOR OF AGED CAST STONE CEMENTITIOUS WASTE FORM ... 61
4.1. Abstract ... 61
4.2. Introduction ... 61
4.3. Materials and methods ... 63
4.3.1. Cementitious waste form preparation and aging ... 63
4.3.2. Dry ingredients ... 64
4.3.3. Salt waste simulant preparation ... 65
4.3.4. Cast stone mixing ... 66
4.3.5. Aging conditions ... 66
4.3.6. X-ray diffraction ... 67
4.3.7. Thermogravimetric analysis ... 67
4.3.8. Total carbon analysis ... 68
4.3.9. Total porosity ... 68
4.3.10. MicroCT imaging ... 69
4.3.11. Microstructural analysis ... 70
4.3.12. Leaching tests ... 71
4.4. Results and discussion ... 73
4.4.1. Cast stone composition and mineralogy after aging ... 73
4.4.2. Impact of aging on the physical microstructure ... 79
4.4.3. Elemental distribution in the microstructure after aging ... 83
4.4.4. Leaching characteristics of aged cast stone ... 89
4.4.4.1. Leaching characteristics of non-reactive constituents ... 94
4.4.4.2. Leaching characteristics of carbonation sensitive species ... 95
4.4.4.3. Leaching characteristics of oxidation sensitive species ... 97
4.5. Conclusions ... 98
4.6. Acknowledgements ... 99

5. GEOCHEMICAL SPECIATION WITH REACTIVE TRANSPORT MODELING OF CARBONATED MICROCONCRETE MATERIALS CONTAINING DIFFERENT FLY ASH REPLACEMENT TYPES 100
5.1. Introduction 100
5.2. Materials and methods 102
5.2.1. Microconcrete preparation and aging conditions 102
5.2.2. pH-dependent leaching test 103
5.2.3. Mass transfer tank leaching test 103
5.2.4. Modeling approach 104
5.2.5. Modeling chemical parameters 104
5.2.6. Modeling physical parameters 108
5.2.7. Log-squared residual analysis 109
5.3. Results and discussion 110
5.3.1. pH-dependent LSP model results 110
5.3.2. Monolith diffusion-controlled leaching model results 121
5.3.3. Effective diffusivity and tortuosity calibration using sodium 130
5.4. Conclusions 133
5.5. Acknowledgements 134
6. CONCLUSIONS AND FUTURE WORK 135

Appendix

A. Supplementary Material for Chapter 2 138
B. Supplementary Material for Chapter 3 140
C. Supplementary Material for Chapter 4 143
D. Supplementary Material for Chapter 5 170
REFERENCES 185

LIST OF TABLES

Table Page

2.1. Microconcrete formulations ... 9

2.2. Microconcrete coding scheme ... 10

2.3. pH and hydroxide, carbonate, and total alkalinity of the components and microconcretes (± mean CV) determined from titrating with 4 N HNO3 from natural pH to a pH of 4.5. Alkalinity measurements are expressed as mg CaCO3 per g-dry of solid material ... 16

2.4. Mass % (± mean CV) of C-S-H, portlandite, vaterite (associated with carbonation of C-S-H), and calcite according to the weight loss of the DTG curve in the respected temperature ranges 19

2.5. Comparison of measured inorganic carbon (wt% ± mean CV) determined from alkalinity, TIC, and TGA in the microconcretes and their components ... 20

2.6. Mean solubility (mg/L) of calcium, aluminum, and silicon (± mean CV) and corresponding natural pH (± 1 pooled σ) for two replicates of each microconcrete material from EPA Method 1313 ... 22

2.7. Elemental distribution (mass wt%) showing species migration between the carbonated and uncarbonated regions and the decalcification of the C-S-H gel in carbonated region in the presence of carbonated portlandite and C-S-H. The remaining mass percentage is assumed to be hydrogen, due to the presence of hydrated phases. ... 24

2.8. Carbonation depth (mm) according to backscattered electron imaging ... 28

2.9. Mean composition (mass wt%) of cement paste excluding aggregates and fly ash ... 28

2.10. Relationship of alkalinity and carbonation ... 30

3.1. Measured mean bulk cement paste porosity and measured mean ITZ porosity (±1 pooled standard deviation, sp=0.02) of the non-carbonated (NC) microconcretes and the uncarbonated region (UC) and carbonated region (C) in the carbonated concretes. The difference in porosity between the UC and C and the bulk cement paste to the ITZ are reported as an absolute difference and as a percent difference. ... 48

4.1. Oxide composition (wt.%) from XRF of the dry ingredients and resultant cast stone mixture prepared with salt waste simulant after 28 days of curing. 64

4.2. HTWOS overall final LAW simulant concentration 65

4.3. Quantitative XRD results (wt.%). Compositions reported account for the known rutile standard concentration added. 74

4.4. Quantitative SEM-EDS spectrum results (wt. % ± 1σ %), where the maximum 1σ observed was 0.1 % 88

5.1. Selected minerals and their formation constants (Log K). 106

5.2. Selected solid-solutions and their formation constants (Log K). 107

5.3. Log-squared residuals for the pH-dependent solubility experimental results and pH-dependent LSP modeling results for all microconcretes as a function of pH for each selected constituent 117

5.4. Log-squared residuals for the monolith mass transfer tank leaching experimental results and monolith diffusion-controlled leaching model results for all microconcretes as a function of exchange interval time for each constituent.. 128

LIST OF FIGURES

Figure Page

2.1. Fourth degree polynomial fit of the titration curves generated for M-00 and MC-00........... 11

2.2. TGA results plotted as the derivative of the mass and temperature versus the temperature for one replication of the A) non-carbonated microconcretes and the B) carbonated microconcretes 18

2.3. EPA Method 1313 for M-00, MC-00, M-02, MC-39, MC-39, M-02, and MC-02 with circles around data point indicating a test position at the material's natural pH..................................... 21

2.4. A-C: 1500x backscattered electron images and C/AS heat maps of the uncarbonated and carbonated regions of A) MC-00, B) MC-39, and C) MC-02 23

2.5. A-C: Backscattered electron image and C/AS heat map with the corresponding C/AS as a function of distance from the exposed surface for A) MC-00, B) MC-39, and C) MC-02. Dark blue areas indicate aggregates that were excluded from the heat map calculations. *The darker red region and C/AS peak highlighted is due to a small carbonated region not connected to the bulk carbonation front.. 27

3.1. M-00 example for A) initial BSE image and B) bulk cement paste region (white) isolated from aggregates, epoxy, and air voids (black) using carbon and silicon EDS data and manual segmentation 45

3.2. Heat mapping of pore distribution near the boundary of an aggregate in sample M-02. Note that in order to show the contrast between the detected pore space of the aggregate and that of the ITZ, the central aggregate has not been segmented in this image. 49

3.3. X-axis bulk cement paste porosity gradients (red) with a 100-column moving mean (blue) overlaid onto the respective BSE images for A) non-carbonated M-00 sample and C) carbonated MC-00 sample and the corresponding heat maps of the detected pore space distribution including the bulk cement paste and ITZ for the B) non-carbonated M-00 sample and D) carbonated MC-00 sample. Black areas in the heat maps represent the detected epoxy, aggregates, and large pores that were excluded in the pore space gradients. 51

3.4. X-axis bulk cement paste porosity gradients (red) with a 100-column moving mean (blue) overlaid onto the respective BSE images for A) non-carbonated M-39 sample and C) carbonated MC-39 sample and the corresponding heat maps of the detected pore space distribution including the bulk cement paste and ITZ for the B) non-carbonated M-39 sample and D) carbonated MC-39 sample. Black areas in the heat maps represent the detected epoxy, aggregates, and large pores that were excluded in the pore space gradients. 52

3.5. X-axis bulk cement paste porosity gradients (red) with a 100-column moving mean (blue) overlaid onto the respective BSE images for A) non-carbonated M-02 sample and C) carbonated MC-02 sample and the corresponding heat maps of the detected pore space distribution including the bulk cement paste and ITZ for the B) non-carbonated M-02 sample and D) carbonated MC-02 sample. Black areas in the heat maps represent the detected epoxy, aggregates, and large pores that were excluded in the pore space gradients. 53

3.6. Calculated ITZ porosity as a function of the assumed ITZ width for all aggregates in the uncarbonated region and for all aggregates in the carbonated region for each carbonated microconcrete (one replicate per microconcrete type shown). The vertical black line indicates the 10 µm ITZ width assumed in this study. 54

4.1. XRD peaks of CS-N (bottom) and CS-OC (top, offset by +3000 counts) where Al=Alite, Ar=Aragonite, B=Belite, C=Calcite, G=Gypsum, M=Mullite, N=Nitratine, P=Potassium Nitrate, R=Rutile (standard), Q=Quartz, T=Tobermorite, V=Vaterite 74

4.2. TGA results of CS-N and CS-OC 78

4.3. Porosity measurements obtained from the modified water exchange method (ηex), BSE imaging (ηBSE), and microCT imaging (ημCT) for the CS-N (red) and CS-OC (green) materials as a function of distance from the exposed surface. 80

4.4. Porosity (red) and a moving average porosity (blue) obtained as a function of depth from the exposed surface (left) and at the interior region of the materials (right) for CS-N (top) and CS-OC (bottom) overlaid on the corresponding BSE large area maps. 82

4.5. Representative SEM-EDS elemental heat maps (wt.%) and BSE image of CS-N 84

4.6. Representative SEM-EDS elemental heat maps (wt.%) and BSE image of CS-OC within the carbonated region. 85

4.7. Elemental heat maps (colored graphs) and elemental concentrations (plotted white line) as a function of depth moving from the carbonated region (left side of images) to the uncarbonated region (right side of images). Y-axis scales represent the concentration of each element and vary in scale across the different elements in order to better represent changes in concentrations for each element. X-axis values are reported in microns. Dashed vertical lines indicate the transition region from carbonated to uncarbonated. *Sharp peak in iron is due to a clustering of fly ash particles in the scan area. 87

4.8. ANC/BNC as a function of measured eluate pH and pH-dependent leaching concentrations for selected constituents for CS-N (red) and CS-OC (green) as a function of pH. The circled data points indicate the natural pH of the respective materials. *Indicates y-axis is not on logarithmic scale.. 90

4.9. Measured eluate pH, eluate concentration of selected constituents, and the calculated flux of selected constituents for CS-N (red) and CS-OC (green) as a function time. The dotted red line that appears for selected constituents indicates the minimum detection limit (MDL) of the constituent. 91

5.1. M-00 pH-dependent solubility experimental results compared to pH-dependent solubility modeling results for the ANC/BNC and selected constituents. *Y-axis not shown on log scale for sodium to highlight differences in sodium solubility as a function of pH. 111

5.2. M-02 pH-dependent solubility experimental results compared to pH-dependent solubility modeling results for the ANC/BNC and selected constituents. *Y-axis not shown on log scale for sodium to highlight differences in sodium solubility as a function of pH. 112

5.3. M-39 pH-dependent solubility experimental results compared to pH-dependent solubility modeling results for the ANC/BNC and selected constituents. *Y-axis not shown on log scale for sodium to highlight differences in sodium solubility as a function of pH. 113

5.4. MC-00 pH-dependent solubility experimental results compared to pH-dependent solubility modeling results for the ANC/BNC and selected constituents. *Y-axis not shown on log scale for sodium to highlight differences in sodium solubility as a function of pH. 114

5.5. MC-02 pH-dependent solubility experimental results compared to pH-dependent solubility modeling results for the ANC/BNC and selected constituents. *Y-axis not shown on log scale for sodium to highlight differences in sodium solubility as a function of pH. 115

5.6. MC-39 pH-dependent solubility experimental results compared to pH-dependent solubility modeling results for the ANC/BNC and selected constituents. *Y-axis not shown on log scale for sodium to highlight differences in sodium solubility as a function of pH. 116

5.7. M-00 mass transfer tank leaching experimental results compared to the monolith diffusion-controlled leaching model results for the eluate pH and selected constituents for each exchange interval 122

5.8. M-02 mass transfer tank leaching experimental results compared to the monolith diffusion-controlled leaching model results for the eluate pH and selected constituents for each exchange interval 123

5.9. M-39 mass transfer tank leaching experimental results compared to the monolith diffusion-controlled leaching model results for the eluate pH and selected constituents for each exchange interval 124

5.10. MC-00 mass transfer tank leaching experimental results compared to the monolith diffusion-controlled leaching model results for the eluate pH and selected constituents for each exchange interval 125

5.11. MC-02 mass transfer tank leaching experimental results compared to the monolith diffusion-controlled leaching model results for the eluate pH and selected constituents for each exchange interval 126

5.12. MC-39 mass transfer tank leaching experimental results compared to the monolith diffusion-controlled leaching model results for the eluate pH and selected constituents for each exchange interval 127

5.13. Effective diffusivity for sodium as a function of depth for non-carbonated and carbonated microconcretes obtained from calibrating the tortuosity to the sodium concentrations in the eluate in the mass transfer test 131

NOMENCLATURE

Abbreviation	**Description**
ANC/BNC	Acid/base neutralizing capacity
BSE	Backscattered scanning electron
C-S-H	Calcium silicate hydrate
C/AS	Calcium to aluminum+silicon ratio
COPC	Constituent of potential concern
CV	Coefficient of variation
EDS	Energy dispersive x-ray spectroscopy
GGBFS	Ground granulated blast furnace slag
HLW	High level waste
HTWOS	Hanford Tank Waste Operations Simulator
IC	Ion chromatography
ICP-MS	Inductively coupled plasma mass spectrometry
ICP-OES	Inductively coupled plasma optical emission spectrometry
ITZ	Interfacial transition zone
LAW	Low activity waste
L/S	Liquid-to-solid ratio
LSP	Liquid-solid partitioning
MDL	Minimum detection limit
MIP	Mercury intrusion porosimetry
MQ	Milli-q
OPC	Ordinary Portland cement
PNNL	Pacific Northwest National Laboratory
PC	Portland cement
RH	Relative humidity
SEM	Scanning electron microscopy
SCM	Supplemental cementitious material
SRNL	Savannah River National Laboratory
SRS	Savannah River Site
TIC	Total inorganic carbon
TGA	Thermogravimetric analysis
U.S. EPA	United States Environmental Protection Agency
w/b	Water-to-binder ratio
XRD	X-ray diffraction
XRF	X-ray fluorescence

CHAPTER 1

INTRODUCTION

1.1. Motivation

Cementitious materials are currently being used and investigated for use as nuclear waste forms or as barriers for nuclear waste in applications including high-level waste disposal, low-level waste disposal, reactor entombment, and dry cask storage. These materials are subjected to numerous environmental attack scenarios (e.g., sulfate attack, chloride attack, carbonation, and oxidation) which could impact their long-term durability and performance. Specifically, the ingress of reactive gases (i.e., carbon dioxide and oxygen) is a key concern because of the ability of carbon dioxide and oxygen to react with the cementitious materials and waste forms to change their physical and chemical properties. Furthermore, carbon dioxide and oxygen are known to be present in the atmosphere and other media including soil or water that may be in contact with the cementitious waste forms or barriers. The reaction of carbon dioxide (i.e., carbonation) reduces the pH of the material, changes the mineralogy of the material, and changes the physical microstructure of the material which may impact the release of constituents of potential concern (COPCs) from cementitious waste forms. In addition, a reduction in pH can result in depassivation of steel reinforcement and eventually lead to cracking in cementitious barriers. In cast stone or salt stone, a cementitious waste form, the reaction of oxygen (i.e., oxidation) affects the solubility of redox sensitive COPCs, notably the technetium (Tc-99) from the salt waste form contained in the cast stone. Therefore, it is important to understand the impact of carbonation and oxidation reactions on cementitious materials in order to predict material performance and durability of these materials and to help mitigate the potential for environmental contamination.

Evaluating the impact of reactive gasses on cementitious waste forms and barriers also requires consideration of the addition of supplemental cementitious materials (SCMs), defined as mineral admixtures that replace the Portland cement (PC). Fly ash and ground granulated blast furnace slag (GGBFS) are two commonly used SCMs in nuclear waste disposal applications because they reduce the required amount of PC, improve the mechanical strength of the material, and in cast stone materials increase the reductive capacity of the material compared to plain PC mixtures. However, the complexity of cementitious materials along with different chemistries of the components that comprise the material presents significant challenges to characterize the ingress and reaction of carbon dioxide and oxygen and the resulting behavior of COPCs over extended periods of time. Furthermore, the variability among components depending on their source creates additional uncertainty to how these materials will behave. Therefore, it is also important to investigate components from many different sources that chemical composition and to determine how this variation impacts the carbonation and oxidation reaction within the cementitious matrix.

The aim of this dissertation is to investigate the impact of aging in the presence of gaseous carbon dioxide and oxygen on the physical and chemical microstructure of cementitious waste forms and barriers and to evaluate the changes in constituent solubility and mass-transfer release for COPCs across different types of cementitious waste forms and barriers. Two specific materials were investigated: 1. Microconcrete materials which serve as surrogates for commercial concretes and 2. Cast stone materials which are being used and investigated as a waste form for low activity nuclear waste disposal. The effects of carbonation in microconcrete materials were investigated and the effects of coupled carbonation and oxidation on cast stone materials were investigated. In both material sets, different types of fly ashes were prepared to determine the impact of fly ash type on these reactions. Specifically, the impact of carbonation and oxidation on the chemical-physical microstructure, solubility of COPCs, and redox behavior under aging scenarios were characterized using a variety of experimental techniques. Finally, the experimental data collected for the microconcretes was used to perform geochemical speciation modeling with reactive transport in order to better understand and predict the leaching performance of cementitious materials after aging in a carbonating environment.

1.2. Objectives and Approach

The overall objective of this research is to investigate and characterize the behavior of cementitious waste forms used in nuclear waste applications and cement materials in the presence of reactive gases, specifically oxygen and carbon dioxide, in order to support long-term performance assessment of these materials. The specific objectives of this research are to:

1. To assess the impact of material alkalinity on the changes in the chemical microstructure, constituent solubility, and extent of reaction as a result of carbonation in microconcrete materials with varying fly ash replacement types
2. To assess the impact of fly ash replacement type on the changes in the physical microstructure of microconcrete materials within the bulk and interfacial transition zone as a result of carbonation
3. To assess the impact aging in the presence of oxygen and carbon dioxide on the changes in the leaching behavior and within the physical and chemical microstructure for a cast stone cementitious waste form
4. To calibrate and verify geochemical speciation with reactive transport models to support long-term assessment for microconcrete materials in carbonating environments.

1.3. Structure of the Dissertation

This dissertation is organized into six chapters. In Chapter 2, the impact of alkalinity on the carbonation reaction in microconcrete mortars was assessed by evaluating the changes in the microstructure, solubility, and migration of major constituents (i.e., calcium, aluminum, and silicon), for cases of partial replacement of the PC with different fly ashes having varying alkalinity. Several experimental techniques (i.e., scanning electron microscopy with energy dispersive x-ray spectroscopy, U.S. EPA Method 1313, total inorganic carbon analysis, and thermogravimetric analysis) were used and compared as tools to characterize changes due to the carbonation reaction. In Chapter 3, backscattered scanning electron microscopy was used to evaluate the porosity patterns found in microconcrete materials to better understand the gaseous diffusion pathways and reaction of CO_2 within the bulk cement paste and interfacial transition zone of microconcrete materials containing different fly ash replacement types. Image segmentation was applied to evaluate the porosity as a function of distance from an exposed surface in the bulk cement paste and from aggregate boundaries in the ITZ in both carbonated and non-carbonated microconcrete materials. Chapter 4 discusses the mineralogy, microstructural characteristics, and leaching behavior of a cementitious waste form for low activity nuclear waste aged in an inert unsaturated environment and in a reactive unsaturated environment containing oxygen and carbon dioxide. Chapter 5 discusses the results from the geochemical speciation with reactive transport modeling performed for non-carbonated and carbonated microconcrete materials prepared with different fly ash types. Finally, Chapter 6 provides a summary of this dissertation and provides recommendations for future work.

CHAPTER 2

IMPACT OF CARBONATION ON THE MICROSTRUCTURE AND SOLUBILITY OF MAJOR CONSTITUENTS IN MICROCONCRETE MATERIALS WITH VARYING ALKALINITIES DUE TO FLY ASH REPLACEMENT OF ORDINARY PORTLAND CEMENT[1]

2.1. Abstract

The impact of alkalinity on the carbonation reaction in microconcrete mortars was assessed by evaluating the changes in the microstructure, solubility, and migration of major constituents (i.e., calcium, aluminum, and silicon), for cases of partial replacement of the Portland cement with different fly ashes having varying alkalinity. Several experimental techniques (i.e., SEM-EDS, U.S. EPA Method 1313, TIC, and TGA) were used and compared as tools to characterize changes due to the carbonation reaction. The rate and extent of carbonation was inversely related to the alkalinity of the material as evident by the increase in carbonation depth, reduction of the natural pH of the material, extent of the changes in the microstructure, and extent of reaction. Calcium migrated to the carbonated region while conversely silicon migrated from the carbonated region in response to relative solubility and therefore different diffusivity in the carbonated and uncarbonated regions for each constituent.

2.2. Introduction

The service life of cement-based materials is a critical parameter for management of virgin and secondary materials in the cement and concrete applications. Structural degradation is especially important for cementitious materials in nuclear waste applications due to the potential for release of radioactive constituents which could adversely affect human health and the environment. Cementitious materials for nuclear waste management include binding matrices

---

[1] This chapter was reproduced with permission from: J.L.Branch, D.S. Kosson, A.C. Garrabrants, and P.J. He, The impact of carbonation on the microstructure and solubility of major constituents in microconcrete materials with varying alkalinities due to fly ash replacement of ordinary Portland cement, Cement and Concrete Research 89 (2016) 297-309. Copyright 2016, Elsevier.

for low-activity waste forms and physical barriers such as grouts for waste tank capping, concrete vaults for waste containment, and mass pours for reactor entombments [1]. Often these materials contain supplemental cementitious materials (SCMs) designed to modify material performance. In these applications, it is desirable that cementitious materials maintain structural, hydraulic and chemical performance to the extent possible for lifetimes up to thousands of years. Although many of the mix designs for nuclear waste applications rely on coarse aggregate, the study of chemical performance and degradation often focus on the reactions and structure of the cement paste or of cement mortars. With regard to leaching and degradation of commercial concretes, microconcretes (i.e., mortars with high levels of fine aggregate that mimic concrete rheology) have been shown effective as surrogates for concretes containing coarse aggregate [2, 3].

Much of the physical and chemical durability of cementitious materials has been attributed to the formation of a highly-buffered alkaline matrix consisting mainly of calcium-silicate-hydrates (C-S-H) and portlandite [$Ca(OH)_2$]. However, a key mechanism for degradation of cementitious matrices is reaction of the alkaline matrix with atmospheric or soil-gas carbon dioxide (CO_2), also known as carbonation. Over the extended material performance intervals for nuclear waste applications, degradation due to carbonation can potentially lead to the release of radionuclides [4]. Atmospheric or soil-gas CO_2 reacts with dissolved minerals in the cement pore water resulting in (i) depletion of matrix alkalinity which neutralizes pore water and affects the solubility of pH-dependent constituents and (ii) precipitation of relative insoluble carbonate phases which alters the pore structure of the matrix. In extreme cases, carbonation may lead to depassivation of reinforcing steel, physical degradation of the cementitious material, and loss of strength due to cracking in both nuclear and non-nuclear applications. Therefore, considerable effort has been placed on characterizing the primary degradation mechanisms of cementitious materials including the penetration of CO_2 and reaction rate of carbonation [5-8].

Microstructural analysis is key to understanding the overall behavior of the material, especially under conditions where changes in the microstructure and porosity occur due to the formation of carbonated products [9]. Analysis of the microstructure can identify the composition, morphology and spatial distribution of phases present in the system providing useful information on the mechanisms of hydration or degradation [10]. Characterization of the cement microstructure and redistribution of elements as a result of carbonation may lead to a better understanding of the macroscopic deterioration that occurs in concrete over extended periods.

This study evaluates the impact of material alkalinity on the carbonation process for three microconcrete materials with different alkalinities by assessing the changes in solubility of the major constituents (i.e., calcium, aluminum, and silicon), microstructure, distribution of elemental constituents across a reacted carbonated front, extent of reaction, and reaction capacity. The results of this study are intended as input to a framework to predict material durability in commercial and nuclear applications and the migration/release of heavy metals and radionuclides from cementitious materials used in nuclear waste applications.

2.3. Carbonation in cementitious media

The penetration CO_2 gas from air or soil media into a porous cement material results in subsequent reaction of aqueous CO_2 with hydration minerals including portlandite, C-S-H, and ettringite [$Ca_6Al_2(SO_4)_3(OH)_{12}\cdot 26H_2O$] to form carbonated products [11, 12]. In particular, the reaction of CO_2 with portlandite is of interest because of its abundance in the material and its responsibility for decreasing the pH of the material. Papadakis et al. [7] represented the overall reaction between portlandite and CO_2 as two steps: the dissolution of the portlandite (Eq.1) and the overall carbonation reaction (Eq.2), which is comprised of other elementary steps.

$$Ca(OH)_2(s) \rightarrow Ca^{2+}(aq) + 2OH^-(aq) \qquad \text{Eq. 1}$$

$$Ca^{2+}(aq) + 2OH^-(aq) + CO_2(g) \rightarrow CaCO_3(s) + H_2O \qquad \text{Eq. 2}$$

These steps are cyclic in that the consumption of free hydroxide ions in the pore solution (Eq. 2) results in further dissolution of portlandite leading to depletion and reduced pH in carbonated materials. Localized depletion of portlandite results in subsequent decalcification of C-S-H [7, 13] according to Eq. 3:

$$x\mathrm{CaO}\cdot\mathrm{SiO_2}\cdot n\mathrm{H_2O} + y\mathrm{H_2O} \rightarrow (x\text{-}y)\mathrm{CaO}\cdot\mathrm{SiO_2}\cdot n\mathrm{H_2O} + y\mathrm{Ca(OH)_2} \qquad \text{Eq. 3}$$

Since portlandite is more soluble (K_{sp}= 5.5x10^{-6} at 25° C) than $CaCO_3$ (K_{sp}=4.7x10^{-9} at 25° C) [14] and there is a shift in the pH of the material, the concentration of constituent ions in the pore solution is expected to be different in the carbonated region of the material compared to the uncarbonated region. Studies of the changes in the leaching behavior upon carbonation of cementitious materials indicate that the differences in the pore solution concentrations of the major constituent ions (i.e., calcium, aluminum, and silicon) will significantly impact the time-dependent leaching of these constituents from concrete materials [2, 15-17]. Therefore, leaching tests intended to characterize the liquid-solid partitioning of calcium, aluminum, and silicon in solid materials can be used to identify changes in constituent solubility and concentration of constituents in the pore water solution due to the phase changes associated with the carbonation reactions.

The carbonation of cementitious materials is a complex process that is further complicated by the addition of SCMs which may be used as replacement for a portion of the Portland cement component in blended cementitious materials. Replacement of a fraction of the Portland cement with SCMs often improves the mechanical performance of these systems and reduces the need for virgin cement. For example, the addition of coal combustion fly ash promotes the conversion of portlandite to C-S-H during hydration and, hence, refines the microstructure of the concrete which ultimately affects the transport properties of the matrix which controls the diffusivity of CO_2 [18, 19]. Previous studies suggest that the presence of fly ash increases the rate of carbonation because of a change in material alkalinity and the availability of portlandite [18, 20-22]. Models have been designed to predict the penetration depth of the carbonation reaction front in concrete materials with fly ash replacement [23, 24], yet more effort is needed to characterize the evolution of the microstructure coupled with the elemental distribution for these materials. However, since the amount of alkalinity provided by fly ash can vary significantly based on coal source and combustion configurations [25], the uncertainty about prediction of the carbonation rate and extent of microstructural effects increased.

2.4. Materials and methods

2.4.1. Microconcretes

Microconcrete mortars with different levels of total alkalinity were prepared by mixing Type I/II ordinary Portland cement (OPC), fly ash (FA02 or FA39), river sand (fine aggregate), and water according to the mix designs shown in Table 2.1 [26]. FA02 is a low calcium (1.9% by mass)

Class F fly ash from the combustion of bituminous coal and FA39 is a high calcium (17.1% by mass) Class C fly ash from the combustion of sub-bituminous coal. The microconcretes include a control material with no fly ash (M-00), a blended microconcrete with 45% of the OPC fraction replaced by FA02 (M-02), and a blended microconcrete with 45% replacement of OPC with FA39 (M-39). A sieve analysis was performed on the fine aggregate (Table A.1, Appendix A). The material source details and characteristic leaching data for these materials have been reported elsewhere [3]; however, the naming scheme for the microconcretes has been simplified to improve the presentation clarity of this study.

Table 2.1. Microconcrete formulations

	Control	Blend	Control	Blend
Nominal Mix (kg/m^3)	514	514		
Fly ash replacement (%)	-	45		
	Composition (wt%)		Composition (kg/m^3)	
Portland Cement	22.2	12.2	301	165
Fly ash	-	10	-	136
Water	9.9	10.1	135	136
Fine Aggregate	67.9	67.7	940	920

For each microconcrete, ten cylindrical monoliths (6.5 cm diameter x 9.0 cm height) were cast and cured for 6 months at 100% relative humidity (RH) in a sealed 19 liter bucket maintained at ambient temperature (21 ±2 °C). After the 6-month cure, three of the monoliths for each microconcrete were carbonated for an additional 6 months in a Thermo Scientific 3531 environmental chamber (Thermo Fisher Scientific, Inc., Waltham, MA) maintained at 5% CO_2, 65% RH, and ambient temperature. These carbonated materials are denoted as samples MC-00, MC-02, and MC-39. In parallel, three monoliths for each microconcrete, labeled M-00, M-02 and M-39, remained in the sealed buckets for an additional 6 months of curing without exposure to CO_2. Four monoliths for each microconcrete were collected after the initial 6-month cure and crushed using a parallel plate grinder until at least 85 percent by mass (wt%) of the material was less than 2 mm in diameter. Half of this granular material was placed in the same carbonation chamber with the monolith samples for 6 months and the remaining half was returned to the sealed bucket for additional 6 months of curing. For the purposes of these experiments, particle size reduction was intended to maximize the extent of carbonation over 6 months by increasing the surface area exposed to CO_2. In addition, United States Environmental Protection Agency (U.S. EPA) Method 1313, thermogravimetric analysis (TGA), and total inorganic carbon (TIC) used to characterize the carbonation reaction require a size reduced material and therefore the crushed microconcretes were used in these test methods. A summary of the microconcretes curing, crushing, carbonation conditions, and test method for each material is summarized in Table 2.2.

Table 2.2. Microconcrete coding scheme

Material Code	Cured	Crushed	Carbonated	Test Method
M-00, M-02, M-39	12 months	No	No	Phenolphthalein, SEM-EDS
MC-00, MC-02, MC-39	6 months	No	6 months	Phenolphthalein, SEM-EDS
M-00, M-02, M-39	12 months	Yes	No	Method 1313, TGA, TIC
MC-00, MC-02, MC-39	6 months	Yes	6 months	Method 1313, TGA, TIC

2.4.2. Major constituent solubility as a function of pH

The liquid-solid partitioning of calcium, aluminum, and silicon between the solid material and a contacting aqueous phase as a function of pH was determined using U.S EPA Method 1313 [28]. This method also provides the acid-base titration curve used to estimate total and carbonate alkalinities. Method 1313 is a standard, pH-dependence leaching method consisting of parallel batch extractions of a solid material under various pH conditions and at a liquid-to-solid ratio (L/S) of 10 mL/g-dry. Details on the procedure and application of this method can be found elsewhere [27-29]. For each carbonated and non-carbonated microconcrete and their components (i.e., OPC, FA02, and FA39), the test was conducted in duplicate. For each microconcrete, the calcium, aluminum, and silicon concentrations in the eluate were determined by inductively couple plasma-optical emission spectrometry (ICP-OES) following U.S. EPA Method 6010C [30]. The titration curve for each material was derived based on the amount of acid added (mol_{H+}/kg-dry) and the resulting end-point pH for each extraction using a best fit fourth degree polynomial from the two replications from the material's natural pH[2] to the pH of 4.5. This data was used to calculate the total, hydroxide, and carbonate alkalinities according to this titration curve for each microconcrete and component. This alkalinity calculations parallel Standard 2320 described in the Standard Methods for the Examination of Water and Wastewater to determine alkalinity [31]. The distribution of the different alkalinity contributions was modified from the Standard Method 2320 because significant bicarbonate alkalinity is not expected in cementitious materials and because of the variation in the inflection point pH near the phenolphthalein alkalinity point (pH 8.3) in the titration curve of each material. Therefore, the hydroxide alkalinity contribution was estimated as the acid addition from the material's natural pH to the inflection point near pH of 8.3 for each material. The carbonate alkalinity contribution was estimated as the acid addition from the inflection point near pH of 8.3 in each material to a pH of 4.5. The total amount of inorganic carbon present in the carbonate form according to the carbonate alkalinity was then calculated for each material. Two representative titration curves and the regions associated with hydroxide and carbonate alkalinities are shown in Figure 2.1. The uncertainty associated with determining the hydroxide, carbonate, and total alkalinity, the inorganic carbon, and solubilities was estimated according to the mean coefficient of variation (CV) across all samples and replicates for each measurement type.

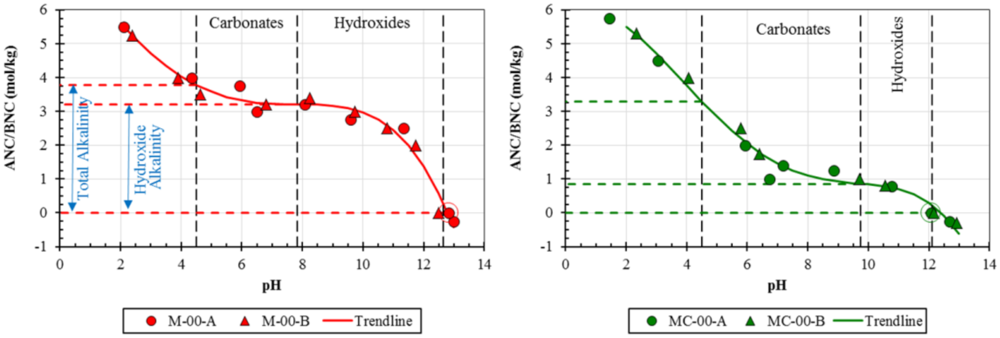

Figure 2.1. Fourth degree polynomial fit of the titration curves generated for M-00 and MC-00.

---

[2] The natural pH, or "own pH," is the end point pH when extracted with only deionized water at liquid-solid ratio of 10 mL/g dry weight

2.4.3. Thermogravimetric analysis

A TA Instruments Q600 SDT analyzer (New Castle, Delaware, USA) was used to estimate the mass fraction of C-S-H, portlandite and their respective carbonation products in granular subsamples of the carbonated and non-carbonated microconcretes and the mass fraction of carbonate present in the fly ashes and OPC. TGA is an accepted method that has been used in many studies to quantify the mass fraction of these mineral phases in cement materials, especially portlandite, because there is little or no interference with other phases in cementitious materials in the portlandite decomposition temperature range [32-34]. For each material, TGA was conducted on duplicate subsamples of approximately 40 mg to determine the mean mass fractions of C-S-H, portlandite, calcite [$CaCO_3$], and vaterite (also $CaCO_3$ but of a less stable form). The uncertainty associated with the reported mass fractions was estimated according to the mean CV across all the materials for each phase. Each TGA run was initially equilibrated at a temperature of 50° C prior to heating to 900° C at a rate of 10.0° C/min. The chamber was continuously flushed with nitrogen throughout the heating process with a flow rate of 100 mL min^{-1}.

Literature values for the specific temperature ranges associated with mass loss from minerals phase vary slightly. For example, the temperature for decomposition of portlandite to lime and water is reported between 400° and 550° C [9, 34-36]; however, the peaks associated with mass loss from portlandite decomposition were observed in the temperature range of 400° to 500° C. For the decomposition of C-S-H, the approach of Jain and Neithalath [37] was adopted where the C-S-H fraction measured by mass loss in the temperature range from 150° to 400° C was adjusted by dividing the measured mass loss by 2.1 to account for hydrated water loss from C-S-H occurring below 150° C. Decalcification during carbonation alters the stoichiometry of C-S-H. However, since the exact stoichiometry is not well agreed upon and the amount of decalcified C-S-H in the materials relative to the amount of C-S-H is not known, the same stoichiometry to estimate C-S-H in the carbonated and non-carbonated materials was used. Therefore, C-S-H in the carbonated materials is only an estimate of the C-S-H.

$CaCO_3$ is identified by the mass loss in the temperature range between 500° and 1000° C according to the varying lower and upper temperature boundaries identified by many different literature sources which is compared and discussed in Haselbach [38]. $CaCO_3$ decomposition over this temperature range is from three different polymorphs that form during carbonation: aragonite, vaterite, and calcite [39]. Calcite forms directly during carbonation, but vaterite and aragonite form during the carbonization of C-S-H and eventually transform into calcite under extended periods of time [35] or when heating at approximately 450° C, as what occurs during TGA [40]. The calcite originating from aragonite and vaterite decomposes at a slightly lower temperature range compared to the calcite formed during carbonation [41]. Based on work done by Villain et al. and the peaks observed in this study, the temperature range of 520° to 650° C was used to identify the amount of calcite originating from vaterite [35]. Vaterite is expected to dominate in well-hydrated cements and therefore aragonite composition was not considered further in this study [42]. The temperature range of 650° to 750° C was used to determine the amount of calcite formed directly during carbonation. Higher temperature ranges associated with the decomposition of calcite originating from aggregates [34] were not evaluated.

The amount of calcium carbonate in fly ash components and OPC sample were determined from the mass loss between 520° and 750° C. This temperature range was based on observations of mass loss peaks for the FA02 and FA39 materials and is consistent with the temperature ranges for determination of vaterite and calcite in the microconcretes as well as the calcium carbonate content in other studies on fly ash materials [43, 44].

In addition, results from TGA were used to assess extent of reaction in each material by evaluating the ratio of calcium that reacted during carbonation compared to the theoretical amount of available calcium that could react (i.e., reaction capacity). Ca (g/g-material) was derived from the stoichiometry of each phase. The relationship used to determine the extent of reaction is shown in Eq. 4.

$$\text{Extent of reaction}=[\Delta(\text{Ca}_{\text{vaterite}} + \text{Ca}_{\text{calcite}})_{\text{carb,non-carb}}]/[(\text{Ca}_{\text{C-S-H}} + \text{Ca}_{\text{portlandite}})_{\text{non-carb}}] \text{ x } 100\% \qquad \text{Eq. 4}$$

Where $\Delta(\text{Ca}_{\text{vaterite}} + \text{Ca}_{\text{calcite}})_{\text{carb,non-carb}}$ is the difference in the total amount of calcium in the vaterite phase ($\text{Ca}_{\text{vaterite}}$) and total amount of calcium in the calcite phase ($\text{Ca}_{\text{calcite}}$) between the carbonated and non-carbonated material, $\text{Ca}_{\text{C-S-H}}$ is the total amount of calcium contained in the C-S-H phase of the non-carbonated material, and $\text{Ca}_{\text{portlandite}}$ is the total amount of calcium contained in the portlandite phase of the non-carbonated material.

2.4.4. Total inorganic carbon

A Shimadzu model TOC-V CPH/CPN combined with a SSM-5000A unit (Shimadzu Scientific Instruments, Columbia, MA, USA) for solid samples was used to estimate the TIC in each microconcrete and component on a mass of approximately 25 mg per material. A volume of 500 µL of concentrated phosphoric acid (85% assay) was added to each standard and sample to release CO_2. The furnace was set to 200°C and zero air at 150 mL/min was used as the carrier gas. Four-point calibration curves using a sodium bicarbonate standard for TIC were generated for an analytical mass range between 10 mg and 75 mg and were accepted with a correlation coefficient of at least 0.995. The uncertainty associated with this method was estimated according to the mean CV across all the materials.

2.4.5. Scanning electron microscopy-energy dispersive x-ray spectrometry

Scanning electron microscopy (SEM) is a common microstructural and elemental analysis tool for concrete and cement research [10, 45]. The microstructure of microconcrete materials was characterized by a combination of backscattered SEM and energy dispersive spectroscopy (EDS) to assess changes in the microstructure and redistribution of species within the material as a result of carbonation. Two interior sections from the top exposed surface of the monolith (2 cm exposed surface x 1 cm depth) were cut for each material to minimize edge effect while retaining the exposed surface. One section was sprayed with 1% solution of phenolphthalein in ethanol for an initial screening assessment to locate the approximate depth of that carbonation front to compare to the SEM analysis. The other section was exchanged with ethanol to remove any remaining pore water, embedded in epoxy, and polished until smooth and flat using a series of specialized polishing cloths with an alcohol-based lubricant Table A.2, Appendix A.

Backscattered electron SEM images (0.25 µm/pixel) and EDS data (1 µm/pixel, 500 frames per site) were collected for the carbonated and non-carbonated microconcretes in environmental SEM mode at 130 Pa, 10 keV accelerating voltage, a working distance of 10.0 mm, and a spot size of 3.0 using an FEI Quanta 650 field emission electron microscope (Hillsboro, Oregon) equipped with an Oxford Instruments 50 mm^2 silicon drift EDS detector (Abingdon, Oxfordshire, UK). A large area scan (approximately 0.9 mm along the expose carbonation edge by 2.5 mm into the matrix) was comprised of multiple smaller sites with a horizontal field width of 256 µm corresponding to a magnification of 496x. In addition, the microstructure was evaluated at a higher magnification of 1500x corresponding to an 86.6-µm horizontal field width for five randomly selected areas for each the carbonated and non-carbonated microconcrete.

The "non-cement" image components (e.g., fly ash particles, sand aggregates, and epoxy-filled pores) were segregated from the cement region in the large area EDS scans (Table A.3, Appendix A) and the remaining cement region was homogenized to remove noise in the data due to the presence of different hydration products and to better represent the changes in the chemical speciation of the cement due to degradation. Homogenization using an elemental moving average value was calculated for each pixel of the EDS map using the mean value of all pixels in a 35 x 35 pixel box centered at the pixel. A heat map indicating the ratio of calcium to aluminum+silicon (C/AS) was produced for each large area. The ratio of these elements was evaluated to normalize the EDS data between different phases. The C/AS was plotted as a function of the distance from the exposed surface using a 10% locally weighted scatterplot smoothing factor to reduce the noise of the plot.

2.5. Results

2.5.1. Material properties

Analysis of total, hydroxide, and carbonate-based alkalinity data from the titration curves (Table 2.3) revealed differences in the alkalinity between the component materials and also between microconcretes. Of the component materials, OPC had a much greater total alkalinity than either of the fly ashes which is attributed to the large hydroxide alkalinity of the OPC. FA02 had very little hydroxide, carbonate, and total alkalinity. FA39 had an intermediate hydroxide and total alkalinity compared to OPC and FA39. However, the true inflection point could not be determined for FA39 and therefore its location was estimated according to the position of the complex root located near the phenolphthalein alkalinity in the 2nd derivative of the polynomial. Therefore, the distribution of hydroxide and carbonated in FA39 may not reflect the true distribution of these alkalinities. In the non-carbonated microconcretes, the material made without fly ash replacement (M-00) had the highest alkalinity mostly attributed to the hydroxide alkalinity and the material created with the lowest alkalinity fly ash (M-02) had the corresponding lowest hydroxide and total alkalinity. These results are consistent with the alkalinity measurements in the component materials and the calcium loading in the microconcrete based on the calcium in the OPC, FA39 and FA02. Upon carbonation, the hydroxide alkalinity in the microconcretes was significantly reduced and the carbonate alkalinity increased for all microconcretes. The carbonated microconcrete material made without fly ash replacement (MC-00) had the highest hydroxide and total alkalinity compared to the carbonated materials made with fly ash. Correspondingly, the carbonated microconcrete made with the lowest alkalinity fly ash (MC-02) had the smallest total alkalinity and hydroxide alkalinity was completely eliminated. These results are consistent with the original alkalinity measurements in their respective non-carbonated microconcretes.

Table 2.3. pH and hydroxide, carbonate, and total alkalinity of the components and microconcretes (± mean CV) determined from titrating with 4 N HNO3 from natural pH to a pH of 4.5. Alkalinity measurements are expressed as mg CaCO3 per g-dry of solid material

	Natural pH (± 1%)	Hydroxide (± 6%)	Carbonate (± 23%)	Total Alkalinity (± 5%)
OPC	12.7	19.2	1.0	20.2
FA39*	12.1	7.7	3.0	10.6
FA02	10.1	0.1	0.1	0.3
M-00	12.7	3.2	0.6	3.8
M-39	12.9	2.4	0.7	3.1
M-02	12.8	2.1	0.3	2.3
MC-00	12.1	0.9	2.5	3.4
MC-39	11.4	0.1	2.7	2.8
MC-02	10.3	-	2.1	2.1

*No true inflection point determined from the FA39 titration curve

TGA (Figure 2.2) showed characteristic mass loss peaks in three general temperature regions corresponding to the temperature ranges described previously. The results in Figure 2.2 also include a peak at approximately 105° C associated with the loss of evaporable water. The first region of interest is the slow mass loss in the temperature range from 150° to 400° C and peaks near 400° C for M-00 and MC-00 which are attributed to the decomposition of C-S-H. A sharp peak in the temperature range of 400° to 500° C, associated with the decomposition of portlandite, is evident for all non-carbonated microconcretes (i.e., M-00, M-02, M-39) and also for the MC-00 carbonated material. However, no peak was observed in this temperature range for either of the carbonated materials containing fly ash (i.e., MC-02 and MC-39) and, therefore, portlandite content is not reported for either MC-02 or MC-39. The final region of interest contains the peaks associated with carbonated phases starting at a temperature of 520° C, progressing to a sharp peak beginning around 650° C, and ending around 750° C. There was a slight variation in the beginning and ending temperatures of the carbonate peaks for the three carbonated microconcrete materials. The slow rise in the carbonate peak, which is indistinguishable itself as a separate peak in the carbonated materials, may be attributed to decomposition of calcite formed from the heating of vaterite, whereas the beginning of the sharp peak may be attributed to the loss of CO_2 from the dissociation of calcite formed directly during carbonation.

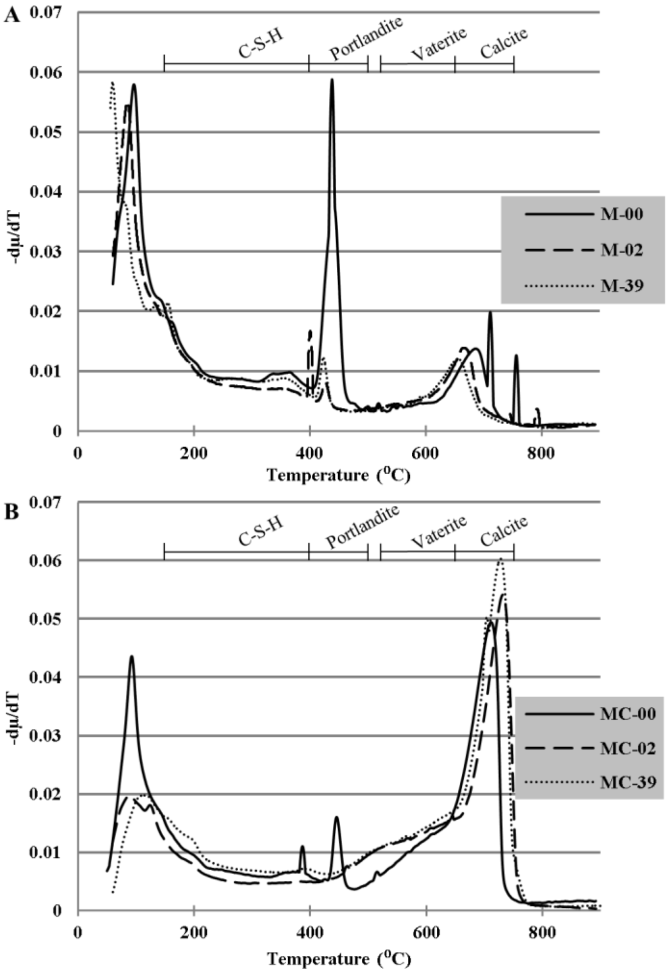

Figure 2.2. TGA results plotted as the derivative of the mass and temperature versus the temperature for one replication of the A) non-carbonated microconcretes and the B) carbonated microconcretes

The mass % of each phase derived from the mass loss associated with the described temperature ranges is summarized in Table 2.4. In addition, the last column in the table compares the percentage of reacted calcium (% Ca Reacted) that was determined from the relative changes in each of these phases between the non-carbonated and carbonated material. The extent of reaction was inversely related to the alkalinity of the original material.

Table 2.4. Mass % (± mean CV) of C-S-H, portlandite, vaterite (associated with carbonation of C-S-H), and calcite according to the weight loss of the DTG curve in the respected temperature ranges

Material	C-S-H (± 3%)	Portlandite (± 6%)	Vaterite (± 10%)	Calcite (± 9%)	% Ca Reacted (± 14%)
M-00	15.2	6.3	1.7	2.3	N/A
M-39	14.6	2.1	1.8	1.1	N/A
M-02	12.8	1.9	1.6	1.4	N/A
MC-00	12.0	2.7	3.4	6.5	26
MC-39	13.0	-	4.0	7.9	54
MC-02	9.3	-	4.0	7.8	58

A comparison of the total wt% of inorganic carbon in carbonate form in each component and the materials as determined from the Method 1313 leaching test titration (i.e., extractions), TIC (i.e., digestion), and TGA (i.e., solid) methods was calculated for comparison purposes and to assess the differences in these techniques to characterize the difference in the uptake of CO_2 during carbonation across materials with different alkalinities (Table 2.5). As expected, the wt% inorganic C determined from all three methods was higher in each carbonated microconcrete compared to their respective non-carbonated microconcrete. The inorganic C increased by approximately 1 wt% according to the alkalinity and TGA data and by approximately 2 wt% according to the TIC data from the non-carbonated to the carbonated materials. In general, the wt% inorganic C in the carbonated microconcretes increased as the alkalinity of the materials decreased according to TGA and TIC analysis. No trend between the alkalinity and the wt% inorganic C in the carbonated materials could be observed in the alkalinity data. In addition there was no trend in the wt% inorganic C in the components especially since the true inflection point could not be determined for FA39 in the titration curve. Therefore, the reported wt% inorganic C of FA39 may not reflect the actual amount of carbon contained in the material.

Table 2.5. Comparison of measured inorganic carbon (wt% ± mean CV) determined from alkalinity, TIC, and TGA in the microconcretes and their components

Material	Alkalinity (± 23%) (Titration)	TIC (± 15%) (Digestion)	TGA (± 12%) (Solid)
OPC	0.6	0.1	0.1
FA39	1.8*	0.1	<0.1
FA02	0.1	0.1	0.2
M-00	0.4	0.2	0.5
M-39	0.4	0.2	0.3
M-02	0.2	0.5	0.4
MC-00	1.5	2.1	1.2
MC-39	1.6	2.4	1.4
MC-02	1.3	2.9	1.4

*No true inflection point determined from the FA39 titration curve

2.5.2. Carbonation depth by pH using phenolphthalein indicator

The carbonation depth was initially estimated by determining the change in color of a 1% solution of phenolphthalein sprayed on a cross-section of each carbonated microconcrete. In each sample, the top exposed layer remained colorless, indicating a pH less than 10 due to carbonation while the interior portion of the sample turned bright pink, indicating the pH remained greater than 10 which corresponds to an uncarbonated region. The depth of the colorless layer varied across the surface for each microconcrete, especially near aggregates, with MC-02 showing the greatest mean depth of carbonation at 1.2 mm and MC-00 showing the smallest mean depth of carbonation at 0.4 mm. MC-39 had a mean carbonation depth at 0.7 mm which is intermediate of the indicated carbonation depths for MC-02 and MC-00.

2.5.3. Liquid-solid portioning of major constituents as a function of pH

Comparison of the calcium, aluminum, and silicon solubility curves plotted as a function of pH from Method 1313 showed the shift in pH-dependent concentration between carbonated and non-carbonated samples (Figure 2.3). For all materials, the measured natural pH decreased in carbonated samples relative to non-carbonated samples (Table 2.6) and the order of decrease was inversely proportional to the alkalinity in each sample (i.e., MC-00 had the highest natural pH and MC-02 had the lowest natural pH). The result of the shift in pH-dependent behavior and the decrease in natural pH is that the solubility of calcium at the natural pH for each microconcrete also decreased for the carbonated materials compared to the non-carbonated materials. Conversely, the solubility of silicon increased in the carbonated materials compared to the non-carbonated materials. There was no significant trend observed for the changes in the aluminum solubility curves between the carbonated and non-carbonated materials. Portions of the data relative to the calcium solubility in materials MC-00 and MC-02 has previously been reported [26].

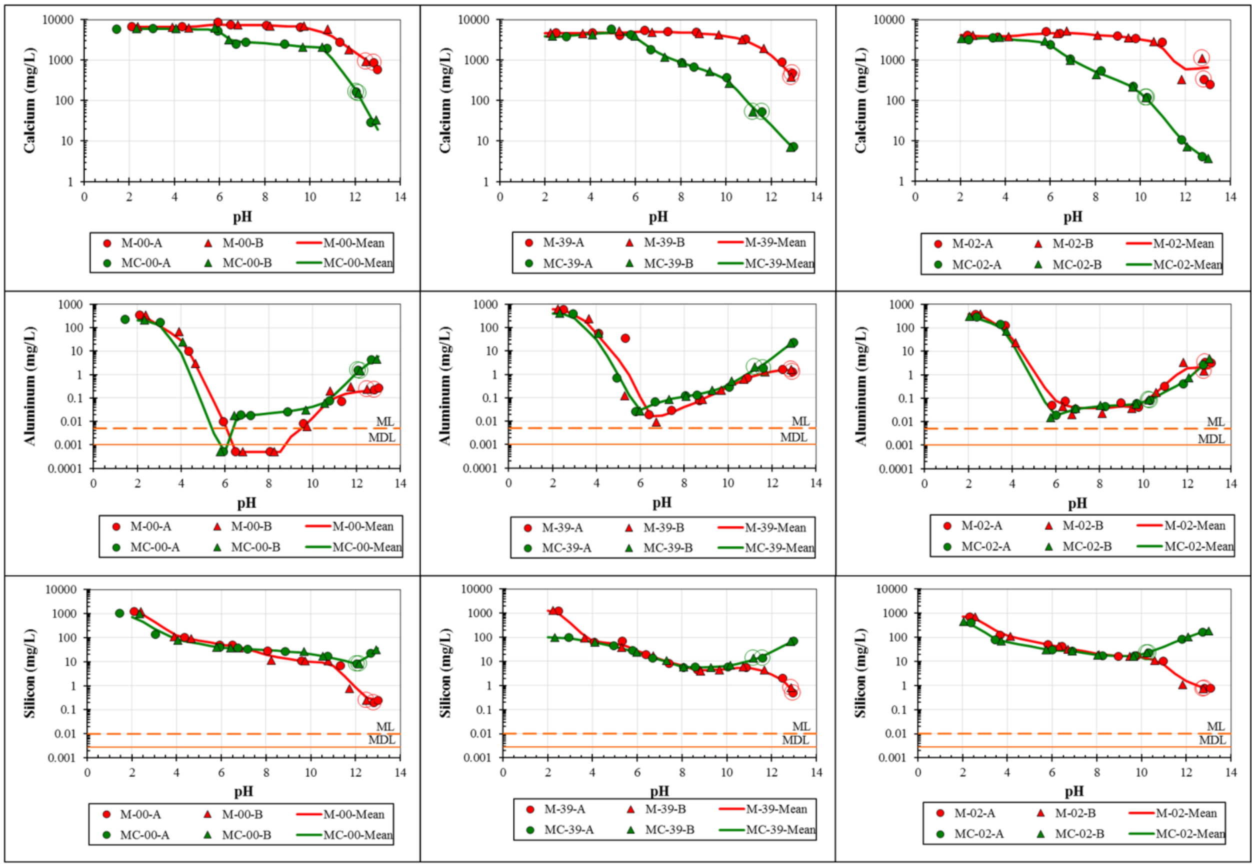

Figure 2.3. EPA Method 1313 for M-00, MC-00, M-02, MC-39, MC-39, M-02, and MC-02 with circles around data point indicating a test position at the material's natural pH.

Table 2.6. Mean solubility (mg/L) of calcium, aluminum, and silicon (± mean CV) and corresponding natural pH (± 1 pooled σ) for two replicates of each microconcrete material from EPA Method 1313

Material	Natural pH (± 1%)	Ca Solubility (± 5%)	Al Solubility (± 16%)	Si Solubility (± 10%)
M-00	12.7	902.6	0.2	0.2
M-39	12.9	426.7	1.5	0.7
M-02	12.8	1119.5	2.4	0.8
MC-00	12.1	156.2	1.5	8.1
MC-39	11.4	52.4	2.0	13.5
MC-02	10.3	117.3	0.1	22.6

2.5.4. Microstructural analysis

Backscattered electron images at 1500x and EDS maps for each microconcrete in the carbonated and non-carbonated materials revealed different elemental composition and microstructure between these two regions (representative images Figure 2.4.A-C). Additionally, the microstructure and composition was different between the three material types. A uniform carbonated phase was observed in MC-00. The bulk concentration of the carbonated region (excluding the aggregate located at the upper left hand region seen in Figure 2.4.A) was increased in calcium and decreased in aluminum and silicon content compared to the bulk of the non-carbonated material (Table 2.7). Other differences in composition for the remaining elements in Table 2.7 were observed between the carbonated and non-carbonated regions.

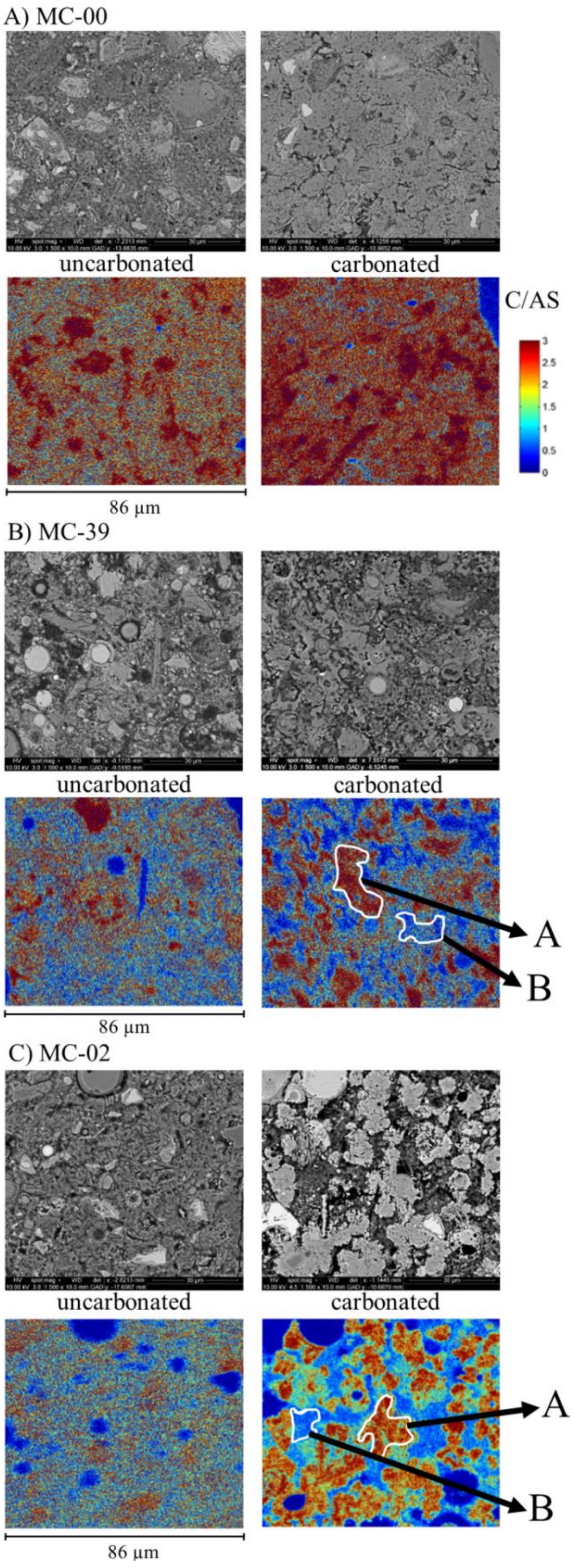

Figure 2.4. A-C: 1500x backscattered electron images and C/AS heat maps of the uncarbonated and carbonated regions of A) MC-00, B) MC-39, and C) MC-02

The heat maps of C/AS ratios for MC-02 & MC-39 shown in Figure 2.4.B & C indicate two distinct phases in the carbonated region: a region where carbonated phases (e.g., calcium carbonate) dominate (Region A, Figure 2.4.B & C) and a region where decalcified C-S-H phase is present (Region B, Figure 2.4.B & C). The presence of minor and trace constituents (i.e., Na, Mg, Al, P, S, and K) from EDS data in these regions indicate that other carbonated or calcium-silicate bearing phases exist to some degree in these two regions although the calcium carbonate and decalcified C-S-H dominate in their respective regions. These two regions are distinguished by the higher calcium and lower silicon in Region A containing carbonated phases relative to Region B containing decalcified C-S-H. In addition, the carbonate phases in Region A show decreases in the sodium, aluminum, and potassium (Table 2.7). Between the two microconcretes containing fly ash, the two separate phases were less pronounced in MC-39. The decalcification of C-S-H during carbonation conditions has been well-documented [9, 46] and observed in backscattered electron images [10] as a darker and more heterogeneous regions than the lighter more homogeneous carbonate phase. In the uncarbonated region, the backscattered electron images showed the presence of both portlandite and normal C-S-H phases.

Table 2.7. Elemental distribution (mass wt%) showing species migration between the carbonated and uncarbonated regions and the decalcification of the C-S-H gel in carbonated region in the presence of carbonated portlandite and C-S-H. The remaining mass percentage is assumed to be hydrogen, due to the presence of hydrated phases.

Material	Region	C	O	Na	Mg	Al	Si	S	K	Ca	Fe	C/AS
M-00	Uncarbonated	7.6	46.7	0.1	0.9	1.6	8.3	1.1	0.4	26.2	2.1	2.7
MC-00	Carbonated	9.1	46.3	0.2	1.0	1.4	5.6	0.9	0.8	26.4	1.8	3.8
MC-39	A	8.2	49.0	1.6	0.8	2.0	3.9	-	1.4	28.4	1.4	4.8
	B	7.6	48.8	2.6	1.0	4.3	11.7	0.2	3.2	14.4	2.8	0.9
MC-02	A	6.9	47.7	0.2	0.7	2.0	7.5	0.6	0.4	24.7	2.1	2.6
	B	8.8	47.8	0.4	0.7	3.1	15.4	0.9	2.0	12.2	2.4	0.7

Large area maps created using the 496x magnification scans revealed the formation of $CaCO_3$ either in the form or calcite or vaterite at the exposed surface of each material (Figure 2.5.A-C) and the formation of these phases was supported by TGA data (Table 2.4). In the large area maps, the carbonation depth was defined as the depth where the lighter grey carbonated products could no longer be observed in the backscattered electron image and is marked by a white line across the backscattered and C/AS maps. The smallest depth of carbonation was observed for the OPC-based microconcrete (MC-00) while increasing carbonation depths were noted for microconcretes containing fly ash (e.g., MC-39 and MC-02). The MC-02 sample had the largest carbonation depth. Measurements taken across the exposed surface (Table 2.8) showed that significant variation in the carbonation depth was observed in MC-02 and MC-39. Conversely, MC-00 had consistent depth of carbonation across the surface area; however, a smaller area of carbonation not connected to the bulk carbonation front was observed at a deeper level in the material and between two large aggregates. This remote carbonation zone may have been the result of a preferential diffusion pathway through the material pore structure during carbonation.

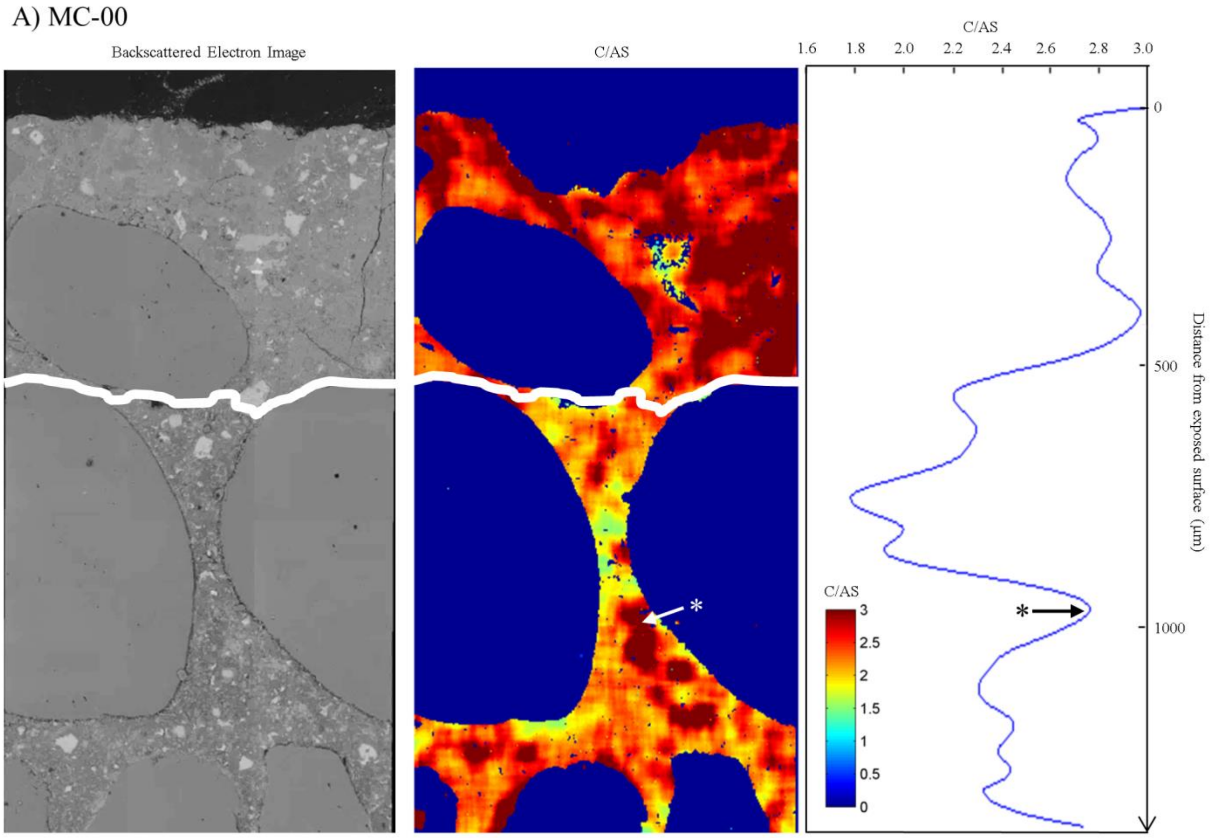

B) MC-39

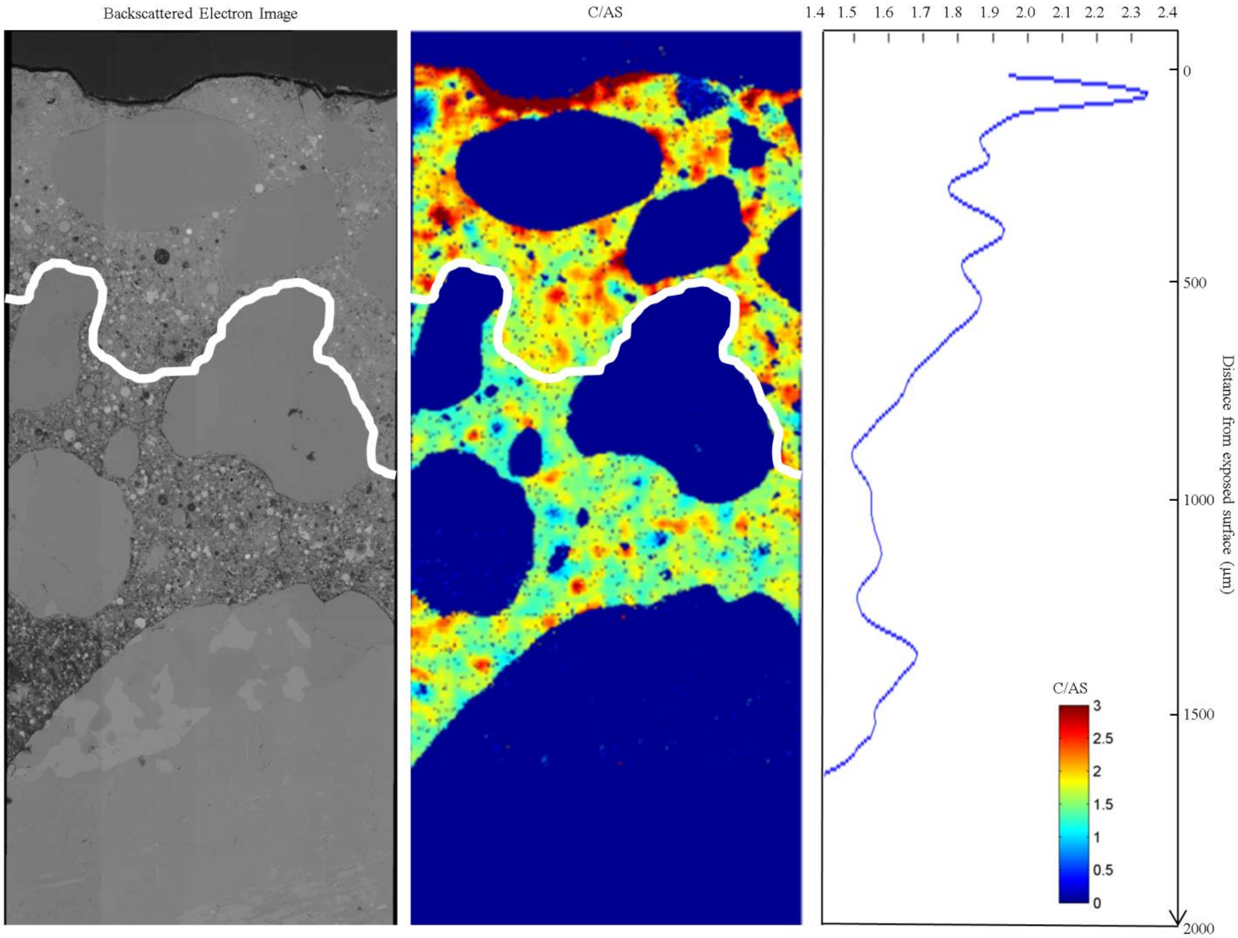
Backscattered Electron Image
C/AS
C/AS
1.4
1.5
1.6
1.7
1.8
1.9
2.0
2.1
2.2
2.3
2.4
0
500
1000
1500
2000
Distance from exposed surface (µm)
C/AS
3
2.5
2
1.5
1
0.5
0

C) MC-02

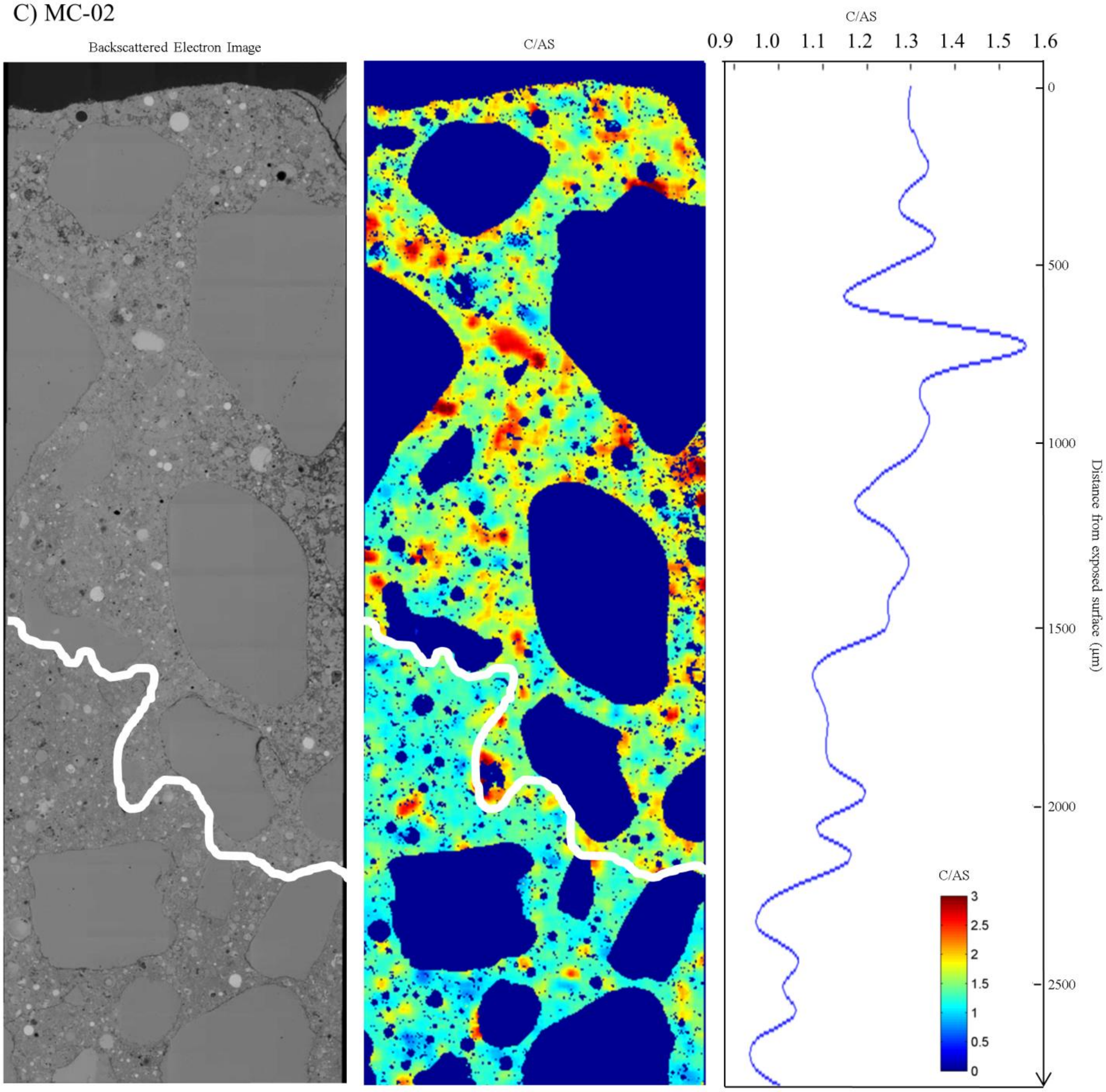

Figure 2.5. A-C: Backscattered electron image and C/AS heat map with the corresponding C/AS as a function of distance from the exposed surface for A) MC-00, B) MC-39, and C) MC-02. Dark blue areas indicate aggregates that were excluded from the heat map calculations. *The darker red region and C/AS peak highlighted is due to a small carbonated region not connected to the bulk carbonation front.

Table 2.8. Carbonation depth (mm) according to backscattered electron imaging

	Mean	Min	Max
MC-00	0.5	0.5	0.5
MC-39	0.8	0.5	1.0
MC-02	1.8	1.5	2.2

For each material, the highest C/AS were observed in the carbonated regions and the lowest ratios were observed in the uncarbonated regions according to the C/AS as a function of distance from the exposed surface plots (Figure 2.5.A-C). In MC-00, the C/AS heat map revealed a significant decrease in the C/AS at the interface of where the calcium carbonate could no longer be observed. The C/AS below this interface was slightly higher, but less than that observed in the carbonated region. The large area maps corresponding to the C/AS showed a decrease in the C/AS as the distance from the exposed surface increased. For MC-39, ratios were not evaluated below a depth of 1.6 mm because an aggregate comprised the entire image area below that depth.

For each microconcrete, the approximate calcium, silicon, and aluminum wt% in the carbonated and uncarbonated regions (excluding the aggregate and large fly ash particles) revealed an increase in the calcium content, a decrease in the silicon content, and a slight decrease in the aluminum content in the carbonated region compared to the uncarbonated region for each material (Table 2.9). This corresponds to the increase in the C/AS observed in the carbonated region. Higher C/AS in the MC-00 were observed in all regions of the sample compared to MC-02 and MC-39 because the material has a higher concentration of calcium in the mixture. A lower C/AS was observed in all regions of the MC-02 material compared to MC-39 because of the lower calcium content in the fly ash.

Table 2.9. Mean composition (mass wt%) of cement paste excluding aggregates and fly ash

	Uncarbonated Region				Carbonated Region			
	Ca	Si	Al	C/AS	Ca	Si	Al	C/AS
MC-00	23.9	8.7	1.4	2.4	24.9	7.7	1.4	2.7
MC-39	18.0	7.9	3.3	1.6	21.2	7.6	2.9	2.0
MC-02	17.1	9.9	3.0	1.3	20.0	9.2	2.8	1.7

2.6. Discussion

This study presents that results of several different, but complimentary, evaluations of carbonation in cementitious material pastes. These results serve as lines of evidence that support improved knowledge of the carbonation process including the role of matrix alkalinity in resisting the carbonation reaction and the depth of carbonate penetration, the distribution of calcium between carbonated and uncarbonated phases, and the impact of fine aggregates on the penetration of a carbonation front.

2.6.1. The role of alkalinity in carbonation

Several observations in this study support that the carbonation reaction is strongly influenced by the alkalinity of the microconcrete. Specifically, the differences in the carbonation depth and microstructure determined from SEM-EDS, measured pH determined from U.S. EPA Method 1313, and extent of reaction determined from alkalinity, TIC, and TGA measurements reveal variations between the materials and impact of material alkalinity on the carbonation reaction. The relationship between these observations and the material alkalinity is summarized in Table 2.10 and are discussed further in this section.

Table 2.10. Relationship of alkalinity and carbonation

Property	Relationship	Note
Total Alkalinity	OPC > FA39 > FA02 M-00 > M-39 > M-02 MC-00 > MC-39 > MC-02	Component alkalinity is related to alkalinity of resultant material
Carbonation Depth	MC-02 > MC-39 > MC-00	Carbonation depth ↑ as alkalinity ↓
Microstructural Changes	MC-02 > MC-39 > MC-00	Extent of microstructural changes ↑ as alkalinity ↓
Extent of Reaction	MC-02 > MC-39 > MC-00	Extent of reaction ↑ as alkalinity ↓
Reaction Capacity	M-00 > M-39 > M-02	Reaction capacity ↑ as alkalinity ↑
Natural pH	OPC > FA39 > FA02 M-00 ≈ M-39 ≈ M-02 MC-00 > MC-39 > MC-02	Natural pH ↑ as alkalinity ↑

2.6.2. Carbonation depth

Estimates of depth of the carbonation reaction front from backscattered electron imaging revealed that the depth of carbonation is inversely related to the alkalinity of the microconcrete. The mix design with the highest initial alkalinity (M-00) resulted in a carbonated material with the smallest depth of carbonation (MC-00). Conversely, the greatest penetration depth (MC-02) was observed for the mix design that provides the least initial alkalinity (M-02).

The differences in the hydroxide alkalinity in the non-carbonated microconcretes support that different reactive capacities exist across the different materials to react with calcium and CO_2 as in Eq. 2. The hydroxide alkalinity was significantly reduced in the carbonated microconcretes because of the consumption of hydroxide in this reaction. It is evident based on the increased carbonation depth and smaller hydroxide alkalinity of MC-02 and MC-39 that there is less capacity to react with diffused CO_2 and therefore unreacted CO_2 can proceed to the interior of the sample to consume hydroxide in deeper portions of the sample. In contrast, the large hydroxide alkalinity of MC-00 suggests that larger amounts of CO_2 can be consumed by the carbonation reaction in the material resulting in a smaller carbonation depth.

The intermediate penetration depth observed in MC-39 is an important finding because this case eliminates the possibility that the differences in the carbonation depth were due solely to the fly ash altering to pore structure of the material and therefore changing the diffusion properties. Although, the addition of fly ash most certainly can reduce the diffusion of CO_2 into the matrix by refining the pore structure and can change the rate of ingress of carbonation as observed in prior studies [18, 19, 47, 48], the relationship between carbonation depth and alkalinity of the three microconcretes and their components supports the conclusion that alkalinity plays an important role in controlling the depth of the carbonation front.

Thus, hydroxide alkalinity can be considered to provide a reactive capacity to the material that resists penetration of the carbonation front into the matrix. On a local level, the reactive capacity limits the transport of unreacted CO_2 until the alkalinity is consumed. The microconcretes with fly ash replacement had less initial hydroxide alkalinity (i.e., portlandite); therefore, the carbonation front penetrated further into the material than in the case of carbonation of the OPC microconcrete. This observation is consistent with the suggestions at that SCMs may lead to an increase in the carbonation ingress rate [22].

The depth measured by backscattered imaging were slightly larger in each microconcrete than the depths measured by phenolphthalein indicating that carbonation occurring near the boundary of the carbonated and uncarbonated region had not yet consumed enough free hydroxide to lower the pH below the threshold required for the color change in phenolphthalein. This suggests that backscattered imaging is a more robust and powerful tool to evaluate the depth of carbonation.

2.6.3. Microstructure

The alkalinity affects the extent of the microstructural changes observed in the carbonated materials predominantly due to the decalcification of the C-S-H gel and formation of $CaCO_3$ in the form of calcite and vaterite according to TGA results. The lower alkalinity non-carbonated materials (M-02 and M-39) showed the formation of the decalcified C-S-H phase and a $CaCO_3$ in their respective carbonated materials (MC-02 and MC-39). Because there was less hydroxide to react with CO_2, a higher extent of reaction occurred in the MC-02 compared to the MC-39. In addition, these two materials also had a higher extent of reaction compared to MC-00. MC-00 only showed the formation of $CaCO_3$ and there was no observable decalcification C-S-H because much more hydroxide from the portlandite is available to dissolve and react with diffused CO_2. MC-39 has an intermediate hydroxide alkalinity so there was less decalcification and reaction of the C-S-H phase compared to MC-02, but this decalcification and reaction was still observed to some extent. This observation is consistent with a study completed by Borges et al. [41] which concluded that smaller initial amounts of portlandite (and, therefore, less alkalinity) in cement materials due to the addition of blast furnace slag increased the extent of carbonation of the C-S-H phase. In addition, regions located near the surface of MC-02 and MC-39 had a much higher extent of carbonation because the carbonation front had passed those regions and was continuing to react at further distances in the sample. Therefore, the formation of the two distinct phases of the decalcified C-S-H and the carbonated phase could be attributed to a greater extent of reaction in those regions.

2.6.4. Extent of reaction

The differences in the alkalinities correlated to the extent of reaction and reaction capacity of hydroxide determined from TGA (Table 2.4). M-00 had a significantly larger amount of portlandite and a slightly larger amount of C-S-H due to its larger calcium concentration compared to the M-02 and M-39, indicating a higher capacity of hydroxide and calcium to react with diffused CO_2. This observation confirms the material's higher alkalinity since alkalinity is directly related to the calcium concentration. C-S-H and portlandite decreased and vaterite and calcite increased in all of the carbonated materials compared to the non-carbonated materials. Portlandite was completely eliminated in the MC-02 and MC-39 materials, whereas some portlandite remained in the MC-00. Therefore, the extent of reaction according to Eq. 4 was highest for the MC-02 and lowest for the MC-00. This supports that the extent of reaction in the microconcrete materials is a function of the original alkalinity of the material.

Differences in the wt% inorganic C values derived from alkalinity, TIC, and TGA measurements for each component and microconcrete are a result of the different limitations associated with each method to determine the exact wt% inorganic C. In the titration curve, silicates and phosphates provide additional buffering capacity which is captured as carbonate alkalinity by this method. Therefore, the measured amount of carbonate determined from the titration curve may be larger than what is in the system. In addition, titration data represents the buffering capacity of the soluble phases in the material and therefore may not reflect the composition of entire material. A limitation of TGA to determine wt% inorganic C is that only vaterite and calcite were calculated based on the stoichiometry of their decomposition over the specified temperature. Other minor carbonated phases such as magnesium carbonate are not captured by this method because 1) these phases may decompose over a different temperature range than the vaterite and calcite 2) the wt% inorganic C was derived based on the stoichiometry of the vaterite and calcite which may not capture other phases decomposing over the same temperature range. Conversely, TIC captures the inorganic carbon from all carbonated species digested during the procedure. This is reflected by the slightly larger wt% inorganic C values measured by TIC compared to TGA for the carbonated materials. Despite these limitations, the wt% inorganic C reported was relatively consistent for all three of the methods. The only major variability between the three methods occurs in the wt% inorganic C determined from titration of FA39. This may due to the lack of a true inflection point in the titration curve.

2.6.5. pH

The alkalinity of the material affected the reduction of the natural pH under carbonating conditions. MC-02 and MC-39, had further reduction in the natural pH for the carbonated microconcretes compared to the respective non-carbonated microconcretes (M-02 and M-39) as determined by Method 1313 than what was observed for the high alkalinity control microconcrete, MC-00. The mean carbonation depth of 1.2 mm determined by the phenolphthalein test for MC-02 indicates a 2 mm granular material would be fully carbonated assuming CO_2 diffused radially inward from all exposed surfaces of the granular material. A mean carbonation depth of 0.7 mm for MC-39 would not fully penetrate the material, therefore only a portion of the sample was carbonated and the natural pH indicated by Method 1313 does not represent the entire carbonated region. A mean carbonation depth of 0.4 mm for MC-00 indicates the majority of the material was not carbonated, therefore only a very slight reduction in pH was observed. Therefore, in addition to the influence of the alkalinity, these penetration depths may also be responsible for the differences in the decrease of the natural pH in the crushed carbonated microconcrete materials.

The differences that alkalinities and the influence of alkalinity in these microconcrete materials on the carbonation reaction suggest that the total alkalinity of the material could be used to determine the relative rates of carbonation depth and extent of reaction between different materials. The alkalinities of the components used in the mixtures were related to the alkalinities of the microconcretes and therefore predicting the carbonation reaction between different materials could be determined based on alkalinities of the components. Moreover, the alkalinities measurements approximated the amount of portlandite and carbonate in each system. However, characterizing the carbonation reaction as a function of alkalinity may only apply for materials with similar porosities, densities, tortuosities, relative saturations, and external CO_2 concentrations. These are additional factors that may need to be considered when estimating the overall impact of carbonation in materials with varying alkalinities.

2.6.6. Solubility of major constituents in carbonated matrices

Coupling the results of the liquid-solid portioning test as a function of pH (Figure 2.3) with the increase in concentration of calcium in the carbonated regions observed in EDS measurements (Table 2.9) suggest that calcium ions in the pore solution from the dissolution of the more soluble portlandite phase in the uncarbonated region diffuse to the carbonated region of the material where the less soluble $CaCO_3$ phase has formed. This results in a slight decalcification of the uncarbonated region and a deposition of calcium in the carbonated region as observed in the EDS heat maps for each material.

The corresponding increase in the solubility of silicon in carbonated materials and the decrease in silicon in the carbonated region also adds further evidence that the dissolution of C-S-H occurs, as discussed in terms of the influence of the alkalinity on the carbonation reaction. While calcium ions are consumed in the carbonation reaction, silicon remains in the pore solution and re-establishes equilibrium by diffusing to the less soluble uncarbonated region where it can react with calcium ions that are in greater concentration in the pore solution to potentially reform C-S-H. The formation of calcite and vaterite in these regions is supported by TGA which indicates a reduction of portlandite and C-S-H and an increase of the vaterite (from carbonation of C-S-H) and calcite phases in the carbonated samples compared to the non-carbonated samples.

Since no significant trends in the aluminum solubility were observed it is unclear whether or not the differences in the aluminum content were a result of differences in the aluminum solubility of carbonated and non-carbonated materials. However, the presence of other calcium-silicate bearing phases such as calcium aluminosilicate hydrate that are expected in cementitious materials [49] indicate that similar migration patterns could be observed if solubility is a contributing factor. Evaluation of this phase and additional calcium-silicate phases was outside the scope of this work.

2.6.7. Aggregates

The amount and orientation of aggregates may be responsible for significant variation in the observed carbonation depth across the same microconcrete. The interfacial transition zone (ITZ) may create a preferential diffusion pathway for CO_2 compared to the bulk paste as shown by the variation of the carbonation depth around the aggregates and the localized pocket in the ITZ between aggregates in Figure 2.5.A. This could be explained by the increase in porosity that is expected in the ITZ [50]. However, aggregates may also inhibit CO_2 diffusion in localized regions because the aggregates themselves are less permeable to gas diffusion compared to the cement paste. Therefore, the aggregates reduce the effective cross-sectional area for CO_2 diffusion and may inhibit the penetration of a carbonation front into the matrix. For example, the heat map for MC-00 (Figure 2.5.A) shows bottleneck region formed between two aggregates where significant decalcification of C-S-H was observed which suggests a localized reaction and limited transport of CO_2. Furthermore, aggregates composed of $CaCO_3$, such as limestone, could significantly alter the localized equilibrium conditions of the pore solution and influence the availability of calcium to react with CO_2.

Although the microconcretes studied here are composed of solely of fine aggregate and not a combination of fine and coarse aggregates, these observation are likely transferrable to concretes because the fraction of aggregates is designed to approximate the same interfacial area of concrete materials [51]. Therefore, robust efforts to model carbonation in concrete matrices should consider the amount, morphology and composition of aggregates to account for the effects of preferential pathways and effective diffusive areas. These ideas necessitate further experimental verification and complex modeling techniques which could account for the variability seen in the carbonation depth.

2.7. Conclusions

The purpose of this study was to characterize the impact of alkalinity derived from the titration curve of the material on the carbonation reaction in microconcrete materials with varying alkalinities due to the partial replacement of the Portland cement with fly ash utilizing a variety of experimental techniques to better understand and predict the long-term performance of cementitious materials containing SCMs. The main conclusions from this study are:

1. Material alkalinity derived from the titration curve of microconcrete is inversely related to the rate of carbonation and the chemical and microstructural alteration in the matrix as shown by multiple experimental characterizations. Therefore, alkalinity derived from the acid-base titration curve of the solid material and their components may provide an estimate of the potential extent of the carbonation reaction and the potential chemical and microstructural changes for other cementitious materials.
2. A powerful and robust characterization of the chemical and microstructural changes in cementitious materials due to carbonation is the result of a combination of different, but complementary analysis. SEM-EDS provides additional detailed information regarding the spatial distribution of elements and microstructural changes, and variability of the carbonation depth.
3. Differences in the solubility of phases formed during carbonation cause the migration and re-precipitation of solubility-sensitive species including calcium and silicon.
4. The quantity and orientation of aggregates can create preferential diffusion pathways for CO_2 gas in some regions of the material or inhibit CO_2 gas diffusion in others because of increased CO_2 diffusion at the aggregate-paste interface which is a consideration for complex carbonation modeling. Work to further characterize the impact of aggregates on the preferential diffusion of CO_2 is ongoing.

2.8. Acknowledgements

The authors would like to thank Rossane Delapp and Kevin Brown at Vanderbilt University for their support during this project.

This document is partially based on work supported by the U. S. Department of Energy, under Cooperative Agreement Number DE-FC01-06EW07053 entitled ‘The Consortium for Risk Evaluation with Stakeholder Participation III’ awarded to Vanderbilt University, David S. Kosson, principal investigator.

This work was also partially supported by the National Science Foundation East Asia Pacific Summer Institute program under award number 1515263.

CHAPTER 3

IMPACT OF CARBONATION ON BULK AND ITZ POROSITY IN MICROCONCRETE MATERIALS[3]

3.1. Abstract

Scanning electron microscopy was used to evaluate the porosity patterns found in microconcrete materials to better understand the gaseous diffusion pathways and reaction of CO_2 within the bulk cement paste and interfacial transition zone (ITZ) of microconcrete materials containing different fly ash replacement types. Image segmentation was applied to evaluate the porosity as a function of distance from an exposed surface in the bulk cement paste and from aggregate boundaries in the ITZ in both carbonated and non-carbonated microconcrete materials. The ITZ region remained more porous compared to the bulk cement paste for all microconcrete types after carbonation despite a change in the porosity profile across the ITZ region. Results indicate that both the carbonation reaction capacity and porosity before carbonation impact the decrease in porosity observed as a result of carbonation in the ITZ and bulk cement paste regions.

3.2. Introduction

This study aims to apply established pore and aggregate segmentation techniques [52, 53] to detect the pore space and calculate the porosity gradient in two-dimensional space – where porosity is defined as the total measured void area divided by the representative area element– in carbonated microconcrete materials without and with two different coal combustion fly ash replacement types (i.e., control with no fly ash, low Ca fly ash replacement, and high Ca fly ash replacement). Microconcretes, mortars that lack coarse aggregates but with increased fine aggregates to maintain the same aggregate-paste interfacial area, have been used as surrogates for concretes containing coarse aggregates for laboratory testing because they are easier to handle in experiments such as equilibrium-based leaching tests [2, 3]. Results from this study provide quantitative information on the combined effects of carbonation and fly ash replacement

---

[3] This chapter was reproduced with permission from: J.L.Branch, R. Epps, and D.S. Kosson., The impact of carbonation on bulk and ITZ porosity in microconcrete materials, Cement and Concrete Research 103 (2018) 170-178. Copyright 2018, Elsevier.

type on porosity specifically within the bulk cement paste as a function of distance from an exposed surface and within the interfacial transition region (ITZ) regions for carbonated microconcrete materials using backscattered scanning electron (BSE) pore segmentation. While it is well known that carbonation in cementitious materials results in a reduction of the total porosity [7, 54, 55] and fly ash replacement influences the bulk and interfacial porosity in cement-based materials [56], results from this study provide a more detailed description of the changes in the porosity caused by both carbonation and fly ash replacement for microconcrete materials. In addition, application of BSE pore segmentation methods that have been previously applied to detect porosity gradients in the interfacial transition zone for non-carbonated concrete matrices [57, 58] are applied to both non-carbonated and carbonated microconcretes in this study. These results provide a more detailed analysis of the impact of carbonation within the ITZ region and the porosity gradient across the exposed surface in the bulk for three microconcretes with different fly ash replacement. This information may be applied to other work such as characterization of the mass-transfer release of constituents from a carbonated mortar [15, 16, 59-62] or estimating the gaseous transport properties from the pore structure [63] before and after carbonation. Additionally, this study demonstrates the capabilities of BSE segmentation in comparing the porosity gradients in microconcretes containing fly ash replacement and a degraded front due to carbonation.

3.2.1. Backscattered scanning electron microscopy to detect pore space

A variety of porosity analysis techniques may be applied to cementitious materials; however, most have their own limitations in both sample preservation and accuracy. Mercury intrusion porosimetry (MIP) is one of the most common methods of pore space analysis, but studies have shown that the conditions required for accurate pore space estimates with MIP are not present in cementitious materials, resulting in lower pore diameter estimates than the expected values [64, 65]. Liquid saturation techniques have also been often explored with a reasonable degree of success [66]. However, liquid saturation techniques cannot detect differences in porosity in different regions of a material and their porosity measurements depend on a variety of factors including adequate penetration of the pores [67].

Due to the limitations of these techniques, pore space estimation from scanning electron microscopy (SEM) is desirable because of its ability to spatially characterize the porosity and determine the pore size distribution across two-dimensional sample cross-sections. SEM has been used extensively to characterize the microstructure in cement-based materials [45]. Specifically, segmentation of the concrete and cement phases on polished samples in BSE imaging has been a frequent topic of study. Through a variety of image manipulation techniques, including gray scale value thresholding and object detection and fill methods, sufficient segmentation of aggregates, various hydration products, and pore space in cement paste, mortar, and concrete samples has been achieved [52, 68-70]. Segmentation of cementitious materials provides the theoretical guidelines for BSE analysis techniques, which have now been applied to more complicated concrete and mortar systems. In addressing phase complexity, the introduction of energy dispersive spectroscopy (EDS) data supplementary to the BSE image enables a verification of the detected phase identities, which may result in more consistent segmentation of the sample image. Efforts towards implementing EDS data and reducing signal static have included advanced data clustering methods [71] and binary separation of EDS data for individual elements [53]. However, one limitation of determining porosity with BSE imaging and EDS is that pore segmentation can only detect features larger than the dimensions of a single pixel [52]. While there are many factors that impact the spatial resolution of BSE imaging and EDS (e.g., electron beam energy and atomic number), the pixel size used to acquire BSE images and EDS must consider the desired spatial resolution and expected pore size distribution. In addition, imaging with polished concrete samples may only be observed in a two-dimensional plane, which will likely result in skewed size representation of non-spherical sample features [45]. The large sample collection time, image processing time, and equipment costs of SEM data processing also make the method less accessible than many other testing methods.

3.2.2. Carbonation and the interfacial transition zone

As a naturally occurring chemical process, carbonation presents a significant limitation to the long-term durability of concrete structures, especially in the context of nuclear waste applications and buried structures. Prolonged exposure to CO_2 alters the microstructure of cement pastes and can eventually lead to corrosion of steel reinforcement, which may incur notable changes to the macroscale physical properties of both cement-based materials and the reinforcing structures [72, 73]. More efficiently and effectively understanding the extent and distribution of carbonation from gaseous CO_2 diffusion on the microscale in cementitious materials would enable an improved means of understanding concrete structures on the macroscale. One of the widely observed features of carbonation is a reduction of the total porosity in cement paste [55, 74]. This change in porosity impacts the ingress of CO_2 and can therefore impact the future rate of carbonation. Porosity is a sensitive parameter in reactive transport models for carbonation rate and constituent release [75]. Therefore, quantitative estimates of the porosity gradients across exposed microconcrete surfaces obtained in this study can be used in reactive transport modeling to provide an initial estimate of porosity before carbonation, the changes in porosity that occur after a known carbonation exposure condition, and an initial carbonation rate constant for three different microconcrete materials.

Additional variations in the porosity occur in the ITZ region which is known to have a higher porosity than the bulk cement paste due to a higher local water-to-cement ratio and difficulty bonding to the aggregates. This relationship between aggregates and cement paste has been shown to have an effect on the durability and transport properties of concrete materials [76, 77]. However, some studies have concluded that when compared to cement mortars without aggregate, the ITZ region may have limited impact on the total diffusivity because aggregates increase the tortuosity and decrease the total porosity [78-80]. Regardless, the ITZ region may provide a pathway for increased gaseous diffusion within the matrix compared to the surrounding cement paste in unsaturated materials. Estimates for ITZ width in concrete materials range from 10 to 50 µm extending from an aggregate surface [81]. Therefore, in addition to analyzing the porosity gradients associated with carbonation, this study seeks to quantify the impact of carbonation on the ITZ porosity and to quantify the porosity in the ITZ as a function of distance from aggregate boundaries in carbonated and uncarbonated regions of carbonated microconcretes and in non-carbonated microconcretes using BSE imaging and EDS.

3.2.3. Impact of fly ash on the microstructure

In efforts to improve waste management techniques, reduce the need for virgin cement, and improve the performance properties of concrete materials, fly ash has been widely used in many concrete mixtures as a supplemental cementitious material [3]. The presence of fly ash alters the concrete microstructure, which typically results in a change to the total porosity depending on the chemistry and physical properties of the fly ash. For example, fly ash fineness has been shown to impact the total porosity in cement mortars [82]. In addition, the impact of calcium concentration in fly ash used to replace Portland cement investigated by Papadakis showed mortars prepared with high calcium fly ash reduced the porosity of the material compared to the control mortars without fly ash while mortars prepared with low calcium fly ash increased the porosity of the material compared to the control [47, 83]. Therefore, the methods in this study for detecting pore space differences in carbonated and uncarbonated regions in carbonated microconcretes and in non-carbonated microconcretes are applied to a microconcrete without fly ash and microconcretes with fly ash replacement using two different fly ash types.

3.3. Materials and methods

3.3.1. Microconcrete properties

Using mix designs and material properties presented in Kosson et al., 2014 [2, 3] and also summarized in supplemental Tables B.1-B.3, Appendix B, a microconcrete control group and two sets of differing coal combustion fly ash types were prepared with ordinary Portland cement and fine aggregates using a water-to-binder ratio of 0.45. These materials were designated as M-00 (i.e., control with no fly ash), M-39 (i.e., 45% cement replacement with high calcium fly ash), and M-02 (i.e., 45% cement replacement with low calcium fly ash) respectively. Each set of microconcrete mixtures was divided into a carbonation treatment group and a secondary control group. Both groups were cured for an initial six months at 100% relative humidity (RH) in sealed buckets. The control (i.e., ‘non-carbonated’) groups (M-00, M-39, M-02) were cured an additional six months in the sealed buckets, while the carbonated groups (MC-00, MC-39, MC-02) were aged for an additional six months at 65% RH in a 5% CO_2 concentration environment. A RH of 65% was chosen because results from relative saturation testing at 65% RH indicate unsaturated conditions for all three microconcretes (Table B.4, Appendix B) which facilitates gaseous transport. A concentration of 5% CO_2 was chosen because it is within the expected range of soil gas CO_2 concentrations [84, 85]. The use of higher CO_2 concentrations in carbonation experiments compared to ambient air CO_2 concentration becomes especially important when evaluating the long-term performance of nuclear waste forms and barriers which are disposed of in the vadose zone [86], as well as for other buried structures. In addition, a 5% CO_2 concentration represents accelerated aging conditions compared to ambient air aging conditions (i.e., ~0.04% CO_2) that allows for measureable carbonation depths within reasonable amounts of time. Previously, studies such as Morandeau, Thiéry, and Dangla, 2014 [9] used a concentration of 10% CO_2 because they determined concentrations ≤10% CO_2 are not expected to result in significantly different microstructures when compared to natural carbonation based on previous observations [87-90].

After curing and carbonation treatment, the samples were extracted from their molds and cut so that a cross-sectional area running perpendicular to the carbonated surface could be evaluated. The samples were then potted in epoxy resin, polished, and mounted for SEM analysis. Further details of the SEM sample preparation can be found in Branch et al., 2016 [91] and are also presented in supplemental Table B.5, Appendix B.

3.3.2. SEM scanning conditions

SEM samples were collected with an FEI Quanta 650 Scanning Electron Microscope (Hillsboro, Oregon, United States) and Oxford Instruments AZtec (Abingdon, Oxfordshire, United Kingdom) SEM processing software. All scans were collected in environmental SEM mode at 130 Pa, 10keV, and a spot size of 3.5. EDS data was collected with a map resolution of 1.0 μm^2/pixel with 300 frames per acquisition area and with a process time of 5. BSE data was collected with an image resolution of 0.0625 μm^2/pixel. The EDS map resolution was reduced relative to the BSE image resolution in order to shorten the combined scan time without compromising BSE image quality. Four areas parallel the sample boundary by fourteen areas parallel to the one-dimensional diffusion pathway were collected for each sample at with a 10% overlap area at a 496x magnification and a horizontal field width of 256 µm. All 56 sites comprised an area of approximately 1 x 3 mm and were montaged to form a single large area for image processing. For each set of sample aging conditions, two sample scans were collected at discrete positions along the epoxy-sample interface.

3.3.3. SEM data processing scripts

3.3.3.1. EDS segmentation

EDS and BSE data were imported and processed using MATLAB (Version 8.3.0.532, The MathWorks, Inc., Natick, MA, 2014). EDS segmentation based on carbon and silicon threshold values was applied to the image area in order to isolate the bulk cement paste from the epoxy used for sample preparation and from the aggregates (Figure 3.1). Carbon was used to segment the epoxy region because the concentration of carbon is much greater in the epoxy relative to the sample. Silicon was used to segment aggregates because the aggregates used in the mixture contain a much greater concentration of silicon relative to the bulk cement paste. Threshold values for carbon and silicon were determined from the probability distribution function of the EDS counts of each element across the image. The carbon threshold value was applied to the image and coupled with object detection and fill methods to detect and remove the epoxy region. Similarly, the silicon threshold value was applied to the image and coupled with object detection and fill methods to detect and remove aggregate regions. In addition, detected aggregate regions with an area <625 μm^2 were removed from the collection of detected aggregates because there is a potential for high concentrations of silicon in small localized regions of the bulk cement paste which could be artificially detected as aggregate space. Analysis of the aggregate particle size distribution indicates that <1% of the total aggregate volume is attributed to aggregates smaller than this area, assuming particles are relatively similar in density regardless of diameter according to the aggregate sieve analysis in Branch et al. [91] and Table B.2, Appendix B. In the event of incompletely segmented sample aggregates, a supplementary manual segmentation was performed. Manual segmentation was only required for aggregates with high aluminum content and therefore did not meet the silicon threshold criteria. Manual segmentation was also performed to remove large air voids > 50 µm in diameter (i.e., air voids with diameters > 5% of the sample image width) because they disproportionately affect the bulk porosity estimates in the relatively small scan areas used. A new BSE image, 'segmented BSE image', was generated with the aggregates, epoxy boundary, and large air voids removed. Estimated threshold values for the silicon (mean= 34%, s=9 %) and carbon (mean= 16 %, s=4%) showed consistency among all the samples.

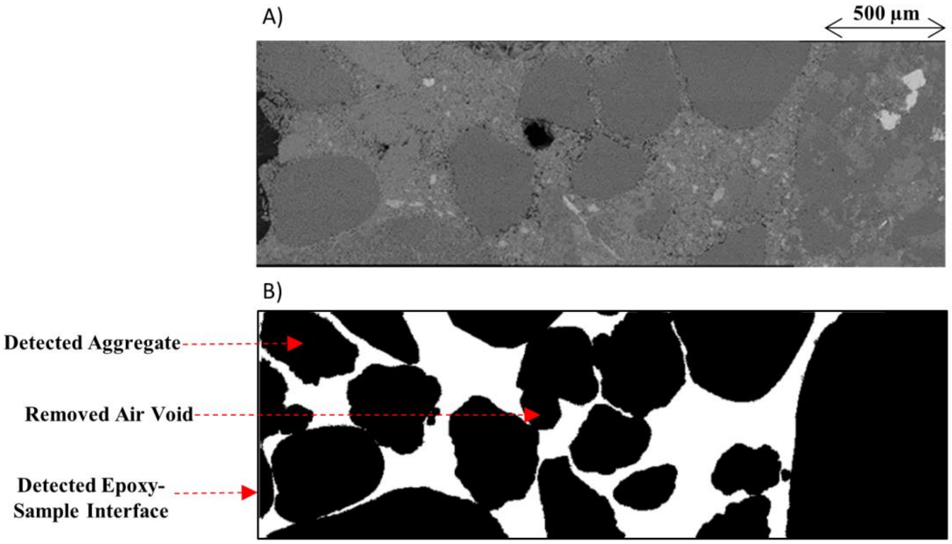

Figure 3.1. M-00 example for A) initial BSE image and B) bulk cement paste region (white) isolated from aggregates, epoxy, and air voids (black) using carbon and silicon EDS data and manual segmentation

3.3.3.2. Pore space detection

Pore space detection was performed using the segmented BSE image and the overflow method discussed in Wong, Head, and Buenfeld [52]. The overflow method calculates the threshold for pore space based on the intersection of the tangent lines of the two linear portions in the cumulative BSE image curve. The threshold value for pore space detection is then considered to be 90% of that value because the original threshold may overestimate the true overflow point. Any scaled signal intensity value below the calculated threshold was then considered to be pore space in the segmented BSE image. Yio, Wong, and Buenfeld have previously investigated the accuracy of the overflow method using 3D Monte Carlo simulation of BSE images of pore and calcium silicate hydrate (C-S-H) boundaries. The authors reported that the overflow method results in errors ~1% for pores ≥1 µm at 10 keV in ideal imaging conditions [92].

3.3.3.3. Interfacial transition zone evaluation

While estimates of ITZ width range from 10 to 50 µm [81], the complexity of the concrete system and close proximity of fine aggregates inhibits the observation of trends occurring over a larger range. Based on the detectable observations in the ITZ, its width is initially estimated at the minimum literature value of 10 µm when segmenting the region from the bulk cement paste in the following evaluations. Using MATLAB object detection on the EDS segmented aggregates, the aggregate borders were determined for the entirety of the sample image, and the ITZ was considered to be the 10 µm distance directly surrounding these detected borders. Any pixel in the BSE image located at a Euclidean distance ≤10 µm from any pixel detected as an aggregate was incorporated into the ITZ region. Further analysis included ITZ porosity measurements from a varied width of an assumed ITZ from 10 µm to 40µm. From each point in the determined borders, an estimated ITZ was expanded radially into the bulk cement paste. The mean porosity as a function of Euclidean distance from all the aggregates' borders was calculated and plotted in increments of 0.25 µm for both uncarbonated and carbonated regions.

3.3.3.4. Overall pore space estimates

The mean porosity of the carbonated region, uncarbonated region, and non-carbonated microconcretes was also evaluated for each microconcrete to compare the relative differences in both the bulk cement paste porosity and ITZ porosity of these regions. The bulk cement paste porosity which excludes aggregates and the ITZ region is hereinafter defined as the total measured area of pores within the bulk cement paste region divided by the total area of the bulk cement paste region. The ITZ porosity is hereinafter defined as the total measured area of pores within the ITZ region divided by the total area of the ITZ region. The mean porosity of the bulk cement paste was calculated across the entire scan area of the segmented BSE image for the each non-carbonated sample. In addition, the mean porosity in all ITZ regions was calculated across the entire scan area of the segmented BSE image for each non-carbonated samples. In the carbonated samples, the approximate location of the carbonated-uncarbonated interface was defined based on visual inspection of microstructural changes (i.e., formation of calcium carbonate) observed in the BSE image. The mean porosity of the bulk cement paste excluding the ITZ and the mean porosity in all ITZ regions were calculated separately for the carbonated region and for the uncarbonated region based on the defined location of the carbonated-uncarbonated interface in each microconcrete.

3.3.3.5. Pore space heat mapping of the bulk paste

Using a spatial averaging of approximately 7.56 µm^2 (i.e., 2.75 x 2.75 µm) on the estimated binary pore space matrices in the bulk paste including the ITZ, regional pore space frequency mapping (referred to as ‘heat maps’) of the relative pore space frequency was performed. The heat mapping script selects a pixel location and then counts the number of registered pores within the spatial averaging field centered on that pixel and assigns the sum value to the same pixel location in a new integer matrix. The field is shifted until each pixel has been evaluated and assigned a value in the new matrix. MATLAB’s “jet” color mapping is applied to the matrix and the values are scaled to a fraction of the occupied moving field so that higher porosity regions are shown as red and lower porosity regions are shown as blue.

3.3.3.6. Porosity as a function of distance from the carbonation front

The cross-sectional interface between the microconcrete sample and epoxy backfill was designated as the origin of the diffusion front and this position was set to 0 on the x-axis. The porosity was then calculated for each unit of distance along the x-axis by taking the percentage of pore space along the identified bulk cement paste region excluding the ITZ region for each column of pixels parallel to the origin of the diffusion front. The ITZ region was excluded from the pore space mapping to reduce variability in the porosity due to heterogeneity in size and location of aggregates in the matrix. In addition, a 100 column (i.e., 25 µm) moving mean of the porosity was calculated. This measurement of porosity as a function of distance from the carbonation front assumes that bulk gaseous diffusion occurs uniformly in the x-direction as a bulk approximation of likely preferential pathways along the ITZ.

3.4. Results

3.4.1. Overall bulk and ITZ porosity in non-carbonated and carbonated microconcretes

The porosity of the bulk cement paste and ITZ of each non-carbonated microconcrete, the uncarbonated region of each carbonated microconcrete, and the carbonated region of each carbonated microconcrete were compared (Table 3.1).

Table 3.1. Measured mean bulk cement paste porosity and measured mean ITZ porosity (±1 pooled standard deviation, sp=0.02) of the non-carbonated (NC) microconcretes and the uncarbonated region (UC) and carbonated region (C) in the carbonated concretes. The difference in porosity between the UC and C and the bulk cement paste to the ITZ are reported as an absolute difference and as a percent difference.

	Mean Porosity (± 0.02)			Difference
	NC	UC	C	UC to C
00- Bulk	0.07	0.06	0.03	-0.03 (-50%)
00- ITZ	0.12	0.12	0.10	-0.02 (-17%)
00- Bulk to ITZ Difference	+0.05 (+71%)	+0.06 (+100%)	+0.07 (+233%)	
39- Bulk	0.06	0.06	0.01	-0.05 (-83%)
39- ITZ	0.08	0.08	0.02	-0.06 (-75%)
39- Bulk to ITZ Difference	+0.02 (+33%)	+0.02 (+33%)	+0.01 (+100%)	
02- Bulk	0.12	0.10	0.10	0 (0%)
02- ITZ	0.19	0.15	0.14	-0.01 (-7%)
02- Bulk to ITZ Difference	+0.07 (+58%)	+0.05 (+50%)	+0.04 (+40%)	

The microconcrete prepared with high calcium fly ash, M-39, had the lowest bulk and ITZ porosities and the microconcrete prepared with low calcium fly ash, M-02, had the highest bulk and ITZ porosities. This relationship was also observed in the uncarbonated and carbonated regions of the respective carbonated microconcretes, with the exception that equivalent bulk porosities were obtained in the uncarbonated regions for MC-00 and MC-39. The measured bulk porosity for the non-carbonated microconcretes was slightly higher in M-00 and M-02 compared to the respective bulk porosity in the uncarbonated regions of MC-00 and MC-02.

Carbonation resulted in a decrease in the measured mean bulk porosity and ITZ porosity for each microconcrete type in the carbonated region compared to the respective uncarbonated region and compared to the respective non-carbonated microconcrete with the exception that equivalent bulk porosity measurements were obtained for the uncarbonated and carbonated region of MC-02. MC-39 had the greatest percent difference and MC-02 had the least percent difference in the measured porosity between the uncarbonated and carbonated regions for both the bulk and ITZ regions.

The measured mean ITZ porosity was greater compared to the measured mean bulk porosity in all regions and for all microconcrete types. M-00 and MC-00 had the greatest percent difference in the measured porosity between the bulk and ITZ regions. The concept of higher porosity occurring in the ITZ of the sample is further supported through visual inspection of the heat maps directly surrounding the aggregates as shown for an example aggregate in Figure 3.2. The red regions directly surrounding sample aggregates suggest that the porosity in the ITZ is notably higher than the porosity occurring in the bulk cement paste.

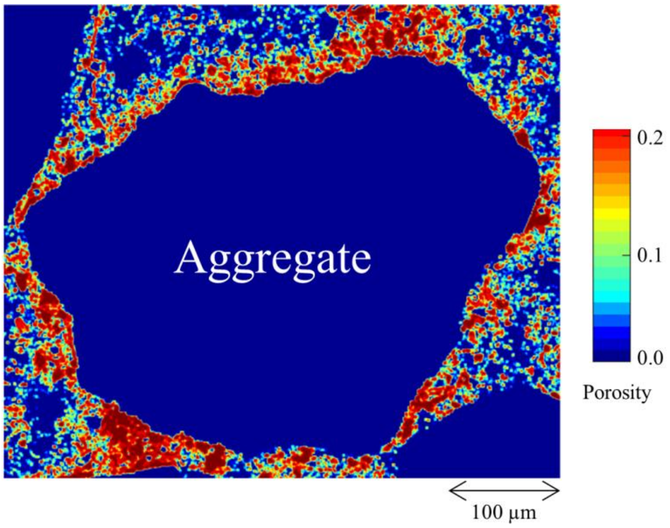

Figure 3.2. Heat mapping of pore distribution near the boundary of an aggregate in sample M-02. Note that in order to show the contrast between the detected pore space of the aggregate and that of the ITZ, the central aggregate has not been segmented in this image.

3.4.2. Porosity gradient in carbonated samples

When moving from the carbonated region to the uncarbonated region in each carbonated microconcrete, an increase in the porosity at the carbonated-uncarbonated interface was observed in the heat mapping on the segmented BSE images and in the measured mean column porosity gradient plot (Figure 3.3Figure 3.5). The transition, defined as the location where the moving mean column porosity begins an initial and sustained increase, occurred at a mean depth of 0.5 mm, 0.9 mm, 1.4 mm for MC-00, MC-39, and MC-02, respectively. These measurements are comparable to the depth of carbonation determined by phenolphthalein previously reported as 0.4 mm, 0.7 mm, and 1.2 mm for MC-00, MC-39, and MC-02, respectively [91]. In contrast, the non-carbonated microconcretes initially have a higher porosity at the exposed surface and do not express the two distinct porosity regions in interior regions of the sample, but do show variation in the measured porosity across the exposed surface that correspond to areas with high proportions of aggregate.

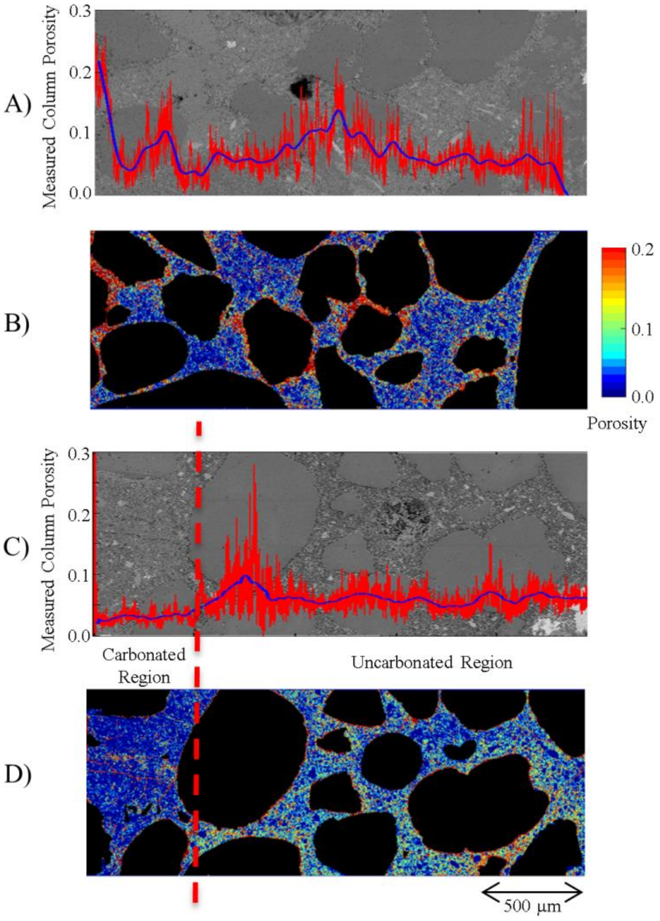

Figure 3.3. X-axis bulk cement paste porosity gradients (red) with a 100-column moving mean (blue) overlaid onto the respective BSE images for A) non-carbonated M-00 sample and C) carbonated MC-00 sample and the corresponding heat maps of the detected pore space distribution including the bulk cement paste and ITZ for the B) non-carbonated M-00 sample and D) carbonated MC-00 sample. Black areas in the heat maps represent the detected epoxy, aggregates, and large pores that were excluded in the pore space gradients.

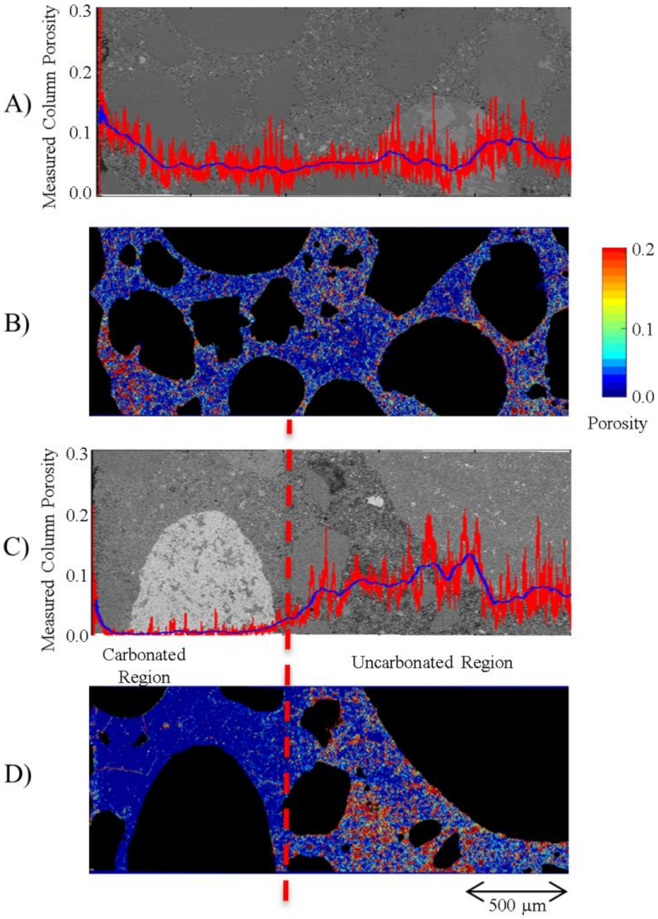

Figure 3.4. X-axis bulk cement paste porosity gradients (red) with a 100-column moving mean (blue) overlaid onto the respective BSE images for A) non-carbonated M-39 sample and C) carbonated MC-39 sample and the corresponding heat maps of the detected pore space distribution including the bulk cement paste and ITZ for the B) non-carbonated M-39 sample and D) carbonated MC-39 sample. Black areas in the heat maps represent the detected epoxy, aggregates, and large pores that were excluded in the pore space gradients.

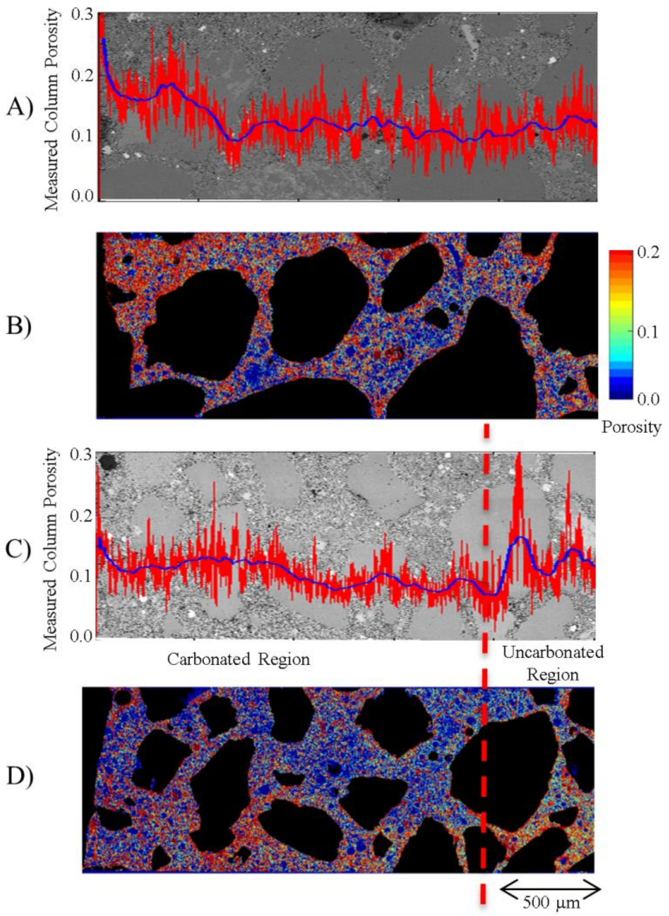

Figure 3.5. X-axis bulk cement paste porosity gradients (red) with a 100-column moving mean (blue) overlaid onto the respective BSE images for A) non-carbonated M-02 sample and C) carbonated MC-02 sample and the corresponding heat maps of the detected pore space distribution including the bulk cement paste and ITZ for the B) non-carbonated M-02 sample and D) carbonated MC-02 sample. Black areas in the heat maps represent the detected epoxy, aggregates, and large pores that were excluded in the pore space gradients.

3.4.3. Interfacial transition zone porosity gradient

The mean porosity as a function of distance from all the aggregates showed an initial increase in porosity as the distance from the aggregate increased in the first ~ 2 µm from the aggregate boundary followed by a gradual decrease in porosity as the distance from the aggregate increased in both the uncarbonated and carbonated regions (Figure 3.6). The ITZ porosity in the carbonated region approached the bulk porosity at smaller distances from the aggregates for all carbonated microconcretes compared to the respective ITZ porosity in the uncarbonated region.

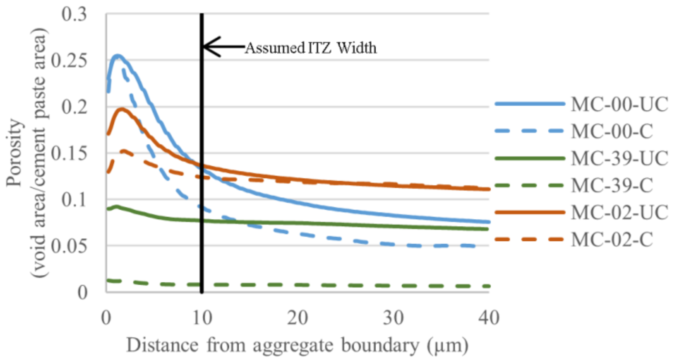

Figure 3.6. Calculated ITZ porosity as a function of the assumed ITZ width for all aggregates in the uncarbonated region and for all aggregates in the carbonated region for each carbonated microconcrete (one replicate per microconcrete type shown). The vertical black line indicates the 10 µm ITZ width assumed in this study.

3.5. Discussion

3.5.1. Impact of fly ash addition on bulk porosity

The measured porosity value was smallest for microconcrete prepared with high calcium fly ash replacement (i.e., M-39) and largest for the microconcrete prepared with low calcium fly ash replacement (i.e., M-02) in both the bulk and ITZ regions. The control microconcrete without fly ash (i.e., M-00) had an intermediate measured porosity. The porosity values obtained in this study coupled with previous observations in Papadakis [47, 83] confirm that the calcium concentration of fly ash used to prepare cementitious materials can provide an indication of the expected relative differences in porosity of cementitious materials. Moreover, the increase in porosity for cementitious materials prepared with low calcium fly ash, as observed for M-02 in this study, suggest increased potential for gaseous CO_2 to diffuse into interior regions based on work by Houst and Whittmann [93] that previously related effective CO_2 diffusivity as a function of porosity.

3.5.2. Non-carbonated and uncarbonated porosity comparison

Slightly different bulk cement paste and ITZ porosities were obtained between the respective non-carbonated and uncarbonated regions across the samples. Bulk cement paste porosity was elevated in approximately the first 100-400 microns of the exposed surface in the non-carbonated microconcretes (Figure 3.3-Figure 3.5). This elevated porosity inflates the mean bulk cement paste porosity obtained for the M-00 and M-02 non-carbonated microconcretes compared to the mean porosity values in the bulk of the uncarbonated region for the respective microconcretes. This suggests that cutting the microconcretes after demolding and before treatment creates an artificially elevated porosity at the exposed surface. As a result, CO_2 may diffuse more rapidly at the exposed surface of microconcrete materials which may increase the initial rate and extent of reaction in microconcrete materials. An initially elevated porosity was not observed at the exposed surface in carbonated microconcretes possibly because after the carbonation exposure time, the impact of carbonation on porosity dominates over the initial effects observed from cutting. This suggests the diffusion and subsequent reaction of CO_2 may progress more slowly after the initial carbonated layer is formed due to a reduction in porosity at the exposed surface relative to a non-carbonated microconcrete.

Other reasons for the differences in porosity obtained in the non-carbonated microconcretes compared to the uncarbonated region of the carbonated microconcretes may be a result of different saturation levels within the materials. Carbonation is a water generating reaction which may elevate the saturation level in carbonated microconcretes. In addition, carbonation reduces the porosity at the exposed surface which may limit the exchange of water with the surrounding environment. Therefore, the porosity may evolve differently over the 6 month aging conditions in 65% RH because of the different saturation levels in the non-carbonated microconcretes compared to the carbonated microconcretes.

3.5.3. Carbonation in the bulk cement paste

The carbonated-uncarbonated interface determined from the transition in the bulk cement paste porosity occurred at slightly larger depths compared to the depth of carbonation determined by phenolphthalein. This indicates that a measurable reduction in porosity may occur after enough available hydroxide in the pore solution has been consumed to reduce the pH below the phenolphthalein indicator color. An accurate measurement of the carbonation depth after an initial exposure time is important when predicting carbonation depths after longer exposure times. For RH above 50%, the relationship between carbonation depth, x_c (mm), and the carbonation rate proportionality constant, A (cm/day$^{1/2}$), as a function of carbonation exposure time, t (days), has been simplified by Papadakis and Fardis, 1989 [7] as:

$$x_c = A\sqrt{t} \qquad \text{Eq. 5}$$

Therefore, x_c identified by the change in porosity rather than by phenolphthalein may be more appropriate to estimate A in Eq. 5. Under this assumption, the estimated A is 0.037, 0.067, and 0.104 mm/day$^{1/2}$ for MC-00, MC-39, and MC-02, respectively, for the conditions used in this study (i.e., 65% RH, 5% CO_2, and 180 day carbonation exposure time).

Previously, Branch et al. [91] reported decreasing alkalinities with corresponding decreases in the carbonation reaction capacities for M-00, M-39, and M-02, respectively. Greater microstructural changes after carbonation were observed in MC-39 and MC-02 relative to MC-00. However, these changes in the microstructure did not translate to significant differences in the measured porosity between the uncarbonated and carbonated regions of MC-02. This may be due to the small reaction capacity in this microconcrete and therefore a reduced potential to react with CO_2 to form carbonated products that decrease the porosity despite the consumption of all available calcium hydroxide. Therefore, microconcretes with lower alkalinities (i.e., reduced reaction capacity) and higher porosities may continue to experience high CO_2 diffusion rates because the pore structure at the exposed surface does not undergo significant changes during carbonation.

In contrast, M-39 has a smaller reaction capacity compared to M-00 and a larger reaction capacity compared to M-02, yet there was a greater difference between the uncarbonated and carbonated porosities in the MC-39 compared to MC-00 and MC-02. However, MC-39 has a lower porosity compared to both MC-00 and MC-02 which indicates that changes in the porosity as a result of carbonation is a property of both the reaction capacity and initial porosity. The smaller porosity in MC-39 may result from a decrease in the pore size distribution due to refinement of the microstructure incited by high calcium fly ash. The impact of pore size on the carbonation reaction is further described in the next section.

3.5.4. Interfacial transition zone porosity

Several studies have previously shown that a region of higher porosity exists in the ITZ and that the porosity in this region is a function of distance from the aggregate boundary in non-carbonated mortars [58, 94-96]. Results from Table 3.1 and Figure 3.6 show that these effects are observed in both non-carbonated microconcretes and in uncarbonated and carbonated regions of carbonated microconcretes for all microconcrete types.

The percent difference between the bulk cement paste porosity and ITZ porosity was greatest for control microconcrete without fly ash in the non-carbonated sample (i.e., M-00) compared to the two non-carbonated microconcretes with fly ash (i.e., M-39 and M-02). In addition, the percent difference between the bulk cement paste porosity and ITZ porosity was greatest in the uncarbonated and carbonated regions of MC-00 compared to the respective regions in MC-39 and MC-02. This is consistent with prior observations that the addition of fly ash refines the ITZ region in cementitious materials [97-99]. Moreover, the percent difference between the bulk cement paste and the ITZ porosity in the carbonated region is especially exaggerated in MC-00 compared to MC-39 and MC-02. Therefore, the ITZ region in microconcretes without fly ash may have a greater impact on CO_2 diffusion compared to microconcretes with fly ash.

In Figure 3.6, the porosity initially increases across the first ~2 µm of the ITZ in all regions before decreasing after ~2 µm. This may be due to the spatial resolution of 1 μm^2/pixel in the EDS map used to segment the aggregates which may limit the accuracy of the measured ITZ porosity in the first ~1 µm due to a potential overlap of the aggregate and ITZ region in the first pixel identified as ITZ region surrounding the aggregates. Additionally, an increased deposition of calcium hydroxide and C-S-H may increase the porosity in the first ~2 µm because aggregate surfaces may serve as a nucleation site for these phases [58, 100]. At distances > 2 µm from the aggregate boundary, the porosity decreases and approaches the porosity of the bulk cement paste.

The ITZ porosity in the carbonated region porosity approaches the porosity of the bulk cement paste at smaller distances compared to the uncarbonated regions in all microconcretes which suggests that carbonation reduces the width of the ITZ region possibly by reacting with the thin film of calcium hydroxide or C-S-H at the aggregate surface and at the outer region of the ITZ. The reaction at the outer region of the ITZ region may be explained by the elevated porosity in the ITZ region which suggests a larger pore size distribution in the ITZ compared to the bulk cement paste. Larger pores are expected to be less water-filled in unsaturated conditions due to capillary action and therefore contain larger amounts of gaseous CO_2. Despite an increased availability of gaseous CO_2, less dissolved calcium is available in the pores to react with the CO_2 in the ITZ region. This effect is further exaggerated since the carbonation reaction produces water and therefore less water will be produced in this region to create water-filled pores to further dissolve calcium hydroxide and C-S-H. Therefore, the preferential reaction may occur at the ITZ-bulk interface where there is more dissolved calcium to react with diffused CO_2. This indicates the ITZ region may remain the preferred diffusional pathway for gaseous CO_2 because they may remain less water-filled due to higher porosities compared to the bulk cement paste.

The assumed 10 μm width in this study may yield artificially low mean ITZ porosities in carbonated regions because it incorporates some of the bulk cement paste and in parallel may yield artificially high mean ITZ porosities in uncarbonated regions because lower porosity regions at further distances from the aggregate in the ITZ region are not incorporated in the mean measurements. However, varying the ITZ width for each aggregate and region was outside the scope of this work because the development of the ITZ region is also a function of the size and chemistry of the aggregate [101] and aggregates used to prepare the microconcretes are heterogeneous in both size and composition. Moreover, the ITZ width may vary depending on the extent of carbonation at different depths in the carbonated layer based on Figure 3.6.

3.5.5. Application of BSE segmentation to carbonated microconcretes with fly ash

Several observations in this study indicate that the overflow method of pore space detection proposed in Wong, Head, & Buenfeld [52] with modifications made in this study can be effectively applied to carbonated microconcretes containing aggregates and fly ash to determine the depth of carbonation, the impact of carbonation on the porosity as a function of depth from the exposed surface, the differences in ITZ region porosity and the bulk cement paste porosity, and the porosity as a function of distance from aggregate boundaries. The supporting observations include: i) visual inspection of the isolated bulk cement paste region from fine aggregates (Figure 3.1), ii) the measured porosity values for the ITZ region in all samples were larger compared to the bulk cement paste regions (Table 3.1) which agrees with prior experimental knowledge for non-carbonated cementitious materials [58], iii) a notable increase in the measured porosity when moving from a carbonated to an uncarbonated region in all carbonated microconcretes was observed (Figure 3.3Figure 3.5), iv) carbonation depths identified by porosity changes are similar to the carbonation depth determined from phenolphthalein [91], and v) consistent porosity values were measured in the non-carbonated microconcretes at all exposure depths and variation was due to increased presence of aggregates (Figure 3.3Figure 3.5). Therefore, application of this method may be appropriate to further characterize the pore structure changes due to carbonation in microconcrete materials with fly ash and aggregate. In addition, the relative differences in porosity measurements obtained from the modified BSE pore segmentation method, possibly in combination with other porosity characterization methods to account for the resolution limits of BSE, can be appropriately applied to future work using reactive-transport modeling to predict the mass-transfer release of constituents from carbonated microconcretes.

3.6. Conclusions

The overflow method applied to BSE imaging coupled with EDS segmentation to characterize the porosity gradient across the exposed surface and in the ITZ regions in microconcretes was successfully applied to non-carbonated and carbonated microconcretes with and without fly ash replacement. Differences in the measured porosity in the non-carbonated microconcretes indicate that the calcium concentration in fly ash used to prepare the microconcretes may provide an indication of microconcrete porosity. For pores measured by BSE imaging, carbonation was observed to decrease the porosity in both the bulk and the ITZ region of all carbonated microconcretes. Differences in the measured porosity changes across each microconcrete after carbonation suggest that both the reaction capacity and pore size distribution determine the extent of microstructural changes. Elevated measured porosities in the ITZ region compared to the bulk cement paste was observed before and after carbonation and this effect was especially exaggerated for the microconcrete containing no fly ash after carbonation. For all microconcrete types, the measured ITZ porosity was found to be a function of distance from the aggregate boundary in both uncarbonated and carbonated regions and carbonation reduced the width of the ITZ.

3.7. Acknowledgements

The authors would like to thank Andrew Garrabrants and Rossane DeLapp at Vanderbilt University for their support during this project.

This document is partially based on work supported by the U. S. Department of Energy, under Cooperative Agreement Number DE-FC01-06EW07053 entitled ‘The Consortium for Risk Evaluation with Stakeholder Participation III’ awarded to Vanderbilt University, David S. Kosson, principal investigator.

Summer support for R. Epps was provided by the Vanderbilt School of Engineering Summer Research Program.

CHAPTER 4

MICROSTRUCTURAL CHARACTERISTICS AND LEACHING BEHAVIOR OF AGED CAST STONE CEMENTITIOUS WASTE FORM[4]

4.1. Abstract

The mineralogy, microstructural characteristics, and leaching behavior of a cementitious waste form for low activity nuclear waste aged in an inert unsaturated environment and in a reactive unsaturated environment containing oxygen and carbon dioxide was investigated. Greater amounts of aragonite, calcite, and vaterite were formed for the material aged in the reactive environment due to the reaction of alite, belite, tobermorite, and Na_2SO_3/Na_2SO_4. A greater amount of gypsum was also observed for the material aged in the reactive environment, likely due to an increased availability of SO_4^{2-} from the oxidation of SO_3^{2-} and from carbonation reactions that favor more dissolution of SO_4^{2-} in to the pore water solution. For the material aged under the reactive scenario, the sodium and sulfur concentration was reduced in the carbonated region with a corresponding increase in sodium and sulfur concentration observed in the uncarbonated region as a result of a wetting-drying front that may have been created by the carbonation reaction in an unsaturated aging environment. Carbonation appears to increase the porosity of the material as supported by several porosity measurement techniques and the mass transport (dissolution and diffusion) controlled release of potassium, lithium, and sodium, possibly both as a result of increased cracking and an overall decrease in molar volume. Differences in the mass transport controlled release of other constituents for the two aging scenarios are attributed to differences in element solubility, material pH, and porosity of the two materials.

4.2. Introduction

Approximately 100 million gallons of high level waste (HLW) was generated in the United States from nuclear weapons production during the 1940's to early 1990's. This HLW has been

---

[4] The results from this chapter are being incorporated in to two manuscripts: 1) J.L.Branch, D.S. Kosson, and A.C. Garrabrants. Microstructural characteristics of an aged cementitious waste form. *Expected submission February 2018*. 2) J.L.Branch, D.S. Kosson, and A.C. Garrabrants. Leaching behavior of an aged cementitious waste form.

stored in underground tanks at the Hanford Site, Savannah River Site (SRS), Idaho National Engineering Laboratory, and West Valley Site [102-104]. Ongoing remediation efforts by the U.S. Department of Energy at these sites mandates that the HLW in the tanks must be retrieved, treated, and properly disposed. A cementitious waste form known as cast stone, is being investigated as a treatment method prior to near-surface disposal for a portion of the low-activity waste (LAW) and secondary waste generated from the treatment of HLW [105]. A similar treatment process is also being used for LAW at SRS's Saltstone Disposal Facility in the form of saltstone (analogous to cast stone but of slightly different blast furnace slag and Portland cement compositions) followed by bulk disposal in large concrete vaults [106].

A key performance concern for cast stone is that the integrity of material could be compromised in the presences of reactive gases, namely oxygen and carbon dioxide, which can alter the chemical and physical characteristics of the material. Changes in the chemical and physical microstructure may ultimately lead to release of radioactive constituents and other constituents of potential concern. For example, gaseous oxygen can react with redox sensitive species in the waste to change their solubility [107]. Additionally, a significant amount of work has been done to study the impact of carbonation on cementitious materials. These studies have shown that gaseous carbon dioxide can react with dissolved constituents in the pore solution to change the material's mineralogy, pH due to reaction of hydroxide, and porosity [7, 16, 54, 55, 91, 108]. However, unlike traditional cementitious materials, cementitious materials for LAW or secondary waste disposal do not contain aggregates and contain very little ordinary Portland cement (OPC). In addition, the complexity of the waste stream and the presence of long-lived radioactive isotopes, such as technetium-99 and iodine-129, present significant challenges to protect human health and the environment under the extended time period required for safe disposal scenarios using cast stone. Therefore, it is expected that the chemical and physical characteristics of these materials will differ considerably from more typical cementitious materials and the materials may behave differently under aging conditions than performance predicted based on initially cured material. However, studies evaluating the effects of aging conditions on cementitious waste forms such as cast stone and saltstone have been very limited, and the impacts of combined carbonation and oxidation on the properties of this class of materials is unclear.

The objective of this study was to characterize the mineralogy, microstructure, and leaching properties in cast stone after aging in an inert environment and reactive environment containing oxygen and carbon dioxide to better understand the impact of aging on the chemical, physical, and leaching properties of cast stone. Evaluating the mineralogy and microstructure provides a basis for evaluating the impact of aging on the physical and chemical integrity of cast stone materials. In parallel, evaluating the leaching properties including constituent solubility and diffusivity after aging may help predict the long-term potential performance for disposal methods using cast stone. Furthermore, characterizing the impact of aging in cast stone may provide additional insights on the long-term integrity for other related cementitious materials waste forms such as saltstone.

4.3. Materials and methods

4.3.1. Cementitious waste form preparation and aging

The general approach in this study was to prepare a reducing cementitious waste form reflective of the family of cementitious waste materials that is currently being considered for use at the Hanford Site in Richland, WA and the SRS in Aiken, SC and then to age them under non-reactive and reactive (i.e., presence of gaseous O_2 and CO_2) environments. The prepared reducing cementitious waste form evaluated in this study hereinafter is referred to as cast stone. The oxide composition of the dry ingredient portion of the cast stone used in this study was compared to other reducing cementitious waste forms that are being evaluated at the Hanford Site and SRS as presented in Table C.1, Appendix C. The specific steps for preparing and aging the cast stone materials used in this study are presented in the following sections. Portions of these steps have previously been described in Branch et al. [109]. Additional aging scenarios and reducing cementitious waste form compositions were also evaluated as a part of this dissertation work. However, inclusion of this data was outside the scope of this particular chapter. Therefore, the preparation steps and leaching data obtained from these additional materials and aging scenarios is presented as supplementary material in Appendix C.

4.3.2. Dry ingredients

Cast stone samples were prepared using an 8:45:47 weight ratio of a Type I/II OPC, Class F coal combustion fly ash, and grade 100 ground granulated blast furnace slag (GGBFS), respectively. The OPC was sourced from a local concrete batch plant facility. The fly ash was obtained from Savannah River National Laboratory (SRNL) and is representative of the fly ash currently being used in their saltstone mixtures. The GGBFS was obtained from the Pacific Northwest National Laboratory (PNNL) and is representative of the GGBFS currently being considered in Hanford Site's cast stone formulations. The oxide composition of each dry ingredient (Table 4.1) was determined from x-ray fluorescence (XRF) using an S4 Explorer X-ray Spectrometer (Bruker-AXS, Germany). Table 4.1 also includes the oxide composition from the resultant cast stone mixture prepared with salt waste simulant (see section 4.3.3) after 28 days of curing.

Table 4.1. Oxide composition (wt.%) from XRF of the dry ingredients and resultant cast stone mixture prepared with salt waste simulant after 28 days of curing.

Element	**OPC**	**Fly Ash**	**GGBFS**	**CS-28 day**
Al_2O3	5.67	34.60	14.40	18.00
CaO	61.20	1.19	40.20	27.30
Cr_2O_3	ND[1]	ND	ND	0.32
Fe_2O_3	3.59	6.48	0.63	4.97
K_2O	0.45	2.53	0.53	1.49
MgO	3.18	1.35	4.57	2.10
MnO	0.11	ND	0.21	0.13
Na_2O	0.50	0.44	ND	7.47
P_2O_5	0.16	0.30	ND	0.34
SiO_2	20.00	51.60	32.40	34.30
SO_3	4.78	ND	6.33	2.22
TiO_2	0.28	1.19	0.39	0.97

[1] ND=Non-detect, where the detection limit is 0.1%

4.3.3. Salt waste simulant preparation

A significant amount of work has been completed by previous groups to develop a salt waste simulant that is representative of the anticipated LAW stream from the waste treatment plant to be solidified and disposed of in the form of cast stone or glass [110, 111]. The Hanford Tank Waste Operations Simulator (HTWOS) simulant from these studies was selected to be used in this work. The specific HTWOS simulant selected was the HTWOS overall average final LAW simulant after charge balancing with reduced fluoride and phosphate to prevent precipitation in the simulant as was observed in prior studies [110, 111]. However, radionuclides, RCRA metals, and other underlying hazardous constituents typically present at very low to trace concentrations were not considered in this study and therefore were not added to the simulant. High purity chemical regents, as listed in Branch et al., 2017 [109], were added to achieve the desired molarity for each waste constituent listed in Table 4.2.

Table 4.2. HTWOS overall final LAW simulant concentration

Waste Constituent	**Molarity (mol/L)**
Na^+	5.0
K^+	0.035
Al^{3+}	0.305
Cl^-	0.04
F^-	0.03
SO_4^{2-}	0.085
PO_4^{3-}	0.05
NO_2^-	0.565
NO_3^-	1.62
CO_3^{2-}	0.275
TOC Total	0.075
Free OH^-	1.56

Chromium, in the form of sodium chromate, was added in the amount necessary to achieve a 0.1 wt.% loading in the final cast stone mixture. Chromium was used as a redox indicator species for technetium. Technetium is a key radionuclide of concern in the waste stream because of its potential increased water-borne mobility (e.g., in the vadose zone and groundwater) after oxidation due to interaction with environment [112]. Therefore, specifically analyzing the behavior of chromium in this work provides additional data that can be used to better understand the changes in the waste form performance under aging conditions where chromium is a useful indicator species sensitive to changing redox conditions and carbonation effects.

4.3.4. Cast stone mixing

The dry ingredients (i.e., OPC, fly ash, and GGBFS) were hand-mixed until homogenized. Simulant was added to the dry ingredients in the amount necessary to achieve a water-to-binder (w/b) ratio of 0.48. The dry ingredients and simulant were mixed with a stand mixer using the mixing times specified by the ASTM Standard C305-14 [113].

The cast stone mixture was poured in to 2.54 cm cylindrical diameter molds filled to a height of approximately 7 cm. The molds were capped and placed in a 100% nitrogen-filled environmental chamber maintained at 100% relative humidity (RH) for 3 days. Samples were then demolded and placed back in to the environmental chamber for a total of 100 days of curing in 100% N_2 and 100% RH.

4.3.5. Aging conditions

Following the 100-day curing period, samples were divided in to two treatment groups: 1) non-reactive aging scenario in an inert nitrogen environment and 2) reactive aging scenario in an environment with oxygen and carbon dioxide. Within each treatment group, two physical forms of the materials were prepared: 1) 1-D diffusion monolithic form (prepared cylinders) and 2) granular material. The monolith forms were prepared by epoxying the cast stone cylinders in plastic molds. The top surface was removed by dry sawing to create a flat epoxy-free exposure surface for 1-D diffusion. The granular materials were prepared by crushing the cast stone cylinders (after 100 days of curing) through a parallel plate grinder until 85 wt.% of the material was < 2 mm in diameter. Materials were handled in nitrogen-filled glove bags to the extent possible throughout the physical preparation steps to minimize exposure to oxygen and carbon dioxide.

The monolithic and granular materials were aged in parallel for 60 days. The non-reactive aging group (CS-N) was aged in an environmental chamber maintained at 100% N_2 and 65% RH. The reactive aging group (CS-OC) was aged in an air-filled environmental chamber maintained at 65% RH. CO_2 gas was injected in to the chamber to maintain a 5% CO_2 environment throughout the reactive aging scenario. The 5% CO_2 concentration represents conditions that may be expected for soil gas concentrations in the vadose zone [84, 85] where cast stone may be ultimately be disposed of in concrete vaults or a lined landfill. A RH of 65% was selected because it has previously been shown that the carbonation rate in cementitious materials reaches a maximum at intermediate RH levels [114, 115].

4.3.6. X-ray diffraction

The mineralogy of CS-N and CS-OC was determined from x-ray diffraction (XRD) using the PANalytical Alpha-1 instrument (Malvern Panalytical, The Netherlands) with a 0.016^0 2θ step size with 0.9 seconds per step from 10^0 to 75^0 for a total scan time of approximately 60 minutes. Samples were crushed to a fine powder in a nitrogen-filled glove bag prior to analysis and dried in a vacuum until constant mass. An internal standard, high purity rutile, was added in 1:10 mass rutile/mass material to the powdered cast stone. The Rietveld method was performed for each scan. Crystalline minerals selected in the Rietveld method were based on previous literature results for similar cementitious waste forms [116-118] and probable phases identified by the X'Pert HighScore Plus software [119]. The crystal structures used in the Rietveld analysis were obtained from the American Mineralogist crystal structure database [120] and the Crystallography Open Database [121].

4.3.7. Thermogravimetric analysis

Thermogravimetric analysis (TGA) is a useful technique to estimate the mass fraction of phases including calcium silicate hydrate (C-S-H), portlandite, and calcite in cementitious materials [32-34, 91]. However, cast stone contains very little OPC content with high quantities of fly ash and GGBFS. Therefore, cementitious materials such as portlandite may not form in the hydrated cast stone. In this study, TGA was used to help validate the presence of mineral phases identified from XRD and was not used as a quantitative method.

TGA was performed on the granular CS-N and CS-OC materials using a TA Instruments Q600 SDT analyzer (New Castle, Delaware, USA). Each sample was run in duplicate using approximately 40 mg of granular material per analysis. A heating rate of 10.0° C/min was used to heat the sample from approximately 50 to 900° C. Nitrogen gas was continuously flushed through the chamber at a flow rate of 100 mL min^{-1} during the analysis.

4.3.8. Total carbon analysis

The total carbon concentration in CS-N and CS-OC was measured using a Shimadzu model TOC-V CPH/CPN combined with a SSM-5000A unit (Shimadzu Scientific Instruments, Columbia, MA, USA). A volume of 500 µL of concentrated phosphoric acid (85% assay) was added to approximately 25 mg of solid material in order to release CO_2. The furnace was set to 200°C and zero air (carbon dioxide free) at 150 mL/min was used as the carrier gas. Duplicate analysis was performed for each cast stone material.

4.3.9. Total porosity

The total porosity (η_{ex}), defined as the ratio of the volume of pores (V_p, cm^3) to the total volume of the material (V_T, cm^3), of CS-N and CS-OC was obtained using a modified water exchange method (Eq. 6 and Eq. 7) that was previously developed to measure the total porosity in cast stone [122]. The modified water exchange method is a gravimetric measurement method derived from ASTM C642 [123]. However, the modified water exchange method obtains the saturated weight of the sample by equilibrating the sample in a 100% RH environment rather than immersing the sample in a liquid because of the presence of highly soluble salts in the solid matrix. Immersing the sample in water could artificially inflate the measured porosity due to the dissolution of the matrix. The modified water exchange method assumes that the solid matrix will reach near 100% saturation in a 100% RH environment because of hygroscopic behavior.

2 cm thick disks were cut from the top exposed surface of CS-N and CS-OC and equilibrated in 100 % RH until a constant mass was observed (m_{sat}, g). The samples were briefly submerged in water and the submerged weight was measured (m_{sub}, g). The samples were oven dried at 65°C until equilibrated to a constant mass (m_{dry}, g). The presence of dissolved constituents in the pore water necessitates the use of a correction factor (F_{sol}, cm^3/g) to account for the density of the pore

water solution and concentration of salts in the pore water. The density of the pore water solution (ρ_{sol}, g/cm^3) and concentration of salts (c_{salt}, g_{salt}/cm^3_{sol}) in CS-N and CS-OC were obtained by a batch leaching extraction using the granular CS-N and CS-OC forms at a low liquid-to-solid ratio of 1.0 mL/g according to U.S. EPA Method 1316 [124].

$$\eta_{ex} = \frac{V_p}{V_T} = \frac{m_{sat} - m_{dry}}{m_{sat} - m_{sub}} * F_{sol} \qquad \text{Eq. 6}$$

$$F_{sol} = \frac{1}{\rho_{sol} - c_{salt}} \qquad \text{Eq. 7}$$

4.3.10. MicroCT imaging

In addition to measuring the total porosity, is desirable to analyze the porosity as a function of distance from the exposed surface. Therefore, microCT imaging was performed using a Scanco Medical AG µCT 50 (Brüttisellen, Switzerland) to evaluate the 3-D porosity gradient across the exposed surface of the CS-N and CS-OC monoliths. 1200 slices were collected on approximately the top 4 mm of each sample with an energy of 70 kV, an intensity of 200 µA and 2000 projections per rotation. Each slice had a diameter of 35.2 mm, a voxel size of 4.3 µm, and an integration time of 2.4 seconds. The porosity, $\eta_{\mu CT}$, was determined for each slice by calculating the number of voxels below a threshold grayscale value in the slice relative to the total number of voxels in the slice. The grayscale threshold value was first estimated based on the histogram of representative slices and then adjusted using user judgment to eliminate noise and improve segmentation. Only the inner 21 mm diameter of each slice was analyzed in order to eliminate the impact of beam hardening in the porosity analysis. A moving average of the porosity for each slice was calculated by averaging the porosity of the current slice and the porosities of the 19 slices proceeding inward into the sample. Samples used for microCT analysis were not perfectly level at the micron scale and therefore some of the initial top slices were not completely occupied by sample space. Therefore, the 0 mm position of the exposed surface was determined from visual analysis based on when the entire field of view was completely occupied by the sample.

4.3.11. Microstructural analysis

Scanning electron microscopy (SEM) with energy dispersive x-ray spectroscopy (EDS) is another technique that can analyze the porosity as a function of distance from the exposed surface. SEM-EDS analyzes the pore structure in essentially 2-D space, but it can provide a much greater resolution compared to microCT imaging and can also provide chemical analysis of the microstructure. Therefore, SEM-EDS was used to evaluate the porosity as a function of distance from the exposed surface and the elemental distribution in the aged monoliths.

Two monolithic forms from each aging scenario were cut perpendicular to the exposed surface to obtain a cross-sectional area for analysis and dried in a vacuum chamber. The cut samples were mounted in a low viscosity epoxy and allowed to cure for 48 hours. After the epoxy had cured, the top 40 mm of the exposed sample was cut from the entire epoxied sample. A sample geometry of 40 mm in length was chosen because it represents a sample size that is manageable for SEM-EDS analysis. This length is also large enough to incorporate the carbonated area which reaches a depth of approximately 25 mm previously measured by phenolphthalein [109] and several mm of uncarbonated area in the carbonated material.

Samples were polished using a series of finer grit sand paper and diamond polishing clothes. Formula B Lube (Electron Microscopy Sciences, Hatfield, PA, USA) was used as the polishing lubricant in order to minimize the dissolution of soluble constituents in cast stone during the polishing procedure.

Polished cast stone samples were analyzed using a FEI Quanta 650 field emission electron microscope (Hillsboro, Oregon, USA) equipped with an Oxford Instruments 50 mm^2 silicon drift EDS detector (Abingdon, Oxfordshire, UK). All scans were performed in environmental SEM mode maintained at a pressure of 130 Pa using an accelerating voltage of 10 keV, spot size of 3.5, and a working distance of 10.00 millimeters. A horizontal field width of 256 µm corresponding to a magnification of 496x was used for each scan area.

SEM-EDS data was collected in the Aztec software of the Oxford Software Suite (Oxford Instruments, Abingdon, Oxfordshire, UK). Prior to collection of SEM-EDS data, a beam optimization within Aztec was performed on a titanium standard. Backscattered scanning electron (BSE) images were collected using a pixel resolution of 1024 x 943 (i.e., 0.25 µm/pixel). EDS area maps were collected using a pixel resolution of 256 x 224 (i.e., 1 µm/pixel) with 300 EDS frames per site, a 100 µs pixel dwell time, and processing time of 5. The montage feature within Aztec was used to collect several scan areas across the exposed surfaces of CS-N and CS-OC. A total of 1 mm of the exposed surface area x 30 mm in depth from the exposed surface area were analyzed for both CS-N and CS-OC. Quantitative analysis was performed for each EDS area map.

The total porosity, defined as the area of measured pores divided by the total scan area, as a function of distance from the exposed surface using BSE imaging (η_{BSE}), was measured using the approach in Branch, Epps, and Kosson, 2018 [108] for CS-N and CS-OC. However, segmentation of aggregates was not required in this study because cast stone lacked aggregate. A mean porosity value from the BSE imaging was also calculated for the C-N material and within the carbonated region of the CS-OC material over an area of approximately 1 x 5 mm for each material.

Heat maps of the chemical composition were also generated for a large area map (i.e., ~0.6 x 1 mm) collected over the transition region (i.e., carbonated to uncarbonated region) in the CS-OC sample to better understand the behavior of constituents across a carbonated front. A moving average of the chemical composition was also plotted with the heat maps to better represent the chemical composition profiles moving across the transition region.

From the large area scans, representative scans of the CS-N and the carbonated region near the exposed surface in CS-OC were further evaluated. EDS heatmaps of the measured concentrations in the representative areas were generated for constituents measured above detection limit in the EDS.

4.3.12. Leaching tests

U.S. EPA Method 1313 [125], a liquid-solid partitioning as a function of extract pH using a parallel batch extraction procedure at a liquid-to-solid ratio of 10 mL/g-dry, was used to characterize the pH-dependent leaching properties of the CS-N and CS-OC granular materials. The milli-q (MQ) water used in the test was bubbled with nitrogen gas, referred to hereinafter as "de-oxygenated MQ", to de-oxygenate the water in order to prevent oxidation occurring during the leaching test. The de-oxygenated MQ along with nitric acid or potassium hydroxide were added to the granular material in the amounts necessary to achieve the target pH points specified while maintaining a liquid-to-solid ratio of 10 mL/g-dry. However, due to the limited buffering capacity of the material, especially in the neutral pH region for CS-OC, some of the specified pH points in the test were difficult to obtain. Therefore, the tolerance level for the pH target points specified by the test was relaxed. Inductively coupled plasma optical emission spectrometry (ICP-OES) and inductively coupled plasma mass spectrometry (ICP-MS) were used to evaluate the concentration of constituents in the eluate at each pH point. Ion chromatography (IC) could not be used to measure the concentration of anions of interest (e.g., NO_2^-, NO_3^-, SO_4^{2-}) because NO_3^- was present in such large concentrations in the eluate at all batch extraction points.

The hydroxide and carbonate alkalinity for CS-N and CS-OC were calculated from the acid/base neutralizing capacity (ANC/BNC) obtained in Method 1313 using Standard 2320 from the Standard Methods for the Examination of Water and Wastewater [31]. A titration curve was fit to the ANC/BNC data points using a best fit fourth degree polynomial for each material. From the calculated titration curve, the amount of acid required to reach the phenolphthalein end point of 8.3 was used to determine the hydroxide alkalinity (mol_{H+}/kg_{solid}) of each material. The amount of acid required to lower the pH from the phenolphthalein end point to the total alkalinity end point of 4.5 was used to calculate the carbonate alkalinity (mol_{H+}/kg_{solid}) of each material.

U.S. EPA Method 1315 [126], a mass transfer test, was performed on the monolithic CS-N and CS-OC materials. However, the 63 day cumulative leaching time specified in the method was extended using additional two-week exchange intervals for a total cumulative leaching time of 133 days. The extended leaching time provides a better description of the long-term leaching behavior in cast stone and allows more time for the leaching front to move through the large carbonation front (~25mm) in the CS-OC. A chemical resistant Tygon tubing was sealed around the top portion of the exposed surface to hold the eluate and was capped with a rubber stopper. Therefore, only the top surfaces exposed during in the aging conditions were exposed to the eluate. This experimental approach allows for a 1-D liquid diffusional front across the aged surface to occur during the test. 50 ml of the de-oxygenated MQ was used as the exchange volume for an approximately liquid-to-surface area of 10 mL/cm^2. For each exchange interval, the pH of the eluate was measured and the concentration of constituents in the eluate was measured using ICP-OES, ICP-MS, and IC.

4.4. Results and discussion

4.4.1. Cast stone composition and mineralogy after aging

The mean total measured carbon was 0.8 wt. % for CS-N and 3.3 wt. % for CS-OC. It is assumed the higher carbon concentration in the CS-OC is from an increase of inorganic carbon due to the uptake and reaction of CO_2.

Analysis of the peaks obtained in XRD for the CS-N and CS-OC (Figure 4.1) using the Rietveld Method and known rutile standard concentration (Table 4.1) showed significantly larger amounts of the calcium carbonate phases (i.e., aragonite, calcite, and vaterite) and gypsum in the CS-OC material compared to the CS-N material. 11Å tobermorite, a crystalline form of C-S-H, and belite, a non-reacted cement clinker phase, were only found in the CS-N material. Due to peak overlap and potential for other forms of tobermorite to form in the system, the 11Å tobermorite identified from the peaks in CS-N is hereinafter generally referred to as “tobermorite”. Alite, another type of non-reacted cement clinker phase, was significantly depleted in the CS-OC material compared to the CS-N material. Mullite was present in the form of $Al_{2.8}S_{1.2}O_{9.6}$ according to the closest identified crystal structure. Less mullite of this stoichiometry was measured in the CS-OC compared to CS-N. More potassium nitrate was measured in the CS-OC compared to CS-N. Nitratine and quartz were detected in both CS-N and CS-OC but the differences in concentrations between CS-N and CS-OC were relatively small. The amorphous content was smaller in the CS-OC material compared to the CS-N material.

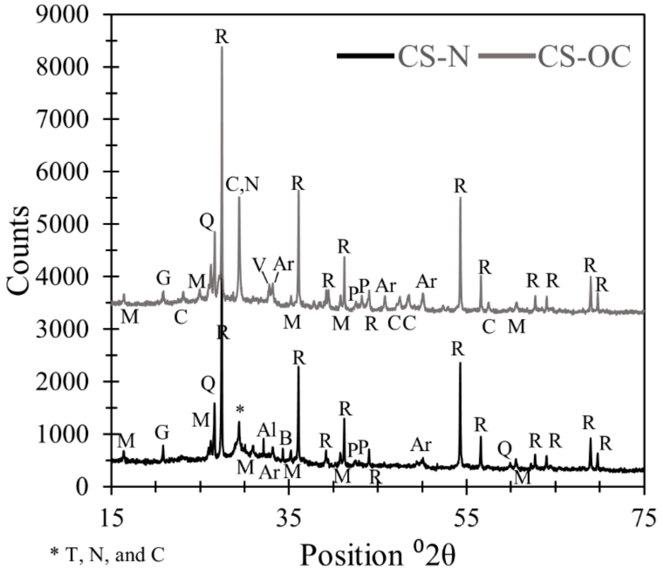

Figure 4.1. XRD peaks of CS-N (bottom) and CS-OC (top, offset by +3000 counts) where Al=Alite, Ar=Aragonite, B=Belite, C=Calcite, G=Gypsum, M=Mullite, N=Nitratine, P=Potassium Nitrate, R=Rutile (standard), Q=Quartz, T=Tobermorite, V=Vaterite

Table 4.3. Quantitative XRD results (wt.%). Compositions reported account for the known rutile standard concentration added.

Mineral/Phase	**CS-N**	**CS-OC**	**Difference (±)**	**% Change (±)**
Alite	1.5	0.6	-0.9	-60
Aragonite	0.1	2.9	+2.8	+2800
Belite	0.7	0.0	-0.7	-100
Calcite	1.1	4.3	+3.2	+290
Gypsum	1.4	3.0	+1.6	+110
Mullite	4.2	3.4	-0.8	-19
Nitratine	2.2	2.4	+0.2	+9
Potassium Nitrate	0.3	0.8	+0.5	+170
Quartz	2.6	2.8	+0.2	+8
Tobermorite	1.3	0.0	-1.3	-100
Vaterite	1.5	4.6	+3.1	+207
Amorphous	83.0	75.2	-7.8	-9

The reduced concentrations of alite and belite observed in the CS-OC material compared to the CS-N material are likely associated with increase in aragonite, calcite, and vaterite observed in

CS-OC due to the carbonation reaction. The carbonation of alite and belite form calcium carbonate according to Eq. 8 and Eq. 9, respectively [127].

$$3(3CaO \cdot SiO_2) + (3-x)CO_2 + \gamma H_2O \rightarrow xCaO \cdot SiO_2 \cdot \gamma H_2O + (3-x)CaCO_3 \qquad \text{Eq. 8}$$

$$2(2CaO \cdot SiO_2) + (2-x)CO_2 + \gamma H_2O \rightarrow xCaO \cdot SiO_2 \cdot \gamma H_2O + (2-x)CaCO_3 \qquad \text{Eq. 9}$$

Other carbonation reactions also likely contribute to the higher concentrations of the calcium carbonate polymorphs. For example, the under prolonged periods of carbonation, C-S-H eventually forms calcium carbonate and silica gel as simplified Eq. 10 [128].

$$C - S - H + CO_2 \rightarrow CaCO_3 + SiO_2 + H_2O \qquad \text{Eq. 10}$$

The resultant type of calcium carbonate polymorph is dependent upon a number of factors including CO_2 concentration and exposure time [40]. The carbonation of alite and belite (Eq. 8 and Eq. 9) also forms additional C-S-H that can react to form additional calcium carbonate. The lower concentration in the amorphous content in the CS-OC compared to the CS-N material may be due to the carbonation of amorphous C-S-H phases and other amorphous phases that are reactive with CO_2 but could not be identified by XRD analysis.

The increase in gypsum observed in CS-OC may originate from the increased availability of SO_4^{2-} in the pore water solution that can react with calcium to form gypsum as a result of both oxidation and carbonation[5]. The ingress and reaction of O_2 can react with available SO_3^{2-} to form more available SO_4^{2-} in the pore water solution. The ingress and reaction of CO_2 may alter the pore water composition that also favors an increase in the availability of SO_4^{2-}. For example, analysis of the chemical microstructure suggests the presence of Na_2SO_3/Na_2SO_4 precipitate in CS-N that forms either in the pore water solution of the material or during the drying process as discussed further in section 4.4.3. During the carbonation, sodium can react with CO_2 to form sodium carbonate. Therefore, less sodium is available to form Na_2SO_3 or Na_2SO_4 which shifts the equilibrium resulting in an increased the amount of free SO_3^{2-}/SO_4^{2-} in the pore water

---

[5] The original wet cast stone mixture contains 0.24% SO_4^{2-}. This percentage assumes that only the HTWOS simulant contributes to the SO_4^{2-} concentration in the cast stone mixture and is based on the amount of SO_4^{2-} prior to any redox interactions with OPC, fly ash, or GGBFS

solution. Therefore, the increased amount of sulfur species can oxidize and react with calcium in the pore water solution to form gypsum. However, calcium may also react during carbonation to form calcium carbonate which decreases its availability to react with SO_4^{2-} to form gypsum. To determine whether gypsum formation was limited by available SO_4^{2-} or calcium, an analysis of the percentage of sulfur contained in the gypsum for the CS-OC material compared to the CS-N was conducted. Using the quantitative XRD results for gypsum and the total sulfur content from XRF, the percentage of sulfur bound in gypsum was calculated at 47% for CS-N and ~100% for CS-OC. This suggests the formation of gypsum during carbonation was limited by the availability of SO_4^{2-} rather than calcium.

Similar to the increase of gypsum observed for CS-OC, the increase of potassium nitrate in CS-OC compared to CS-N suggests an increased availability of NO_3^- in the pore water solution that may be due to the reaction of NO_2^- with oxygen to form more NO_3^- or a shift in the pore water chemistry during carbonation to favor an increased availability of NO_3^-.[6]

The presence of nitratine detected by XRD analysis in this study was also previously observed in Snyder and Stutzman, 2013 in the prepared saltstone grout [118]. Snyder and Stutzman concluded that nitratine was a result of sample drying and it was not present in the wet sample. The precipitation of nitratine during the drying processes indicates dissolved sodium and NO_3 are originally present in the pore water solution of CS-N and CS-OC. A slightly greater amount of nitratine in the CS-OC may indicate increased availability of NO_3^- in the pore water solution as previously discussed.

Most of the mullite in CS-N and CS-OC originates from the fly ash used in the dry ingredients to prepare the cast stone. The reduced mullite concentration in the CS-OC material compared to the CS-N material is likely due to the increased reaction of mullite in the CS-OC material due to a shift in pore water chemistry and material pH.

It should be noted that no ettringite was observed in the CS-N and CS-OC material which differs from observations for the prepared cast stone in Chung et al., 2012 [117]. Both this study and

---

[6] The original wet cast stone mixture contains 0.77% of NO_2^- and 1.69% NO_3^-. This percentage assumes that only the HTWOS simulant contributes to the NO_2^- and %NO_3^- concentrations and is based on the amount of NO_2^- and %$NO_3{}^-$ prior to any potential redox interaction with the OPC, fly ash, or GGBFS.

Chung et al., 2012 prepared cast stone with 8:45:47 ratios of Type I/II OPC, Class F fly ash, and grade 100 GGBFS. However, the Class F fly used in this study had a significantly lower calcium concentration compared to the Class F fly as used in Chung et al, 2012. Therefore, the resultant CS-N and CS-OC materials have significantly less calcium in the mixture which may create a pore water chemistry that does not favor the formation of ettringite. In addition, the CS-N and CS-OC materials were cured and aged for a total of 160 days compared to a cure time of 28 days used for the samples in Chung et al., 2012. It is possible that some ettringite formed early in the hydration process in the CS-N and CS-OC of this study, but the ettringite reacted to form other minerals at the later stages of the hydration process. The lack of ettringite in hydrated cementitious waste forms was also reported in Snyder and Stutzman, 2013 [118] for saltstone grouts. In Snyder and Stutzman, 2013, the saltstone grouts contained similar calcium concentrations to the CS-N and CS-OC materials (Figure C.1, Appendix A) and no ettringite was observed in XRD analysis.

According to the TGA results (Figure 4.2) greater mass loss occurred in CS-N compared to CS-OC over the temperature range of ~50 to 200°C possibly due to the decomposition of tobermorite, amorphous C-S-H phases, and moisture loss. A small peak in the derivative of the mass and temperature curve occurs at approximately 260°C in the CS-N material possibly due to the decomposition of amorphous aluminum hydroxide gel which has previously been noted to lose its water around 270°C [129]. However, in addition to tobermorite, amorphous C-S-H, and amorphous aluminum hydroxide, the decomposition of several phases also identified by XRD (Table 4.1) may occur at temperatures below 250°C. For example, dehydration of gypsum also occurs at temperatures below 250°C [129]. The decomposition of tobermorite may also occur over a wide temperature range of 50 to 600°C [129]. After examining the TGA results, evolved gas analysis (data not shown) was conducted to assist with deconvolution of the peaks. For CS-N, the majority of the water loss occurs from approximately 50 to 400^{0}C, which supports the decomposition of C-S-H, gypsum, and amorphous aluminum hydroxide in this temperature region. For CS-OC, the majority of the water loss occurs until about 200^{0}C, which is likely associated with dehydration of the gypsum.

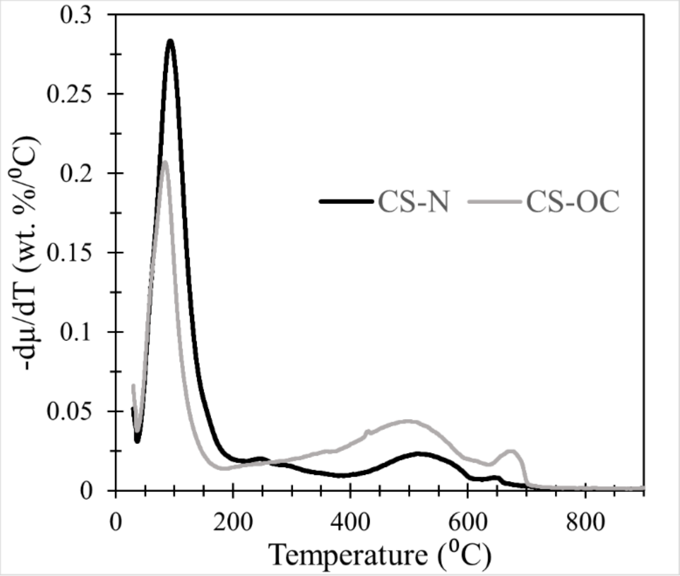

Figure 4.2. TGA results of CS-N and CS-OC

In the temperature range from 200 to 700°C, more mass loss occurred in the CS-OC compared to the CS-N. From the evolved gas analysis, a sharp rise in CO_2 evolved gas is detected beginning around 200°C with the peak ranging from 200 to 600°C and another CO_2 peak appears from about 650 to 700°C in CS-N and CS-O. However, the CO_2 peaks are larger in the CS-OC.

It is known from prior studies that liberation of CO_2 from the calcium carbonate polymorphs (i.e., aragonite, vaterite, and calcite) is expected to occur over the range of 520 to 750°C. Aragonite and vaterite recrystallize to form calcite without mass change during the heating process in TGA at ~460°C for aragonite and between ~350 to 400°C for vaterite [130]. The decomposition of calcite originating from the recrystallization of vaterite and aragonite decomposes at a slightly lower temperature range of 520 to 650°C and the more stable calcite formed directly during carbonation decomposes at a higher temperature range of 650 to 720°C [35]. Therefore, the CO_2 and mass loss peak occurring from 650 to 700°C is likely associated with the decomposition of calcite formed during carbonation. The peak occurring from 200 to 600°C that is mostly attributed to CO_2 loss is likely associated with the decomposition of vaterite and aragonite as well as other carbonated phases that are potentially in the system including magnesium carbonate which decomposes between 500 and 600°C [129]. Other less stable carbonate phases that decompose at lower temperature ranges could account for the liberation of

CO_2 beginning at a temperature of ~200°C. Additionally, during carbonation, CO_2 gas can adsorb between the layers of the silica gel which is then released at temperatures below 400°C [35]. Thus, the CO_2 gas detected at temperatures below 400°C may be due to the presence of silica gel formed during carbonation.

4.4.2. Impact of aging on the physical microstructure

According to the total porosity measurements obtained from the modified exchange method, the porosity in CS-OC (η_{ex}=0.42) was greater than the porosity in CS-N (η_{ex}=0.34). Previously, the porosity was characterized using the modified water exchange method for three cast stone materials that were not intentionally aged under carbonating conditions [122]. From these three materials, the measured porosity material with the most similar composition was 36.4 which compares reasonably well the porosity obtained for CS-N. The porosity for the other two CSMs were reported as 38.6 and 53.3.

To compare the different porosity measurement results obtained from the three methods, the porosity as a function of distance from the exposed surface obtained from the modified water exchange method, BSE imaging, and microCT imaging was plotted in Figure 4.3 for CS-N and CS-OC. The porosity obtained from the modified water exchange method was plotted at a constant value for the two materials because no spatial information about the porosity can be derived across the sample size used. In both BSE and microCT imaging, the CS-OC material had a higher porosity than the CS-N after excluding the initially elevated porosity region at the surface. These "baseline" porosity values are reported in Figure 4.3. Porosity measurements obtained from the BSE imaging and microCT imaging do not contain the entire pore size distribution of the CS-N and CS-OC. The effective minimum pore size detection by these methods are dependent upon the selected pixel or voxel size used in the imaging as well as a number of factors such as the beam interaction volume in BSE imaging or the spot size of the x-ray source in microCT imaging. Therefore, these limitation must be considered when comparing the three porosity methods used in this study. In general, the pore diameter sizes represented in the porosity measurements are on the order of ≥ 0.25 µm (i.e., image pixel resolution) for BSE imaging and ≥ 4.3 µm (i.e., voxel size) for microCT imaging.

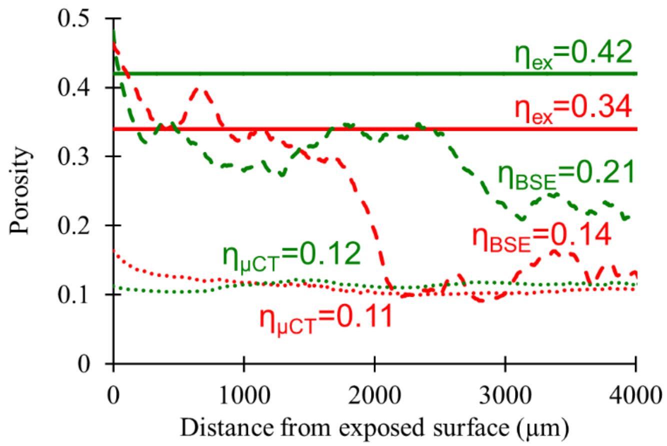

Figure 4.3. Porosity measurements obtained from the modified water exchange method (ηex), BSE imaging (ηBSE), and microCT imaging (ηµCT) for the CS-N (red) and CS-OC (green) materials as a function of distance from the exposed surface.

According to BSE imaging, the exposed surface has a slightly elevated porosity in both CS-N and CS-OC. This effect was only observed in CS-N from the microCT imaging results. The elevated porosity in both materials near the surface is most likely a combination of drying that occurs during aging at 65% RH and due to surface disruption of the samples that occurred when cutting the top surface of the sample prior to aging. In addition, the elevated porosity in CS-N at the surface may also be attributed to a small layer of carbonation that formed despite limited exposure to air during material preparation and handling. This is likely because of the limited hydroxide buffering capacity of the material as discussed in section 4.4.4.

The lower baseline porosity values reported in BSE and microCT imaging compared to the modified water exchange method are most likely a result of the detected pore size resolution of the two methods. For CS-N, the baseline porosity values obtained from the BSE imaging and microcT imaging are 50% and 28%, respectively, of the porosity value obtained from the modified water exchange method. For CS-OC, the baseline porosity values obtained from the BSE imaging and microCT imaging are 41% and 32%, respectively, of the value obtained from the modified water exchange method. These differences are similar to the 15-30% difference observed between porosity values obtained from BSE imaging and oven-drying technique for cement pastes and mortars evaluated in Lange, Jennings, and Shah, 1994 [131].

In the BSE imaging, the relative differences in the baseline porosity values between CS-N and CS-OC were similar to the relative differences obtained from the modified water exchange method. This suggests that some of the porosity in CS-N and CS-OC is from pores ≤ 0.25 μm in diameter, but the reaction that occurs in CS-OC may not significantly affect pores ≤ 0.25 μm in diameter.

Higher porosity measurements were obtained for the BSE imaging compared to the microCT imaging. In addition, the relative differences in porosity between the CS-N and CS-OC were greater in the BSE imaging compared to the microCT imaging. This suggests that a significant fraction of pores ≤ 4.3 μm diameter are present in CS-N and CS-OC. When combined with the differences between BSE imaging and the modified water exchange method, this data also suggest that the reaction that occurs in CS-OC significantly effects pores with diameters in the range of 0.25 μm ≤ pore size ≤ 4.3 μm.

BSE imaging was also used to evaluate the porosity at greater depths in the sample in order to capture the porosity change moving from the carbonated to the uncarbonated region (i.e., ~25 mm as identified by the phenolphthalein test) in CS-OC and also at the same depth for CS-N (Figure 4.4). The porosity results obtained near the surface that were shown in Figure 4.3 were also included for reference in Figure 4.4 and overlaid on the BSE image. Relatively constant porosity measurements between a depth of ~5 and 21 mm were obtained in CS-N and in CS-OC. Therefore, the porosity measurements as a function of depth from 5 to 21 mm are not shown in Figure 4.4 in order to increase clarity of the porosity plots.

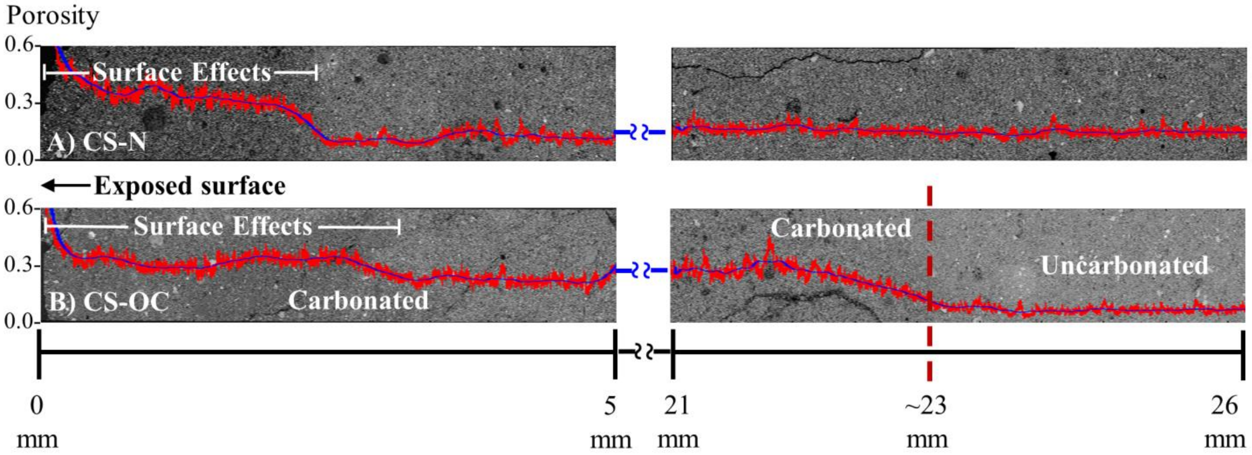

Figure 4.4. Porosity (red) and a moving average porosity (blue) obtained as a function of depth from the exposed surface (left) and at the interior region of the materials (right) for CS-N (top) and CS-OC (bottom) overlaid on the corresponding BSE large area maps.

As discussed previously, the exposed surface of CS-N and CS-OC is initially elevated in porosity due to material preparation and drying effects. In the CS-N material, a relatively constant porosity is observed (after the initial drop due to surface effects) throughout the entire 25 mm depth of the scan. For CS-OC, the porosity decreases significantly when moving from the carbonated and uncarbonated region at a depth of approximately 23 mm which is consistent with the 25 mm depth of carbonation measured by the phenolphthalein test.

The higher porosity obtained in the carbonated region of CS-OC compared to porosity throughout CS-N suggests that carbonation increases the porosity in cast stone materials. This observation is different from what has been observed in other cementitious materials with large amounts of portlandite and C-S-H. Carbonation of portlandite [7] and C-S-H [7, 132] increase the molar volume which decreases the porosity. However, in cast stone with no portlandite and very little C-S-H, the increase in porosity suggests that on average the phases that are formed during carbonation have a smaller molar volume than the phases reacting formed. A decrease in the molar volume after carbonation in other cementitious materials such as those that contain large amounts of ettringite could also occur. The carbonation of ettringite forms calcite, gypsum, amorphous aluminum hydroxide [133]. Based on the differences in the molar volume of these phases, a decrease in molar volume would be expected. In addition, significant cracking was observed in the CS-OC monoliths and throughout the BSE imaging in CS-OC which likely contributes to the increased measured porosity in CS-OC.

4.4.3. Elemental distribution in the microstructure after aging

The microstructure and elemental composition were evaluated in more detail for CS-N and in the carbonated region of CS-OC. A representative area of CS-N and a representative area within the carbonated region of CS-OC are shown in Figure 4.5 and Figure 4.6, respectively. As discussed in section 3.2, the top exposed ~2-3 mm was not representative of the microstructure in CS-N and CS-OC, and therefore the representative areas in Figure 4.5 and Figure 4.6 are from more interior regions of the samples.

The appearance of sodium and sulfur rich regions ~100 µm in length (Region A) relative to the rest of material (Region B) were observed in the CS-N material at depths > 2mm. The absence of the sodium and sulfur rich regions in the first ~2 mm of the CS-N suggests that a small layer of carbonation may have formed in the CS-N as previously noted in section 4.4.2. The elemental composition measured by EDS for Region A and B in Figure 4.5 is reported in Table 4.4. In Region A, the relative amounts of sodium, sulfur, and oxygen after subtracting the oxide contribution from other elements in Region A (i.e., Al, C, Ca, Cr, Fe, K, Mg, and Si) suggests precipitation of Na_2SO_4, possibly in combination with Na_2SO_3. The sodium and sulfur rich regions observed in CS-N were not observed in CS-OC across the entire carbonated region. However, in the uncarbonated region of CS-OC (i.e., depths > 23 mm), the appearance of the sodium and sulfur rich regions were observed. The disappearance of the Na_2SO_3/Na_2SO_4 precipitate in the carbonated region of CS-OC is possible due to the change in the pore water chemistry and redox effects that favor the formation of less soluble sodium carbonate and gypsum as discussed in 4.4.1. The drying process required for SEM-EDS analysis may also have facilitated an increased precipitation of Na_2SO_3/Na_2SO_4 in the pores that previously contained dissolved Na^+ and SO_3^{2-}/SO_4^{2-} in the pore water solution. However, it assumed for the remainder of this discussion that the precipitation of Na_2SO_3/Na_2SO_4 occurs to some degree within the material prior to drying and therefore the measured Na^+ and SO_3^{2-}/SO_4^{2-} are in the form of Na_2SO_3/Na_2SO_4.

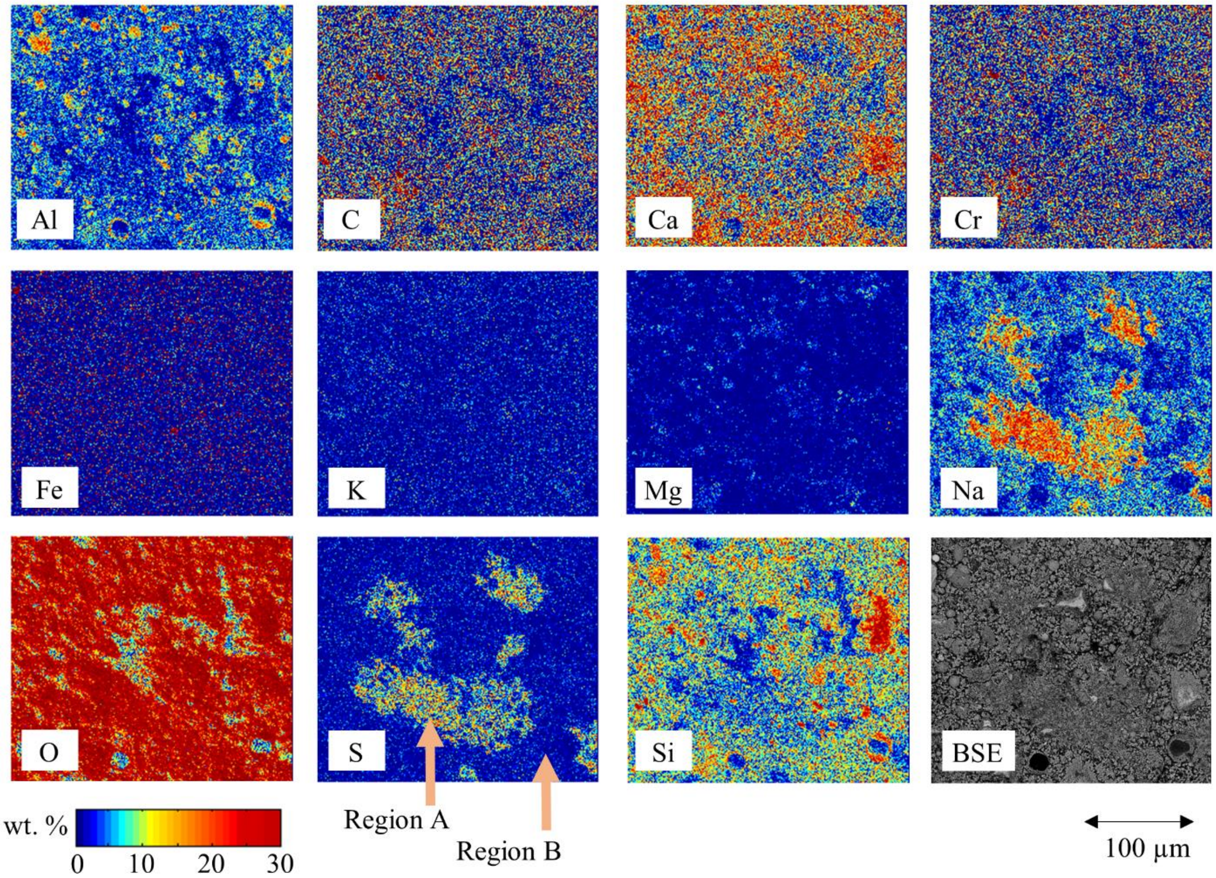

Figure 4.5. Representative SEM-EDS elemental heat maps (wt.%) and BSE image of CS-N

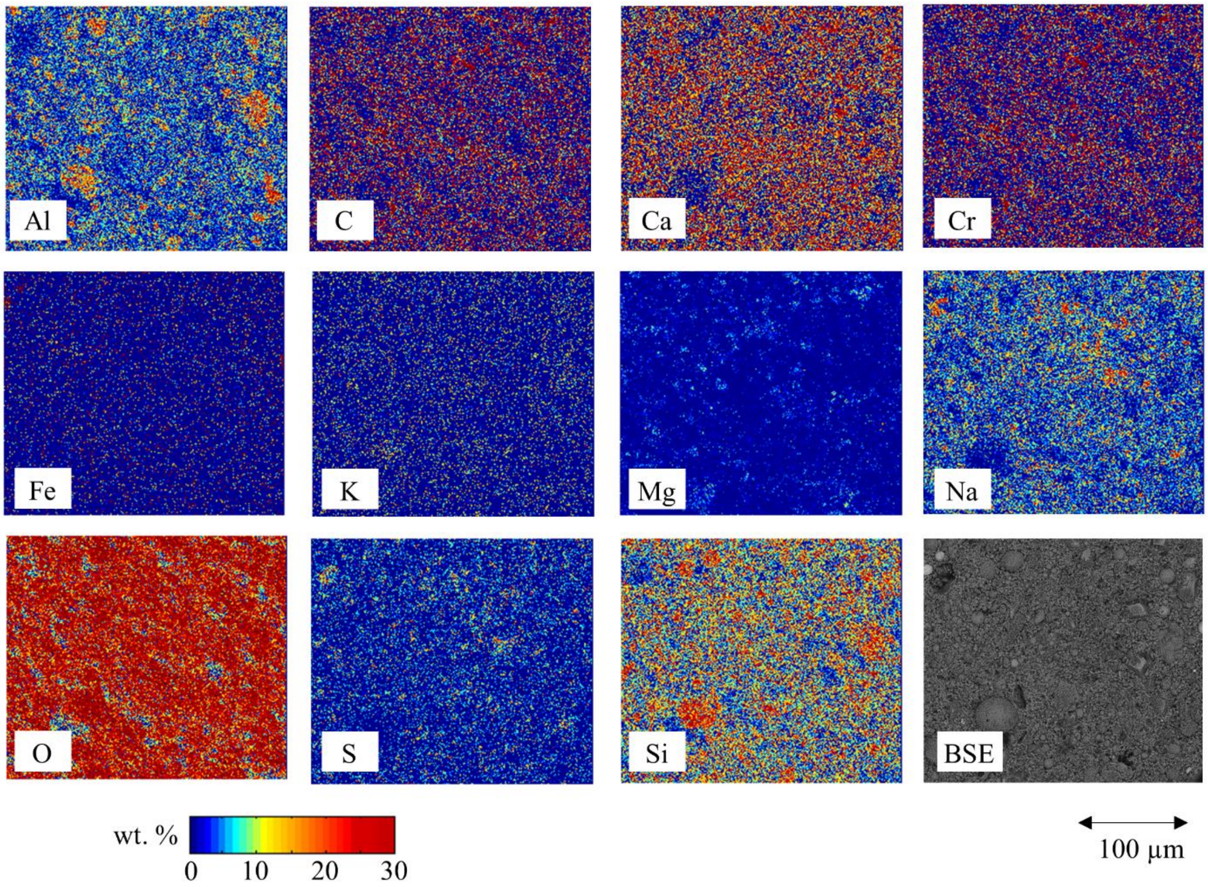

Figure 4.6. Representative SEM-EDS elemental heat maps (wt.%) and BSE image of CS-OC within the carbonated region.

The elemental concentrations moving from the carbonated to uncarbonated region for CS-OC were plotted as function of depth (Figure 4.7) to better understand the elemental profiles that occur across the transition region (i.e., region within the material where the carbonation front ends and the uncarbonated region begins). The mean elemental concentration within the carbonated region identified in Figure 4.7 and within the mean elemental concentration of the uncarbonated region identified in Figure 4.7 are reported in Table 4.4. The transition region identified through inspection of the BSE image is marked by the two dashed vertical lines and this region was not included in the calculations. When compared to the mean elemental concentration of CS-N (Column 3, Table 4.4) the sodium and sulfur concentrations measured in carbonated region near the transition region were lower. Alternatively, the sodium and sulfur concentrations measured in the uncarbonated region near the transition region were higher compared to CS-N. Figure 4.7 shows the increase in concentration of these two species across the transition region when moving from the carbonated to the non-carbonated region. The increase in sodium and sulfur concentration corresponds with the appearance of the sodium-sulfur rich regions that only occur in the uncarbonated region of CS-OC.

The depletion of sodium and sulfur observed in the carbonated region and the increase of sodium and sulfur observed in the uncarbonated region at the interface of the carbonated-uncarbonated region of CS-OC relative to concentrations in CS-N is potentially due to a wetting-drying front that occurs during the aging of CS-OC in an unsaturated environment. The carbonation reaction produces water which in turn creates a wetting front that allows for increased dissolution of Na_2SO_3/Na_2SO_4 which can accumulate at the front. Because the samples are stored in 65% RH environment, a drying front competes with the wetting front induced from the carbonation. As this wetting-drying front proceeds inwards, the dissolved ions from Na_2SO_3/Na_2SO_4 may be pushed inwards in to the material. However, reaction products containing sodium and sulfur, such as gypsum, also compete with this movement of ions. Therefore, some of the sodium and sulfur is expected to remain in the carbonated region in reacted phases formed during carbonation.

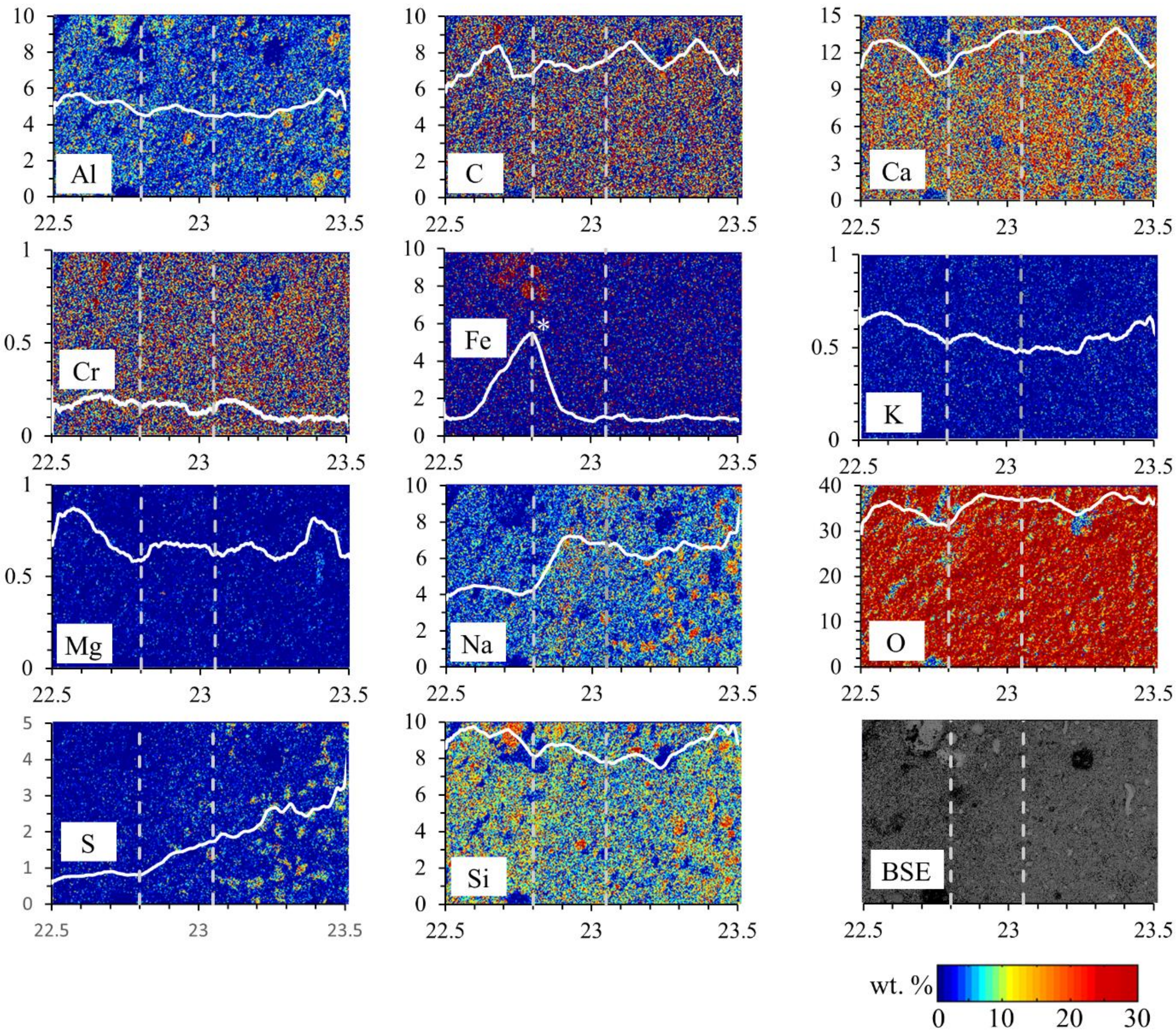

Figure 4.7. Elemental heat maps (colored graphs) and elemental concentrations (plotted white line) as a function of depth moving from the carbonated region (left side of images) to the uncarbonated region (right side of images). Y-axis scales represent the concentration of each element and vary in scale across the different elements in order to better represent changes in concentrations for each element. X-axis values are reported in microns. Dashed vertical lines indicate the transition region from carbonated to uncarbonated. *Sharp peak in iron is due to a clustering of fly ash particles in the scan area.

Table 4.4. Quantitative SEM-EDS spectrum results (wt. % ± 1σ %), where the maximum 1σ observed was 0.1 %

Element	CS-N Region A[1]	CS-N Region B[2]	CS-N Mean	CS-OC-Carbonated Region Mean	CS-OC-Uncarbonated Region Mean
Al	4.3	4.9	6.0	5.8	4.5
C	6.4	6.4	6.8	8.4	6.2
Ca	9.3	14.4	12.4	12.1	12.3
Cr	0.2	0.4	0.2	0.2	0.2
Fe	1.1	1.0	1.4	1.5	1.0
K	0.6	0.8	0.9	0.8	0.5
Mg	0.6	0.9	0.9	0.9	0.6
Na	14.1	4.7	5.7	5.1	6.9
O	40.2	34.1	36.2	37.7	34.1
S	7.9	1.3	1.8	1.6	3.0
Si	7.5	9.6	10.4	10.5	7.9

[1] Region A: Sodium and sulfur rich region observed in Figure 4.5 for CS-N

[2] Region B: Region not including the sodium and sulfur rich region observed in Figure 4.5 for CS-N

In Figure 4.7 the asterisk that notes the sharp increase followed by a sharp decrease in the iron concentration is due to a clustering of high iron fly ash particles that was identified by BSE imaging and is not necessary associated with the carbonation reaction. In addition, it should be noted that the other measured elemental concentrations showed no general trend moving from the carbonated to the uncarbonated region in Figure 4.7, despite differences in the mean elemental concentrations of some elements in the carbonated region and uncarbonated reported in Table 4.4. Therefore, it is unclear the impact that carbonation or the wetting-drying front has on the migration and deposition of the other elements measured. However, based on the shift in pH that occurs in CS-OC and the pH-dependent solubility trends observed for other constituents as discussed in 4.4.4, it is likely that some migration and deposition occurs for other constituents in response to changes in constituent solubility.

4.4.4. Leaching characteristics of aged cast stone

The results from the U.S. EPA Method 1313 pH-dependent leaching test (Figure 4.8) and from the U.S. EPA Method 1315 mass transfer test (Figure 4.9) were compared for CS-N and CS-OC. Only selected constituents of interest were compared in Figure 4.8 and Figure 4.9. The ANC/BNC curve from the U.S. EPA 1313 test is also shown in Figure 4.8. The pH of eluate as a function of time in the mass-transfer test was also compared for CS-N and CS-OC in Figure 4.9. The leaching data for all measured constituents and the conductivity measurements obtained in EPA Method 1313 and EPA Method 1315 for CS-N and CS-OC are reported in Appendix C for reference.

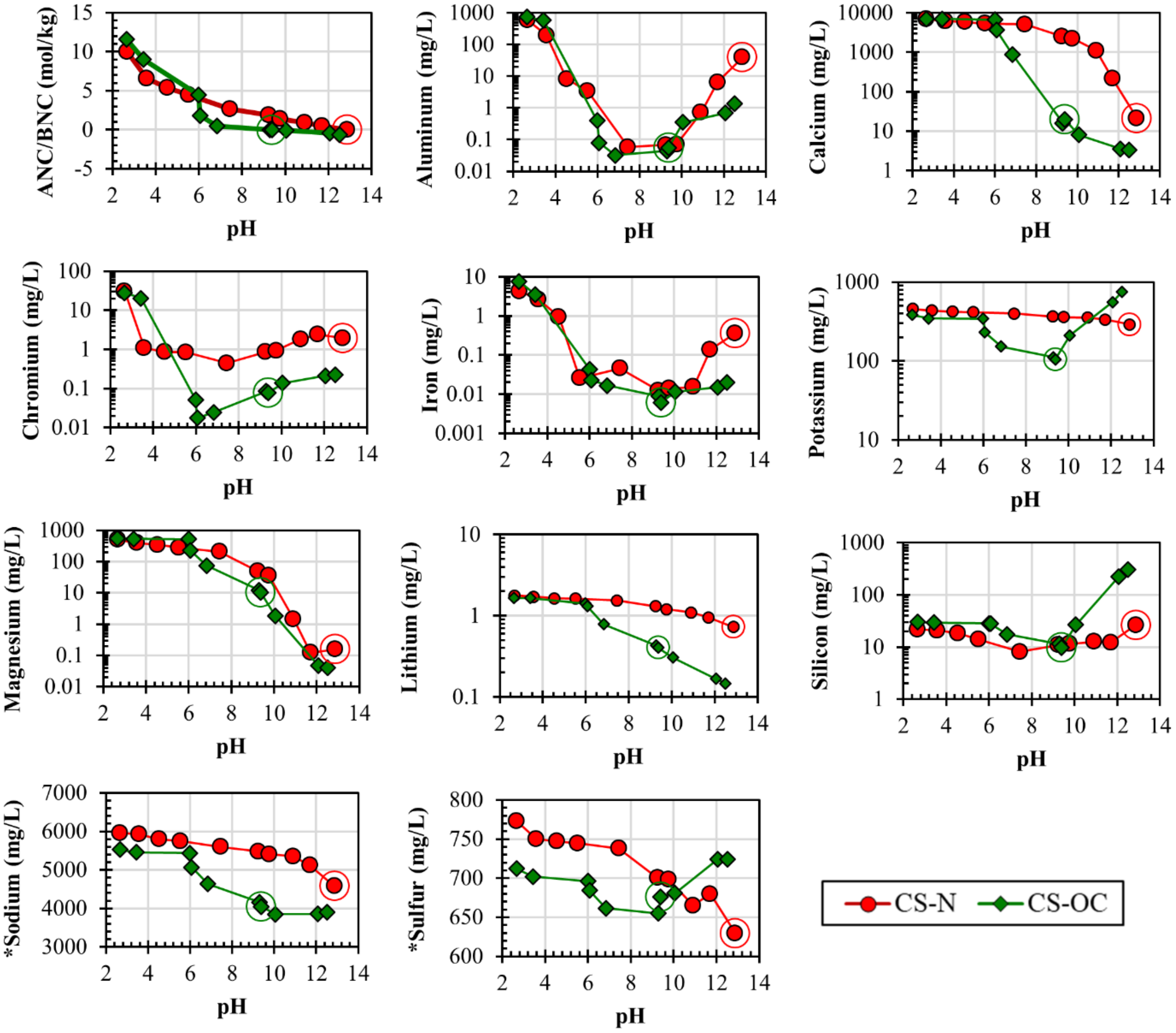

Figure 4.8. ANC/BNC as a function of measured eluate pH and pH-dependent leaching concentrations for selected constituents for CS-N (red) and CS-OC (green) as a function of pH. The circled data points indicate the natural pH of the respective materials. *Indicates y-axis is not on logarithmic scale.

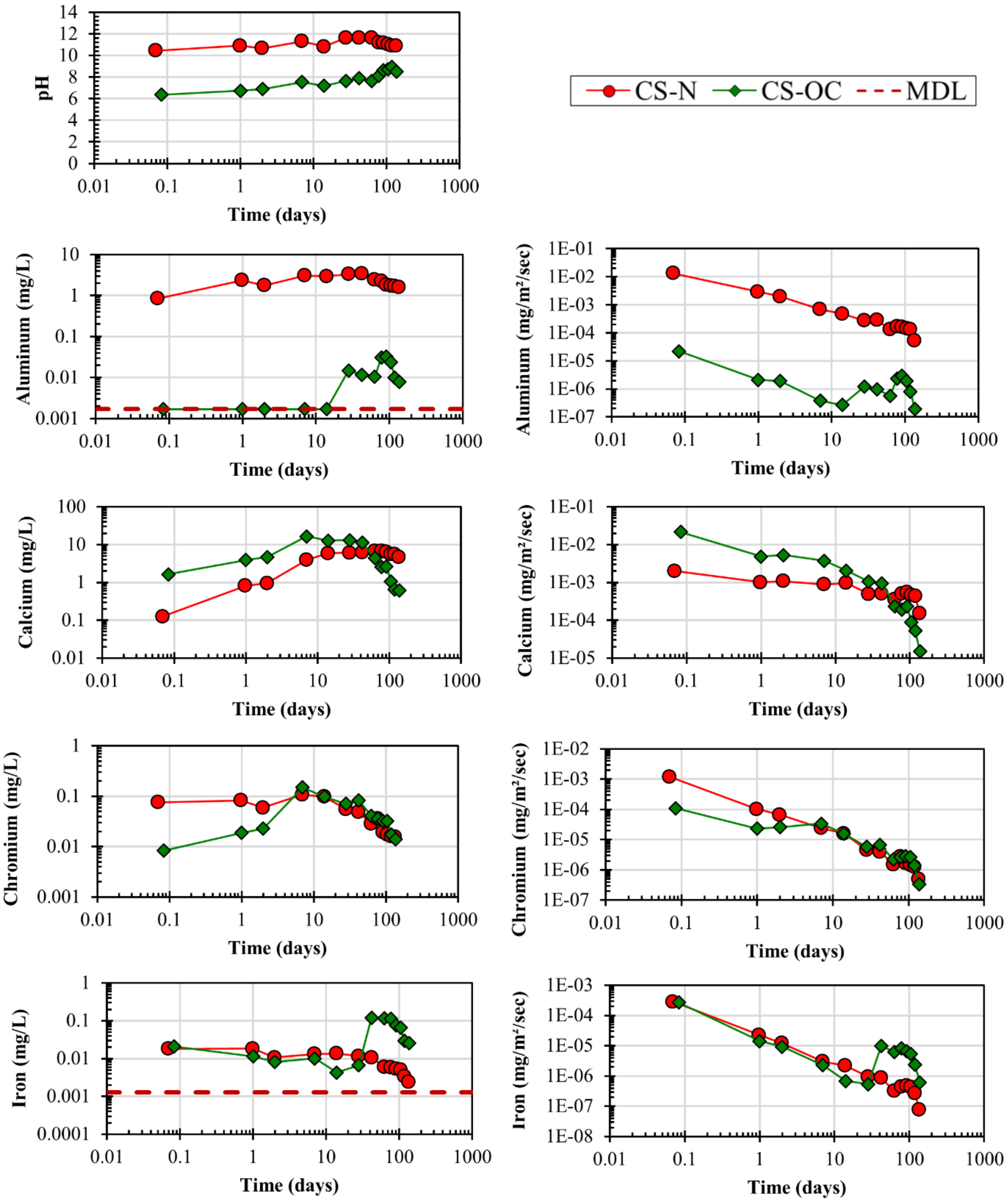

Figure 4.9. Measured eluate pH, eluate concentration of selected constituents, and the calculated flux of selected constituents for CS-N (red) and CS-OC (green) as a function time. The dotted red line that appears for selected constituents indicates the minimum detection limit (MDL) of the constituent.

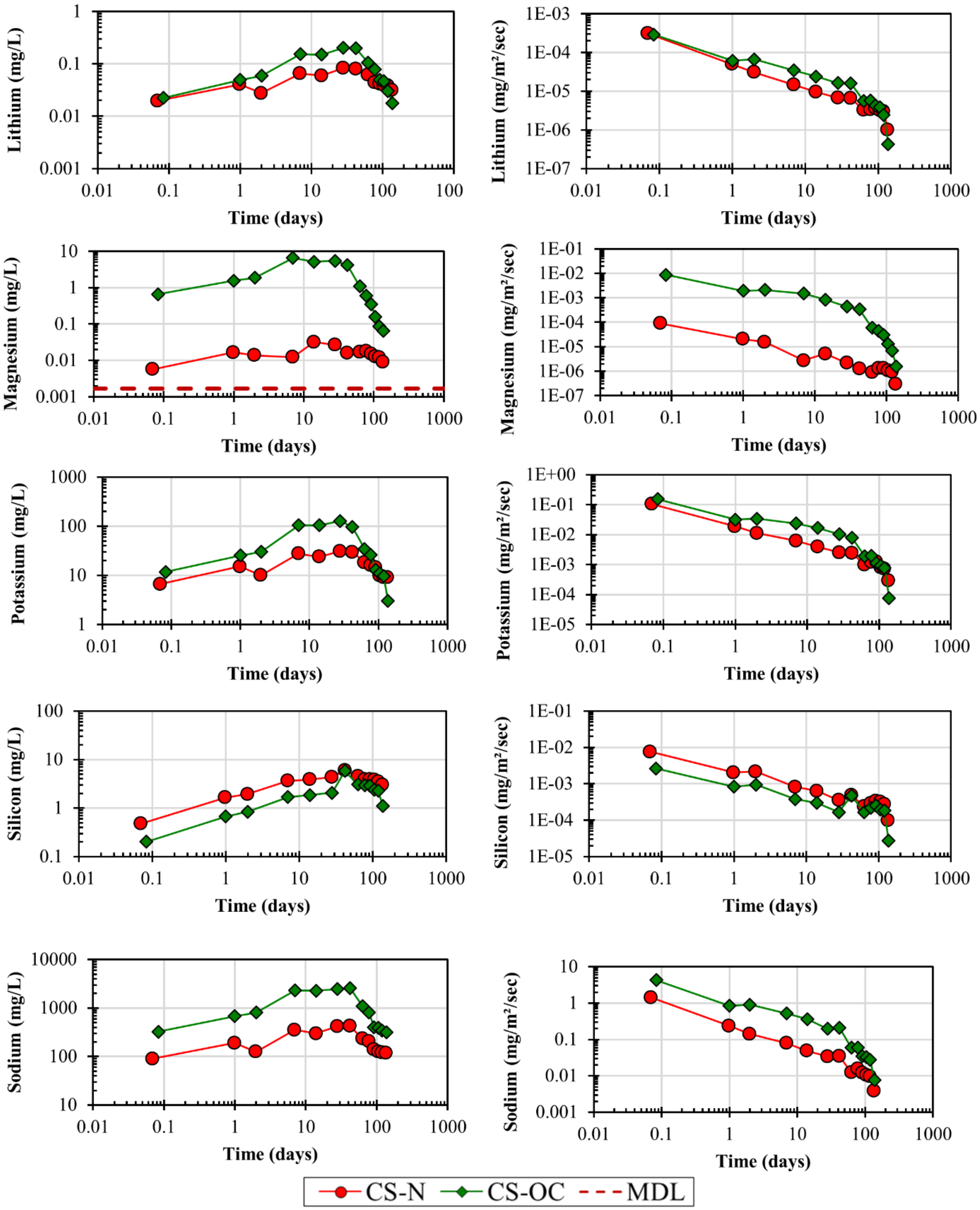

Figure 4.9. (continued)

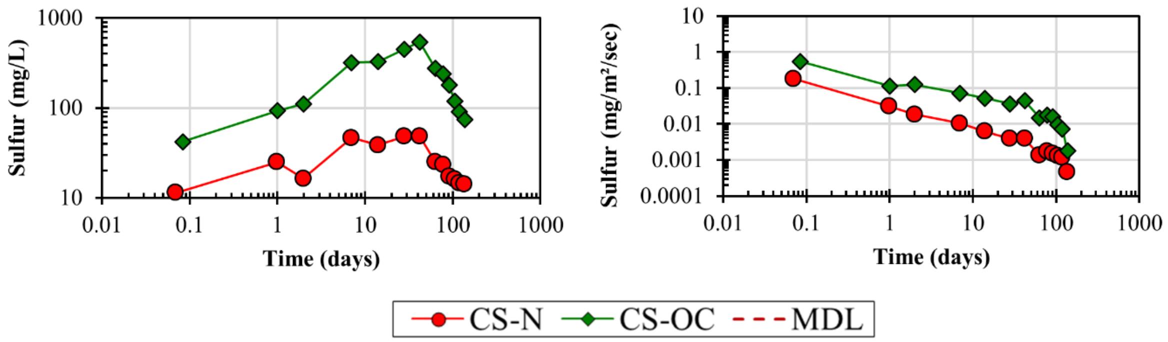

Figure 4.9. (continued)

The measured natural pH[7] was 12.88 for CS-N and at 9.38 for CS-OC. Correspondingly, the calculated hydroxide alkalinity was higher for CS-N (2.51 mol_{H+}/kg_{solid}) compared to CS-OC which had no remaining hydroxide alkalinity (0 mol_{H+}/kg_{solid}). The lack of hydroxide alkalinity in CS-OC indicates the carbonation reaction that occurs in the conditions used in this study completely consumed all the available hydroxide alkalinity. In addition, the carbonate alkalinity was smaller in the CS-N (5.35 mol_{H+}/kg_{solid}) compared to the CS-OC (6.34 mol_{H+}/kg_{solid}) which suggests the carbonation reaction resulted in an increased carbonic acid buffering capacity from the formation of the calcium carbonate polymorphs identified in section 4.4.1 and other carbonated phases.

The measured eluate pH from Method 1315 was significantly lower for CS-OC compared to the CS-N material for all exchanges and is consistent with increased carbonic acid buffering at pH ~6.3 for the CS-OC material as indicated by increased carbonate alkalinity. In general, after 63 days of cummulative leaching, the measured eluate pH started to decrease for the CS-N material. Contrarily, after 63 days of cummulative leaching, the measured eluate pH started to increase for the CS-OC material. The increase in pH for the CS-OC material may be a result of the leaching front moving towards the uncarbonated region where additional hydroxide ions are available in the pore water solution. The decrease in the pH in the eluate for the CS-N material after 63 days of leaching may be due to the overall limited availability of dissolved hydroxide ions in the pore water solution realtive to the diffusion rate of hydroxide ions in the system.

---

[7] The natural pH, or "own pH," is the end point pH when extracted with only deionized water at liquid-solid ratio of 10 mL/g dry weight.

Overall, the relative changes in solubility of the selected constituents discussed in the following sections support a change in the mineralogy and redox state of the material due to the different aging conditions. The differences in the mass transfer release that change as a function of time and in combination with a change in the eluate pH suggest different depths of the carbonation and oxidation fronts as well as differences in porosity. These changes in the pH-dependent leaching behavior and mass-transfer of constituents may be further explained by the use of geochemical speciation modeling in future work.

4.4.4.1. Leaching characteristics of non-reactive constituents

The difference in the physical parameters that control the diffusion of constituents, including tortuosity and porosity, may be inferred from mass transfer release data of relatively non-reactive constituents. Lithium, potassium, and sodium are three relatively non-reactive species that were evaluated in this study and also commonly used a tracer species for diffusion in cementitious materials. The patterns in the mass transfer release data for lithium, potassium, and sodium discussed next suggest that the leaching front reaches the carbonation front after approximately 63 days of cumulative leaching time.

The solubility of potassium, lithium, and sodium at the natural pH of CS-OC was smaller than respective solubilities at the natural pH of CS-N. In addition, the pH-dependent solubility was reduced in CS-OC for pH>6 for lithium and sodium and was reduced in CS-OC for potassium at 6<pH<10. (Note in Figure 4.9, the sodium concentration in the eluate was not shown on a logarithmic scale). The reduced solubility of lithium, potassium, and sodium is likely due to the formation of carbonated species including the reaction of Na_2SO_3/Na_2SO_4 to less soluble sodium carbonate as previously discussed. Despite a reduction in the potassium, lithium, and sodium solubilities for the CS-OC material, the mass transfer release of these constituents were higher for the CS-OC material compared to CS-N material. This observation is likely because potassium, lithium, and sodium are relatively non-reactive and therefore the increased porosity observed for CS-OC allows for a greater release of these constituents from the CS-OC material. After 63 days of leaching, the potassium, lithium, and sodium mass transfer release decreases significantly for the CS-OC. A decrease in the mass transfer release of potassium lithium, and sodium was also observed for CS-N, but the change was smaller relative to the CS-OC. The changes in the mass transfer release for potassium, lithium, and sodium for CS-N and CS-OC indicate a change in the physical parameters (i.e., porosity and tortuosity) at the location of the front of the material or a limited availability of these constituents relative the diffusion rate of the species. The relatively greater change in the release of potassium, lithium, and sodium for CS-OC compared to CS-N indicates a potentially greater change in the physical parameters (i.e., porosity and tortuosity) at the leaching front and that the shift in the pH of the eluate are responsible for decrease of the mass transfer release for CS-OC. Therefore, this indicates that the leaching front approaches the uncarbonated region after the 63 days of cumulative leaching where there is more available hydroxide and a reduction in porosity

4.4.4.2. Leaching characteristics of carbonation sensitive species

Examining the solubility and mass transfer release of carbonation sensitive species may also provide an indication of the depth of the carbonation front relative to the leaching front. Based on the known carbonation induced reactions and the changes in the mineralogy identified by XRD, aluminum, calcium, magnesium, silica, and sulfur were evaluated to determine the impact of carbonation on solubility and mass transfer release.

The solubility of aluminum as function of pH for CS-N and CS-OC are nearly equivalent at pH<10. However, because the solubility of aluminum is strongly associated with pH, the solubility of aluminum at the natural pH for CS-OC is approximately 3 orders of magnitude lower than the solubility of aluminum at the natural pH for CS-N. Correspondingly, the aluminum mass transfer release was significantly reduced in CS-OC compared to CS-N in the mass transfer test. The aluminum release was below detection for the first 14 days in CS-OC. After 14 days, the release of aluminum was >1 order of magnitude higher in the CS-N compared to the CS-OC material. Therefore, the release of aluminum in the mass transfer test appears to be driven by the pH of the material and resultant solubility as a result of the pH shift induced by carbonation. In addition, more dissolved organic carbon present in the carbonated region of CS-OC may also delay the release due to the potential presence of more organically bound aluminum. However, because the aluminum release was below or near detection for CS-OC in the mass transfer release, it is unclear how other factors such as a change in tortuosity or porosity may contribute to the aluminum release.

The solubility of calcium was reduced in the CS-OC relative to the CS-N material from pH 6 to 13 possibly due to the formation of the relatively insoluble calcium carbonate polymorphs as a result of carbonation. However, the calcium solubility was slightly higher at the natural pH in the CS-OC material compared to the calcium solubility at the natural pH in the CS-N. As a result, the calcium release was higher in the CS-OC material in the mass transfer test compared to the CS-N in the initial exchange intervals. After approximately 63 days of cumulative leaching, the calcium release was greater in the CS-N compared to the CS-OC material as a result of the shift in the pH and change in calcium mineralogy in the eluate possibly as a result of the leaching front approaching the uncarbonated region of CS-OC.

The solubility of magnesium was slightly reduced in the CS-OC material compared to the CS-N material across pH >6. However, the solubility of magnesium was approximately three orders of magnitude higher at the natural pH in CS-OC compared to the natural pH of CS-N. Correspondingly, the release of magnesium was much higher in the mass transfer test for CS-OC compared to CS-N. After 63 days of leaching, the release of magnesium dropped significantly in CS-OC which indicates the release of magnesium may be controlled by the pH of the material and the phases containing Mg as the leaching front moves from the carbonated to the uncarbonated region.

In general, the solubility of silica was higher in the CS-OC material compared to the CS-N material over the entire pH range measured in EPA Method 1313. However, the solubility of silica was lower for CS-OC at the natural pH of CS-OC compared to the solubility of CS-N at the natural pH of CS-N. Therefore, the mass transfer release was lower for CS-OC compared to CS-N until 63 days of leaching possibly due to the leaching front in CS-OC reaching the uncarbonated region of CS-OC as discussed previously. After 63 days of leaching, the mass transfer release concentrations were similar for CS-OC and CS-N.

Although sulfur is sensitive to oxidation, it was assumed based on the following discussion that the carbonation has a greater impact the mass transfer release of sulfur. The solubility of sulfur was lower for pH<10 and higher at pH>12 in the CS-OC compared to CS-N, however the differences were relatively small due to solubility of sulfur being relatively insensitive to the pH compared to other constituents (Note in Figure 4.9, the sulfur concentration in the elute was not shown on a logarithmic scale). The decrease in the solubility of sulfur over a majority of the pH range is likely a result of the formation of less soluble gypsum during oxidation/carbonation. The solubility of sulfur was slightly higher at the natural pH of the CS-OC material compared to the solubility at the natural pH of the CS-N material. The very small differences in the solubility of sulfur for the two materials and across the pH range suggest that the mass transfer release of sulfur will not be controlled by solubility or pH, but rather a change in the physical properties (i.e., porosity and tortuosity) induced by carbonation. The mass transfer release was higher in the CS-OC material compared to the CS-N material which suggests that the higher porosity observed for CS-OC discussed in section 4.4.2 is responsible for the increased release of sulfur since sulfur solubility is relatively insensitive to pH. In both materials, the mass transfer release of sulfur decreases for both CS-N and CS-OC likely as a result of change in porosity and tortuosity of the two materials as the leaching front proceeds inwards in to the material.

4.4.4.3. Leaching characteristics of oxidation sensitive species

Examining the solubility and mass transfer release of redox sensitive species may provide an indication of the depth of the oxidation front relative to the leaching front or carbonation front. The two redox sensitive evaluated in this study were chromium and iron. Although sulfur may be sensitive to redox conditions, the observations in this study suggest it is more sensitive to the effects of carbonation as discussed in section 4.4.4.2. The change in the release of redox sensitive chromium and iron occurred at earlier time frames compared in the release of other constituents that are mostly sensitive to the carbonation effects (e.g., Al, Ca, and Mg) which suggests that the oxidation front is located at a smaller depth compared to the carbonation front. The specific changes in solubility and mass transfer release are discussed for chromium and iron.

The solubility of chromium was reduced in the CS-OC material compared to the CS-N material at pH >6 and at the natural pHs of the respective materials. Correspondingly, the release of chromium was lower in CS-OC for the first 7 days in the mass transfer test. After 7 days, the chromium release of CS-N and CS-OC were nearly equivalent in response to the change in pH as measured by the eluate as well as potentially a change in the redox state of the chromium at the position of the leaching front at 7 days.

The solubility of iron was reduced in CS-OC compared to CS-N at the respective natural pH in each material. However, the release of iron was nearly equivalent in the mass transfer test for the initial 28 days. This might be a result of the relatively small change in the solubility of iron from pH 6 (i.e., ~measured eluate pH for the initial exchanges of CS-OC in the mass transfer test) to pH 10 (i.e., ~measured eluate pH for the initial exchanges of CS-N). After 28 days, the release of iron increases considerably in CS-OC indicating a potential redox effect controlling the release of the material when the leaching front moves past the oxidation front. Organically bound iron present may also delay the release of iron in CS-OC due to increased concentrations of dissolved organic carbon. Therefore, carbonation and oxidation likely both influence the release of iron observed in the mass transfer leaching test to some degree.

4.5. Conclusions

The impact of carbonation on the physical-chemical microstructure in the cast stone cementitious waste form studied in this work is different from what has been observed in traditional Portland cement materials as a result significant differences in the mineralogy of hydrated cementitious waste forms compared to materials without salt waste and with larger amounts of Portland cement. The carbonation reaction of the cast stone studied in this work strongly favors the formation of aragonite, calcite, gypsum, and vaterite due to reaction and subsequent depletion of alite, belite, Na_2SO_3/Na_2SO_4, tobermorite, and amorphous phases. Oxidation of cast stone may also favor the reaction of Na_2SO_3/Na_2SO_4 to form gypsum as a result of increased availability of SO_4. Carbonation of the cast stone cementitious waste form studied in this work increases the porosity of the material as a result of increased cracking and possibly a reduction in molar volume. The increase in porosity was supported by several porosity measurement techniques which provides a useful quantitative description of the changes in porosity that occur as a result of carbonation. Based on the results of this work and other work studying cementitious waste forms, the composition of the supplemental cementitious materials used in the formulation of cementitious waste forms influences the mineralogy of the hydrated material and which may have implications over the long term disposal scenarios required for nuclear cementitious waste forms.

Carbonation and oxidation both influence the solubility and mass transfer rates of constituents in the cast stone studied in this work. Mass transfer release patterns of specific constituents indicate that the carbonation front reached a greater depth compared to the oxidation front in the specific cementitious waste form and under the specific aging conditions used in this study. Additional work to characterize the geochemical speciation of cementitious waste forms may be beneficial to explain the change in mineralogy and resultant change in leaching behavior of cementitious waste forms.

4.6. Acknowledgements

The authors would like to thank Rossane Delapp, Deela McGill, Robert Epps, Rich Teising, Peng Zhang, Dan Perrien, and Ryan Murray at Vanderbilt University for their support during the project. The authors would also like to thank David Swanberg, Dr. Wooyong Um, and Dr. Albert Kruger at Pacific Northwest National Laboratory for their assistance with material acquisition and thermogravimetric analysis. The authors also thank Professor Ching-Hua Huang, Dr. Jay Renew, and Wenlong Zhang at Georgia Institute of Technology for their assistance with x-ray diffraction.

This document is based on work supported by the U. S. Department of Energy, under Cooperative Agreement Number DE-FC01-06EW07053 entitled 'The Consortium for Risk Evaluation with Stakeholder Participation III' awarded to Vanderbilt University, David S. Kosson, principal investigator.

CHAPTER 5

GEOCHEMICAL SPECIATION WITH REACTIVE TRANSPORT MODELING OF CARBONATED MICROCONCRETE MATERIALS CONTAINING DIFFERENT FLY ASH REPLACEMENT TYPES[8]

5.1. Introduction

Understanding the aging mechanisms of cementitious materials used as radioactive containment structures as well as those used across the cement industry is important for predicting the integrity and service-life of these cementitious materials. Cementitious materials often contain supplemental cementitious materials (SCMs) including fly ash because SCMs can improve material strength and durability and offer a beneficial reuse application for SCMs. However, the use of fly ash creates additional complexity and uncertainty in understanding the performance of cementitious materials during aging due to varying chemical compositions of fly ash. The key aging mechanisms of concern that may compromise the service-life of cementitious materials include carbonation, chloride attack, and sulfate attack because they can alter the chemical and physical properties of the cementitious materials. Of particular concern is the change in constituent leaching behavior that may occur as a result of the chemical and physical changes during aging and how the addition of fly ash impacts the constituent release [134, 135], especially during aging. Therefore, the impact of aging on the leaching from cementitious materials prepared using fly ash of different concentrations of constituents must be understood to predict contaminant retention and the overall performance and service-life of cementitious materials, especially those used in radioactive containment structures due their long service-life.

The use of geochemical speciation with reactive transport modeling is one approach to provide insights and describe the changes in the leaching behavior incited by chemical and physical changes of the cementitious materials after aging. The objective of this research was to investigate one specific aging condition, carbonation, by applying geochemical speciation with reactive mass transport modeling to both non-carbonated and carbonated microconcretes of

---

[8] The results from this chapter are being incorporated the anticipated manuscript: 1) J.L.Branch, K.G. Brown, A.C. Garrabrants, H.A. van der Sloot, J.C.L Meeussen, and D.S. Kosson. Geochemical speciation with reactive transport modeling of carbonated microconcretes with different fly ash replacement types.

different formulations using a common set of minerals and solid-solutions phases (i.e., reaction set) to describe the pH-dependent solubility and monolith leaching of these materials. Geochemical speciation modeling [75, 136-141] and reactive transport modeling [142, 143] have previously been used to describe leaching mechanisms for many other cementitious materials. However, the applicability of geochemical speciation modeling to non-carbonated and carbonated cementitious materials especially with different fly ash formulations as applied in this study is less understood. Moreover, this study attempts to describe the changes in the eluate pH and solubility of both major and trace species. Because carbonation is expected to occur in radioactive waste disposal scenarios, it also critical to apply this type of modeling to describe and predict the leaching mechanisms after carbonation.

Carbonation is a naturally occurring aging process where gaseous CO_2 from the atmosphere or in the soil reacts with the cementitious matrix. The reaction can change the mineralogy, reduce the alkalinity, alter constituent solubilities [91], and change the porosity [7, 54, 55, 108] of the cementitious material. The impact of carbonation on these properties and the rate of carbonation depends on many factors including the addition of supplemental cementitious materials [22, 91, 144], external CO_2 concentration [87, 145, 146], relative humidity (RH) [114, 145], and time exposed [18, 87, 145]. To investigate the impact of fly ash on the leaching of constituents after carbonation, three different microconcrete formulations were prepared with and without fly ash and aged in non-carbonated and carbonated aging scenarios. Microconcretes are concrete materials without coarse aggregate and were used in this study because they are easier to handle and have previously been shown as effective surrogates in leaching studies for concrete materials with coarse aggregates [3]. Previously, the leaching behavior of the non-carbonated microconcretes [134, 135] and the microstructure and solubility of the non-carbonated and carbonated microconcrete materials have been characterized [91, 108] which is used as the experimental basis for the geochemical speciation modeling performed in this work.

5.2. Materials and methods

5.2.1. Microconcrete preparation and aging conditions

Microconcretes evaluated in this study were previously prepared and analyzed for their leaching characteristics [3, 91], extent of carbonation [91], and impact of carbonation on the porosity [108] using the mix designs outline in Kosson et al., 2014 [3]. For these studies, microconcrete materials were prepared into cylindrical monoliths approximately 10 cm in diameter and 20 cm in length. After setting, the top molded surface was removed from the monoliths and the monoliths were cut in half lengthwise to be used in the remainder of this work. A control microconcrete without fly ash (00) using Type I/II ordinary Portland cement (OPC), river sand (fine aggregate), and water was prepared. In addition, several blended microconcretes with 45% fly ash replacement of the OPC were prepared. Three of the microconcretes from these studies were selected to be further evaluated in this work: 1) control microconcrete without fly ash (00), 2) blended microconcrete with a high calcium Class C fly ash from the combustion of sub-bituminous coal (FA39), and 3) blended microconcrete with the low calcium Class F fly ash from the combustion of bituminous coal (FA02). The selection of these microconcrete materials allows for a comparison of microconcretes with and without fly ash as well as varying alkalinities [91].

Two aging conditions were evaluated in this study: 1) non-carbonated and 2) carbonated. Both aging sets were initially cured for 6 months at 100% RH and ambient temperature (21 ± 2 °C) in a sealed bucket. Three of the microconcrete cylinders per microconcrete type were cured for an additional 6 months in the sealed bucket (i.e., M-00, M-39, and M-02). Three microconcrete cylinders per microconcrete type were placed in an environmental chamber maintained at 65% RH and ambient temperature with 5% CO_2 for 6 months (i.e., MC-00, MC-39, and MC-02).

Both granular and monolithic forms were required for the leaching tests used in this study. Therefore, after the initial 6-months cure, four of the microconcrete cylinders per microconcrete type were ground using a parallel plate grinder until 85% by mass (wt%) of the particles were < 2 mm in diameter. The granular material was mixed until homogenized for each microconcrete. For each granular microconcrete type, the material was divided in half by mass with each half aged in parallel with the cylinders in the non-carbonated and carbonated aging conditions described previously.

5.2.2. pH-dependent leaching test

U.S. EPA Method 1313 [29, 125] was used to determine the liquid-solid equilibrium of the microconcretes as further detailed in Kosson et al., 2014 [60]. EPA Method 1313 is a pH-dependent solubility leaching test with parallel batch extractions at nine target pH points between 2 and 13 (±0.5). A liquid-to-solid ratio of 10 mL/g-dry is used with dilute acid (HNO_3) or base (KOH) added to achieve the target pH points.

EPA Method 1313 was performed in duplicate for each microconcrete type and aging condition using the granular microconcretes. Granular microconcretes were used because a size reduced material is needed in EPA Method 1313 to reach equilibrium in the specified contact time. The pH and conductivity were measured in the eluate after filtration. The constituents in the eluate were measured by inductively coupled plasma mass spectrometry (ICP-MS) for Sb, As, Be, Cd, Cs, Cr, Pb, Mo, Se, Tl, Sn, U, inductively coupled plasma optical emission spectrometry (ICP-OES) for Al, Ba, B, Ca, Co, Cu, Fe, Li, Mg, Mn, Ni, P, K, Si, Na, Sr, S, Ti, V, Zn, ion chromatography (IC) for F, Cl, NO_2, Br, NO_3, SO_4, and PO_4, and total organic carbon analysis (dissolved inorganic carbon and dissolved organic carbon). The results from the duplicate tests were combined to create a single pH-dependent leaching set for each microconcrete type and aging conditions.

5.2.3. Mass transfer tank leaching test

U.S. EPA Method 1315 [126, 147] was used to determine the mass transfer release of constituents from the microconcretes. EPA Method 1315 is a tank leaching test using reagent water for monolithic or compacted granular materials with pre-defined leaching time intervals. The concentration of each constituent in the eluate is measured after each time interval, and fresh reagent water is used in the subsequent leaching interval.

Paired EPA Method 1315 tests were performed using the cylindrical monoliths for each microconcrete type and aging conditions. All faces of the monoliths were in contact with the deionized water for a cumulative leaching time of 63 days. The eluate was analyzed using the same procedure described in the pH-dependent leaching test.

5.2.4. Modeling approach

Geochemical speciation modeling was used to simulate the equilibrium liquid-solid partitioning (LSP) of constituents in the batch leaching extractions obtained in EPA Method 1313 (i.e., pH-dependent LSP model) and the mass transfer release of constituents in EPA Method 1315 (i.e., monolith diffusion-controlled leaching model). The modeling framework, ORCHESTRA [148] embedded in the data handling software, LeachXS [149] was used to perform the speciation modeling. The aqueous phase speciation reaction set used in the modeling were from the thermodynamic database, minteq.v4 [150, 151], which is used in ORCHESTRA. The integrated software package and thermodynamic database is hereafter referred to as LeachXS/ORCHESTRA (LXO).

The LXO monolith diffusion-controlled leaching model assumes the monolith can be reasonably represented by a set of well mixed cells that are successively larger in width for interior cells as described in Seignette, 2015 [152] and Meeussen and Brown, 2015 [153]. Constituent diffusion from each cell is based on the fully-explicit finite difference scheme described in Meeussen and Brown, 2015 [154]. Local equilibrium conditions were met, which assumes that the chemical reaction takes place much faster than the transport process within each cell [155].

A multi-ionic diffusion approach was used to model the diffusivity of the constituents in the monolith diffusion-controlled leaching model. Known free liquid diffusivity coefficients, D_i^0, for specific constituents were used to calculate the diffusivity of the constituent on a per primary-entity basis. If D_i^0 could not be found for a particular constituent, the diffusivity of the geometric mean D_i^0 per electron of all the known D_i^0 was used to calculate the D_i^0 of the constituent. The D_i^0 used for each primary entity and corresponding constituent is summarized in Table D.1.

5.2.5. Modeling chemical parameters

For each microconcrete type and aging condition, the total available leaching content (i.e., ‘available content’) of each constituent used in the pH-dependent LSP model and across each cell in the monolith diffusion-controlled leaching model was set to the maximum measured release of the constituent across the pH domain in EPA Method 1313 except for potassium, nitrate, and carbonate. Since potassium hydroxide and nitric acid were used to achieve the targeted endpoint pH conditions in the test, the available content used for K and nitrate excluded concentrations from any pH values obtained by adding base or acid for K or nitrate, respectively. The carbonate available content was selected from the range of carbonate concentrations derived from the carbonate alkalinity, TGA, and TIC as reported in Branch et al., 2016 (Table 5) for each microconcrete [91]. Within this range, the carbonate value that yielded the minimum log-squared residual of the model results as a function of the measured pH in the eluate of the mass-transfer leaching test was used in both the monolith diffusion-controlled leaching modeling and the pH-dependent LSP modeling. A summary of the available content values for each constituent and each material is provided in Appendix D.

Adsorption models were used in the pH-dependent LSP and monolith-diffusion controlled leaching for the clay, humic acid, and hydrous ferrous oxides as described in van der Sloot and Kosson, 2012 [156]. These adsorption models were calibrated over the relevant pH range based on simulation results for several constituents, including phosphate and arsenic. The pe was calibrated over the relevant pH range based on the iron and/or chromium. A summary of the pe and adsorption model parameter values is provided in Appendix D.

In the monolith diffusion-controlled leaching model for the carbonated microconcretes, a slight variation in the previously described approach was taken to account for the position of the carbonation front and, therefore, potentially different available content for constituents within each cell. The available contents were varied across the cells based on the measured location of the carbonation front according to Branch et al., 2016 [91] for each carbonated microconcrete. The available contents obtained for the non-carbonated microconcretes were used for the interior, uncarbonated cells where carbonation had not occurred. In the outer carbonated cell(s), the available contents obtained from the respective carbonated microconcretes were used.

A single mineral set (Table 5.1) was used in the pH-dependent LSP and monolith diffusion-controlled leaching models for all microconcrete types and aging conditions. A subset of CEMDATA14 [157] served as the initial basis for this mineral set with additional species added to improve model results based on reducing residuals when comparing simulation results to testing data. When deriving the final mineral set, the monolith diffusion-controlled leaching model results were found to be more sensitive to the mineral set compared to the pH-dependent LSP model, likely because of the lower liquid-to-solid ratios within the microconcrete pores during the mass transfer tank leaching test. Therefore, the mineral set selection was iteratively calibrated using the monolith diffusion-controlled leaching model and then applied to the pH-dependent LSP model for verification. The formation constants for the minerals denoted with an asterisk in Table 5.1 were obtained through calibration with several other cementitious materials prior to this work [158].

Table 5.1. Selected minerals and their formation constants (Log K).

Mineral	Notation[1]	Log K[2]	Reference
$AlO(OH)$	Diaspore	15.82	[150]
$Al(OH)_3$	Gibbsite	15.12	[157]
$AlOHSO_4$	$AH\bar{S}_2$	25.92	[150]
$CaCO_3$	Calcite	9.47	[157]
$CaO \cdot Al_2O_3 \cdot 10H_2O$	CAH_{10}	7.60	[157]
$Ca(OH)_2$	Portlandite	-22.79	[157]
$Ca(SO_4) \cdot 2(H_2O)$	Gypsum	4.58	[157]
$Ca(SO_4)$	Anhydrite	4.36	[157]
$Ca_2H_2O_9S_2$	Hemihydrite	3.59	[157]
$Ca_4Al_2(SO_4)0.5Cl(OH)_{12} \cdot 6H_2O$	Kuzel's Salt	-27.46	[157]
$4CaO \cdot Al_2O_3 \cdot SO_3 \cdot 12H_2O$	Monosulfoaluminate	-26.73	[157]
$4CaO \cdot Fe_2O_3 \cdot SO_3 \cdot 12H_2O$	Fe-monosulfate	-24.42	[157]
Cd_2SiO_4		6.06	*
Co_2SiO_4		6.29	*
Cr_2O_3		137.1	[150]
$K_2Ca(SO_4)_2 \bullet (H_2O)$	Syngenite	7.20	[157]
$Mg(OH)_2$	Brucite	-16.84	[157]
Fe_2O_3	Maghemite	36.79	[150]
Ni_2SiO_4		8.50	*
SiO_2	Silica	25.72	[157]
$Zn_2(SiO_4)$	Willemite	6.29	*

[1] Common mineral name or cement notation used: A=Al_2SO_4, C=CaO, $\bar{C}$=CO_2, F=Fe_2O_3, H=H_2O, M=MgO, S=SiO_2, and $\bar{S}$=SO_3

[2] Log K values are based on the primary entities mapping. See supplementary Table D.1.

[*] LogK values obtained from personal communication with Hans A. van der Sloot [158]

C-S-H and ettringite leaching were modeled using ideal solid-solutions (Table 5.2) because of the variable stoichiometry for C-S-H and because other divalent cations may substitute for Ca^{2+}

in ettringite. The formation constants for the ettringite solid solutions were obtained through calibration of several other cementitious materials prior to this work [158].

Table 5.2. Selected solid-solutions and their formation constants (Log K).

End Member	Formula	Log K[1]	Reference
JenniteD	$C_{1.5}S_{0.67}H_{2.5}$	-13.39	[157]
JenniteH	$C_{1.33}SH_{2.17}$	0.83	[157]
TobermoriteD	$C_{5/6}S_{2/3}H_{1.83}$	1.70	[157]
TobermoriteH	$C_{2/3}SH_{1.5}$	14.72	[157]
AsO_4-Ettringite	-	27.10	[158]
Ba-Ettringite	-	4.01	*
BO_3-Ettringite	-	-42.59	*
$Cd(OH)_4^{2-}$-Ettringite	-	-54.18	*
$Co(OH)_4^{2-}$-Ettringite	-	-55.02	*
CrO_4-Ettringite	-	-8.59	*
$Cu(OH)_4^{2-}$-Ettringite	-	-50.98	*
Ettringite	-	-11.69	*
Fe-Ettringite	-	-49.51	*
$Mn(OH)_4^{2-}$-Ettringite	-	-58.19	*
MoO_4-Ettringite	-	-4.59	*
$Ni(OH)_4^{2-}$-Ettringite	-	-53.93	*
$Pb(OH)_4^{2-}$-Ettringite	-	-51.69	*
PO_4-Ettringite	-	39.41	*
$Sb(OH)_6^{-}$-Ettringite	-	-30.44	*
SeO_4^{2-}-Ettringite	-	-10.59	*
Sr-Ettringite	-	1.01	*
VO_3-Ettringite	-	-56.34	*
$Zn(OH)_4^{2-}$-Ettringite	-	-49.69	*

[1] Log K values are based on the primary entities mapping. See supplementary Table S1.

*Formation constant obtained through personal communication with Hans van der Sloot [158]

Only selected constituents (i.e., Al, Ba, Ca, Cr, Fe, K, Mg, Na, S, Si, and Sr) were considered further in the modeling. The selected constituents were chosen based on their importance in cementitious materials and if measured eluate concentrations were above the minimum detection limit (MDL) in both the pH-dependent LSP and mass transfer tank leaching tests. Constituents were also selected to ensure the final mineral set consisted of species with varying solid concentrations (i.e., major, minor, or trace) and differently charged species (i.e., cationic or anionic). Indicator species (i.e., K and Na) were also represented in the final selected constituent set.

5.2.6. Modeling physical parameters

Within each cell, the physical parameters required for the monolith diffusion-controlled modeling are porosity, skeletal density, saturation, and tortuosity. A summary of the physical parameter values used for each microconcrete is provided in Appendix D.

The total porosity in the non-carbonated microconcretes was first estimated from the water-saturated mass, dry mass, and submerged mass using liquid-pyconmetry for cement-based materials described by Aligizaki, 2005 [67]. The porosity for each cell was then varied according to the measured porosity as a function of distance from the exposed surface obtained from backscattered scanning election microscopy (BSEM) reported in Branch, Epps, and Kosson, 2018 [108] for both non-carbonated and carbonated microconcretes. Porosity measurements obtained from BSEM may not adequately represent the true porosity because the resolution limits the size of pores that can be measured and air voids may not be adequately represented in the scan area. Therefore, an additive factor was applied to the BSEM image based on the measured total porosity of the non-carbonated microconcretes to obtain an estimated porosity for each cell. In the modeling, the porosity in the interior, uncarbonated cells of the carbonated microconcretes was assumed to be equivalent to the porosity of the non-carbonated microconcretes. The skeletal density of each microconcrete was also determined from liquid-pyconmetry based on the sample geometry and measured dry weight. Changes in the porosity were not expected to significantly alter the density of the material and, therefore, the density was assumed to be constant throughout the monolith.

It was assumed that each cell is quickly saturated during the EPA Method 1315 test and, therefore, the relative saturation was assumed to be 1.0 for every cell in each microconcrete.

The tortuosity for each cell was calibrated based on the measured sodium release in EPA Method 1315. Sodium has previously been used as an indicator species for diffusion because it is relatively non-reactive [137]. For each microconcrete, the final tortuosity values determined for each cell were based on the tortuosity values that yielded the minimum sum log-squared residual of the simulated versus the measured sodium release curve for the first replicate. The final tortuosity values were then verified based on the measured sodium release curve in the second replicate and for potassium which is often considered as another relatively non-reactive species.

The effective diffusivity coefficient of the liquid phase for sodium, ${D_{Na}}^{e,p}$, was calculated as a function of depth using the calibrated tortuosity factor, τ, the assumed 1.0 saturation, S (m^3/m^3) , and the free liquid diffusivity coefficient, ${D_{Na}}^{o}$ (m^2/s), of sodium according to Eq. 11 from Samson and Marchand, 2007 [155].

$${D_{Na}}^{e,p} = {D_{Na}}^{o}\left(\frac{S^{7/3}}{\tau^2}\right) \qquad \text{Eq. 11}$$

5.2.7. Log-squared residual analysis

The log-squared of the residuals, logRSS, for the experimental results (y) and pH-dependent LSP model results ($\hat{y}$) as shown in Eq. 12 was calculated and summed for each constituent as a function of pH over the pH range of interest. The pH range of interest was selected based on the highest batch extraction pH of ~13 and first dissociation constant for carbonic acid at 21°C, pK1=6.3 ±0.5. Therefore, the log-squared residuals within this pH range (calculated by comparing the simulation result at the same pH as the measured pH for the experimental result within the target pH range[9]) were grouped into pH groups (±0.5) of 7, 8, 9, 10.5, 12, and 13 that correspond to the target pH values specified by EPA Method 1313. For each microconcrete, if more than one experimental data point met the criteria for a pH group, then the mean of the log-squared of the residuals from the experimental and model prediction was reported. Experimental data points that were at or below the MDL were not included in the residual analysis. The log-squared of the residual for each pH group was summed across all the microconcretes for each constituent. The log-squared of the residual of iron was not reported because the concentration of iron in the eluate was below the MDL across the entire pH range of interest.

$$logRSS = \sum(\log\left(\frac{\hat{y}}{y}\right))^2 \qquad \text{Eq. 12}$$

---

[9] For example, if the Method 1313 experimental results for pH 8.0±0.5 was at a measured pH=8.3, then the simulation result at pH=8.3 was used for calculating the residual and then reported in the target group at pH 8.

The log-squared values of the residuals for the experimental results (y) and monolith diffusion-controlled leaching model results ($\hat{y}$) were also calculated and summed for each constituent as a function of the exchange time using Eq. 12. Experimental data points below the MDL were not included in the residual analysis. For each microconcrete, the mean of the log-squared of the residuals from the experimental and model prediction for the two replicates was used. The log-square residual for each exchange time was summed across all the microconcretes for each constituent.

5.3. Results and discussion

5.3.1. pH-dependent LSP model results

The experimental results obtained from EPA Method 1313 and the results obtained from the pH-dependent LSP model are compared for each microconcrete (i.e., M-00, M-02, M-39, MC-00, MC-02, and MC-39) in Figure 5.1 through Figure 5.6. The potassium concentrations measured in the batch extractions at conditions with pH greater than the natural pH of the material are not representative of the potassium LSP due to the addition of KOH. However, this potassium data was included in the pH-dependent LSP results for sake of completeness.

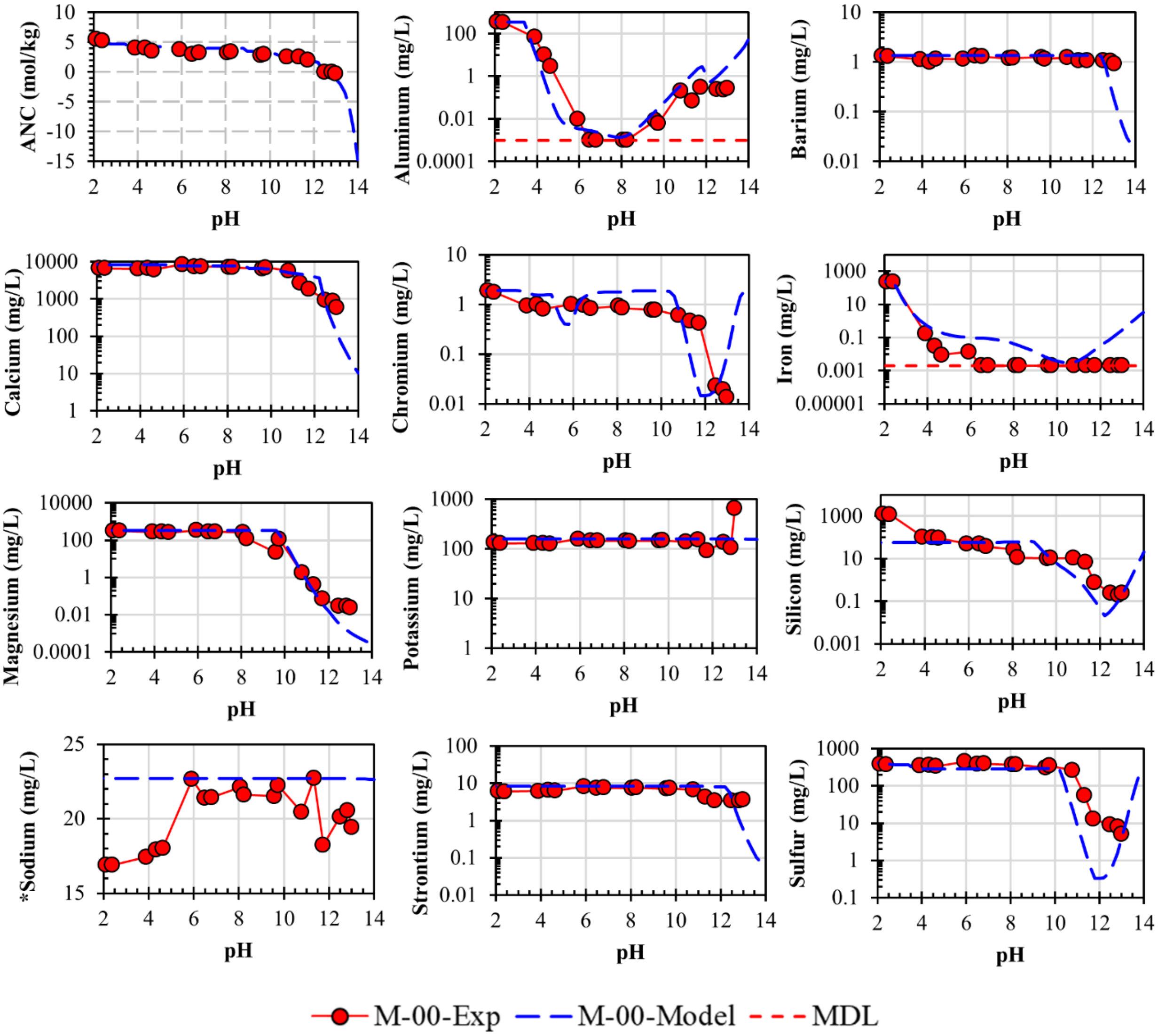

Figure 5.1. M-00 pH-dependent solubility experimental results compared to pH-dependent LSP modeling results for the ANC/BNC and selected constituents. *Y-axis shown on linear scale for sodium to highlight differences in sodium solubility as a function of pH.

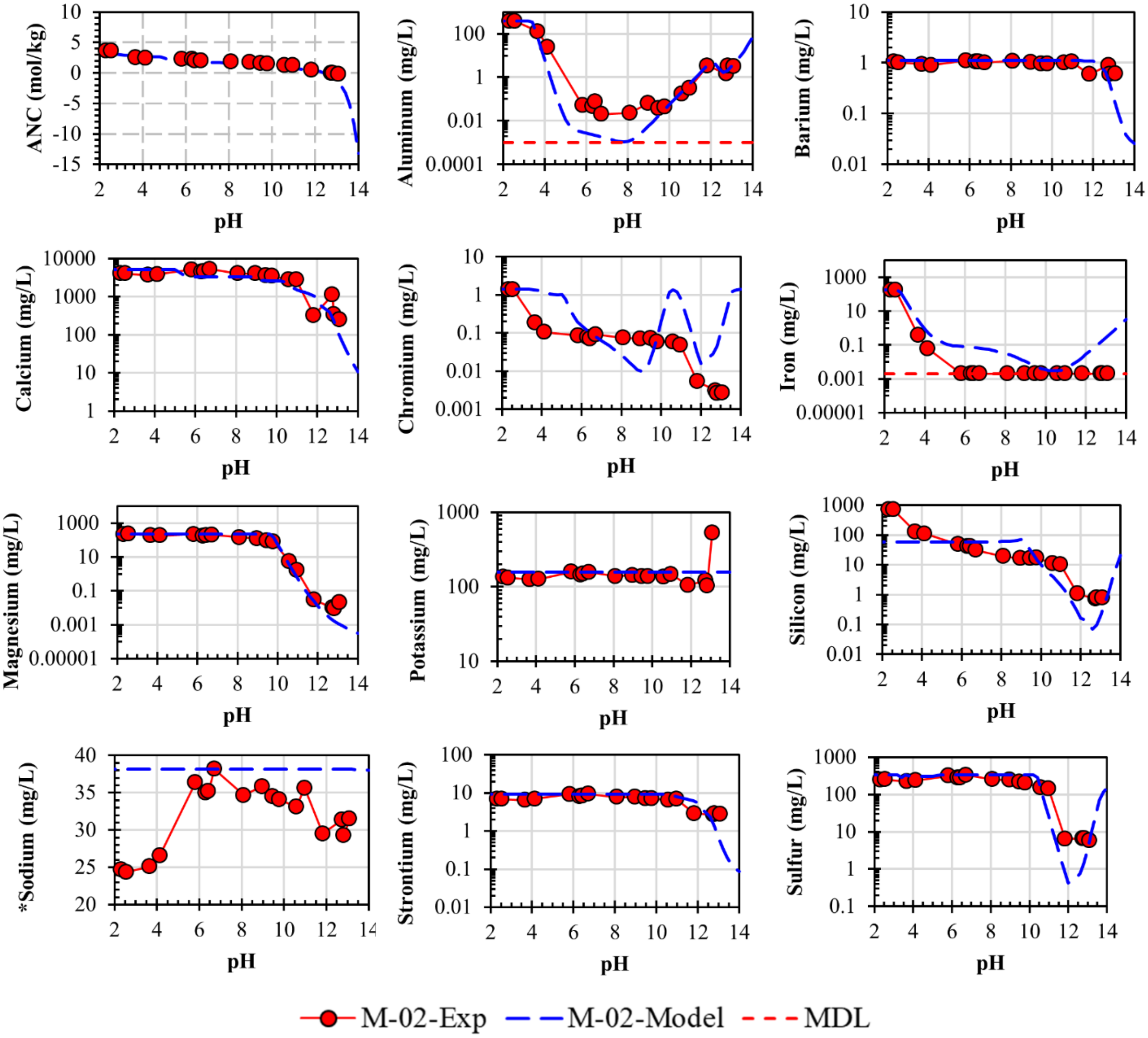

Figure 5.2. M-02 pH-dependent solubility experimental results compared to pH-dependent LSP model results for the ANC/BNC and selected constituents. *Y-axis shown on linear scale for sodium to highlight differences in sodium solubility as a function of pH.

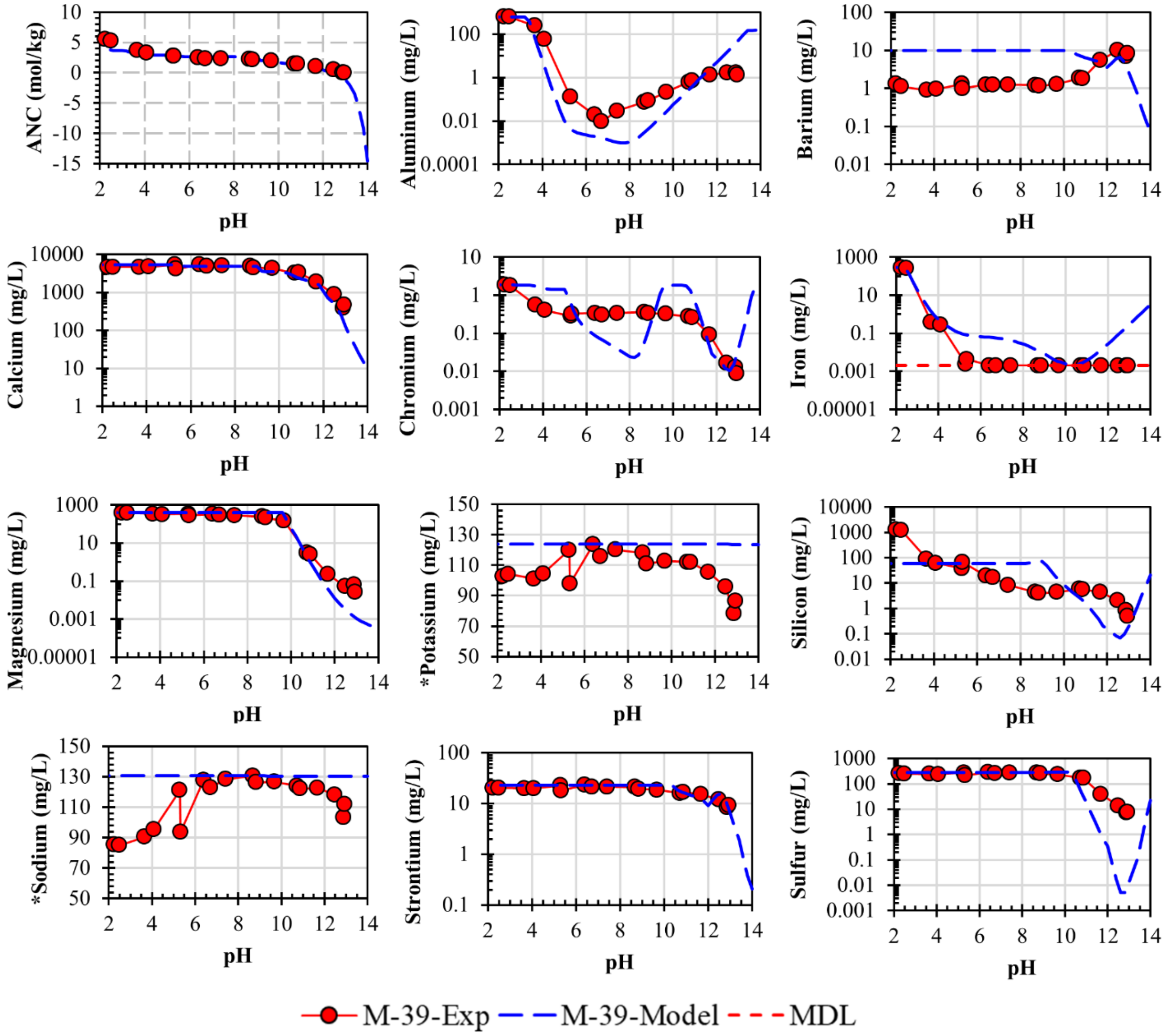

Figure 5.3. M-39 pH-dependent solubility experimental results compared to pH-dependent LSP model results for the ANC/BNC and selected constituents. *Y-axis shown on linear scale for sodium to highlight differences in sodium solubility as a function of pH.

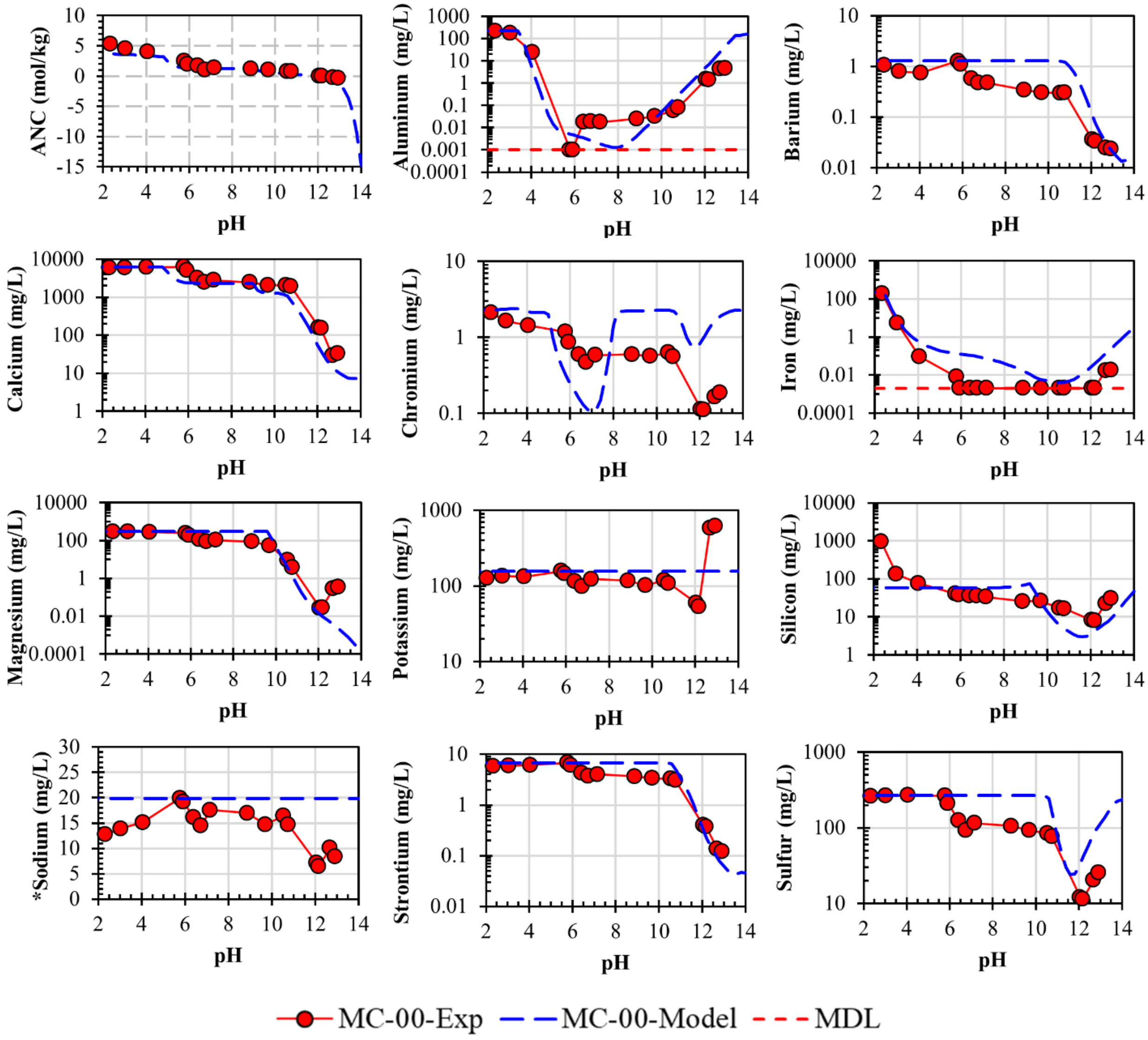

Figure 5.4. MC-00 pH-dependent solubility experimental results compared to pH-dependent LSP model results for the ANC/BNC and selected constituents. *Y-axis shown on linear scale for sodium to highlight differences in sodium solubility as a function of pH.

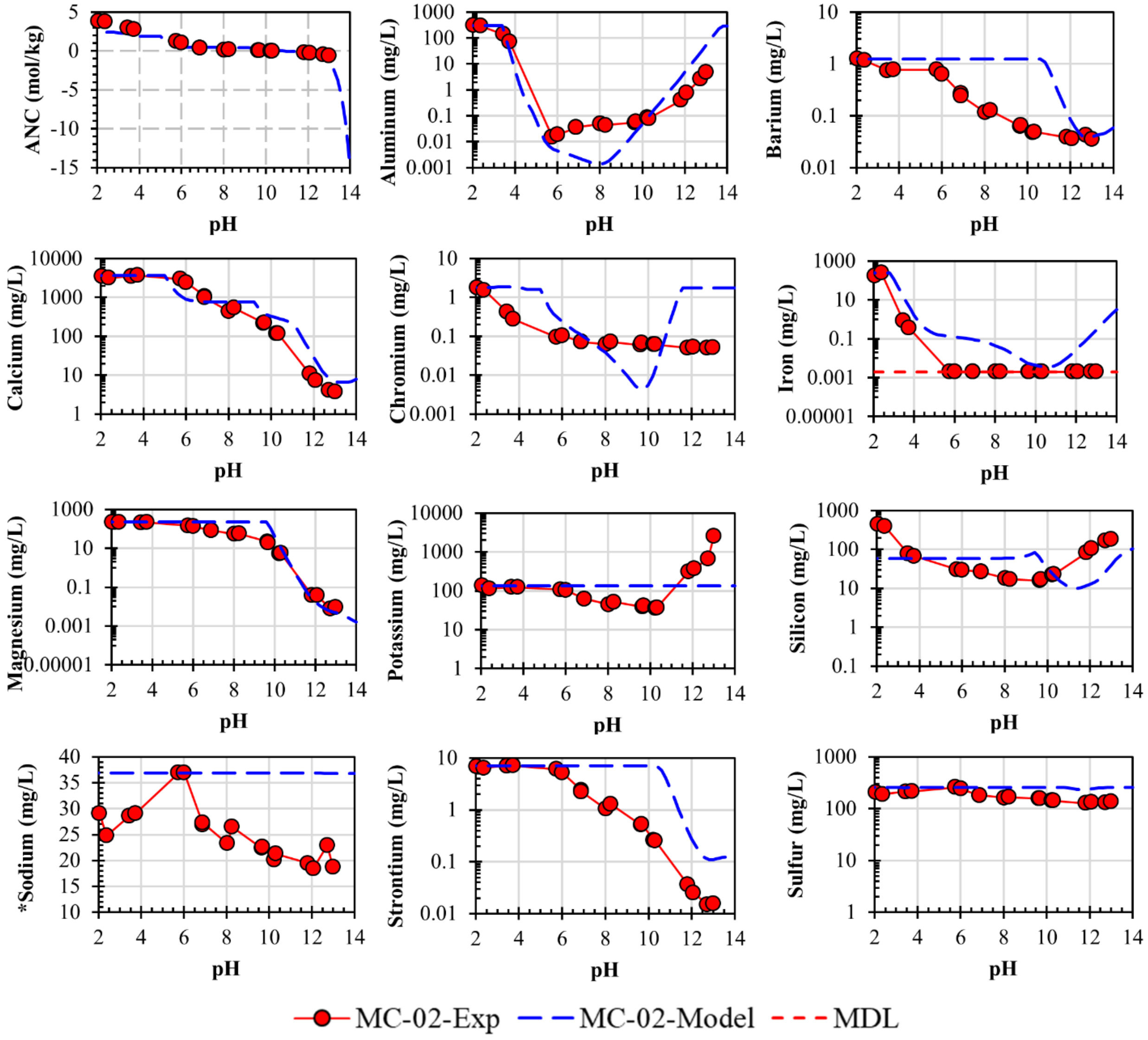

Figure 5.5. MC-02 pH-dependent solubility experimental results compared to pH-dependent LSP model results for the ANC/BNC and selected constituents. *Y-axis shown on linear scale for sodium to highlight differences in sodium solubility as a function of pH.

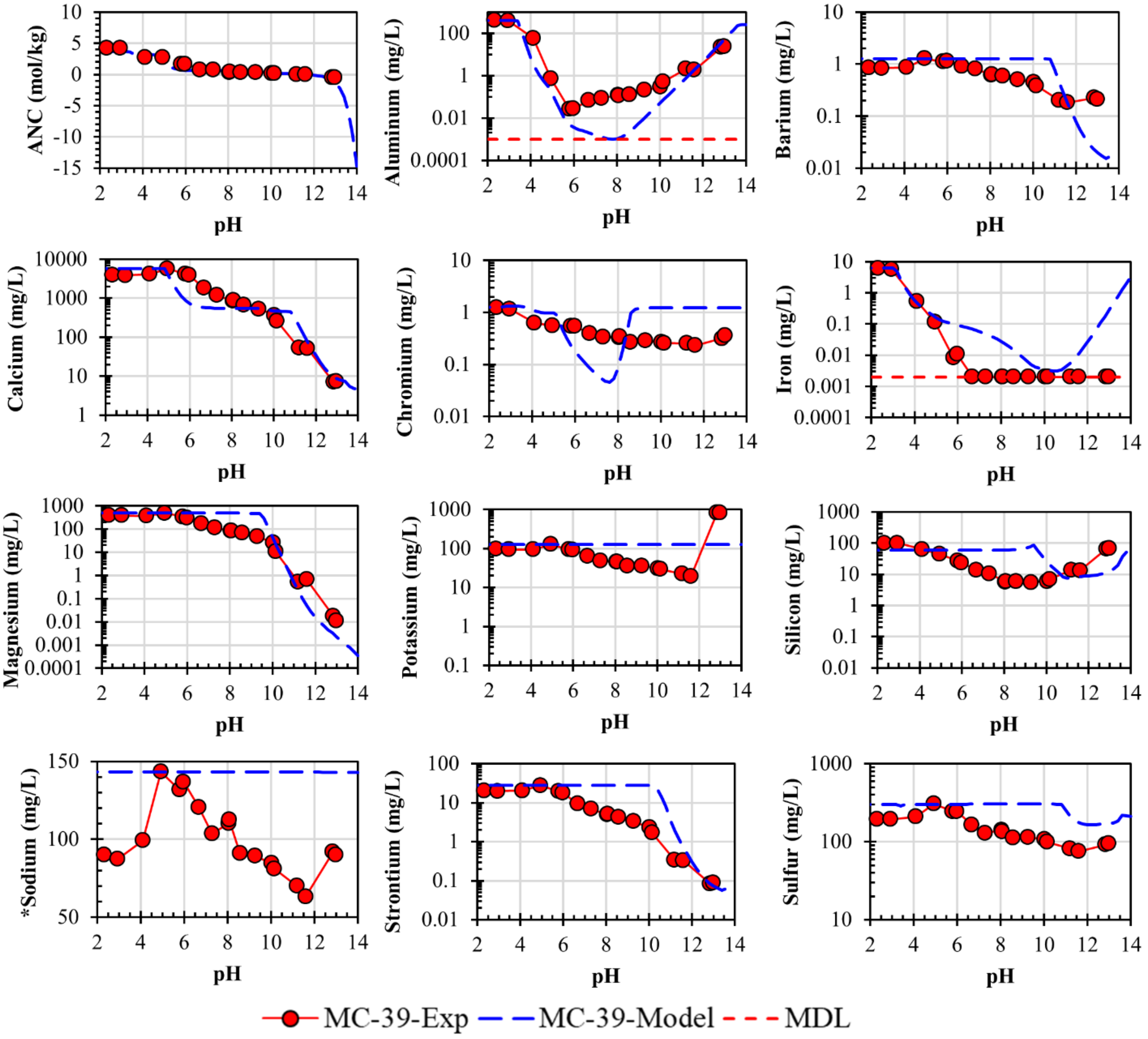

Figure 5.6. MC-39 pH-dependent solubility experimental results compared to pH-dependent LSP model results for the ANC/BNC and selected constituents. *Y-axis shown on linear scale for sodium to highlight differences in sodium solubility as a function of pH.

The sum of the log-squared residuals across all the microconcretes for each pH group and for each constituent of interest are reported in Table 5.3. The sum of the log-squared residuals of each constituent across the entire pH range of interest and the sum of the log-squared residuals of each pH group across all the constituents are also reported. The log-squared residuals for each individual microconcrete and each constituent are reported in Appendix D. The residual analysis reported for each constituent as a function of pH provides an indication for the model uncertainty over different regions in the pH where the relationship between solubility and pH may change.

For example, the solubility of aluminum is strongly associated with pH above pH ~8, but is relatively flat between pH ~6 and 8. In addition, experimental values are near or below detection limit for aluminum from pH ~6 to 8. Therefore, describing the residuals for aluminum within both of these regions indicates model uncertainty over a region where there is substantial change in pH, over a region where there is very little change in pH, and where there is greater experimental uncertainty due to low concentrations. The residual analysis reported for the microconcrete materials from this study in combination with other cementitious materials may also be used as a basis to develop model uncertainty as a function of pH in further work.

Table 5.3. Log-squared residuals for the pH-dependent solubility experimental results and pH-dependent LSP modeling results summed for all microconcretes (6 cases) as a function of pH for each selected constituent.

Target pH group	7	8	9	10.5	12	13	SUM
Al	8.02	10.46	4.79	1.09	3.09	4.74	32.19
Ba	1.51	2.29	3.02	2.94	0.60	1.33	11.69
Ca	0.23	0.09	0.11	0.35	1.33	0.79	2.90
Cr	1.76	1.53	3.11	3.44	5.45	5.41	20.70
Mg	0.75	1.39	3.02	0.55	1.45	8.74	15.91
K	0.29	0.43	0.64	0.74	1.00	2.12	5.22
Si	1.22	3.42	2.69	1.69	4.03	2.90	15.94
Na	0.04	0.05	0.11	0.13	0.42	0.23	0.98
Sr	0.59	1.25	2.17	3.48	1.83	1.02	10.35
S	0.32	0.36	0.50	2.08	9.24	10.22	22.73
SUM	14.73	21.28	20.16	16.50	28.44	37.50	138.61

In general, the trend in the pH-dependent LSP model results captures the pH-dependent solubility leaching behavior across the constituents considered in this work. The model results for specific constituents, specific differences between measurements and corresponding model predictions, and the minerals controlling LSP according to the geochemical speciation results (data not shown) are described as follows.

The solubility of aluminum decreases several orders of magnitude moving from the highly alkaline region to the neutral pH region, especially for M-00. The low solubility of aluminum across the target pH groups of 7, 8, and 9 is captured well by the model results for M-00. However, according to the experimental results, the decrease in the aluminum solubility in the neutral pH region is not as extreme for MC-00 (carbonated) compared to M-00, yet the model results predict a similar decrease in aluminum solubility for both M-00 and MC-00. A similar result is seen for the MC-02 and MC-39 materials. Geochemical speciation results indicate that diaspore controls aluminum solubility along with some aluminum bound in the dissolved organic carbon across the target pH groups of 7,8, and 9 for non-carbonated and carbonated microconcretes. For this work, the dissolved organic carbon content was calibrated considering only the measured pH in the eluate of the mass transfer tank leaching test. Therefore, refinement of the dissolved organic carbon content used in the carbonated materials that also considers aluminum speciation may further improve model predictions for aluminum in the carbonated materials. Differences between the model results and experimental results for M-02 and M-39 are also more notable in the pH region of 7, 8, and 9. These differences may be due to different speciation of aluminum for materials with fly ash compared to M-00 that is not accounted for when the mineral set was developed for the M-00 material.

For barium and strontium, larger differences in the pH-dependent LSP model results compared to the experimental results were observed for the carbonated microconcretes compared to the non-carbonated materials because the reduction in the solubility of barium and strontium observed in experimental data for the carbonated materials is not captured by the model, especially for MC-02. The reduction in the barium and strontium solubility in the carbonated microconcretes suggests that the barium and strontium react during carbonation to form less soluble minerals and these minerals are not represented in the mineral set used in the pH-dependent LSP model. Therefore, refinement of the mineral set to include barium or strontium carbonate phases may improve the carbonated microconcrete model predictions for barium and strontium. Efforts to describe the barium or strontium carbonate phases using available minerals in minteq.v4 did not improve the model results. Therefore, a more complex speciation of barium or strontium carbonate phases may exist that could be used to improve model results. Furthermore, refinement of the ettringite solid solution may also improve barium and strontium model results for the carbonated materials.

Larger differences in the pH-dependent LSP model results compared to the experimental results for barium also occur for M-39 because the increase in solubility observed for barium above pH ~11 was not captured by the model. The addition of the FA39 fly ash appears to alter the barium speciation in M-39 that is not captured by the mineral or solid solutions set applied to all the microconcretes. Correspondingly, the solubility of barium increases slightly for pH above ~11 in the MC-39, whereas the model results show a decrease in barium solubility for pH greater than ~11.

The solubility of calcium is relatively independent of pH below pH ~11 in the non-carbonated microconcretes. For the carbonated microconcretes, the calcium solubility is reduced in the alkaline region compared to the non-carbonated microconcretes and the solubility is a function of pH across the entire pH domain. The different trends in the calcium solubility are captured by the model results for all the microconcretes. Geochemical speciation results indicate that portlandite is the main calcium-bearing phase controlling solubility for pH greater than ~12 in the non-carbonated materials but disappears below pH 12. Monosulfoaluminate, calcite, the ettringite solid solution, the C-S-H solid solution, and gypsum are also present in significant quantities in the model results for the non-carbonated materials within the relevant pH range. In the carbonated microconcretes, portlandite disappears and calcium solubility is controlled mostly by calcite with some remaining C-S-H solid solution phases. The pH-dependent LSP model appears to adequately describe the distribution of calcium in the calcium bearing phases for all fly ash types and aging conditions evaluated in this work using a common mineral and solid solutions set.

The behavior of chromium according to the experimental results is captured by the model for M-00, M-02, and M-39 over the relevant pH range except for the M-02 model which over predicts chromium solubility at pH ~10-11. In the carbonated microconcretes, the solubility of chromium in the model is within approximately one order of magnitude over the relevant pH range, and in general the trend in the chromium solubility is well described by the model except for the chromium solubility trend in MC-02. The deviation of the chromium model results from the experimental results may be due to a different speciation of chromium in FA02, which has a greater impact of the chromium solubility than the chromium phases selected in the model (i.e., Cr_2O_3 and ettringite solid solution with chromium end member).

Experimental data for iron pH-dependent solubility was below detection for all batch extractions in the relevant pH range. However, the experimental data and model results for pH below ~6 agree well. In all the microconcretes, the geochemical speciation results indicate iron solubility is mostly controlled by maghemite over the entire relevant pH range of interest with some iron bound to the dissolved organic carbon below pH ~11. Further insights on the leaching behavior of iron and the modeling capabilities are discussed in the monolith diffusion-controlled leaching model results.

The leaching behavior of magnesium is captured well by the model results across all the microconcretes. According to the geochemical speciation, magnesium solubility is controlled by brucite above pH ~9 for all microconcrete types and aging conditions.

Sodium and potassium are often used as indicator species for diffusion because they are assumed to be non-reactive. The mineral and solid solutions set used in this work reflects this assumption as shown by the model results that show solubility of sodium and potassium are independent of pH. However, there may be some minor reactivity of sodium and potassium based on the experimental results that becomes even more pronounced after carbonation. The reactivity of sodium and potassium after carbonation may be due to the formation of sodium-carbonate/potassium-carbonate phases or solid solutions possibly with calcite during carbonation that are not as readily soluble. The implications of the reactivity of sodium and potassium are discussed further in 5.3.3.

In general, the behavior of silicon is captured by the model results, despite silicon solubility likely being kinetically controlled. The approach used in this work to model the pH-dependent solubility of constituents does not account for kinetics and, therefore the model predictions for silicon have greater uncertainty compared to other constituents. According to the geochemical speciation in the model for all microconcretes, SiO_2 controls the solubility of silicon below pH ~9 and the C-S-H solid solution controls the solubility of silicon above pH ~9.

The general trend in sulfur solubility is captured well for each microconcrete in the respective model results despite different trends in sulfur solubility observed in the experimental data and predicted by the model across the different microconcretes. According to the geochemical speciation results, sulfur solubility is controlled by the gypsum below pH ~10.5, the ettringite solid solution from pH ~10.5 to 13.5, and by monosulfoaluminate above pH 13.5 with some slight overlap of these minerals. In the MC-02 model, sulfur solubility is only controlled by the ettringite solid solution above pH ~10.5. For MC-00 and MC-39 models, sulfur solubility is controlled by ettringite solid solution from pH ~10.5 to 13.5 and by monosulfoaluminate above pH ~13.5. Therefore, the ettringite solid solution in combination with the gypsum and monosulfoaluminate used in this work appears to be able to describe changes in the sulfur solubility as a result of different fly ash types and carbonation.

5.3.2. Monolith diffusion-controlled leaching model results

The experimental results obtained from the mass transfer tank leaching test using EPA Method 1315 and the results obtained from the monolith diffusion-controlled modeling were compared for each microconcrete (i.e., M-00, M-02, M-39, MC-00, MC-02, and MC-39) in Figure 5.7-Figure 5.12.

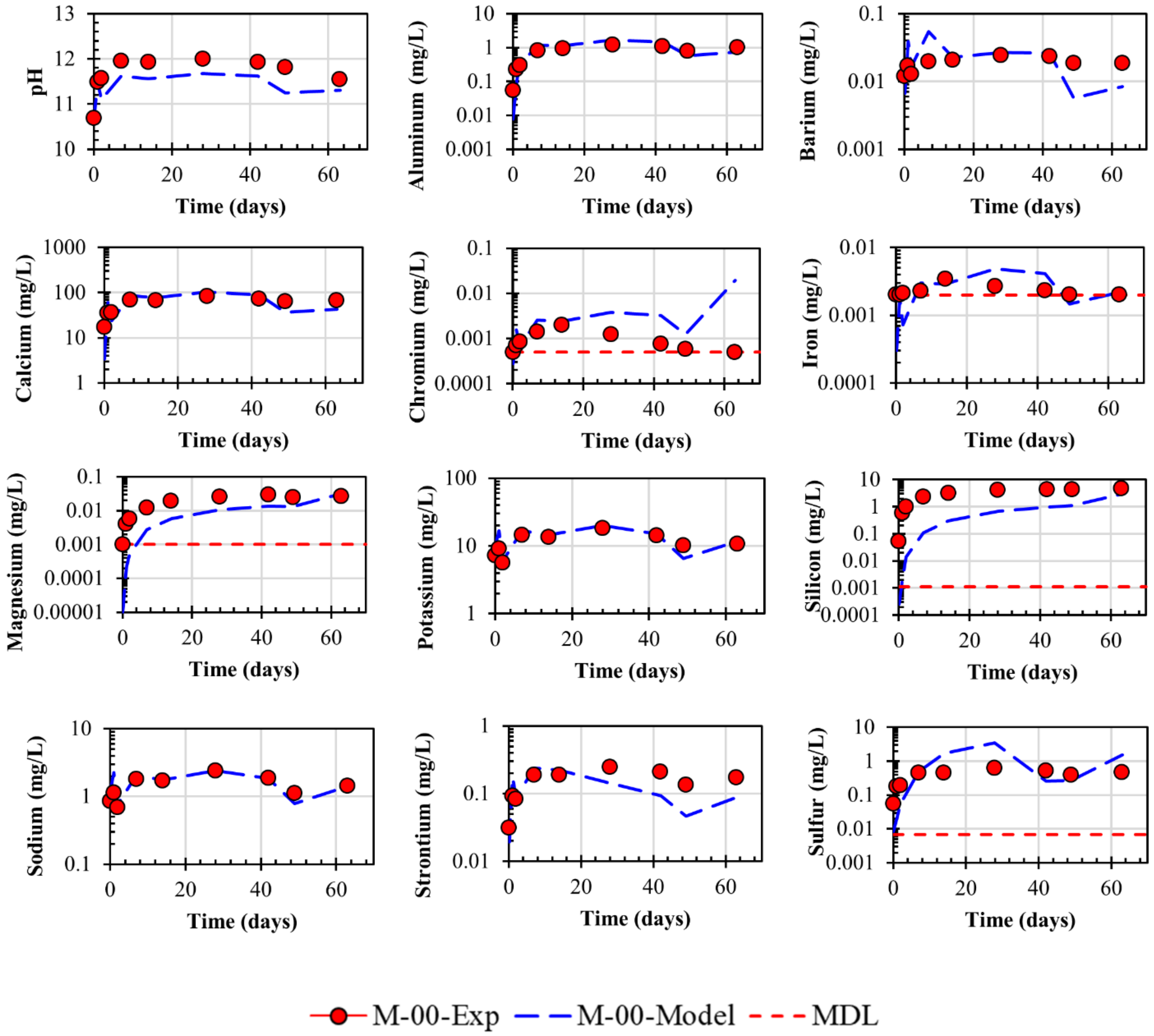

Figure 5.7. M-00 mass transfer tank leaching experimental results compared to the monolith diffusion-controlled leaching model results for the eluate pH and selected constituents for each exchange interval.

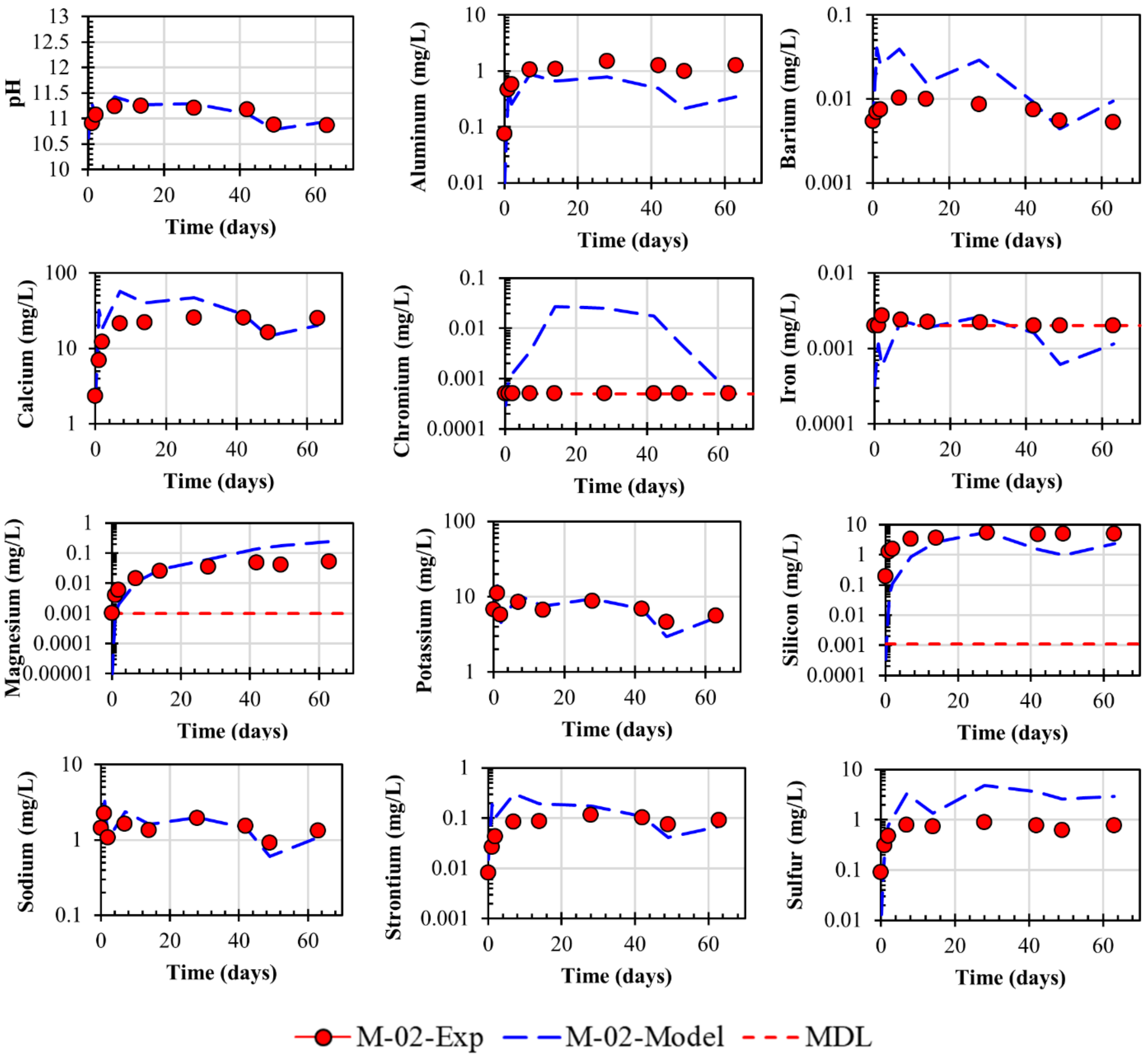

Figure 5.8. M-02 mass transfer tank leaching experimental results compared to the monolith diffusion-controlled leaching model results for the eluate pH and selected constituents for each exchange interval.

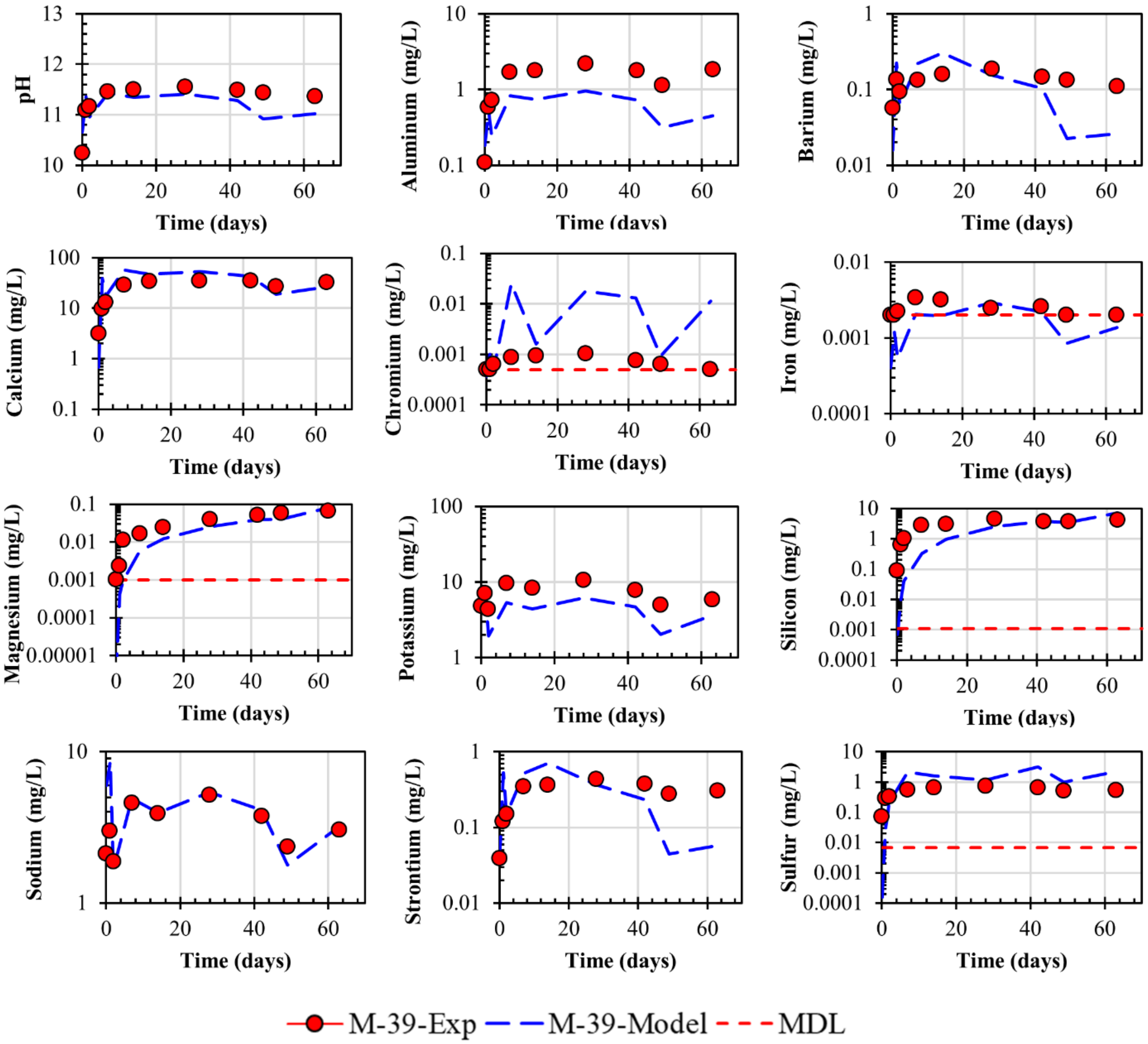

Figure 5.9. M-39 mass transfer tank leaching experimental results compared to the monolith diffusion-controlled leaching model results for the eluate pH and selected constituents for each exchange interval.

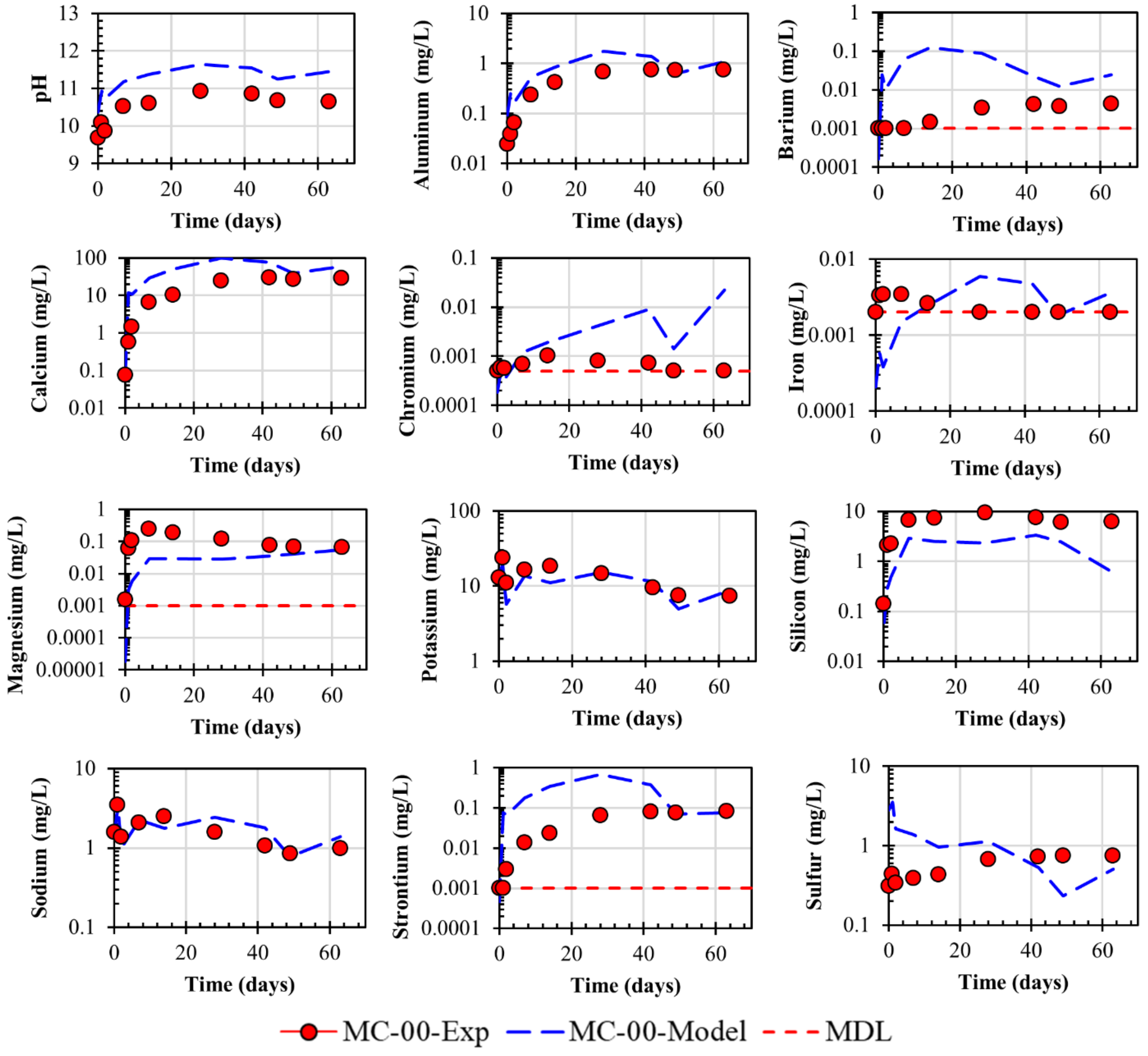

Figure 5.10. MC-00 mass transfer tank leaching experimental results compared to the monolith diffusion-controlled leaching model results for the eluate pH and selected constituents for each exchange interval.

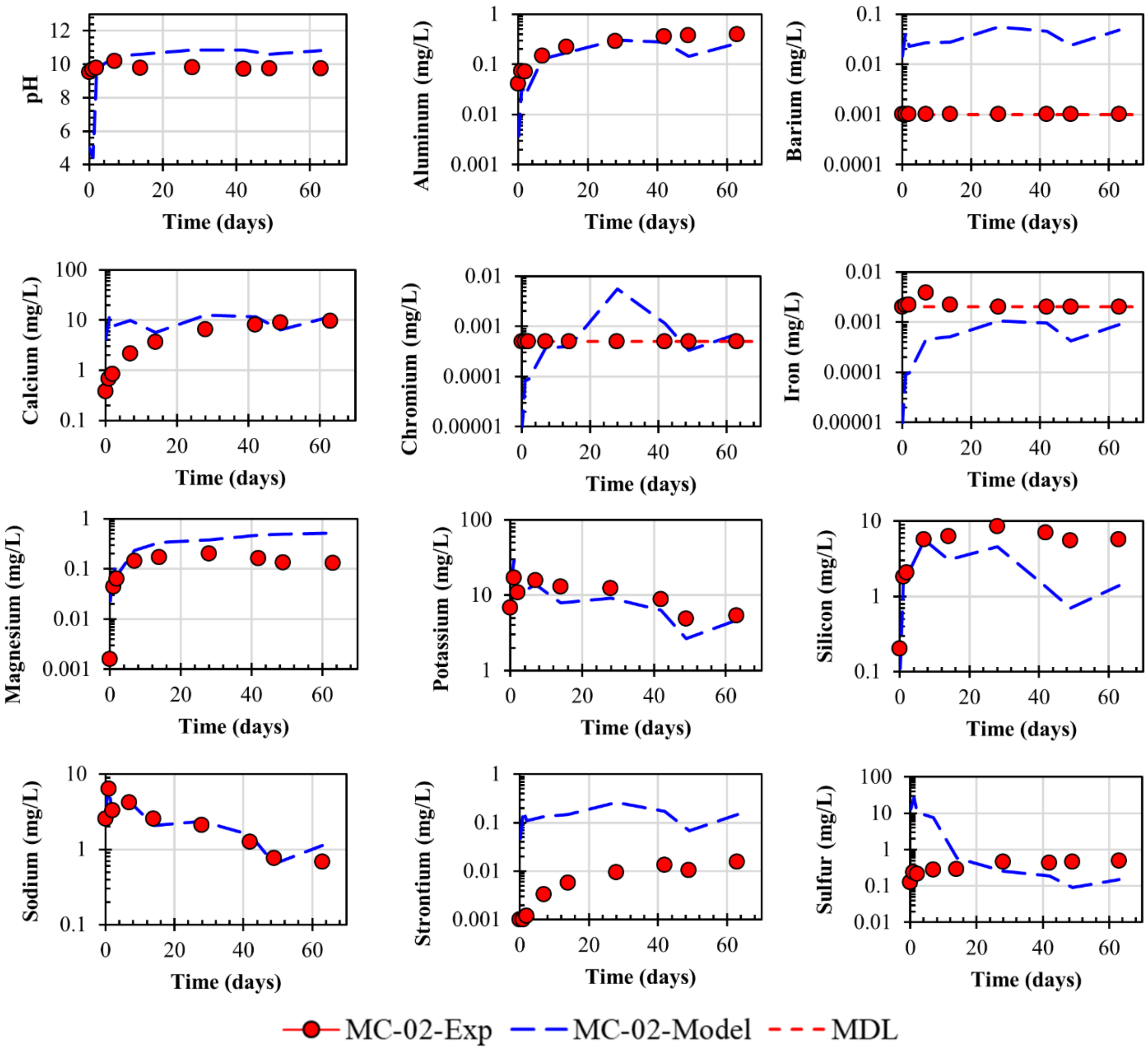

Figure 5.11. MC-02 mass transfer tank leaching experimental results compared to the monolith diffusion-controlled leaching model results for the eluate pH and selected constituents for each exchange interval.

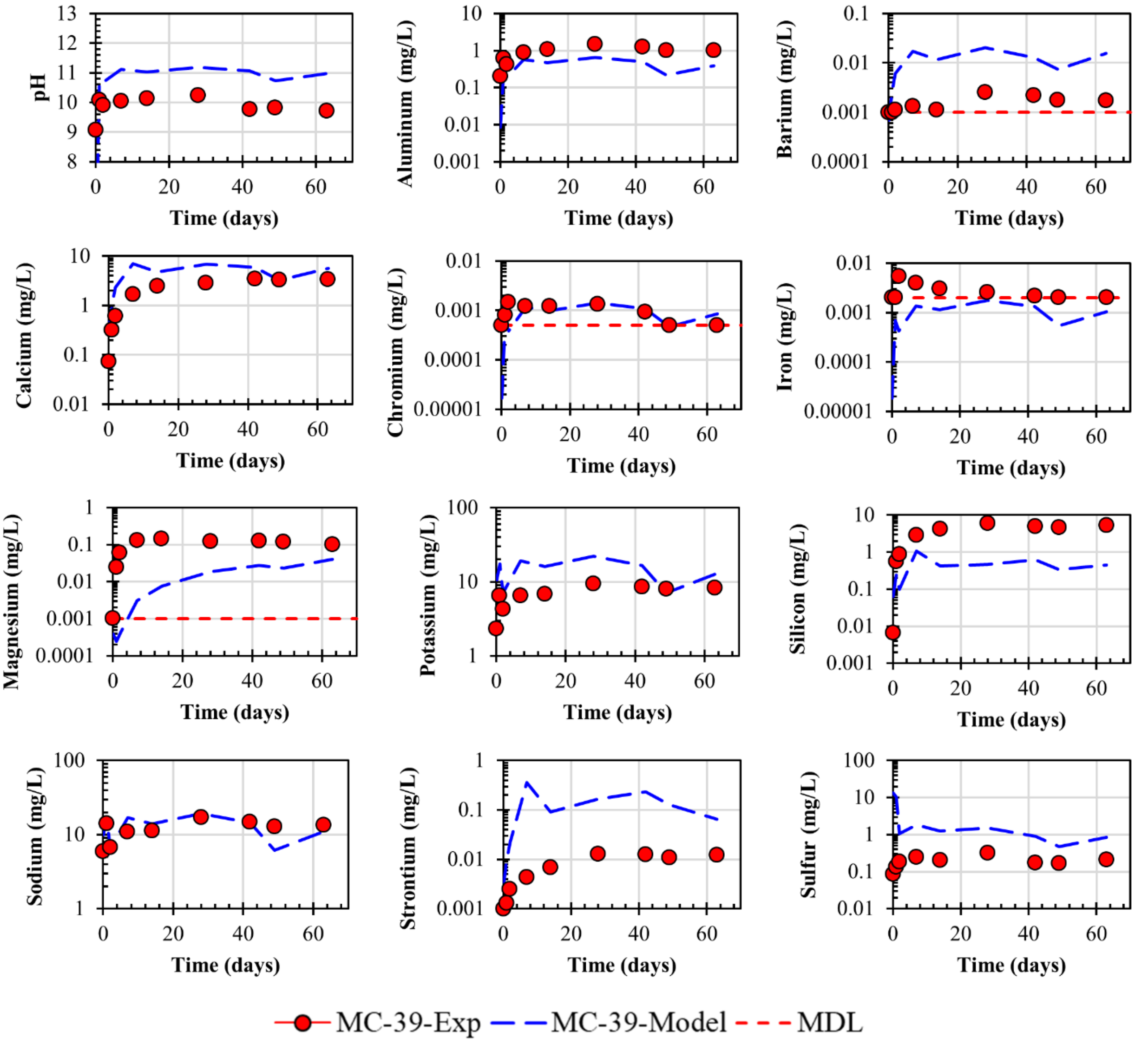

Figure 5.12. MC-39 mass transfer tank leaching experimental results compared to the monolith diffusion-controlled leaching model results for the eluate pH and selected constituents for each exchange interval.

The sum of the log-squared residuals across all the microconcretes (6 cases) for each exchange interval and for each constituent of interest are reported in Table 5.4. The total log-squared residual of each constituent across the entire 63-day cumulative leaching and the total log-squared residual for each exchange interval across all the constituents are also reported. The log-squared residuals for each microconcrete and each constituent are reported in Appendix D. The log-squared residuals of these materials in combination with residual analysis from other cementitious materials may be used as a basis to evaluate model uncertainty as a function of cumulative leaching time in further work.

Table 5.4. Log-squared residuals for the monolith mass transfer tank leaching experimental results and monolith diffusion-controlled leaching model results summed for all microconcretes (6 cases) as a function of exchange interval time for each constituent.

Cumulative leaching time (days)	0.08	1	2	7	14	28	42	49	63	SUM
Al	4.92	1.05	0.86	0.32	0.44	0.52	0.59	1.37	0.92	10.96
Ba	0.37	0.77	0.89	1.82	4.88	3.16	1.16	1.50	2.04	16.59
Ca	2.43	4.44	2.10	1.54	0.69	0.71	0.27	0.12	0.22	12.52
Cr	0.05	0.24	0.58	2.96	3.18	5.17	5.53	1.20	0.00	18.91
Fe	-	2.45	5.00	1.27	0.64	0.12	0.10	-	-	9.58
Mg	5.05	8.32	8.81	4.16	2.73	1.39	1.09	1.39	1.02	33.96
K	0.63	0.32	0.26	0.32	0.30	0.22	0.16	0.33	0.09	2.63
Si	18.49	12.23	7.95	3.22	2.64	2.30	2.13	3.08	2.71	54.7
Na	0.31	0.34	0.02	0.07	0.05	0.03	0.06	0.17	0.09	1.14
Sr	3.11	7.09	6.80	7.85	4.81	4.48	3.49	2.73	2.13	42.49
S	18.27	10.60	4.27	3.89	1.40	1.71	1.67	1.45	1.65	44.91
SUM	53.63	47.85	37.54	27.42	21.76	19.81	16.25	13.34	10.87	248.47

The initial exchanges have larger log-squared residuals for the experimental data and the model results for the initial exchanges compared to longer leaching intervals. This result may be due to several effects including: 1) surface wash-off that occurs during the first exchange interval, 2) sample preparation effects at the exterior surface, and 3) saturation effects during the initial leaching times. Therefore, a greater uncertainty exists for the experimental results and model performance in the initial exchanges and only the leaching behavior of the constituents after one day of cumulative leaching may be representative of the material.

In general, the monolith diffusion-controlled leaching model results are within one order of magnitude of the experimental results across all the microconcretes and constituents for aluminum, calcium and silicon. Eluate pH is also captured by the model results with slightly greater differences between the model and experimental results for MC-02 and MC-39. The model results for other constituents and exchange intervals are discussed further as follows.

Differences in the monolith diffusion-controlled leaching model results from the experimental results correlate with the differences observed in the pH-dependent LSP model. For example, barium and strontium are over-predicted in the model results compared to the experimental results for the carbonated materials possibly due to the lack of the lower solubility barium and strontium carbonate phase(s) as discussed previously. The chromium experimental results are near or below the detection limit and, therefore, it is difficult to assess the effectiveness of the model to capture chromium mass transfer release. However, the model appears to perform poorly, especially for M-02, as seen in the pH-dependent LSP modeling work, which further supports the need for an additional chromium bearing phase possibly from the FA02 fly ash used in M-02.

The concentration of iron in the eluate is near or below detection limit for a majority of the exchanges. Correspondingly, the model results show an iron concentration below detection limit for a majority of the experimental data points reported as below detection limit. For experimental data points above the detection limit, the model results are within one order of magnitude, except for the initial exchanges that show similar deviation from the experimental results as noted for other constituents in this section. Larger concentrations of dissolved organic carbon used in the model compared to what is present in the microconcretes could explain the delayed release of iron in the model results. Further refinement of the dissolved organic carbon concentration used in the model that considers the iron could improve the model results for iron.

Magnesium solubility for the model results are within one order of magnitude for all the microconcretes with the exception of the initial exchanges for M-39 and MC-39. This exception corresponds to the pH-dependent LSP model where magnesium solubility is slightly under-predicted at the pH corresponding to the respective eluate pH measured in the mass transfer tank leaching test for the initial exchanges. However, at longer cumulative leaching times, the monolith diffusion-controlled leaching model results for magnesium are in better agreement.

The potassium monolith diffusion-controlled leaching results track well with the calibrated sodium monolith diffusion-controlled leaching results except for a slightly higher log-squared residual observed for the M-39. This difference may be due to assumption that sodium and potassium are non-reactive. However, as discussed previously, the pH-dependent solubility experimental results indicate that the solubility of these constituents are a function of pH, which is especially pronounced for M-39 and MC-39. Therefore, accounting for additional minerals in the potassium may improve the model results for potassium especially in M-39 and MC-39.

The mass transfer release of sulfur is adequately described in the model results except for the initial exchanges in the carbonated microconcretes, where the model results indicate a higher release of sulfur compared to the experimental results. However, at longer cumulative leaching times, the sulfur release in the model results is within one order of magnitude of the experimental results. The initial differences correspond with the differences between the model and experimental results for the pH-dependent solubility as discussed previously.

5.3.3. Effective diffusivity and tortuosity calibration using sodium

The effective diffusivity for sodium as a function of depth was compared between the non-carbonated and carbonated materials for each microconcrete type (Figure 5.13). The effective diffusivity was not plotted for cells located at depths greater than 3 mm because changing the tortuosity in the cells located at greater depths did not impact the model predictions for sodium over the 63-day cumulative leaching period. Therefore, it is assumed that the leaching front and diffusion processes only occur within the first 3 mm of the material over the 63-day cumulative leaching period.

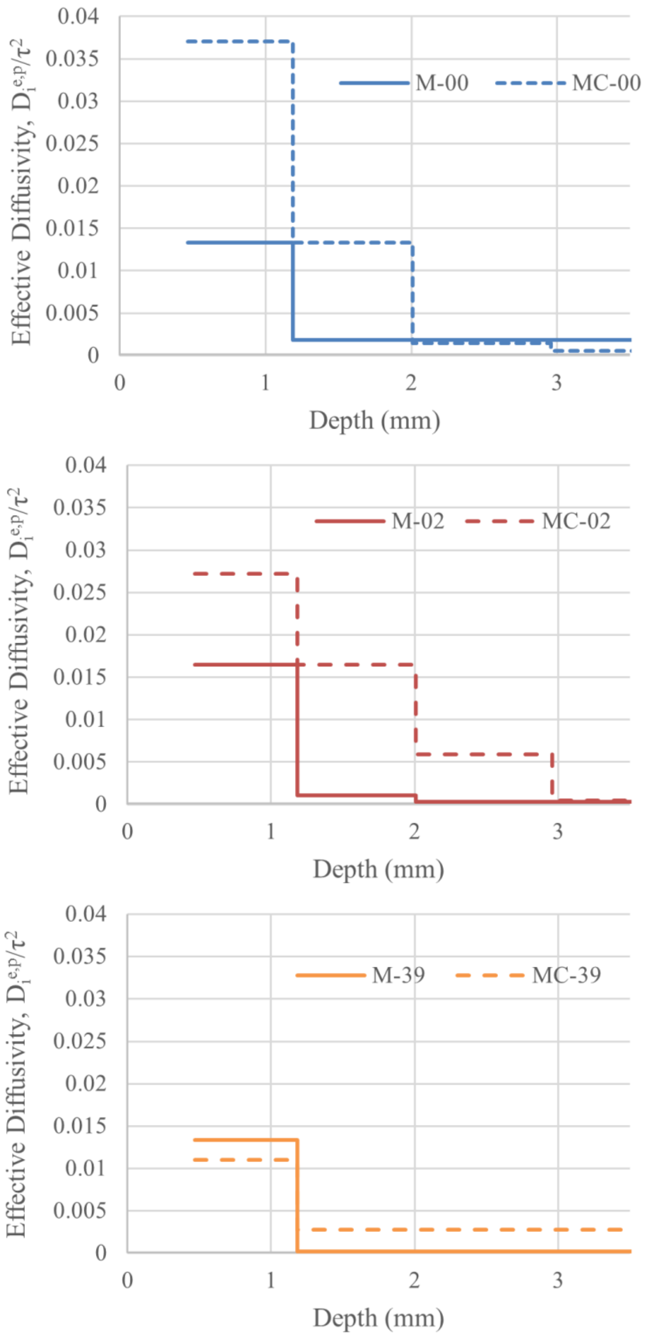

Figure 5.13. Effective diffusivity for sodium as a function of depth for non-carbonated and carbonated microconcretes obtained from calibrating the tortuosity to the sodium concentrations in the eluate in the mass transfer test

The effective diffusivity obtained from calibrating the tortuosity using sodium is higher at the outer cells for the MC-00 and MC-02 compared to the M-00 and M-02, respectively. The effective diffusivity is slightly higher in the M-39 compared to the MC-39 for the first cell, but

MC-39 has a slightly higher effective diffusivity at more interior cells. However, the carbonation reaction appears to reduce the porosity in the microconcrete materials based on experimental work performed [108], which would suggest that a decrease in effective diffusivity for the carbonated materials should be obtained from the tortuosity calibration. Although the changes in porosity were obtained from SEM measurements were limited to pore sizes greater than the image resolution used (i.e., 0.0625 μm^2/pixel) and did not incorporate air voids, it is not expected that porosity would increase for the pores outside the SEM pore size detection range. Therefore, this evidence suggests that the use of sodium to calibrate the tortuosity may have some limitations in cementitious materials, especially when applied to carbonated microconcretes.

One limitation for using sodium to calibrate the tortuosity may be a result of the reduction in the sodium solubility for the carbonated microconcretes compared to the non-carbonated microconcretes observed in the pH-dependent solubility test for pH values greater than 8. This reduction in sodium solubility is likely a result of the reaction of dissolved sodium in the pore solution with CO_2 to form sodium carbonate or other sodium-carbonate type minerals as discussed previously. An underlying assumption for using sodium in the tortuosity calibration is that sodium is non-reactive and the availability of sodium is based on the highest concentration of sodium in the eluate obtained from the pH-dependent solubility test. In carbonated microconcretes, the solubility of the sodium-carbonate type phases lowers the solubility of sodium and, therefore, the tortuosity values obtained from the calibration may not be reflective of the influence of sodium solubility on the mass transport during the leaching test. Additionally, a reduced available content of sodium in the carbonated region compared to the sodium available content used in the monolith diffusion model may impact the calibrated tortuosity values. Therefore, more experimental work is needed to better understand the sodium-carbonate phases that may be forming during carbonation in the microconcretes to account for changes in sodium LSP. In addition, better understanding the impact of carbonation of the available content of sodium within the material during carbonation may provide further insights on the effective diffusivities obtained from the tortuosity calibration.

An additional limitation to using sodium to calibrate the tortuosity in carbonated materials may be due to the migration and deposition of sodium in the carbonated region in response to changes in the relative sodium solubility as a result of carbonation and also from water migration due to the generation of water during carbonation. Branch et al., 2016 [91] reported that calcium migrated towards the exposed surface in carbonated microconcretes in response to the reduced calcium solubility in the carbonated region of the microconcretes. Similar to calcium, the sodium solubility was lower in the carbonated microconcretes compared to the non-carbonated microconcretes as discussed previously. Compared to calcium, quantifying the concentration of sodium as a function of depth using SEM-EDS has a greater uncertainty because of the low concentration of sodium in the material. However, based on the similar reduction in the sodium and calcium solubility in the carbonated microconcretes compared to the non-carbonated microconcretes, the migration of sodium towards the exposed surface might be expected during carbonation. Therefore, the available content of sodium at the exposed surface may be greater than the available content of sodium at the interior regions. As a result, the difference in the sodium concentration profiles after carbonation may impact that calibrated tortuosity values obtained in the monolith diffusion modeling. Further work is needed to better understand the distribution of sodium within carbonated microconcretes to determine the effective diffusivity of carbonated microconcretes.

It should also be noted that other non-reactive constituents (i.e., potassium, nitrate, and chloride) were also considered for the tortuosity calibration. However, potassium also appears to change solubility as a result of carbonation and, therefore, may have the same implications in the tortuosity calibration as sodium. Nitrate and chloride were below detection limit in a majority of the eluate exchanges for the mass transfer test and therefore could not be used to calibrate the tortuosity.

5.4. Conclusions

The pH-dependent LSP and monolith diffusion-controlled leaching behavior were modeled for non-carbonated and carbonated microconcretes with varying fly ash replacements using a common mineral and solid solutions. In general, the model results reasonably described the experimental leaching behavior across the different constituents considered in this work for all microconcrete types and aging conditions. Some limitations in applying a common mineral and solid solutions set to all the microconcretes considered in this work were identified such as the potential reaction of barium, sodium, potassium, and strontium during carbonation and the different speciation of chromium present in different fly ash types. The residual analysis performed in this work provided an indication of model uncertainty as a function of pH and cumulative leaching time for constituents of interest. In the monolith diffusion-controlled leaching model, greater differences in the model and experimental data appears at earlier exchange intervals likely as a result of sample properties and the small exchange times.

5.5. Acknowledgements

This document is based on work supported by the U. S. Department of Energy, under Cooperative Agreement Number DE-FC01-06EW07053 entitled ‘The Consortium for Risk Evaluation with Stakeholder Participation III’ awarded to Vanderbilt University, David S. Kosson, principal investigator.

CHAPTER 6

CONCLUSIONS AND FUTURE WORK

This dissertation investigated the impact of aging in cementitious materials similar to those being used and investigated as cementitious waste forms or barriers for radioactive waste disposal. The specific conclusions for each chapter of this dissertation are presented below.

Chapter 2 investigated the impact of alkalinity on the changes in constituent solubility and microstructure as a result of carbonation for microconcrete materials prepared with different fly ash type. The alkalinity of the fly ash used in the microconcrete formulation corresponded with the alkalinity of the resultant microconcrete. A lower alkalinity of the microconcrete material was associated with a lower natural pH of the material and a decrease in the carbonation reaction capacity of the material. A lower alkalinity of the microconcrete also resulted a greater depth of carbonation, extent of reaction, and extent of microstructural changes after carbonation. Variability in the carbonation depth within each microconcrete was observed likely as a result of aggregate geometry and orientation in the material which can create preferred gaseous diffusional pathways around the more porous ITZ region. Constituent migration and deposition of calcium in the carbonated region was observed in response to changes in calcium solubility as a result of the reaction products formed during carbonation. Results from Chapter 2 indicate that the alkalinity of the fly ash material used in cementitious materials should be considered when evaluating and predicting the long-term performance of cementitious materials that may potentially be exposed to gaseous CO_2 over their lifetimes.

Chapter 3 investigated the impact of ash type on the porosity and the changes in porosity that occur as a result of carbonation using BSE imaging for the microconcretes investigated in Chapter 2. Specifically, the porosity within the bulk and ITZ region was quantified for non-carbonated and carbonated microconcretes prepared with different fly ash replacement types. Results from this chapter indicate that the selected methodology using BSE imaging from SEM is an appropriate method to quantify the bulk and ITZ porosity for carbonated and non-carbonated microconcretes with fly ash replacement. Furthermore, the results support the presence of a more porous ITZ region and that the difference in porosity between the bulk and ITZ region may be become more exaggerated after carbonation due to the availability to react within the ITZ region and the degree of saturation within the ITZ region. Fly ash type influenced the bulk and ITZ porosities as well as the relative differences between the two regions. Results from Chapter 3 indicate that the fly ash replacement type as well as the development of the ITZ region may influence the long-term performance of cementitious materials exposed to gaseous CO_2.

Chapter 4 investigated the impact of aging in an inert environment and in a reactive environment containing oxygen and carbon dioxide for a cementitious material similar to cementitious waste forms being used or considered for low activity nuclear waste disposal. Results from this chapter indicate that mineralogy and microstructural changes that occur as a result of carbonation in cast stone are different from what has been observed for traditional Portland cement-based materials likely as a result of the high replacement of the Portland cement using SCMs and the addition of salt waste. Alite, aragonite, belite, calcite, gypsum, mullite, nitratine, potassium nitrate, quartz, tobermorite, and vaterite were the crystalline phases identified in the prepared cast stone. Precipitation of Na_2SO_3/Na_2SO_4 was also observed in the cast stone material aged in the inert environment. Alite, belite, tobermorite, and Na_2SO_3/Na_2SO_4 were depleted in the oxidized/carbonated material and an increase in aragonite, calcite, gypsum, and vaterite concentrations were observed in the oxidized/carbonated material in response to changes in the pore water chemistry and redox reactions. The carbonation reaction was found to increase the porosity of the cast stone material especially for pore sizes $0.25\ \mu m \leq$ pore size $\leq 4.3\ \mu m$ as a result of increased cracking and possibly an overall decrease in molar volume of the material. Constituent solubility and mass transfer rates were different for the cast stone aged in reactive environment compared to the inert environment as a result of different mineralogy and differences in the porosity and tortuosity between the materials.

In Chapter 5, geochemical speciation with reactive transport modeling was performed for the microconcretes evaluated in Chapters 2 and 3 to better understand the change in mineralogy and leaching behavior that occurs as a result of carbonation. With some identified limitations, a common mineral and solid solution set can be used to model the pH-dependent LSP and monolith diffusion-controlled leaching in non-carbonated and carbonated microconcretes with varying fly ash replacement type. Further refinement of the mineral set to include carbonated species and other minerals for different fly ash types could improve model results for specific microconcrete types or aging conditions.

There are many additional research questions and future areas of work that arise from the overall conclusions and findings of this dissertation. For example, future work could include analyzing the leaching behavior and microstructural characteristics of the additional cast stone materials prepared with different fly ash types as presented in Appendix C to better understand the role of fly ash composition on the mineralogy of cementitious waste forms and leaching behavior after aging. These results could also be used to extend the work performed in Chapter 5 to create a geochemical speciation with reactive transport model that describes the leaching behavior for a family of cementitious waste forms and barriers.

The impact of aging within microconcrete and cast stone materials was only investigated at one relative humidity and CO_2 concentration. However, in field conditions varying levels of relative humidity and CO_2 concentrations may be present that can alter the transport and reaction of reactive gases. Therefore, a natural extension of this work is to investigate the impact of relative humidity and CO_2 concentration on the aging mechanisms and overall impact on material performance for cementitious materials.

APPENDIX A

SUPPLEMENTARY MATERIAL FOR CHAPTER 2

Table A.1. Sieve analysis of 300 grams of fine aggregate according to ASTM Standard C33 [159]

Sieve Nominal Size	Cumulative Mass % Retained
9.5-mm	0
4.75-mm	3
2.36-mm	12
1.18-mm	24
600-µm	54
300-µm	92
150-µm	99
75-µm	99

Table A.2. Polishing lubricants and polishing cloths used for each SEM-EDS polishing step. Step 1 was polished by hand and steps 2-5 were polished using the Allied MetPrep 3 grinder/polisher[1]

Step	Duration (mins)	Polishing Lubricant	Polishing Cloth
1	2	Blue lube[1]	240 grit silicon carbide sandpaper[2]
2	6	Blue lube	320 grit silicon carbide sandpaper disc[3]
3	2	Blue lube	600 grit silicon carbide sandpaper disc[3]
4	8	Blue lube + 6 µm diamond paste[3]	Very dense, woven, low-nap silk cloth disc[1]
5	8	Blue lube + 1 µm diamond paste[3]	Very dense, woven, low-nap silk cloth disc

[1] Allied High Tech Products, Inc., Rancho Dominguez, CA

[2] Norton Abrasives, Worcester, MA

[3] Buehler, Lake Bluff, IL

Table A.3. Threshold values (wt%) to remove non-cement components based on the average composition of a 3 x 3 pixel area surrounding each image pixel. Threshold values were derived from the composition of the fine aggregate used in the microconcretes, the epoxy used in sample mounting, and prior SEM-EDS scans of each fly ash.

Element	Criteria	Threshold	Rationale
C	>	15	Epoxy
Al	>	15	Fly Ash
Si	>	20	Sand
Ca	<	5	Non-cement
Fe	>	5	Fly Ash

APPENDIX B

SUPPLEMENTARY MATERIAL FOR CHAPTER 3

Table B.1. Facility configurations for coal combustion fly ash sources.*

Sample code:	**FA02**	**FA39**
Fly ash class	F	C
Total calcium (wt. %)	4	23
Annual production	50–200 K tons	50–200 K tons
Boiler type	Pulverized coal	Pulverized coal
Unit size	667 MW	550 MW
Coal type	Bituminous	Sub-bituminous
Particulate capture	Baghouse filter	Cold-side electrostatic precipitator
Hg sorbent injection	None	None

*Derived from Kosson et. al, 2014 [3]

Table B.2. *Sieve analysis of 300 grams of fine aggregate according to ASTM Standard C33 [159]

Sieve Nominal Size	Cumulative Mass % Retained
9.5-mm	0
4.75-mm	3
2.36-mm	12
1.18-mm	24
600-µm	54
300-µm	92
150-µm	99
75-µm	99

*From Branch et. al, 2016 [91]

Table B.3. Mix designs for microconcrete samples.*

	Control	**Blend**
Nominal mix (kg/m^3)	514	514
Fly ash replacement (%)	–	45
Composition (wt. %)		
Ordinary Portland cement	22.2	12.2
Fly ash	–	10.0
Water	9.9	10.1
Fine aggregate	67.9	67.7
Sample codes	M-00	M-02 M-39

*Derived from Kosson et al., 2014 [3]

Table B.4. Mean relative saturation for three replicates of each non-carbonated microconcretes in air at 65% RH, (θ_{65}), according to Equation B1

Material	(θ_{65})
M-00	0.648
M-39	0.771
M-02	0.754

Equation B1*:

$$\theta_{65} = \frac{(m_{65} - m_{dry})}{(m_{sat} - m_{dry})}$$

where m_{65} is the measured equilibrated mass of the sample in air at 65% RH (g)
m_{dry} is the oven-dried (105°C) equilibrated mass of the sample (g), and
m_{sat} is the equilibrated mass of a saturated sample submerged in water (g)

*Notes: Derived from Garrabrants and Kosson, 2003 [160]. Relative saturation testing was conducted on rectangular prisms with dimensions of approximately 2x2x1cm

Table B.5. Polishing lubricants and polishing cloths used for each SEM-EDS polishing step. Step 1 was polished by hand and steps 2-5 were polished using the Allied MetPrep 3 grinder/polisher[1]

Step	Duration (mins)	Polishing Lubricant	Polishing Cloth
1	2	Blue lube[1]	240 grit silicon carbide sandpaper[2]
2	6	Blue lube	320 grit silicon carbide sandpaper disc[3]
3	2	Blue lube	600 grit silicon carbide sandpaper disc[3]
4	8	Blue lube + 6 µm diamond paste[3]	Very dense, woven, low-nap silk cloth disc[1]
5	8	Blue lube + 1 µm diamond paste[3]	Very dense, woven, low-nap silk cloth disc

[1] Allied High Tech Products, Inc., Rancho Dominguez, CA

[2] Norton Abrasives, Worcester, MA

[3] Buehler, Lake Bluff, IL

*From Branch et al., 2016 [91]

APPENDIX C

SUPPLEMENTARY MATERIAL FOR CHAPTER 4

Impact of de-coupled oxidation and carbonation reactions on the leaching behavior in cementitious waste forms

In addition to the inert aging condition (-N) and the aging condition in gaseous oxygen and carbon dioxide (-OC) presented in Chapter 4, two additional aging conditions were studied to evaluate the de-decoupled effect of oxidation and carbonation in cementitious waste forms. The first additional aging condition (-O) was conducted under air with no CO_2 to mimic an atmospheric condition without CO_2 in order to evaluate the sole effect of oxidation. The second additional aging condition (-C) was conducted under 95% N_2 and 5% CO_2 (i.e., no O_2) to evaluate the sole effect of carbonation. The samples were handled and prepared identical to the –N and –OC materials prior to aging. The samples were then aged in their respective environments for the same amount of time as the –N and –OC conditions (i.e., 60 days).

Impact of fly ash composition on the leaching behavior in cementitious waste forms

In chapter 4, a single material composition containing a specific fly ash, “FAF”, was evaluated. To evaluate the impact of material composition on the leaching behavior after aging, two additional cementitious waste forms were prepared using fly ash with different compositions. However, the same dry weight ingredient proportions, LAW simulant, mixing procedures, and aging procedures that were used to prepare the cementitious waste form presented in Chapter 4 we also used to prepare the additional cementitious waste forms. A Class F fly ash, NFA02 was used to prepare a cementitious waste form denoted as CS-NFA02 and a Class C fly ash, NFA18 was used to prepare a cementitious waste form denoted as CS-NFA18.

The nomenclature for material containing FAF fly ash was denoted as CS-N and CS-OC for simplicity in Chapter 4. However, in the following supplemental section, the material contain FAF fly ash is denoted as CS-FAF to distinguish the material from CS-NFA02 and CS-NFA18. All four aging conditions (i.e., -N, -O, -C, and –OC) were evaluated for CS-FAF, CS-NFA02 and CS-NFA18.

The oxide composition of the dry ingredient portion (i.e., OPC, fly ash, GGBFS) for the three cementitious waste forms evaluated in this study, a cast stone prepared by PNNL, and a saltstone prepared with dry ingredients sourced from SRNL were compared in order to better understand the relationship between different cementitious waste forms. The composition of the dry ingredient portion (i.e., OPC, fly ash, and GGBFS) for CS-FAF, CS-NFA02, and CS-NFA18 was calculated from the XRF results of the respective dry ingredients used in the formulations. The total oxide composition of the PNNL and SRNL cementitious waste forms was calculated from the reported oxide composition of the dry components used in the PNNL cast stone [117] and from the reported oxide composition of the dry components used in the saltstone prepared with dry ingredients from SRNL [118]. The OPC:FA:GGBFS of the respective dry ingredients was used to determine the total oxide composition of the dry ingredient portion for the cementitious waste forms.

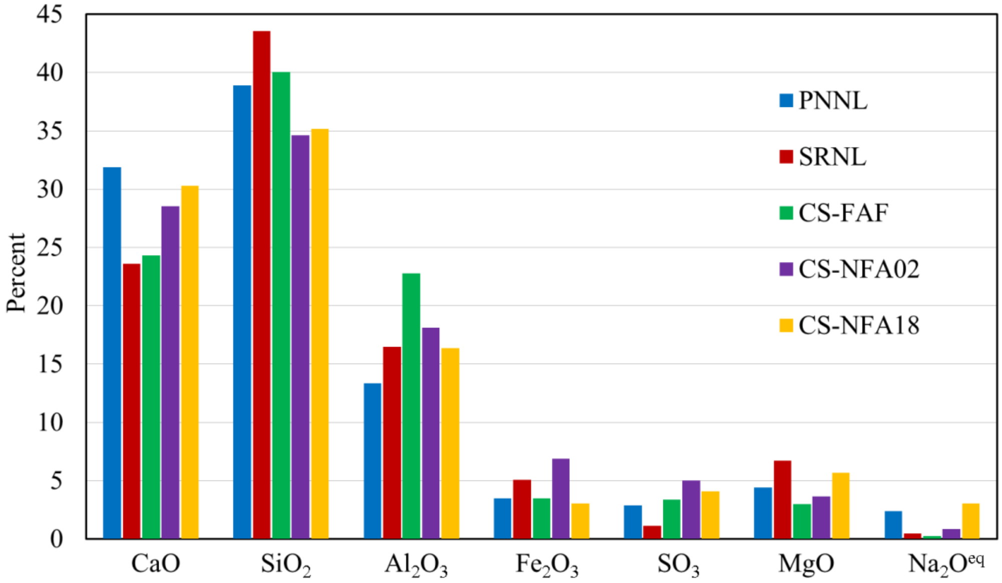

Figure C.1. Comparison of the calculated oxide composition of the dry ingredient portion of different cementitious waste forms (wt.%)

Leaching behavior results

U.S. EPA Method 1313 [125] and U.S. EPA Method 1315 [126], as described in section 4.3.12, were performed for the three cementitious waste forms (i.e., CS-FAF, CS-NFA02, CS-NFA18) aged under the four different conditions (i.e., -N, -O, -C-, and –OC). The presented data for CS-FAF-N and CS-FAF-OC is an extension of the leaching data presented in Chapter 4 for CS-N and CS-OC. The results from EPA Method 1313 and EPA Method 1315 for each material under each aging condition are presented in Figures C.2-C.7. Future work will include further analysis of the leaching behavior for the different materials and aging conditions to better understand the impact of fly ash composition on the leaching behavior of cementitious waste forms aged under specific environments.

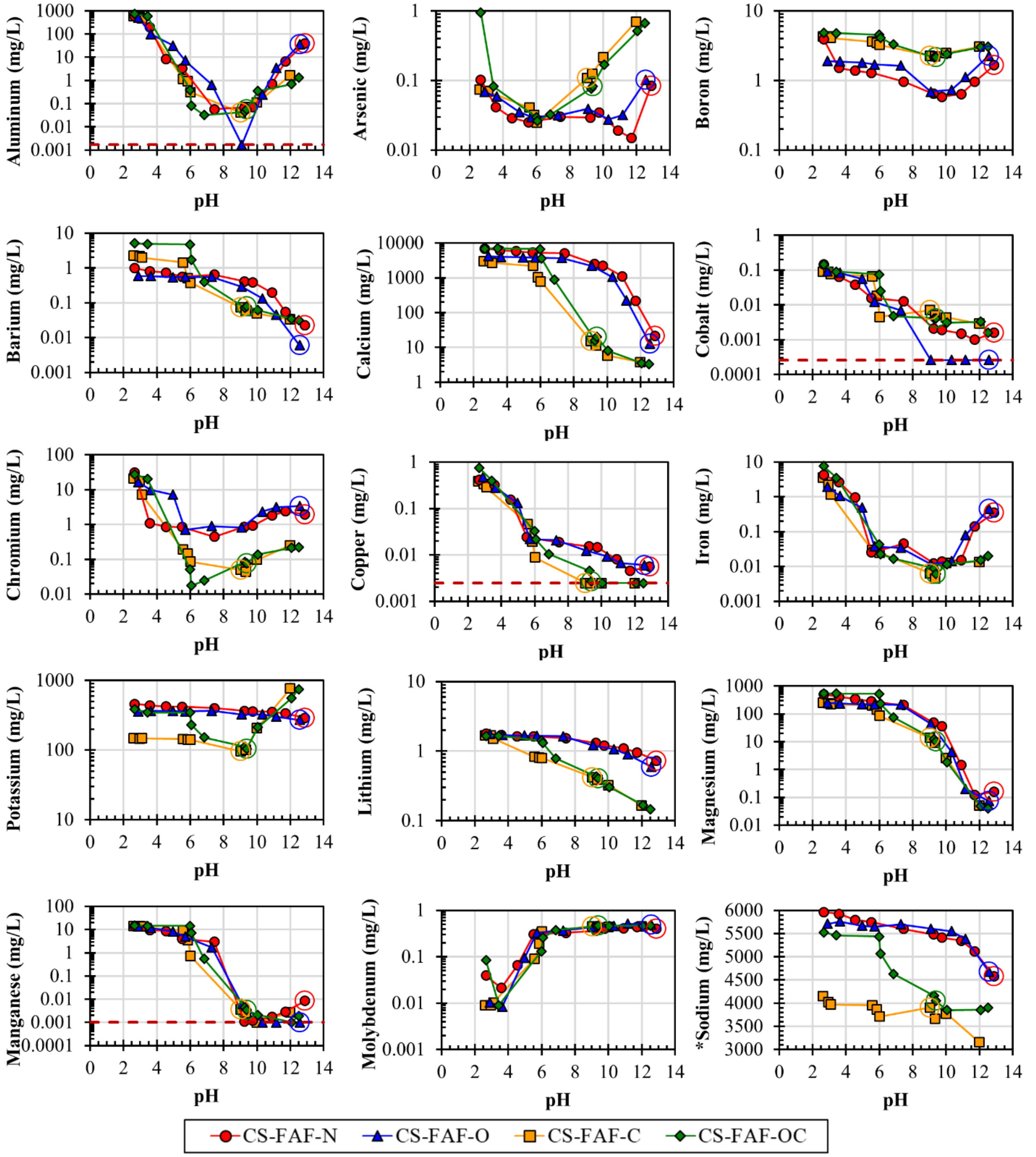

Figure C.2. pH-dependent solubility leaching concentrations of constituents, ANC/BNC, and conductivity measurements for CS-FAF-N (red), CS-FAF-O (blue), CS-FAF-C (orange) and CS-FAF-OC (green) as a function of pH. The circled data points indicate the natural pH of the respective materials. The dotted red line that appears for selected constituents indicates the minimum detection limit of the constituent. *Indicates y-axis is not on logarithmic scale.

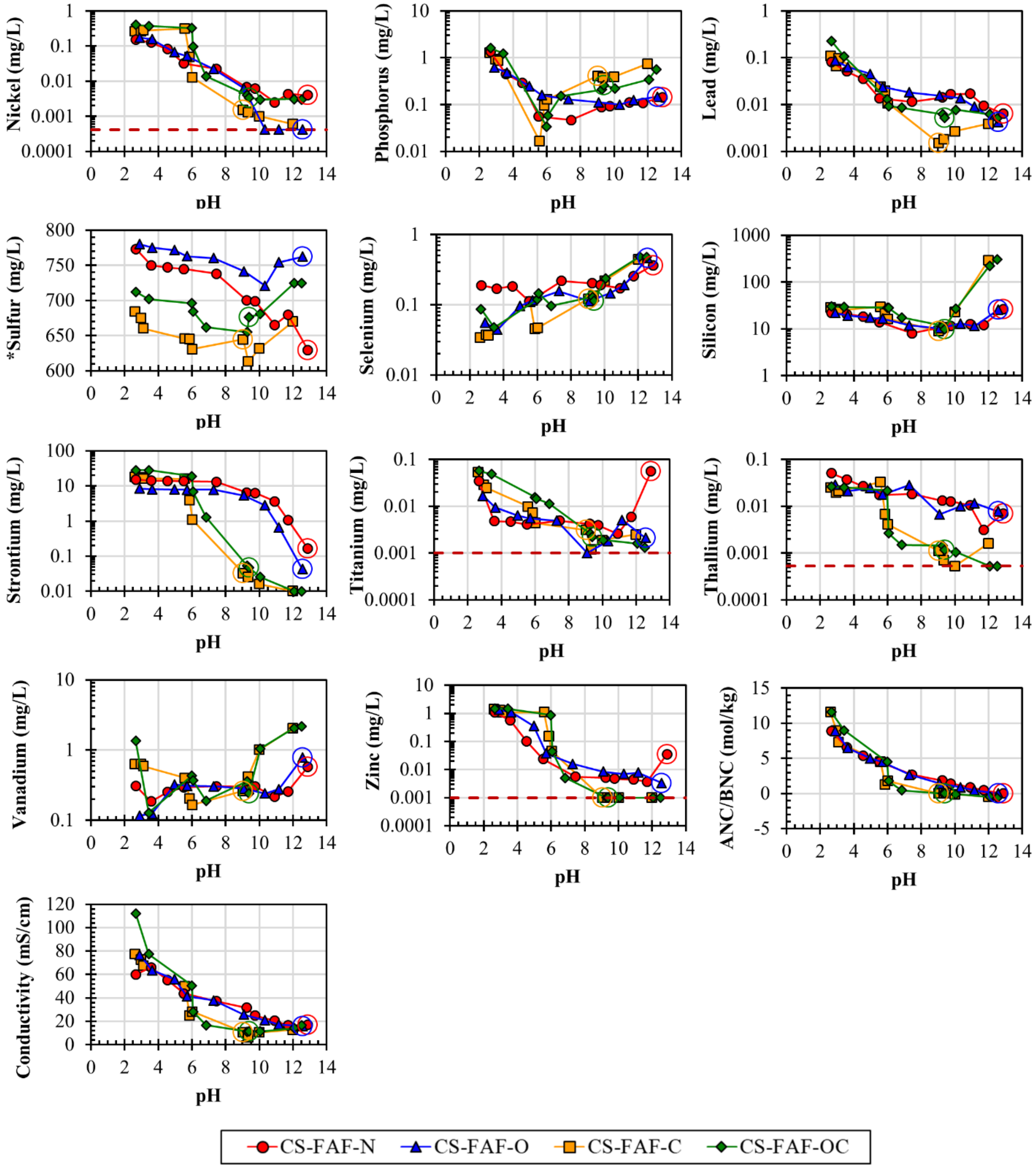

Figure C.2. (continued)

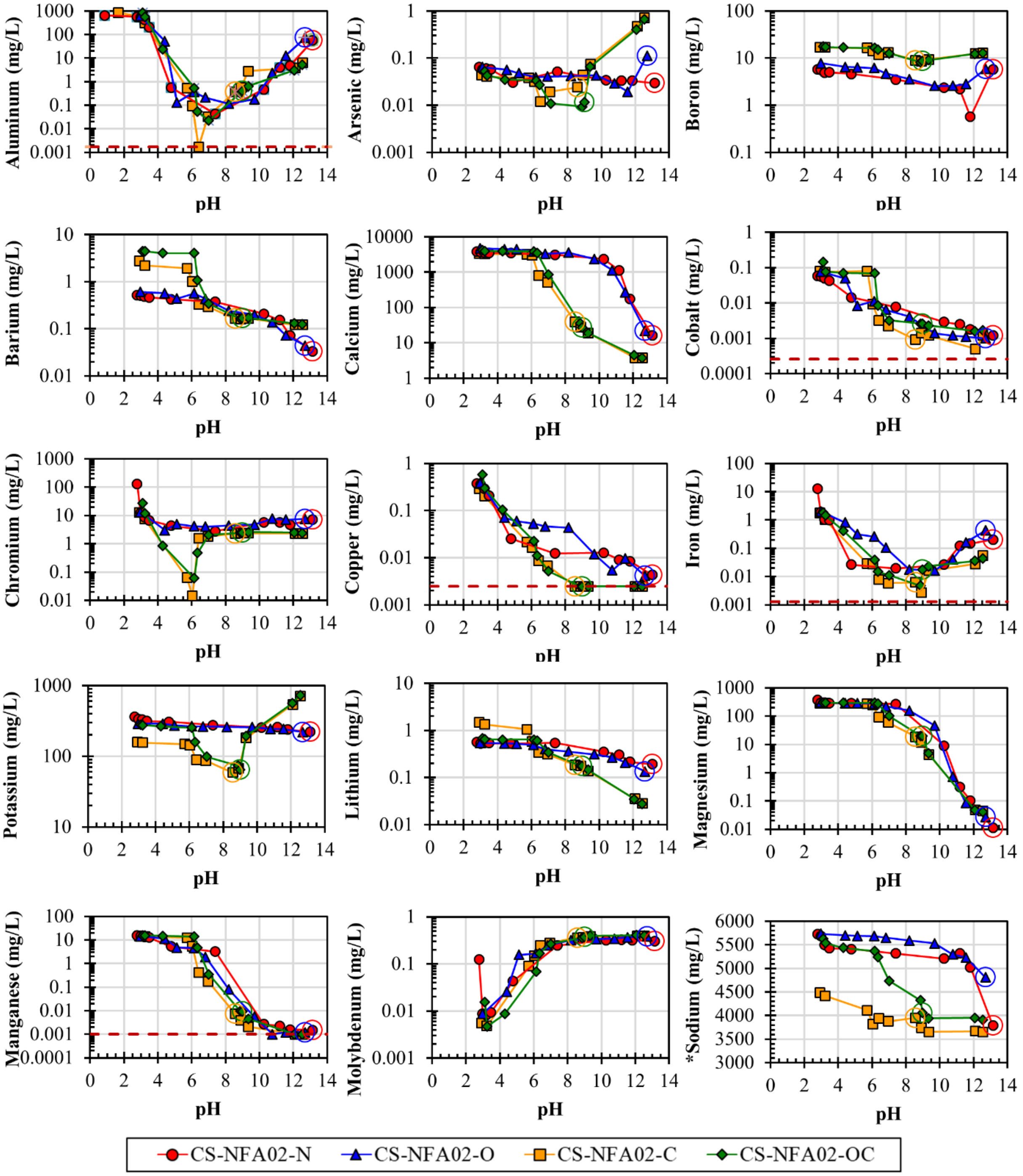

Figure C.3. pH-dependent solubility leaching concentrations of constituents, ANC/BNC, and conductivity measurements for CS-NFA02-N (red), CS-NFA02-O (blue), CS-NFA02-C (orange) and CS-NFA02-OC (green) as a function of pH. The circled data points indicate the natural pH of the respective materials. The dotted red line that appears for selected constituents indicates the minimum detection limit of the constituent. *Indicates y-axis is not on logarithmic scale.

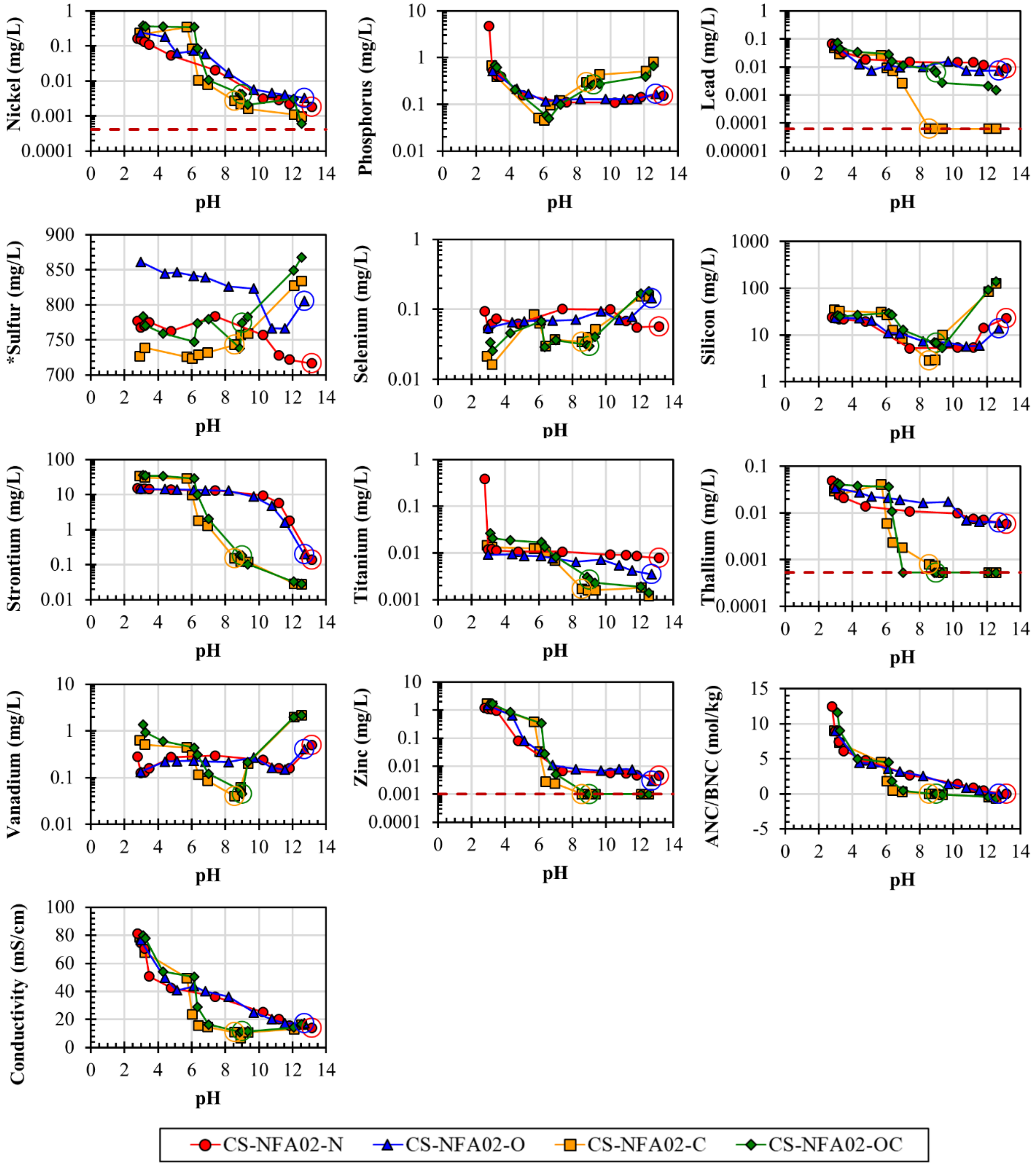

Figure C.3. (continued)

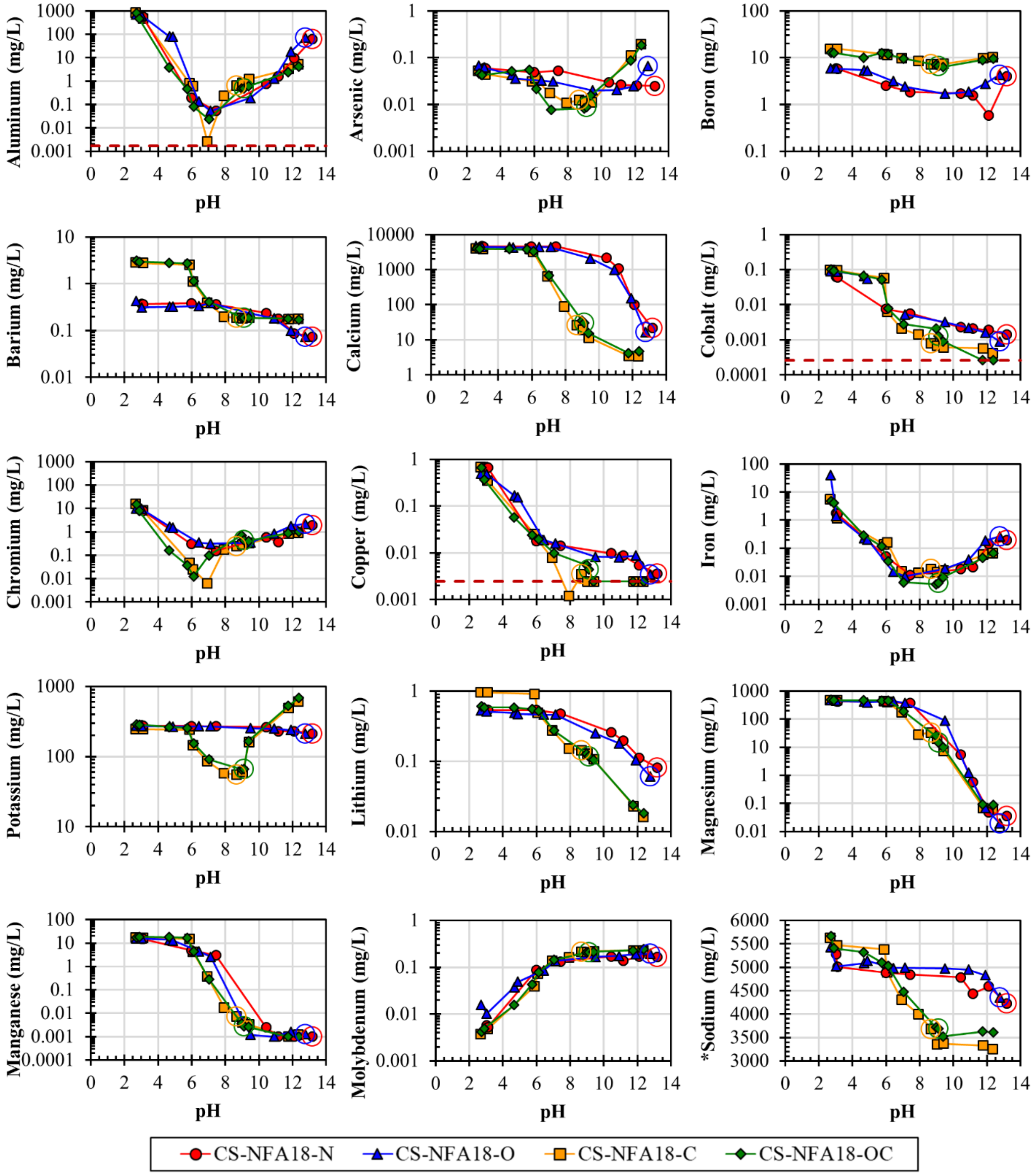

Figure C.4. pH-dependent solubility leaching concentrations of constituents, ANC/BNC, and conductivity measurements for CS-NFA18-N (red), CS-NFA18-O (blue), CS-NFA18-C (orange) and CS-NFA18-OC (green) as a function of pH. The circled data points indicate the natural pH of the respective materials. The dotted red line that appears for selected constituents indicates the minimum detection limit of the constituent. *Indicates y-axis is not on logarithmic scale.

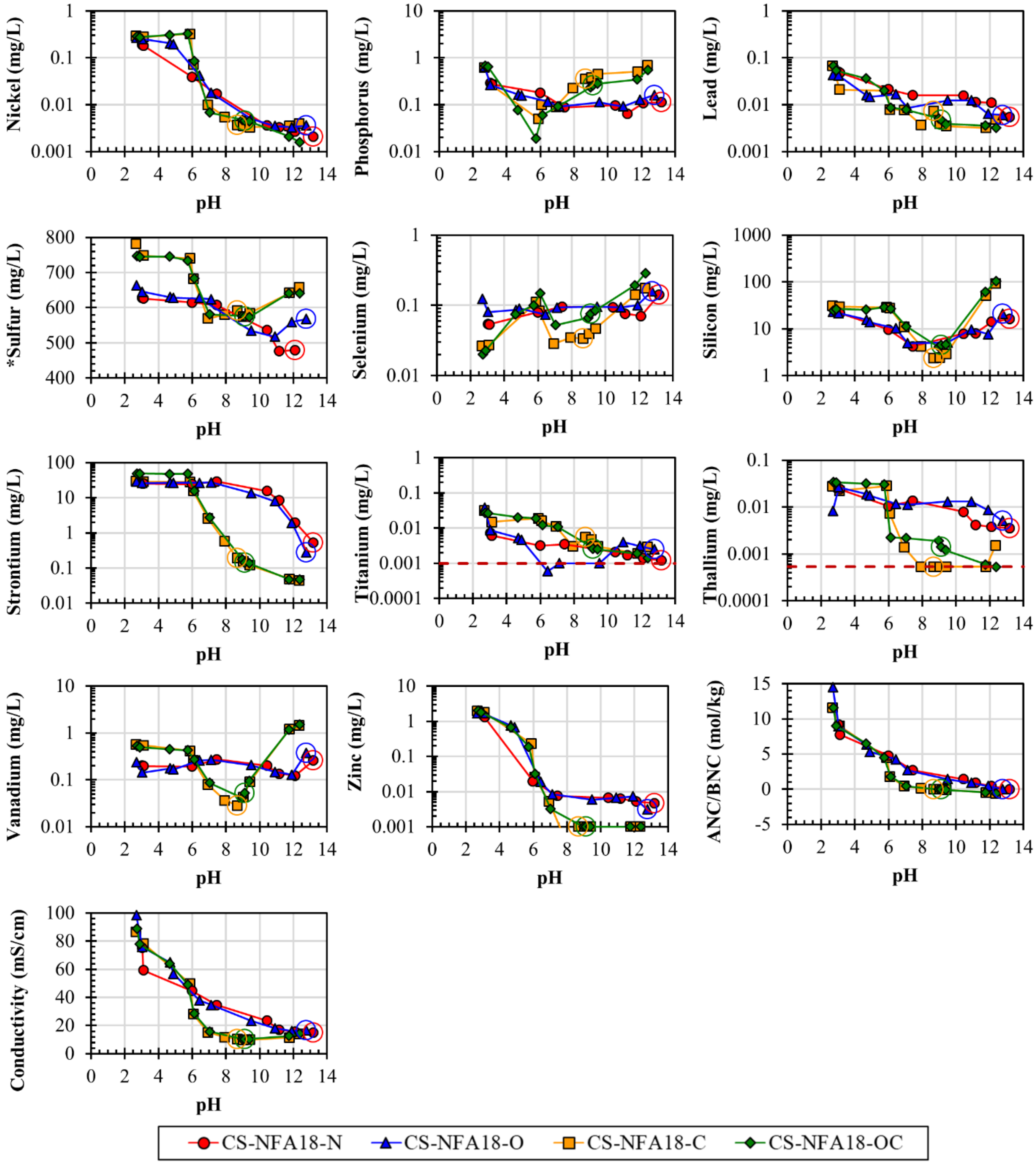

Figure C.4. (continued)

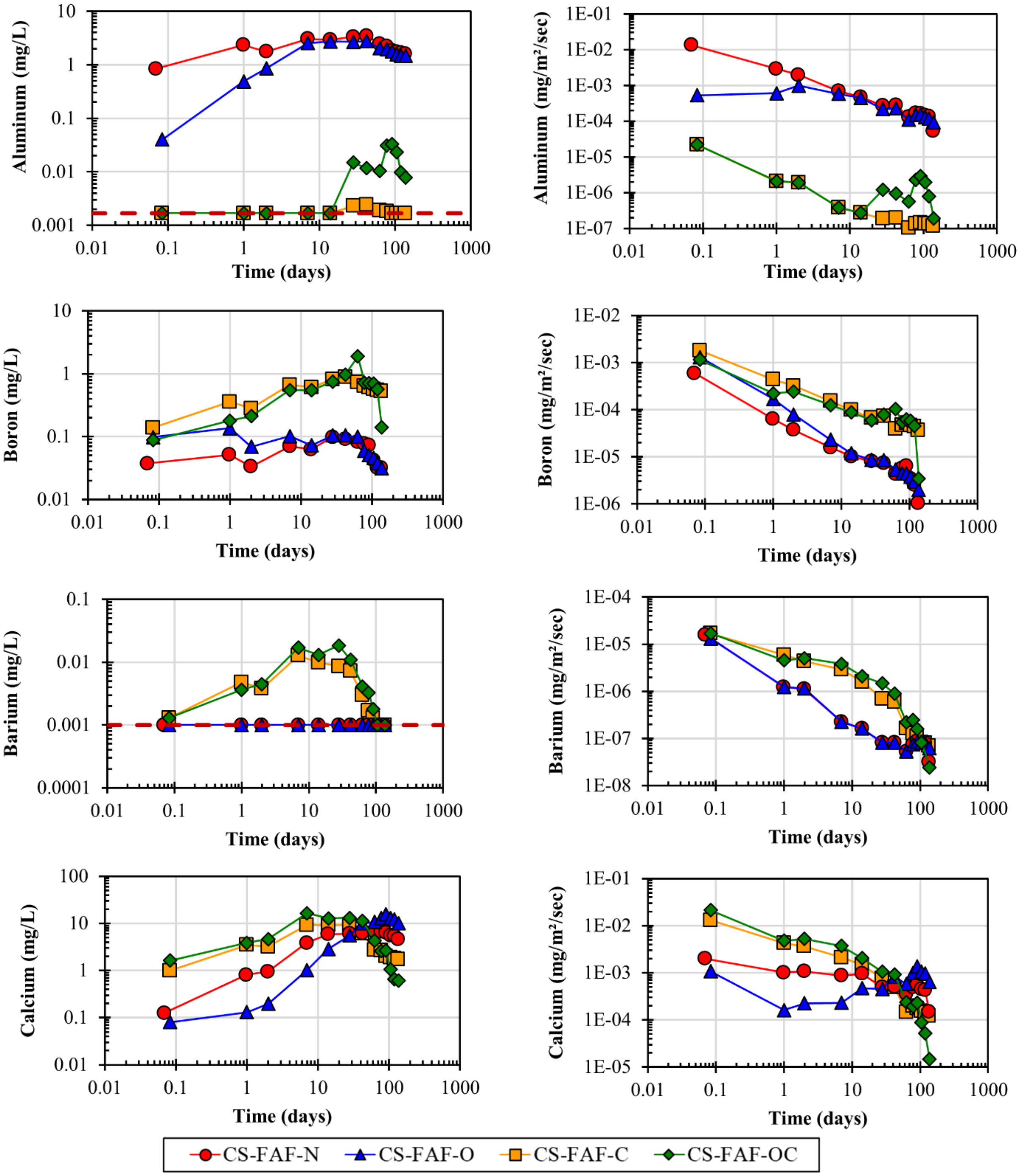

Figure C.5. Measured eluate pH, eluate concentration of constituents, and the calculated flux of constituents for CS-FAF-N (red), CS-FAF-O (blue), CS-FAF-C (orange), and CS-FAF-OC (green) as a function time. The dotted red line that appears for selected constituents indicates the minimum detection limit of the constituent.

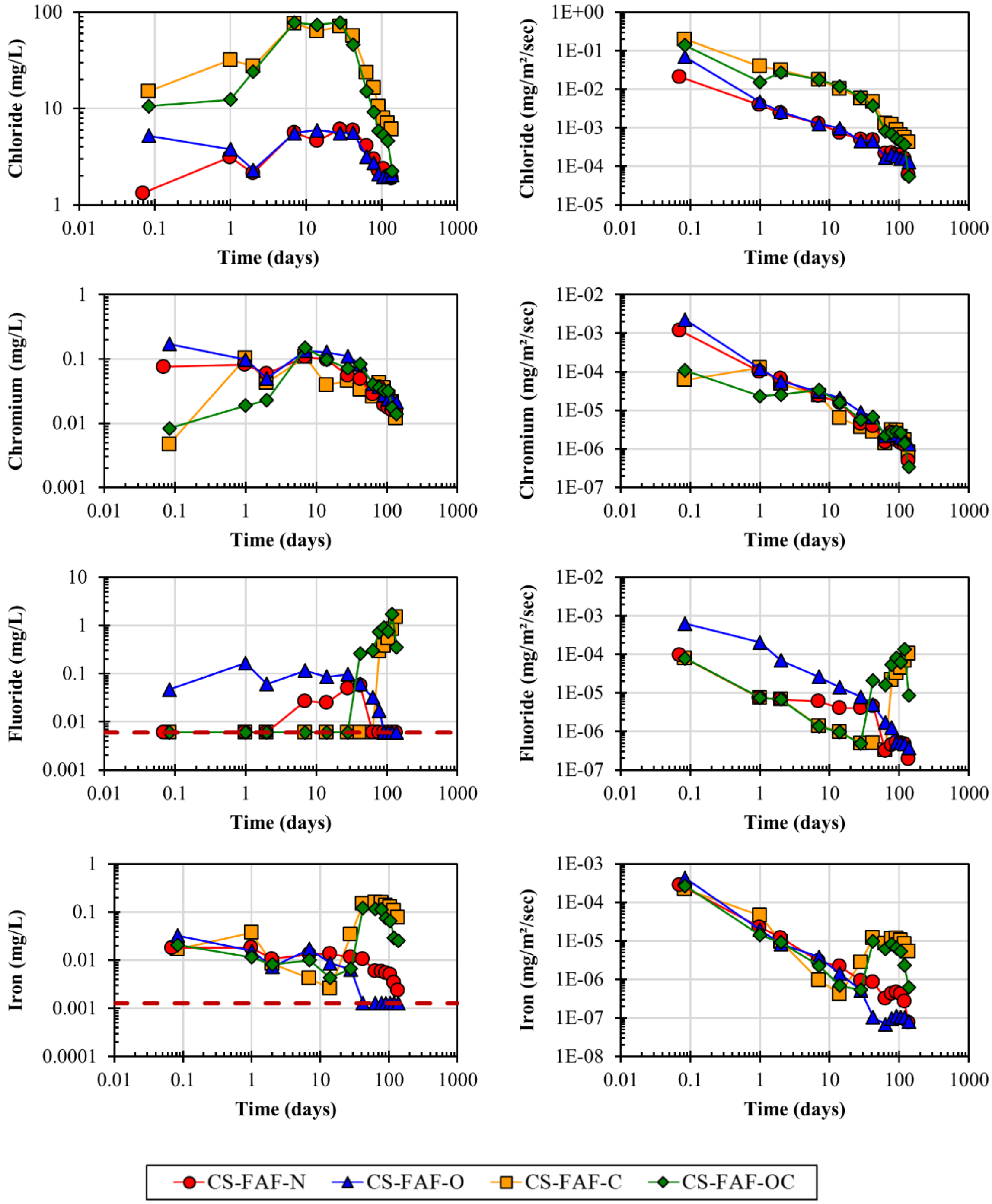

Figure C.5. (continued)

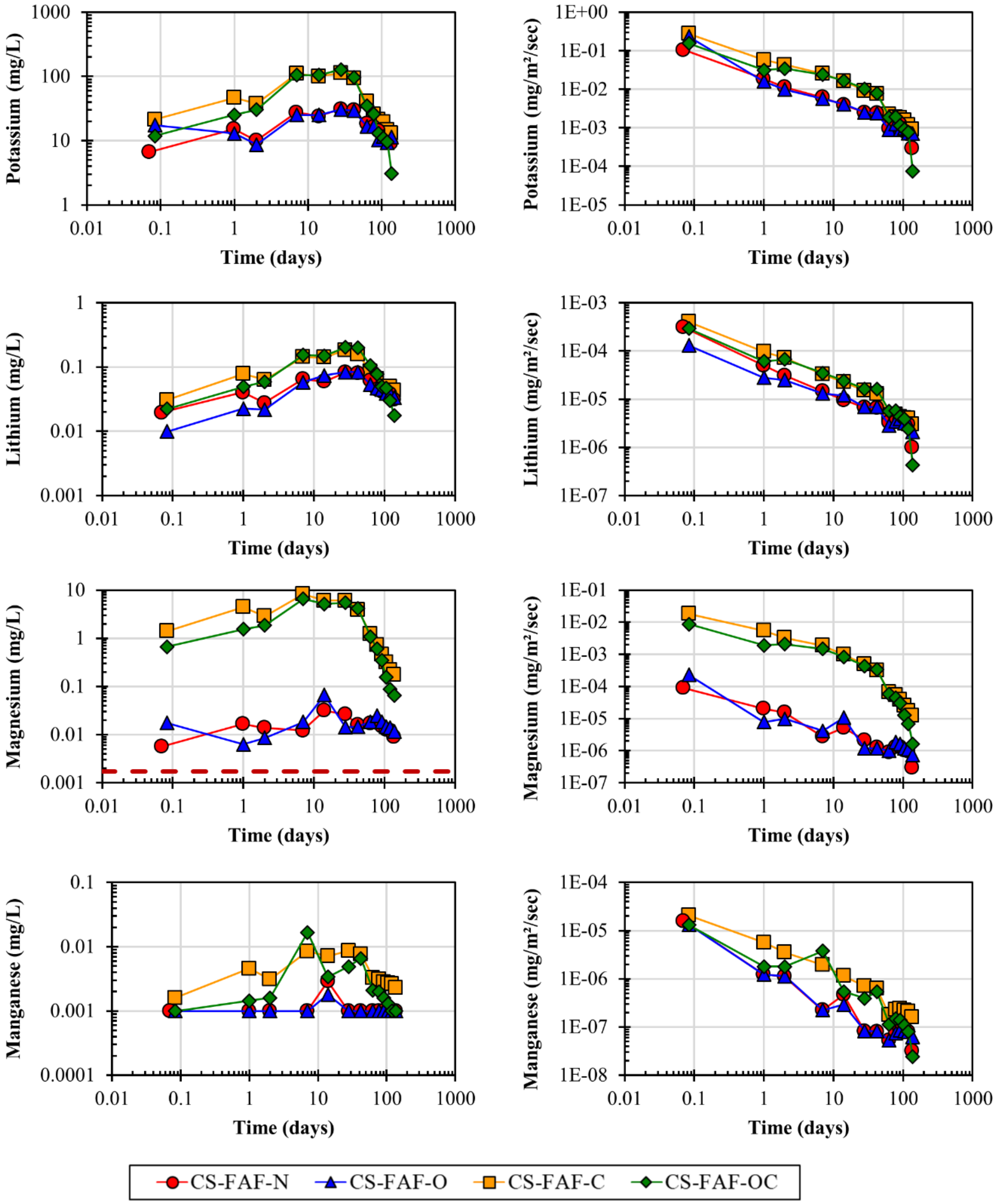

Figure C.5. (continued)

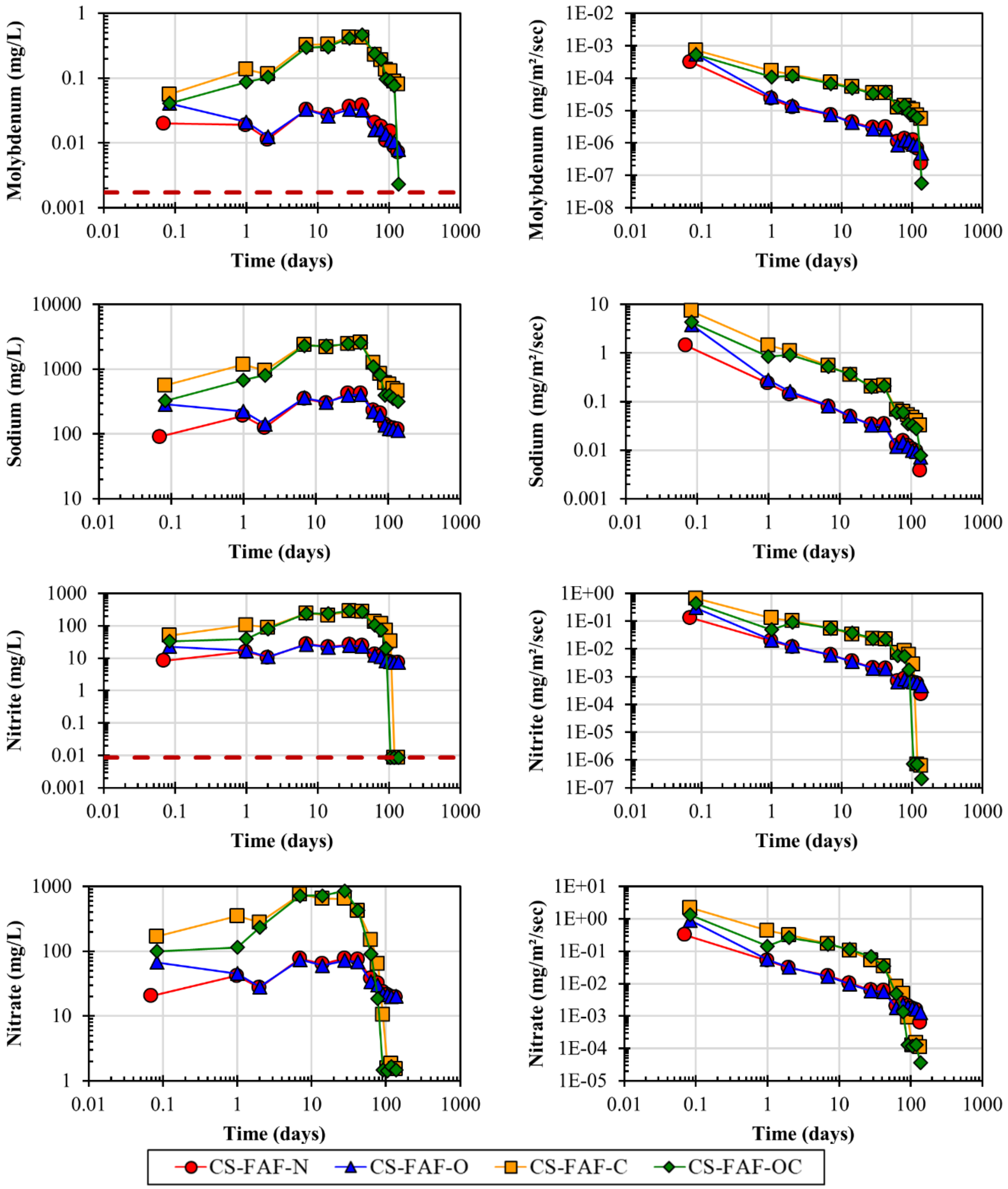

Figure C.5. (continued)

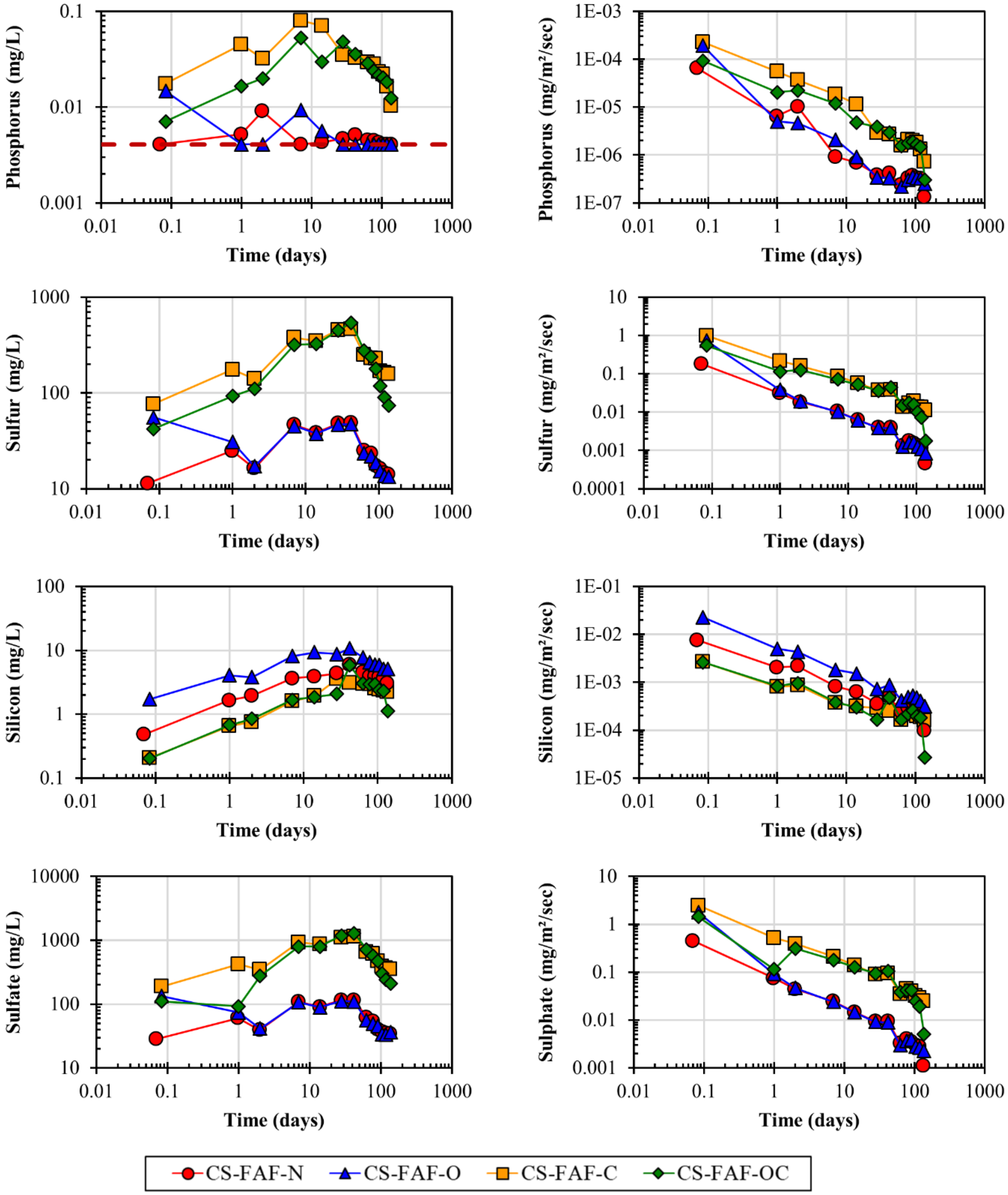

Figure C.5. (continued)

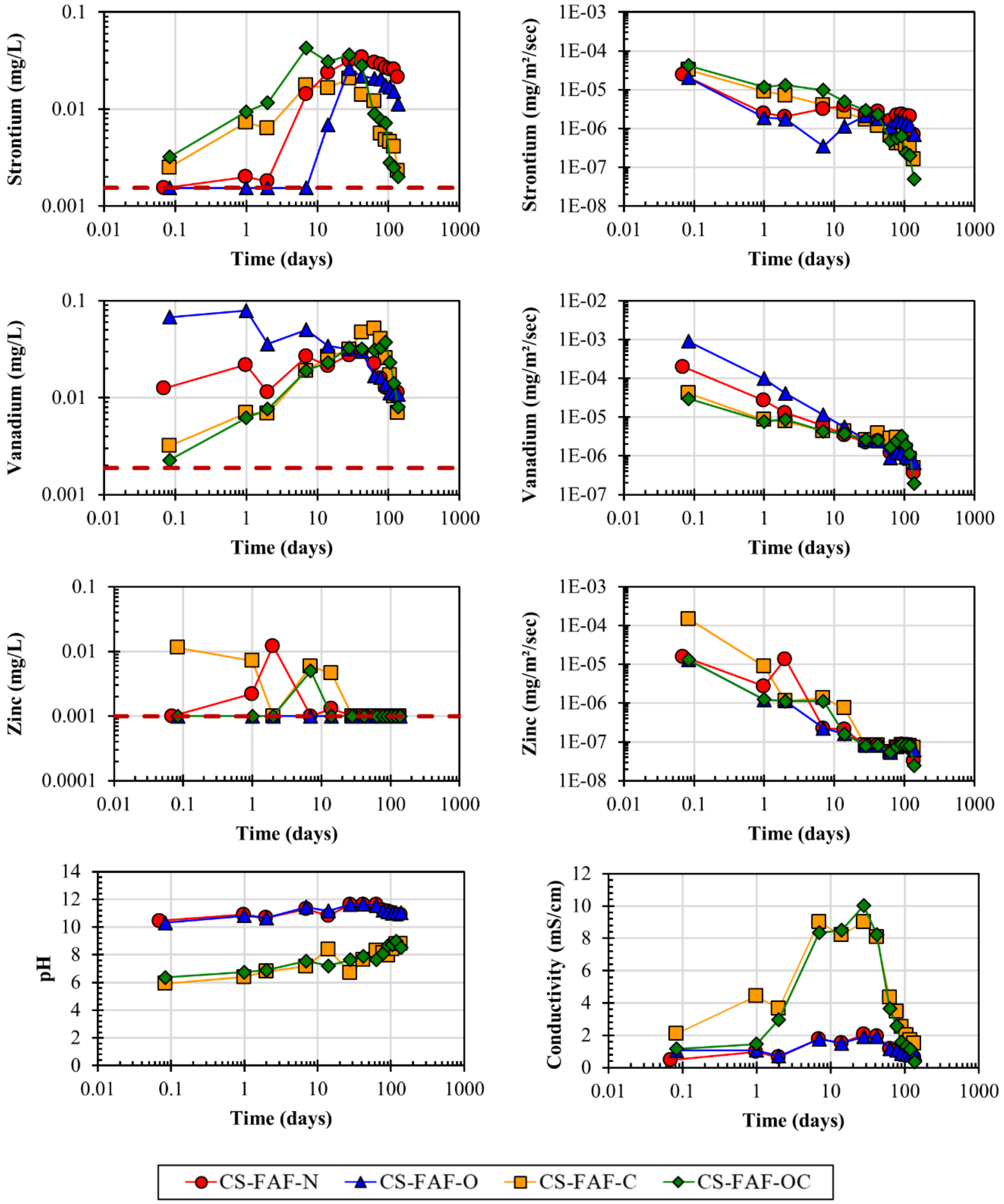

Figure C.5. (continued)

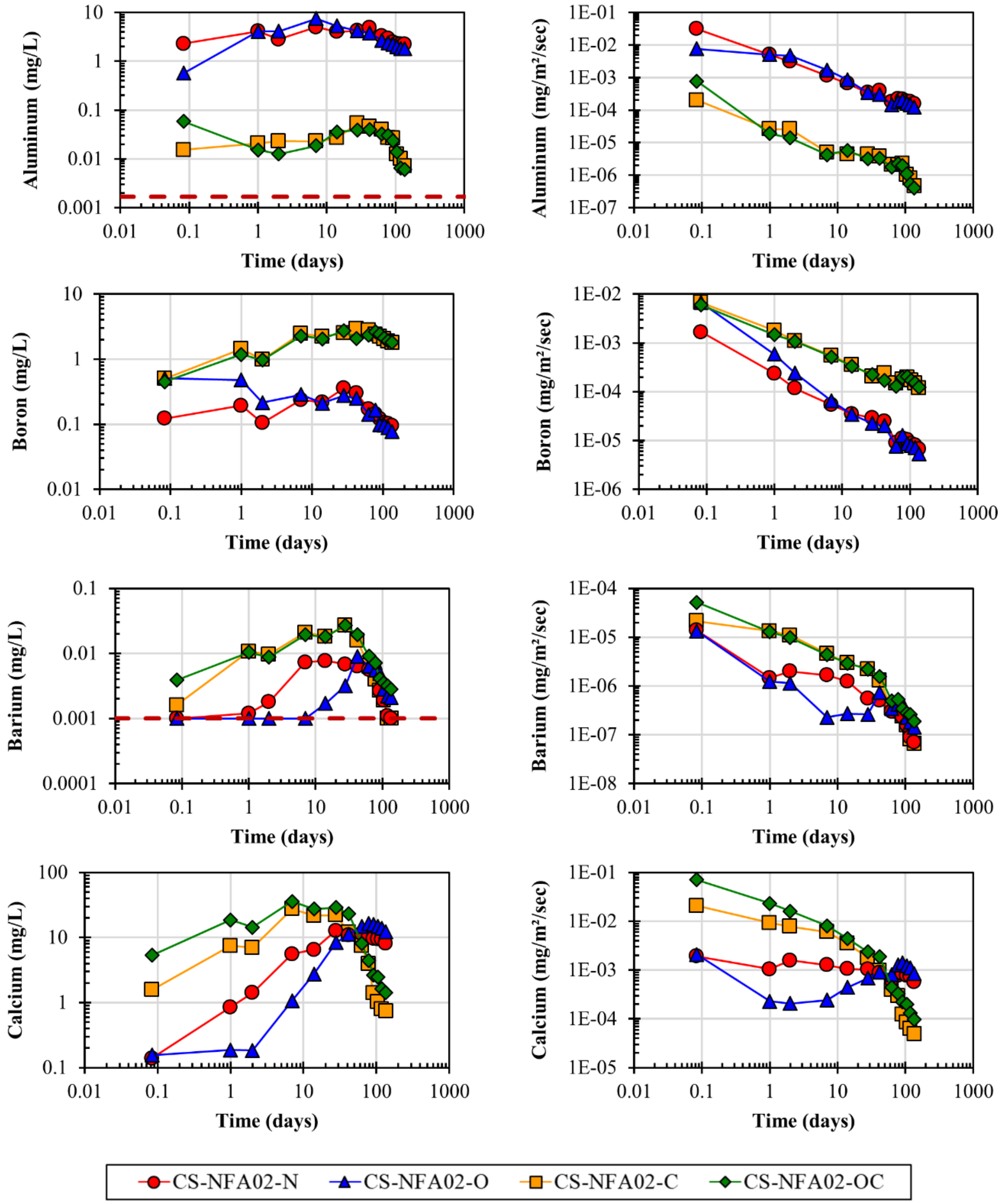

Figure C.6. Measured eluate pH, eluate concentration of constituents, and the calculated flux of constituents for CS-NFA02-N (red), CS-NFA02-O (blue), CS-NFA02-C (orange), and CS-NFA02-OC (green) as a function time. The dotted red line that appears for selected constituents indicates the minimum detection limit of the constituent.

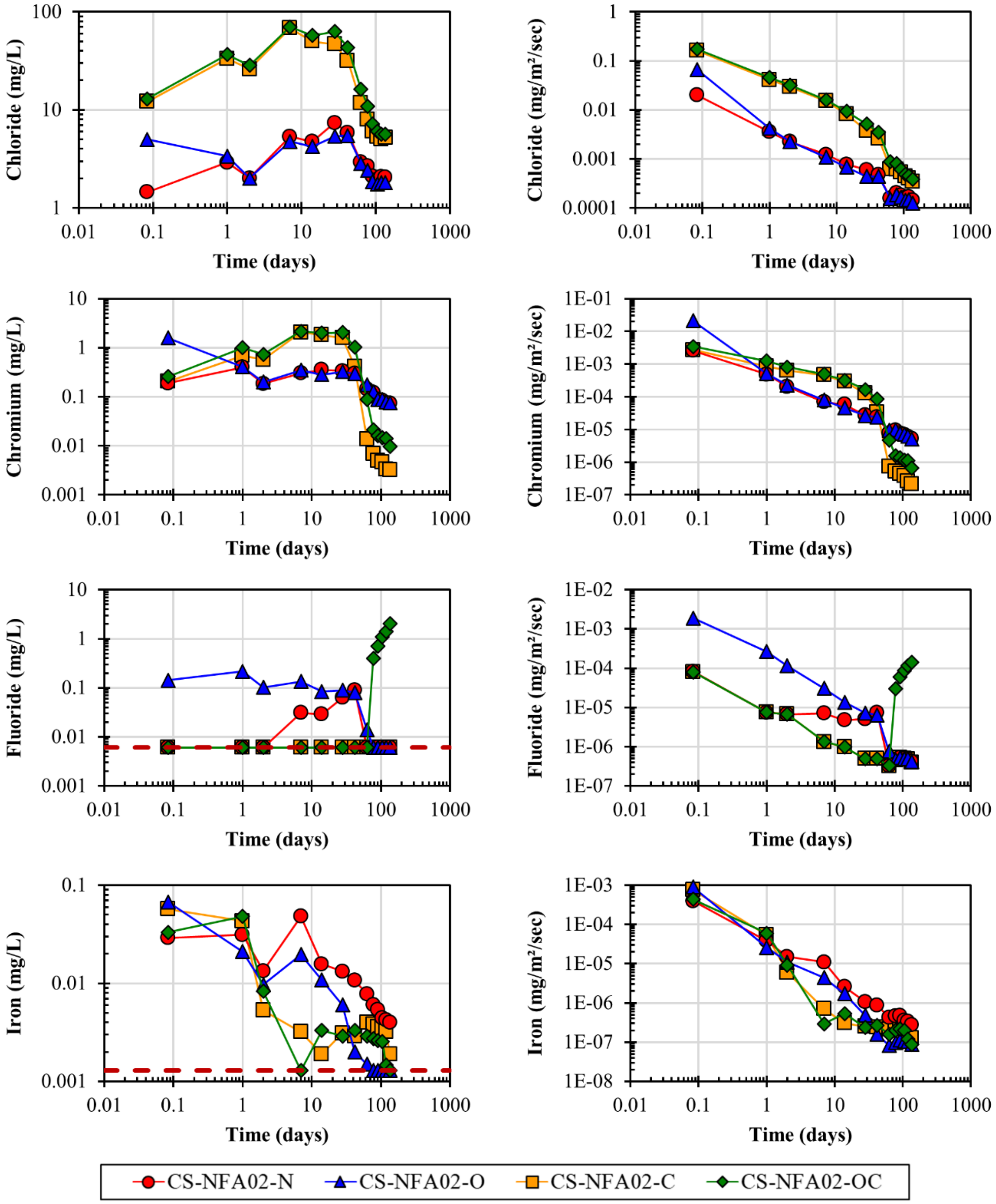

Figure C.6. (continued)

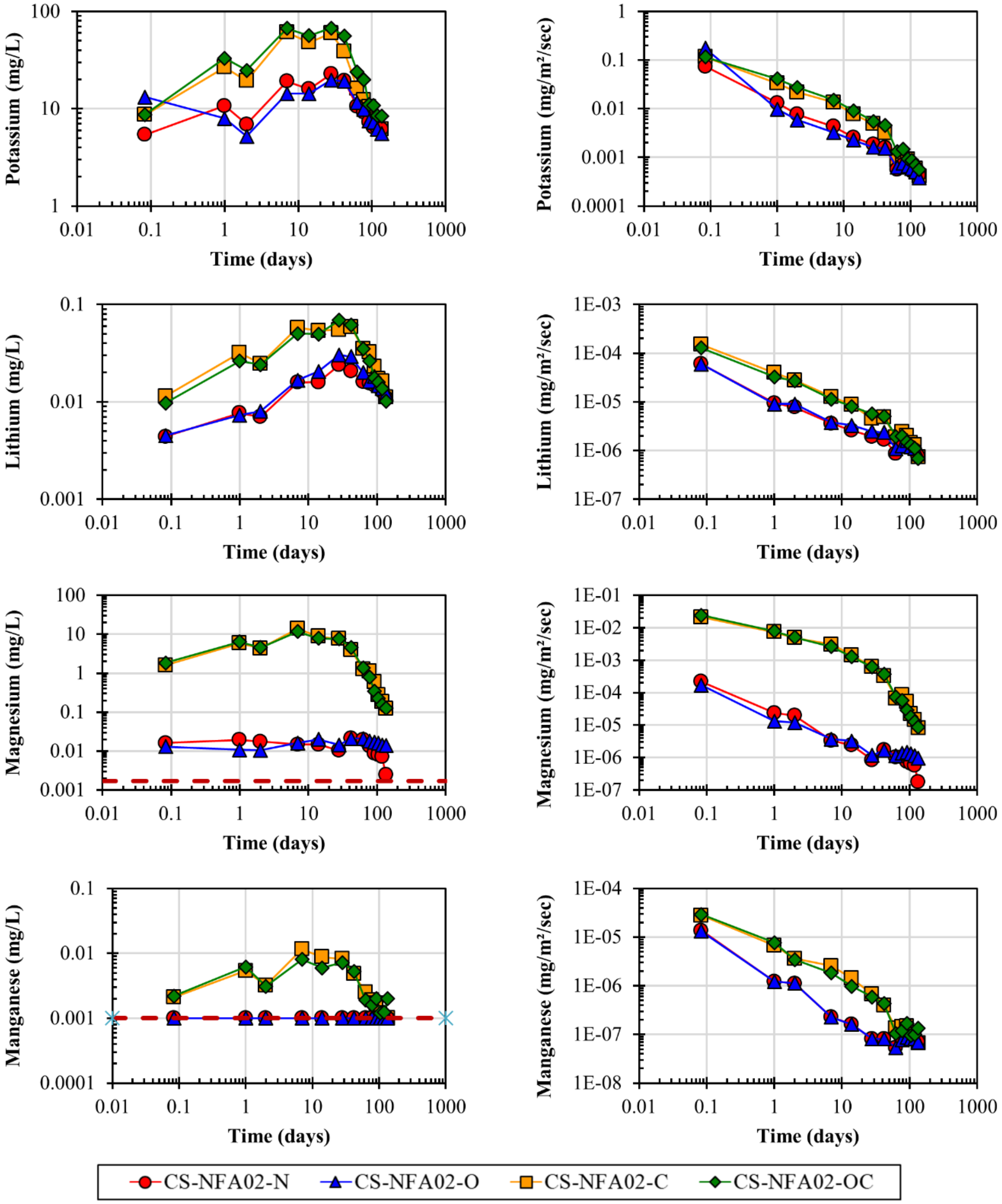

Figure C.6. (continued)

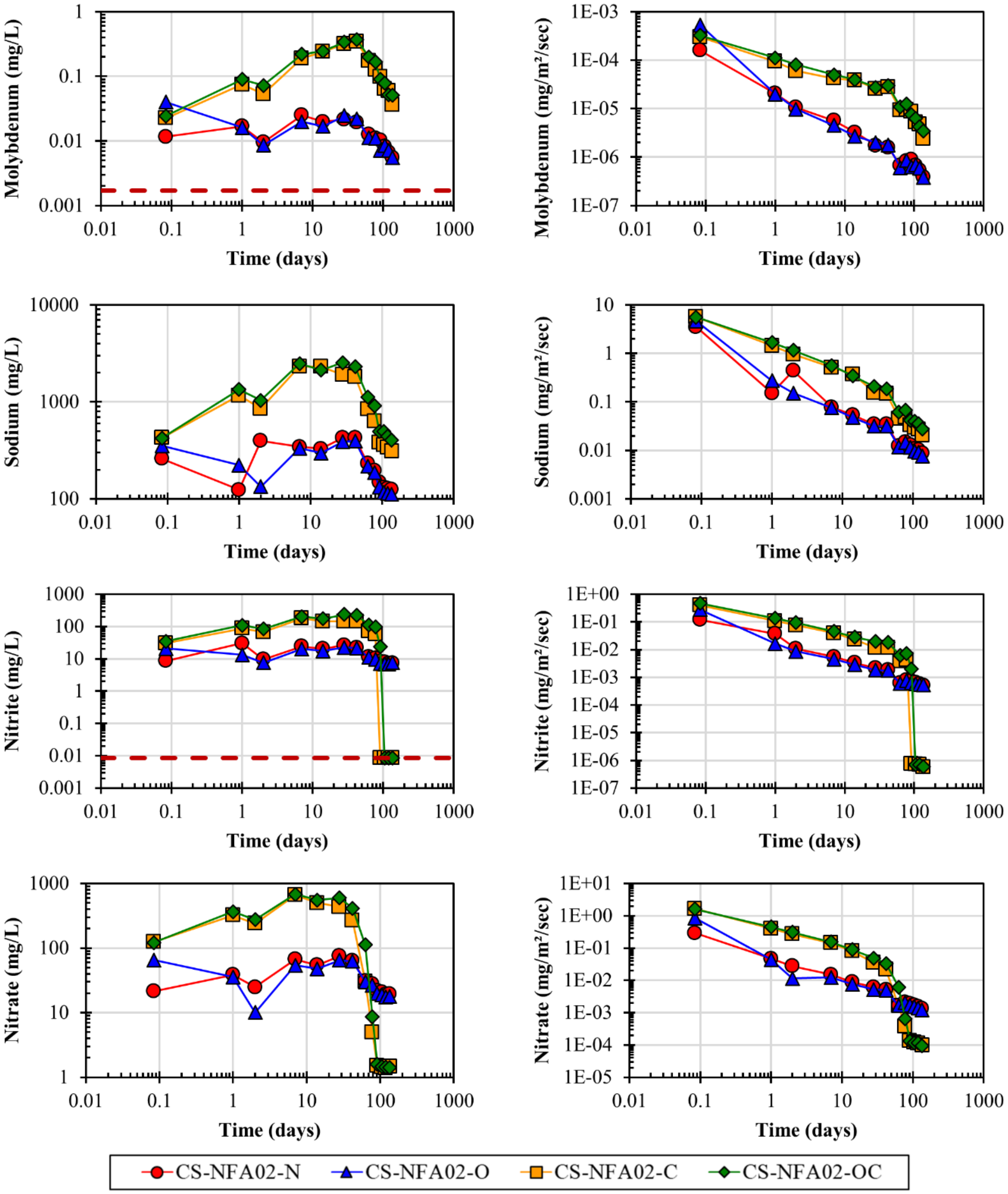

Figure C.6. (continued)

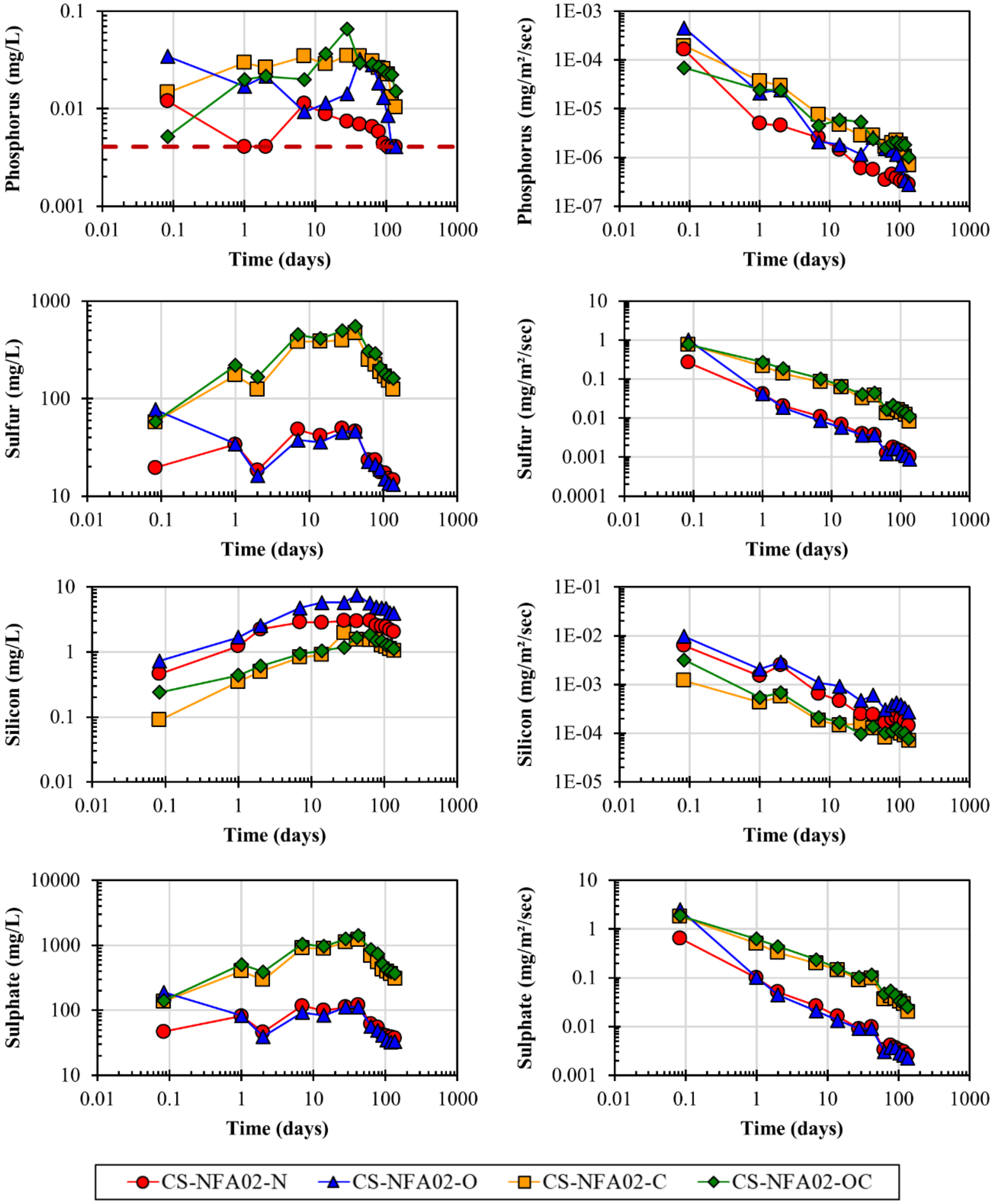

Figure C.6. (continued)

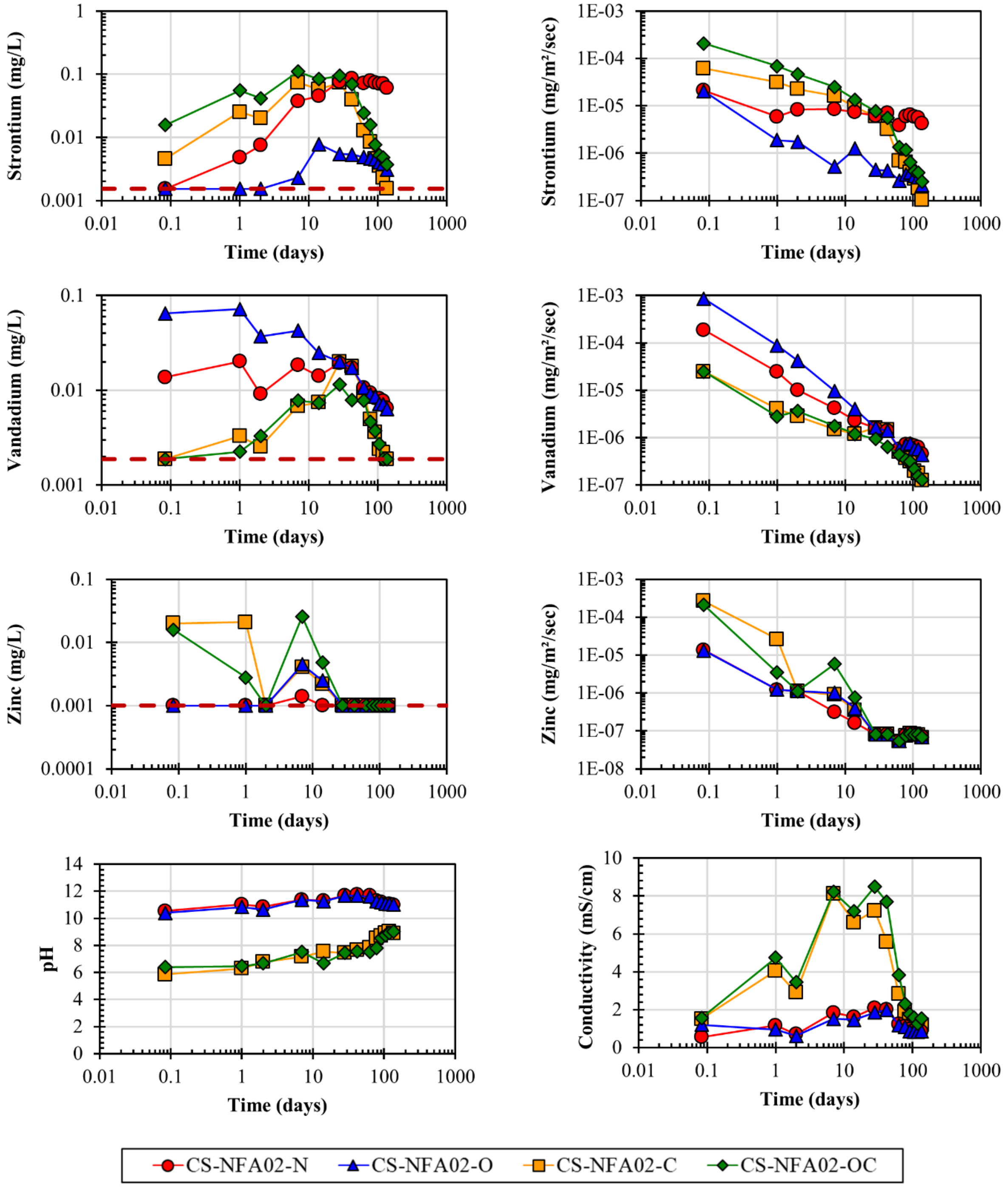

Figure C.6. (continued)

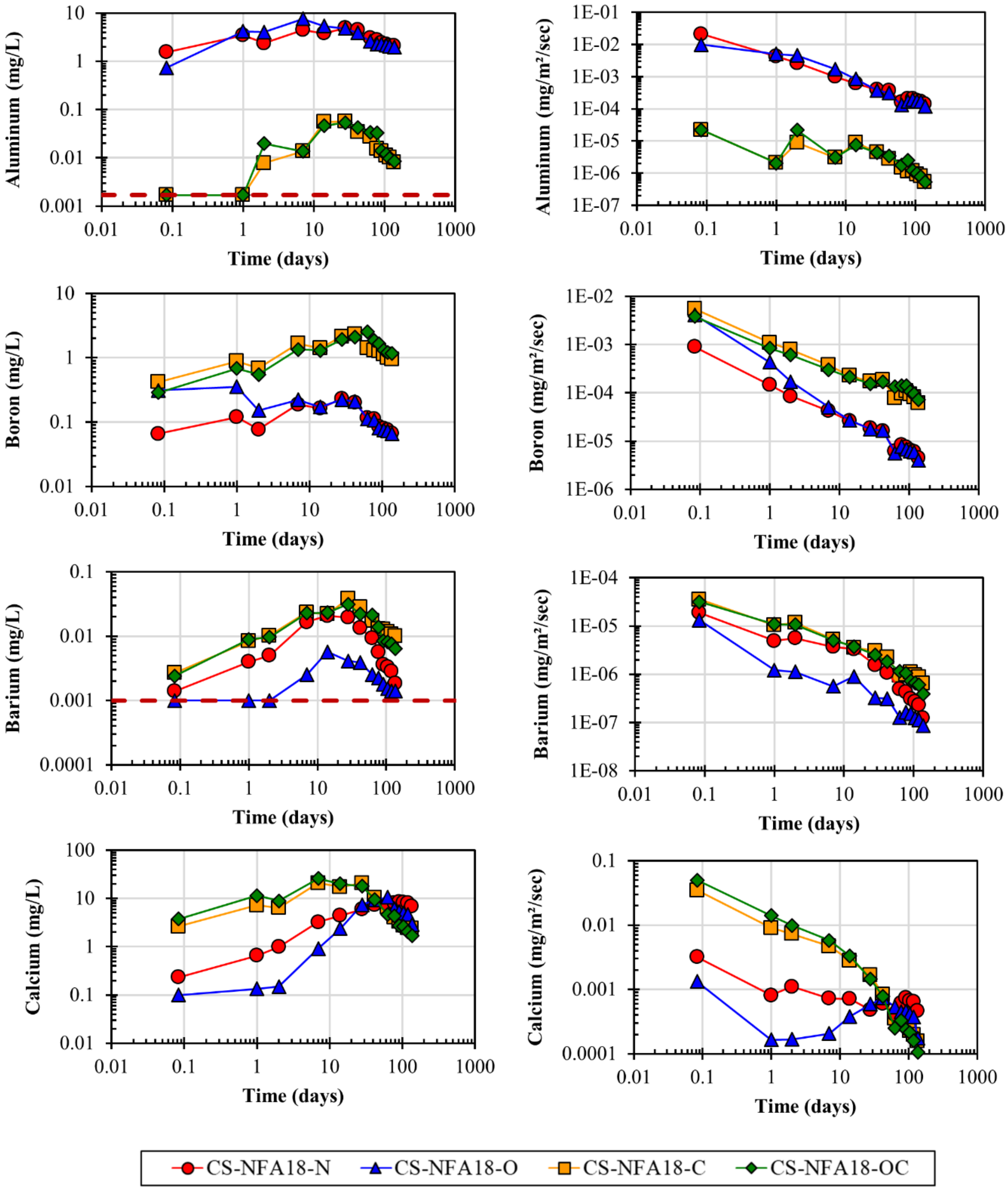

Figure C.7. Measured eluate pH, eluate concentration of constituents, and the calculated flux of constituents for CS-NFA18-N (red), CS-NFA18-O (blue), CS-NFA18-C (orange), and CS-NFA18-OC (green) as a function time. The dotted red line that appears for selected constituents indicates the minimum detection limit of the constituent.

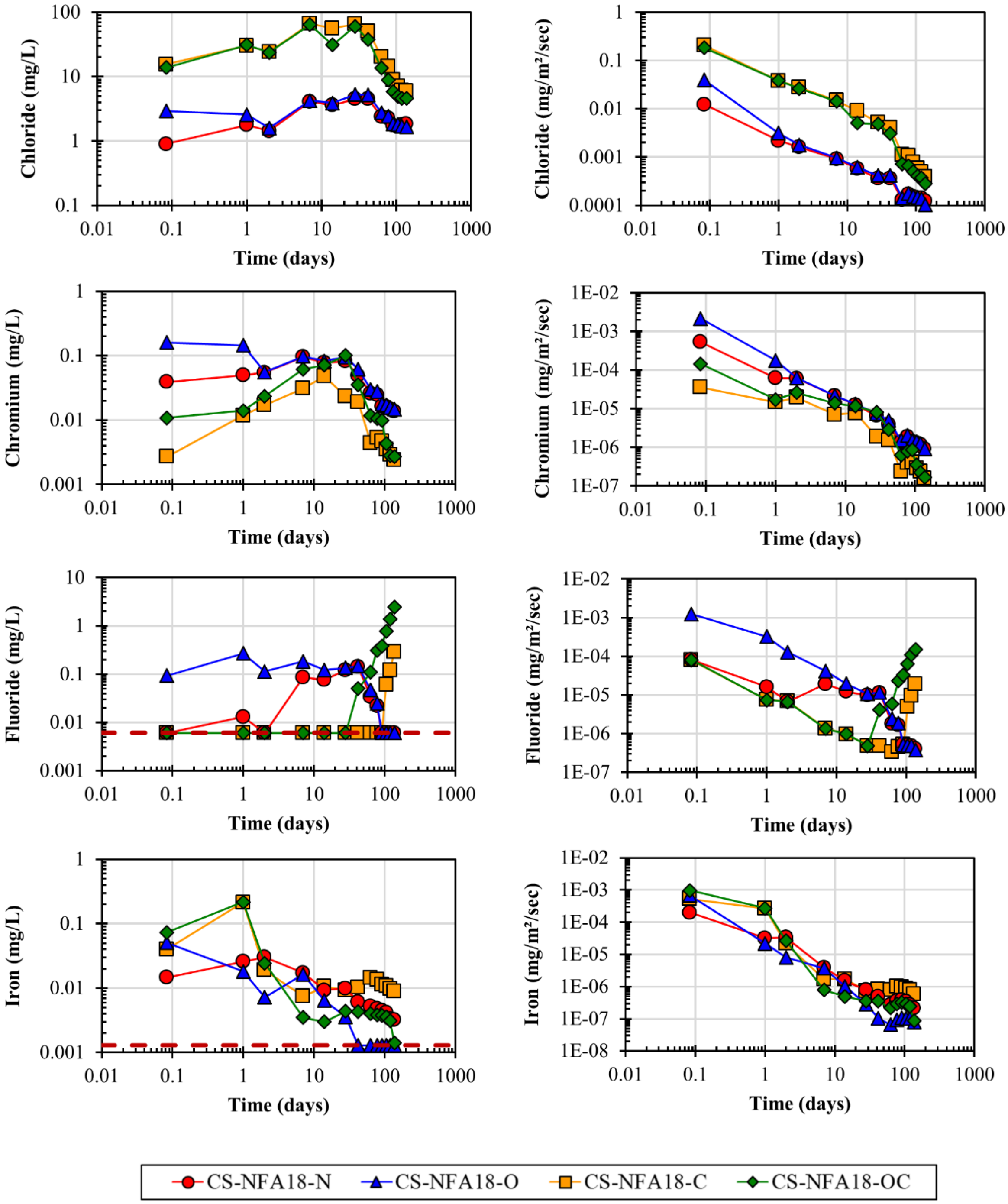

Figure C.7. (continued)

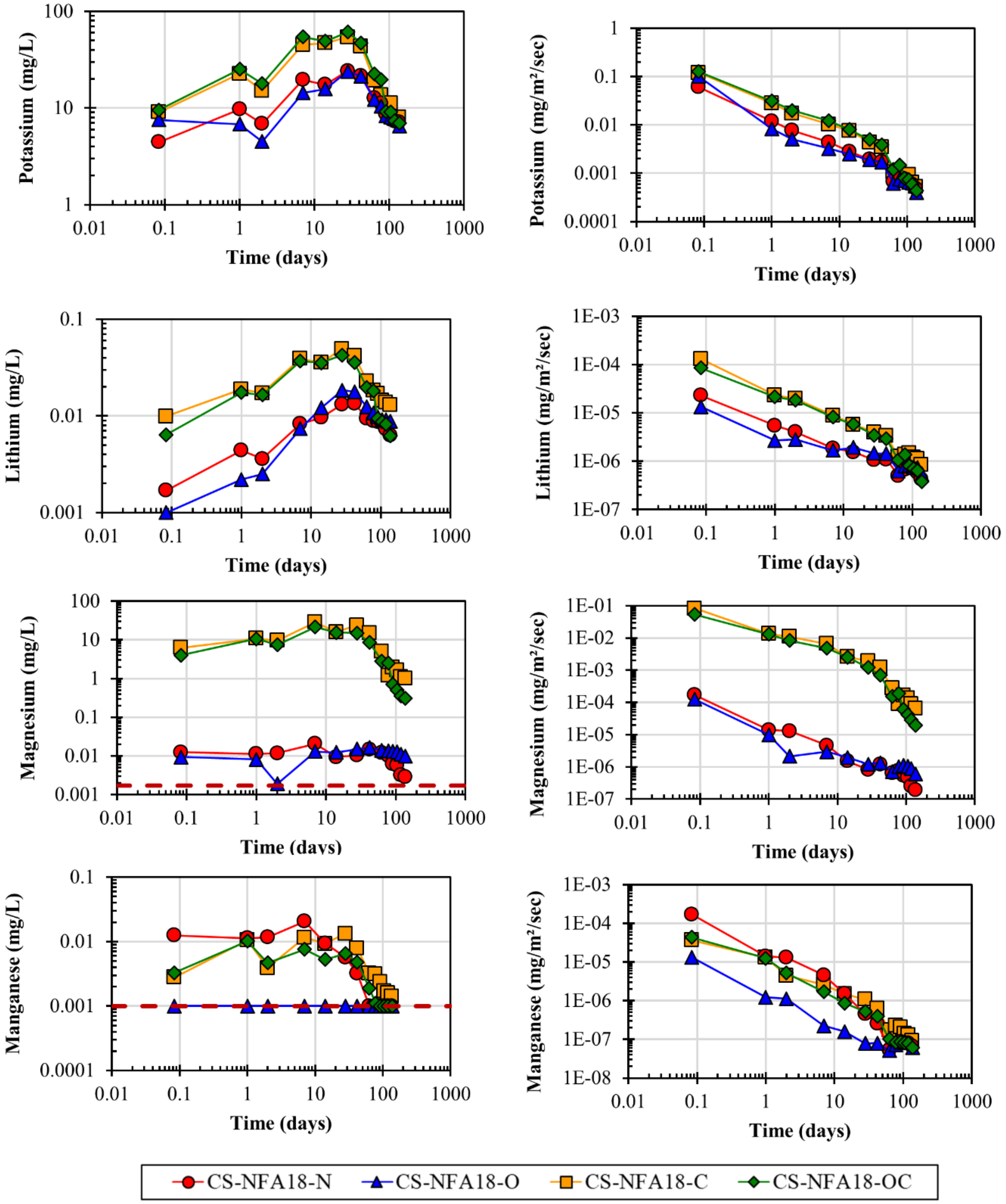

Figure C.7. (continued)

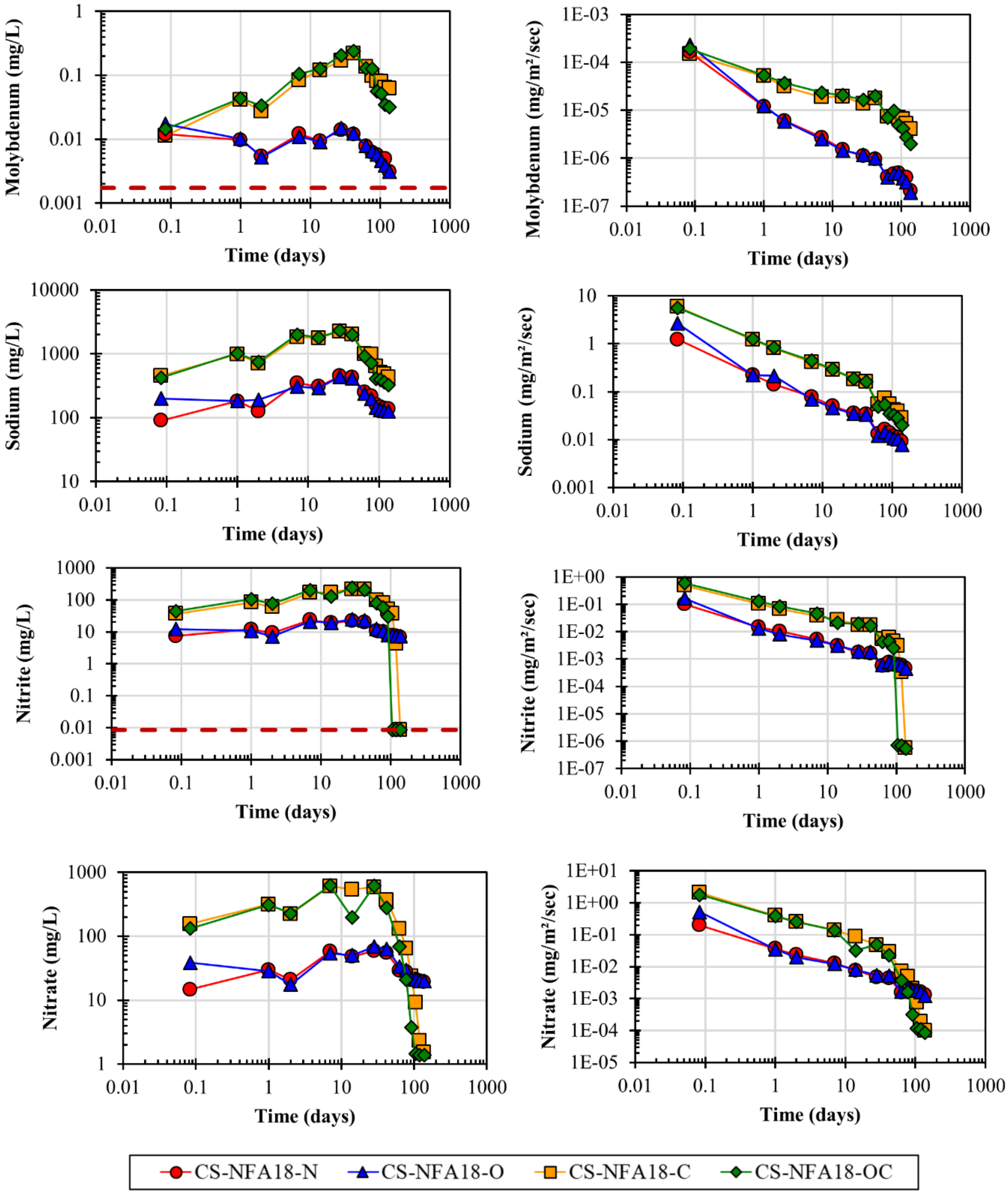

Figure C.7. (continued)

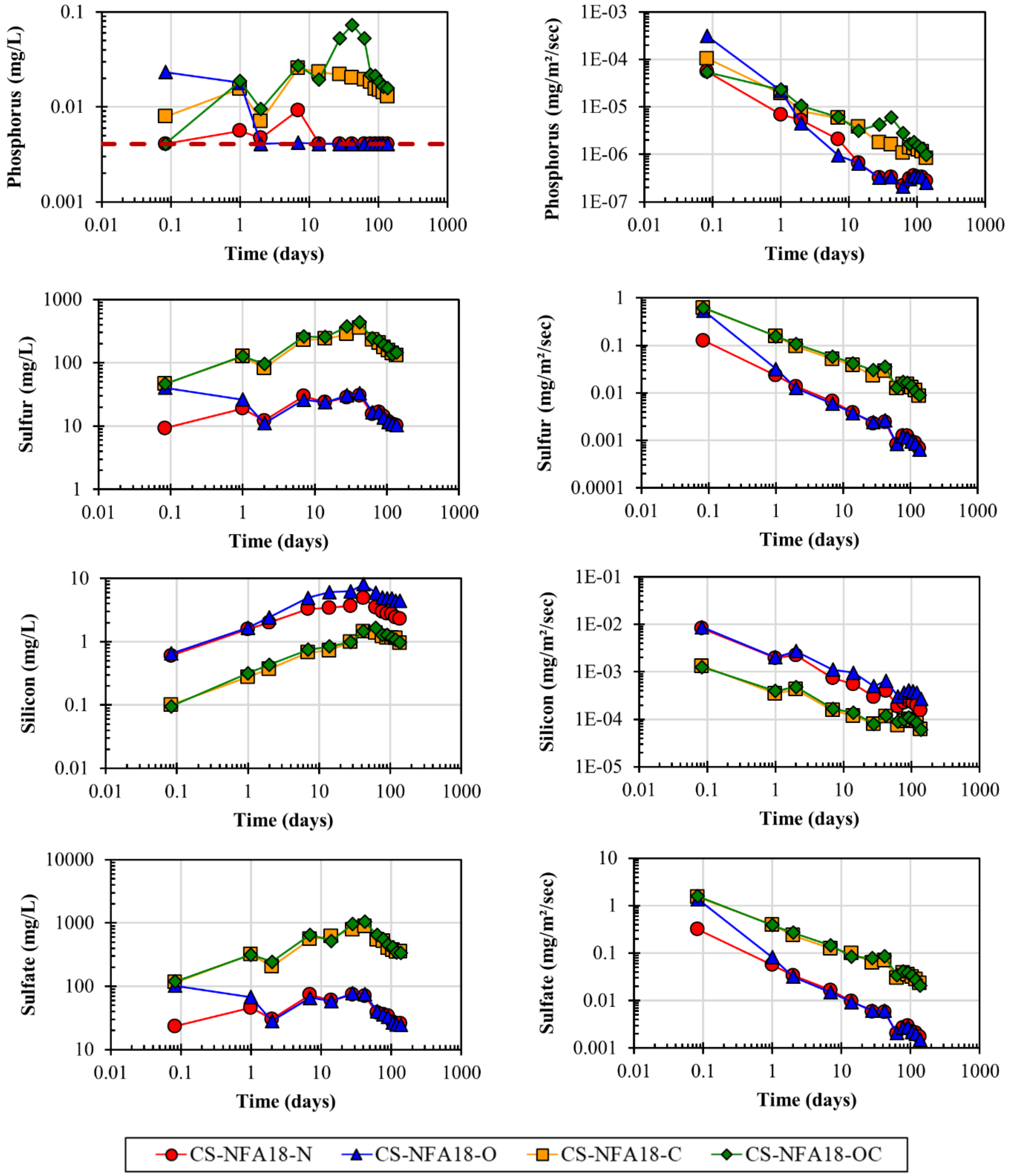

Figure C.7. (continued)

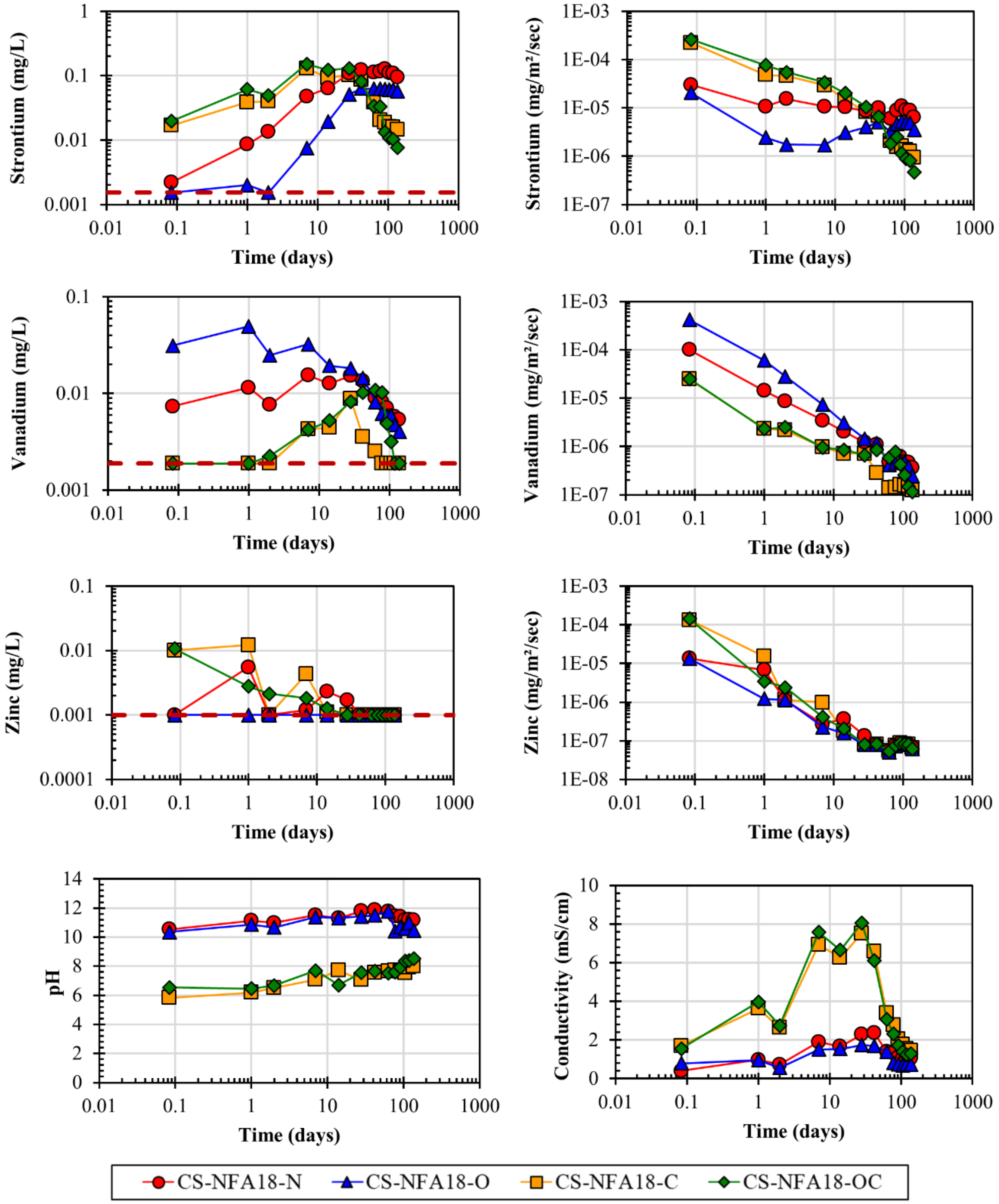

Figure C.7. (continued)

APPENDIX D

SUPPLEMENTARY MATERIAL FOR CHAPTER 5

Table D.1. Primary entities mapping of constituents and free liquid diffusivity coefficients

Constituent	**Primary entity**	**D_i^0 (10^{-9} m^2/s)**	**Reference**
Acetic acid	Acetate$^-$	1.089	[161]
Ag	Ag^+	1.648	[161]
Al	$Al[OH]_4^-$	3.120	[162]
As	AsO_4^{3-}	3.360^1	-
B	$H_2BO_3^-$	1.120^1	-
Ba	Ba^{2+}	1.694	[161]
Br	Br^-	2.080	[161]
Ca	Ca^{2+}	1.584	[161]
Cd	Cd^{2+}	1.438	[161]
Cl	Cl^-	2.032	[161]
Co	Co^{2+}	1.464	[161]
CO_3^{2-}, DIC	CO_3^{2-}	1.846	[161]
Cr	CrO_4^{2-}	2.264	[161]
Cu	Cu^{2+}	1.428	[161]
F	F-	1.475	[161]
Fe	$Fe[OH]_4^-$	1.257	[163]
Hg	Hg^{2+}	1.826	[161]
H_2O	H_2O	2.300	[164]
K	K^+	1.957	[161]
Li	Li^+	1.029	[161]
Mg	Mg^{2+}	1.412	[161]
Mn	Mn^{2+}	1.424	[161]
Mo	MoO_4^{2-}	3.968	[161]
Na	Na^+	1.334	[161]
Ni	Ni^{2+}	1.322	[161]
NO3	NO_3^-	1.902	[161]
P	PO_4^{3-}	2.472	[161]
Pb	Pb^{2+}	1.890	[161]

Table D.1. (continued)

Constituent	**Primary entity**	**D_i^0 (10^{-9} m^2/s)**	**Reference**
pe	e^-	2.130[2]	-
pH	H^+	5.273[3]	[161]
S	SO_4^{2-}	2.130	[161]
Sb	$Sb[OH]_6^-$	0.849	[161]
Se	SeO_4^{2-}	2.016	[161]
Si	$H_2SiO_4^{2-}$	1.697	[163]
Sn	Sn^{2+}	2.240[1]	-
Sr	Sr^{2+}	1.582	[161]
Th	Th^{4+}	6.120	[165]
U	UO_2^+	0.852	[161]
V	VO_2^+	1.120[1]	-
Zn	Zn^{2+}	1.406	[161]

[1] Based on the geometric mean per electron of D_i^0 for the known D_i^0 of all species listed above

[2] Based on dominant redox-sensitive species, SO_4^{2-}

[3] D_i^0 of OH^- used because system is alkaline

Table D.2. Available content for each constituent and each microconcrete material

Constituent (mol/kg)	M-00	M-02	M-39	MC-00	MC-02	MC-39
Acetic acid	1.000E-12	1.000E-12	1.000E-12	1.000E-12	1.000E-12	1.000E-12
Ag	1.000E-12	1.000E-12	1.000E-12	1.000E-12	1.000E-12	1.000E-12
Al	1.305E-01	1.421E-01	2.321E-01	8.272E-02	1.131E-01	1.528E-01
As	1.088E-05	5.059E-05	2.883E-05	3.414E-06	4.551E-05	5.976E-07
B	9.417E-04	3.124E-03	4.607E-03	1.161E-03	3.470E-03	5.339E-03
Ba	9.796E-05	8.024E-05	7.278E-04	9.284E-05	9.109E-05	9.316E-05
Br	4.199E-07	4.199E-07	4.199E-07	4.199E-07	4.199E-07	4.199E-07
Ca	2.112E+00	1.309E+00	1.336E+00	1.575E+00	9.119E-01	1.437E+00
Cd	2.340E-06	1.432E-06	1.601E-06	9.697E-07	1.699E-06	1.414E-06
Cl	1.372E-04	2.264E-04	1.146E-02	7.164E-07	4.874E-04	2.192E-04
Co	3.292E-05	4.191E-05	6.109E-05	4.921E-05	4.819E-05	5.260E-05
CO32-	1.400E-01	4.800E-01	1.400E-01	1.000E+00	7.200E-01	1.300E+00
Cr	3.596E-04	2.673E-04	3.519E-04	4.346E-04	3.423E-04	2.385E-04
Cu	7.365E-05	8.564E-05	2.115E-04	7.111E-05	9.489E-05	1.967E-04
F	1.326E-06	1.326E-06	1.326E-06	1.326E-06	1.263E-04	2.842E-04
Fe	4.212E-02	3.208E-02	5.001E-02	4.143E-02	4.374E-02	1.114E-03
Hg	1.000E-12	1.000E-12	1.000E-12	1.000E-12	1.000E-12	1.000E-12
K	4.024E-02	4.033E-02	3.166E-02	4.013E-02	3.480E-02	3.240E-02
Li	7.085E-04	6.696E-04	5.819E-04	2.499E-04	5.890E-04	4.618E-04
Mg	1.362E-01	9.524E-02	1.614E-01	1.237E-01	9.216E-02	1.991E-01
Mn	4.104E-03	3.888E-03	3.801E-03	3.786E-03	3.930E-03	2.272E-03
Mo	1.053E-06	4.722E-06	7.338E-06	2.668E-06	6.389E-06	5.055E-06
Na	9.877E-03	1.660E-02	5.678E-02	8.652E-03	1.605E-02	6.230E-02
Ni	1.279E-04	1.034E-04	1.103E-04	1.258E-04	9.021E-05	9.535E-05
NO3	2.289E-04	5.911E-05	5.726E-05	2.839E-05	3.081E-05	4.339E-05
P	1.130E-03	3.223E-03	9.215E-05	2.511E-03	7.840E-03	4.856E-05
Pb	2.032E-07	3.822E-06	5.985E-07	6.129E-07	1.390E-05	8.349E-07
S	1.401E-01	1.040E-01	8.877E-02	8.422E-02	8.046E-02	9.521E-02
Sb	3.384E-06	3.022E-06	3.302E-06	6.529E-06	2.484E-06	3.655E-07
Se	5.205E-06	5.484E-06	1.355E-05	6.649E-06	2.204E-06	9.271E-06
Si	4.352E-01	2.540E-01	4.617E-01	3.613E-01	1.585E-01	3.562E-02
Sn	1.323E-06	5.459E-07	4.119E-06	1.078E-06	3.420E-07	2.948E-08
Sr	9.389E-04	1.072E-03	2.650E-03	7.786E-04	8.155E-04	3.157E-03
Th	1.000E-12	1.000E-12	1.000E-12	1.000E-12	1.000E-12	1.000E-12
U	2.550E-06	3.336E-06	5.588E-06	2.727E-06	4.537E-06	3.995E-06
V	5.376E-05	1.520E-04	2.555E-04	1.198E-04	8.407E-05	4.424E-05
Zn	1.935E-04	1.692E-04	2.171E-04	1.902E-04	1.722E-04	2.051E-04

Table D.3. pe, pH, and adsorption model parameters for each microconcrete material

Parameter	M-00	M-02	M-39	MC-00	MC-02	MC-39
pe	3.95	1.20	1.70	3.50	3.30	3.90
pH	12.66	12.79	12.91	12.12	10.28	11.40
Clay (kg/kg)	1.000E-03	1.000E-03	1.000E-03	1.000E-03	1.000E-03	1.000E-03
Hydrous Ferric Oxide	1.500E-04	1.500E-04	1.500E-04	1.500E-04	1.500E-04	1.500E-04
Solid Humic Acid	4.399E-05	4.399E-05	4.399E-05	4.399E-05	4.399E-05	4.399E-05

Table D.4. Physical parameters for M-00 in the monolith diffusion-controlled leaching model

Cell #	Depth (m)	Thickness (m)	Leach Surface Area (m^2)	Volume (L)	Density (kg/m^3)	Porosity Fraction	Saturation Index	Tortuosity Factor
1	0.00006	0.00006	0.04268	0.00320	2.57	0.21	1	12
2	0.00015	0.00010	0.04254	0.00414	2.57	0.21	1	12
3	0.00028	0.00013	0.04237	0.00536	2.57	0.21	1	12
4	0.00045	0.00017	0.04214	0.00693	2.57	0.21	1	12
5	0.00066	0.00021	0.04184	0.00893	2.57	0.158	1	30
6	0.00094	0.00028	0.04146	0.01149	2.57	0.158	1	30
7	0.00130	0.00036	0.04097	0.01473	2.57	0.158	1	30
8	0.00177	0.00047	0.04033	0.01880	2.57	0.158	1	30
9	0.00239	0.00061	0.03951	0.02387	2.57	0.158	1	30
10	0.00318	0.00080	0.03845	0.03007	2.57	0.158	1	30
11	0.00422	0.00104	0.03710	0.03750	2.57	0.158	1	30
12	0.00556	0.00135	0.03538	0.04613	2.57	0.158	1	30
13	0.00731	0.00175	0.03320	0.05567	2.57	0.158	1	30
14	0.00958	0.00227	0.03048	0.06543	2.57	0.158	1	30
15	0.01254	0.00296	0.02711	0.07402	2.57	0.158	1	30
16	0.01638	0.00384	0.02303	0.07906	2.57	0.158	1	30
17	0.02138	0.00500	0.01822	0.07708	2.57	0.158	1	30
18	0.02787	0.00649	0.01280	0.06405	2.57	0.158	1	30
19	0.03632	0.00844	0.00719	0.03813	2.57	0.158	1	30
20	0.04729	0.01098	0.00230	0.00840	2.57	0.158	1	30

Table D.5. Physical parameters for M-02 in the monolith diffusion-controlled leaching model

Cell #	Depth (m)	Thickness (m)	Leach Surface Area (m^2)	Volume (L)	Density (kg/m^3)	Porosity Fraction	Saturation Index	Tortuosity Factor
1	0.00006	0.00006	0.04268	0.00320	2.56	0.209	1	9
2	0.00015	0.00010	0.04254	0.00414	2.56	0.209	1	9
3	0.00028	0.00013	0.04237	0.00536	2.56	0.209	1	9
4	0.00045	0.00017	0.04214	0.00693	2.56	0.209	1	9
5	0.00066	0.00021	0.04184	0.00893	2.56	0.168	1	35
6	0.00094	0.00028	0.04146	0.01149	2.56	0.168	1	35
7	0.00130	0.00036	0.04097	0.01473	2.56	0.168	1	70
8	0.00177	0.00047	0.04033	0.01880	2.56	0.168	1	70
9	0.00239	0.00061	0.03951	0.02387	2.56	0.168	1	70
10	0.00318	0.00080	0.03845	0.03007	2.56	0.168	1	70
11	0.00422	0.00104	0.03710	0.03750	2.56	0.168	1	70
12	0.00556	0.00135	0.03538	0.04613	2.56	0.168	1	70
13	0.00731	0.00175	0.03320	0.05567	2.56	0.168	1	70
14	0.00958	0.00227	0.03048	0.06543	2.56	0.168	1	70
15	0.01254	0.00296	0.02711	0.07402	2.56	0.168	1	70
16	0.01638	0.00384	0.02303	0.07906	2.56	0.168	1	70
17	0.02138	0.00500	0.01822	0.07708	2.56	0.168	1	70
18	0.02787	0.00649	0.01280	0.06405	2.56	0.168	1	70
19	0.03632	0.00844	0.00719	0.03813	2.56	0.168	1	70
20	0.04729	0.01098	0.00230	0.00840	2.56	0.168	1	70

Table D.6. Physical parameters for M-39 in the monolith diffusion-controlled leaching model

Cell #	Depth (m)	Thickness (m)	Leach Surface Area (m^2)	Volume (L)	Density (kg/m^3)	Porosity Fraction	Saturation Index	Tortuosity Factor
1	0.00006	0.00006	0.04268	0.00320	2.6	0.169	1	10
2	0.00015	0.00010	0.04254	0.00414	2.6	0.169	1	10
3	0.00028	0.00013	0.04237	0.00536	2.6	0.169	1	10
4	0.00045	0.00017	0.04214	0.00693	2.6	0.169	1	10
5	0.00066	0.00021	0.04184	0.00893	2.6	0.153	1	80
6	0.00094	0.00028	0.04146	0.01149	2.6	0.153	1	80
7	0.00130	0.00036	0.04097	0.01473	2.6	0.153	1	80
8	0.00177	0.00047	0.04033	0.01880	2.6	0.153	1	80
9	0.00239	0.00061	0.03951	0.02387	2.6	0.153	1	80
10	0.00318	0.00080	0.03845	0.03007	2.6	0.153	1	80
11	0.00422	0.00104	0.03710	0.03750	2.6	0.153	1	80
12	0.00556	0.00135	0.03538	0.04613	2.6	0.153	1	80
13	0.00731	0.00175	0.03320	0.05567	2.6	0.153	1	80
14	0.00958	0.00227	0.03048	0.06543	2.6	0.153	1	80
15	0.01254	0.00296	0.02711	0.07402	2.6	0.153	1	80
16	0.01638	0.00384	0.02303	0.07906	2.6	0.153	1	80
17	0.02138	0.00500	0.01822	0.07708	2.6	0.153	1	80
18	0.02787	0.00649	0.01280	0.06405	2.6	0.153	1	80
19	0.03632	0.00844	0.00719	0.03813	2.6	0.153	1	80
20	0.04729	0.01098	0.00230	0.00840	2.6	0.153	1	80

Table D.7. Physical parameters for MC-00 in the monolith diffusion-controlled leaching model

Cell #	Depth (m)	Thickness (m)	Leach Surface Area (m^2)	Volume (L)	Density (kg/m^3)	Porosity Fraction	Saturation Index	Tortuosity Factor
1	0.00006	0.00006	0.04268	0.00320	2.57	0.11	1	6
2	0.00015	0.00010	0.04254	0.00414	2.57	0.11	1	6
3	0.00028	0.00013	0.04237	0.00536	2.57	0.11	1	6
4	0.00045	0.00017	0.04214	0.00693	2.57	0.11	1	6
5	0.00066	0.00021	0.04184	0.00893	2.57	0.158	1	10
6	0.00094	0.00028	0.04146	0.01149	2.57	0.158	1	10
7	0.00130	0.00036	0.04097	0.01473	2.57	0.158	1	30
8	0.00177	0.00047	0.04033	0.01880	2.57	0.158	1	30
9	0.00239	0.00061	0.03951	0.02387	2.57	0.158	1	30
10	0.00318	0.00080	0.03845	0.03007	2.57	0.158	1	30
11	0.00422	0.00104	0.03710	0.03750	2.57	0.158	1	30
12	0.00556	0.00135	0.03538	0.04613	2.57	0.158	1	30
13	0.00731	0.00175	0.03320	0.05567	2.57	0.158	1	30
14	0.00958	0.00227	0.03048	0.06543	2.57	0.158	1	30
15	0.01254	0.00296	0.02711	0.07402	2.57	0.158	1	30
16	0.01638	0.00384	0.02303	0.07906	2.57	0.158	1	30
17	0.02138	0.00500	0.01822	0.07708	2.57	0.158	1	30
18	0.02787	0.00649	0.01280	0.06405	2.57	0.158	1	30
19	0.03632	0.00844	0.00719	0.03813	2.57	0.158	1	30
20	0.04729	0.01098	0.00230	0.00840	2.57	0.158	1	30

Table D.8. Physical parameters for MC-02 in the monolith diffusion-controlled leaching model

Cell #	Depth (m)	Thickness (m)	Leach Surface Area (m^2)	Volume (L)	Density (kg/m^3)	Porosity Fraction	Saturation Index	Tortuosity Factor
1	0.00006	0.00006	0.04268	0.00320	2.56	0.15	1	7
2	0.00015	0.00010	0.04254	0.00414	2.56	0.15	1	7
3	0.00028	0.00013	0.04237	0.00536	2.56	0.15	1	7
4	0.00045	0.00017	0.04214	0.00693	2.56	0.15	1	7
5	0.00066	0.00021	0.04184	0.00893	2.56	0.15	1	7
6	0.00094	0.00028	0.04146	0.01149	2.56	0.15	1	9
7	0.00130	0.00036	0.04097	0.01473	2.56	0.168	1	9
8	0.00177	0.00047	0.04033	0.01880	2.56	0.168	1	15
9	0.00239	0.00061	0.03951	0.02387	2.56	0.168	1	55
10	0.00318	0.00080	0.03845	0.03007	2.56	0.168	1	70
11	0.00422	0.00104	0.03710	0.03750	2.56	0.168	1	70
12	0.00556	0.00135	0.03538	0.04613	2.56	0.168	1	70
13	0.00731	0.00175	0.03320	0.05567	2.56	0.168	1	70
14	0.00958	0.00227	0.03048	0.06543	2.56	0.168	1	70
15	0.01254	0.00296	0.02711	0.07402	2.56	0.168	1	70
16	0.01638	0.00384	0.02303	0.07906	2.56	0.168	1	70
17	0.02138	0.00500	0.01822	0.07708	2.56	0.168	1	70
18	0.02787	0.00649	0.01280	0.06405	2.56	0.168	1	70
19	0.03632	0.00844	0.00719	0.03813	2.56	0.168	1	70
20	0.04729	0.01098	0.00230	0.00840	2.56	0.168	1	70

Table D.9. Physical parameters for MC-39 in the monolith diffusion-controlled leaching model

Cell #	Depth (m)	Thickness (m)	Leach Surface Area (m^2)	Volume (L)	Density (kg/m^3)	Porosity Fraction	Saturation Index	Tortuosity Factor
1	0.00006	0.00006	0.04268	0.00320	2.6	0.1	1	10
2	0.00015	0.00010	0.04254	0.00414	2.6	0.1	1	10
3	0.00028	0.00013	0.04237	0.00536	2.6	0.1	1	10
4	0.00045	0.00017	0.04214	0.00693	2.6	0.1	1	10
5	0.00066	0.00021	0.04184	0.00893	2.6	0.1	1	10
6	0.00094	0.00028	0.04146	0.01149	2.6	0.153	1	22
7	0.00130	0.00036	0.04097	0.01473	2.6	0.153	1	80
8	0.00177	0.00047	0.04033	0.01880	2.6	0.153	1	80
9	0.00239	0.00061	0.03951	0.02387	2.6	0.153	1	80
10	0.00318	0.00080	0.03845	0.03007	2.6	0.153	1	80
11	0.00422	0.00104	0.03710	0.03750	2.6	0.153	1	80
12	0.00556	0.00135	0.03538	0.04613	2.6	0.153	1	80
13	0.00731	0.00175	0.03320	0.05567	2.6	0.153	1	80
14	0.00958	0.00227	0.03048	0.06543	2.6	0.153	1	80
15	0.01254	0.00296	0.02711	0.07402	2.6	0.153	1	80
16	0.01638	0.00384	0.02303	0.07906	2.6	0.153	1	80
17	0.02138	0.00500	0.01822	0.07708	2.6	0.153	1	80
18	0.02787	0.00649	0.01280	0.06405	2.6	0.153	1	80
19	0.03632	0.00844	0.00719	0.03813	2.6	0.153	1	80
20	0.04729	0.01098	0.00230	0.00840	2.6	0.153	1	80

Table D.10. M-00 log-squared residuals of the experimental results and pH-dependent solubility model results of each constituent

Target pH group	7	8	9	10.5	12	13	SUM
Al	-	-	0.36	0.06	1.21	0.63	2.26
Ba	0.00	0.00	0.00	0.00	0.01	0.13	0.14
Ca	0.00	0.00	0.00	0.00	0.09	0.18	0.27
Cr	0.06	0.09	0.15	0.02	1.15	0.08	1.55
Mg	0.00	0.09	0.72	0.00	0.08	1.24	2.14
K	0.00	0.00	0.00	0.00	0.03	0.02	0.05
Si	0.02	0.33	0.01	0.68	1.06	0.35	2.44
Na	0.00	0.00	0.00	0.00	0.01	0.00	0.01
Sr	0.00	0.00	0.00	0.01	0.11	0.14	0.27
S	0.02	0.01	0.00	1.07	2.05	0.92	4.08
SUM	0.10	0.53	1.24	1.85	5.80	3.69	13.21

Table D.11. M-02 log-squared residuals of the experimental results and pH-dependent solubility model results of each constituent

Target pH group	7	8	9	10.5	12	13	SUM
Al	1.72	1.60	0.62	0.02	0.00	0.03	3.99
Ba	0.00	0.00	0.00	0.00	0.07	0.06	0.13
Ca	0.03	0.01	0.01	0.04	0.26	0.20	0.55
Cr	0.01	0.24	0.49	1.70	0.57	1.45	4.46
Mg	0.01	0.04	0.11	0.10	0.01	0.52	0.79
K	0.00	0.00	0.00	0.00	0.03	0.02	0.05
Si	0.05	0.25	0.24	0.33	0.37	0.79	2.03
Na	0.00	0.00	0.00	0.00	0.01	0.01	0.02
Sr	0.00	0.01	0.01	0.01	0.10	0.09	0.22
S	0.00	0.02	0.03	0.23	0.81	0.46	1.55
SUM	1.82	2.17	1.51	2.43	2.23	3.63	13.79

Table D.12. M-39 log-squared residuals of the experimental results and pH-dependent solubility model results of each constituent

Target pH group	7	8	9	10.5	12	13	SUM
Al	1.31	1.93	1.26	0.08	0.51	2.15	7.24
Ba	0.82	0.84	0.83	0.33	0.02	0.11	2.95
Ca	0.00	0.00	0.00	0.01	0.03	0.15	0.19
Cr	0.65	0.55	0.39	0.47	0.05	0.18	2.29
Mg	0.02	0.04	0.08	0.07	0.98	2.25	3.44
K	0.00	0.00	0.00	0.00	0.01	0.03	0.04
Si	0.51	1.36	0.93	0.14	1.69	0.40	5.03
Na	0.00	0.00	0.00	0.00	0.00	0.01	0.01
Sr	0.00	0.00	0.01	0.00	0.01	0.00	0.02
S	0.00	0.00	0.01	0.33	5.89	8.31	14.54
SUM	3.31	4.72	3.51	1.43	9.19	13.59	35.75

Table D.13. MC-00 log-squared residuals of the experimental results and pH-dependent solubility model result of each constituent

Target pH group	7	8	9	10.5	12	13	SUM
Al	0.82	0.58	0.00	0.29	0.38	0.78	2.85
Ba	0.18	0.32	0.39	0.38	0.19	0.01	1.47
Ca	0.00	0.00	0.04	0.10	0.32	0.16	0.62
Cr	0.45	0.33	0.36	0.33	0.84	1.00	3.31
Mg	0.24	0.28	0.33	0.15	0.15	4.15	5.30
K	0.03	0.02	0.04	0.02	0.20	0.34	0.65
Si	0.05	0.17	0.00	0.23	0.09	0.27	0.81
Na	0.01	0.01	0.02	0.01	0.22	0.11	0.38
Sr	0.06	0.07	0.09	0.07	0.02	0.04	0.35
S	0.18	0.17	0.22	0.16	0.25	0.38	1.36
SUM	2.02	1.95	1.49	1.74	2.66	7.24	17.10

Table D.14. MC-02 log-squared residuals of the experimental results and pH-dependent solubility model result of each constituent

Target pH group	7	8	9	10.5	12	13	SUM
Al	1.32	2.25	0.15	0.01	0.80	1.06	5.59
Ba	0.48	1.03	1.66	1.99	0.18	0.00	5.34
Ca	0.02	0.04	0.06	0.16	0.31	0.09	0.68
Cr	0.03	0.11	1.38	0.46	2.37	2.39	6.74
Mg	0.18	0.37	0.91	0.15	0.09	0.05	1.75
K	0.12	0.21	0.29	0.33	0.16	1.04	2.15
Si	0.12	0.28	0.31	0.00	0.76	0.53	2.00
Na	0.02	0.03	0.05	0.06	0.08	0.06	0.30
Sr	0.24	0.62	1.30	2.07	1.02	0.75	6.00
S	0.02	0.04	0.05	0.07	0.07	0.08	0.33
SUM	2.55	4.98	6.16	5.30	5.84	6.05	30.88

Table D.15. MC-39 log-squared residuals of the experimental results and pH-dependent solubility model result of each constituent

Target pH group	7	8	9	10.5	12	13	SUM
Al	2.85	4.10	2.40	0.63	0.19	0.09	10.26
Ba	0.03	0.10	0.14	0.24	0.13	1.02	1.66
Ca	0.18	0.04	0.00	0.04	0.32	0.01	0.59
Cr	0.56	0.21	0.34	0.46	0.47	0.31	2.35
Mg	0.30	0.57	0.87	0.08	0.14	0.53	2.49
K	0.14	0.20	0.31	0.39	0.57	0.67	2.28
Si	0.47	1.03	1.20	0.31	0.06	0.56	3.63
Na	0.01	0.01	0.04	0.06	0.10	0.04	0.26
Sr	0.29	0.55	0.76	1.32	0.57	0.00	3.49
S	0.10	0.12	0.19	0.22	0.17	0.07	0.87
SUM	4.93	6.93	6.25	3.75	2.72	3.30	27.88

Table D.16. M-00 log-squared residual of the experimental results and monolith diffusion-controlled leaching model results of each constituent

Cumulative leaching time (days)	0.08	1	2	7	14	28	42	49	63	SUM
Al	0.70	0.11	0.00	0.03	0.01	0.02	0.02	0.02	0.02	0.93
Ba	0.06	0.13	0.01	0.20	0.00	0.00	0.00	0.26	0.12	0.78
Ca	0.49	0.08	0.03	0.01	0.00	0.01	0.01	0.06	0.04	0.73
Cr	-	0.13	0.01	0.07	0.01	0.25	0.41	0.11	-	0.99
Fe	-	-	0.22	0.02	0.01	0.07	0.06	-	-	0.38
Mg	-	1.63	1.10	0.40	0.26	0.15	0.11	0.07	0.01	3.73
K	0.02	0.07	0.00	0.01	0.00	0.00	0.00	0.04	0.00	0.14
Si	5.38	5.93	3.38	1.74	1.06	0.59	0.43	0.36	0.04	18.91
Na	0.02	0.09	0.00	0.00	0.00	0.00	0.00	0.02	0.00	0.13
Sr	0.04	0.08	0.00	0.01	0.01	0.06	0.13	0.21	0.08	0.62
S	0.67	0.84	0.29	0.00	0.33	0.56	0.09	0.03	0.26	3.07
SUM	7.38	9.09	5.04	2.49	1.69	1.71	1.26	1.18	0.57	30.41

Table D.17. M-02 log-squared residual of the experimental results and monolith diffusion-controlled leaching model results of each constituent

Cumulative leaching time (days)	0.08	1	2	7	14	28	42	49	63	SUM
Al	0.85	0.00	0.12	0.01	0.04	0.08	0.17	0.43	0.31	2.01
Ba	0.00	0.59	0.29	0.34	0.04	0.28	0.01	0.01	0.07	1.63
Ca	0.00	0.45	0.04	0.18	0.07	0.07	0.00	0.00	0.01	0.82
Cr	0.05	0.10	0.17	0.70	3.03	2.9	2.39	1.06	0.00	10.40
Fe	-	-	0.44	0.00	0.01	0.01	-	-	-	0.46
Mg	-	0.34	0.21	0.01	0.01	0.06	0.21	0.41	0.47	1.72
K	0.02	0.01	0.01	0.01	0.00	0.00	0.00	0.04	0.00	0.09
Si	7.57	2.01	1.29	0.34	0.02	0.00	0.24	0.48	0.10	12.05
Na	0.01	0.03	0.00	0.03	0.01	0.00	0.00	0.03	0.01	0.12
Sr	0.07	0.72	0.16	0.31	0.12	0.03	0.00	0.07	0.02	1.50
S	0.71	0.01	0.05	0.39	0.07	0.55	0.46	0.39	0.34	2.97
SUM	9.28	4.26	2.78	2.32	3.42	3.98	3.48	2.92	1.33	33.77

Table D.18. M-39 log-squared residual of the experimental results and monolith diffusion-controlled leaching model results of each constituent

Cumulative leaching time (days)	0.08	1	2	7	14	28	42	49	63	SUM
Al	0.05	0.00	0.23	0.10	0.15	0.13	0.15	0.31	0.37	1.49
Ba	0.31	0.05	0.03	0.05	0.08	0.01	0.02	0.59	0.39	1.53
Ca	0.44	0.36	0.02	0.09	0.02	0.03	0.01	0.02	0.01	1.00
Cr	-	-	0.01	2.13	0.06	1.51	1.53	0.03	-	5.27
Fe	-	-	0.38	0.05	0.05	0.01	0.00	-	-	0.49
Mg	-	0.54	1.15	0.21	0.09	0.03	0.01	0.03	0.01	2.07
K	0.03	0.00	0.12	0.07	0.07	0.06	0.05	0.15	0.04	0.59
Si	4.37	3.43	1.95	0.84	0.25	0.06	0.00	0.00	0.05	10.95
Na	0.21	0.21	0.00	0.00	0.00	0.00	0.00	0.01	0.00	0.43
Sr	0.00	0.41	0.00	0.03	0.09	0.01	0.04	0.63	0.53	1.74
S	7.05	1.07	0.04	0.34	0.15	0.04	0.46	0.08	0.39	9.62
SUM	12.46	6.07	3.93	3.91	1.01	1.89	2.27	1.85	1.79	35.18

Table D.19. MC-00 log-squared residual of the experimental results and monolith diffusion-controlled leaching model results of each constituent

Cumulative leaching time (days)	0.08	1	2	7	14	28	42	49	63	SUM
Al	0.34	0.67	0.16	0.14	0.10	0.17	0.07	0.00	0.02	1.67
Ba	-	-	-	-	3.71	2.03	0.54	0.26	0.55	7.09
Ca	0.00	1.74	0.76	0.43	0.48	0.36	0.17	0.02	0.10	4.06
Cr	-	0.00	0.05	0.06	0.07	0.51	1.19	-	-	1.88
Fe	-	0.57	0.91	0.13	0.00	-	-	-	-	1.61
Mg	3.68	1.66	1.60	0.82	0.67	0.41	0.11	0.05	0.01	9.01
K	0.00	0.01	0.08	0.01	0.05	0.00	0.01	0.03	0.01	0.20
Si	0.14	0.74	0.44	0.13	0.22	0.36	0.12	0.15	1.00	3.30
Na	0.00	0.00	0.02	0.00	0.02	0.03	0.05	0.00	0.02	0.14
Sr	-	-	1.86	1.24	1.35	1.04	0.46	0.00	0.00	5.95
S	0.92	0.82	0.46	0.30	0.12	0.05	0.02	0.25	0.03	2.97
SUM	5.08	6.21	6.34	3.26	6.79	4.96	2.74	0.76	1.74	37.88

Table D.20. MC-02 log-squared residual of the experimental results and monolith diffusion-controlled leaching model results of each constituent

Cumulative leaching time (days)	0.08	1	2	7	14	28	42	49	63	SUM
Al	1.09	0.07	0.23	0.00	0.01	0.00	0.01	0.18	0.03	1.62
Ba	-	-	-	-	-	-	-	-	-	-
Ca	1.09	1.52	0.91	0.44	0.04	0.09	0.03	0.02	0.01	4.15
Cr	-	-	-	-	-	-	-	-	-	-
Fe	-	1.88	1.83	0.85	0.40	-	-	-	-	4.96
Mg	1.37	0.14	0.01	0.05	0.09	0.07	0.22	0.33	0.36	2.64
K	0.12	0.05	0.00	0.00	0.04	0.02	0.02	0.07	0.00	0.32
Si	0.07	0.00	0.00	0.00	0.10	0.07	0.52	0.81	0.38	1.95
Na	0.02	0.00	0.00	0.00	0.01	0.00	0.01	0.01	0.05	0.10
Sr	2.80	5.11	3.86	2.59	1.98	2.09	1.23	0.67	0.96	21.29
S	4.06	4.27	2.84	2.09	0.10	0.06	0.12	0.50	0.27	14.31
SUM	10.62	13.04	9.68	6.02	2.77	2.40	2.16	2.59	2.06	51.34

Table D.21. MC-39 log-squared residual of the experimental results and monolith diffusion-controlled leaching model results of each constituent

Cumulative leaching time (days)	0.08	1	2	7	14	28	42	49	63	SUM
Al	1.89	0.20	0.12	0.04	0.13	0.12	0.17	0.43	0.17	3.27
Ba	-	-	0.56	1.23	1.05	0.84	0.59	0.38	0.91	5.56
Ca	0.41	0.29	0.34	0.39	0.08	0.15	0.05	0.00	0.05	1.76
Cr	-	0.01	0.34	0.00	0.01	0.00	0.01	-	-	0.37
Fe	-	-	1.22	0.22	0.17	0.03	0.04	-	-	1.68
Mg	-	4.01	4.74	2.67	1.61	0.67	0.43	0.50	0.16	14.79
K	0.44	0.18	0.05	0.22	0.14	0.14	0.08	0.00	0.04	1.29
Si	0.96	0.12	0.89	0.17	0.99	1.22	0.82	1.28	1.14	7.59
Na	0.05	0.01	0.00	0.04	0.01	0.00	0.00	0.10	0.01	0.22
Sr	0.20	0.77	0.92	3.67	1.26	1.25	1.63	1.15	0.54	11.39
S	4.86	3.59	0.59	0.77	0.63	0.45	0.52	0.20	0.36	11.97
SUM	8.81	9.18	9.77	9.42	6.08	4.87	4.34	4.04	3.38	59.89

REFERENCES

[1] K.G. Brown, R.R. Seitz, G.A. Taylor, D.W. Esh, Summary of Department of Energy and Nuclear Regulatory Commission Performance Assessment Approaches, Volume 2: Sensitivity and Uncertainty Analysis, CBP-TR-2009-001, Rev. 0, Overview of the U.S. Department of Energy and Nuclear Regulatory Commission Performance Assessment Approaches, Cementitious Barriers Partnership, Aiken, SC and Nashville, TN. Available from: http://cementbarriers.org/. 2009.

[2] A.C. Garrabrants, D.S. Kosson, R. DeLapp, H.A. van der Sloot, Effect of coal combustion fly ash use in concrete on the mass transport release of constituents of potential concern, Chemosphere, 103 (2014) 131-139.

[3] D.S. Kosson, A.C. Garrabrants, R. DeLapp, H.A. van der Sloot, pH-dependent leaching of constituents of potential concern from concrete materials containing coal combustion fly ash, Chemosphere, 103 (2014) 140-147.

[4] J.C. Walton, L.E. Plansky, R.W. Smith, Models for estimation of service life of concrete barriers in low-level radioactive waste disposal, 1990, pp. Medium: ED; Size: Pages: (38 p).

[5] C.F. Chang, J.W. Chen, The experimental investigation of concrete carbonation depth, Cement and Concrete Research, 36 (2006) 1760-1767.

[6] M. Thiery, G. Villain, P. Dangla, G. Platret, Investigation of the carbonation front shape on cementitious materials: Effects of the chemical kinetics, Cement and Concrete Research, 37 (2007) 1047-1058.

[7] V.G. Papadakis, C.G. Vayenas, M.N. Fardis, A reaction engineering approach to the problem of concrete carbonation, AIChE Journal, 35 (1989) 1639-1650.

[8] V.G. Papadakis, C.G. Vayenas, M.N. Fardis, Experimental investigation and mathematical modeling of the concrete carbonation problem, Chemical Engineering Science, 46 (1991) 1333-1338.

[9] A. Morandeau, M. Thiéry, P. Dangla, Investigation of the carbonation mechanism of CH and C-S-H in terms of kinetics, microstructure changes and moisture properties, Cement and Concrete Research, 56 (2014) 153-170.

[10] H.F.W. Taylor, Cement chemistry, Thomas Telford, 1997.

[11] K. Kobayashi, K. Suzuki, Y. Uno, Carbonation of concrete structures and decomposition of C-S-H, Cement and Concrete Research, 24 (1994) 55-61.

[12] T. Nishikawa, K. Suzuki, S. Ito, K. Sato, T. Takebe, Decomposition of synthesized ettringite by carbonation, Cement and Concrete Research, 22 (1992) 6-14.

[13] J. Carey, P. Lichtner, Calcium silicate hydrate (CSH) solid solution model applied to cement degradation using the continuum reactive transport model FLOTRAN, Transport Properties and Concrete Quality: Materials Science of Concrete, 73 (2007) 106.

[14] T. Ishida, K. Maekawa, Modeling of pH Profile in Pore Wate Based on Mass Transport and Chemical Equilibrium Theory, Concrete Library of JSCE, 37 (2001) 131-146.

[15] Q. Yu, S. Nagataki, J. Lin, T. Saeki, M. Hisada, The leachability of heavy metals in hardened fly ash cement and cement-solidified fly ash, Cement and Concrete Research, 35 (2005) 1056-1063.

[16] T. Van Gerven, G. Cornelis, E. Vandoren, C. Vandecasteele, A.C. Garrabrants, F. Sanchez, D.S. Kosson, Effects of progressive carbonation on heavy metal leaching from cement-bound waste, AIChE Journal, 52 (2006) 826-837.

[17] F. Sanchez, C. Gervais, A.C. Garrabrants, R. Barna, D.S. Kosson, Leaching of inorganic contaminants from cement-based waste materials as a result of carbonation during intermittent wetting, Waste Management, 22 (2002) 249-260.

[18] K. Sisomphon, L. Franke, Carbonation rates of concretes containing high volume of pozzolanic materials, Cement and Concrete Research, 37 (2007) 1647-1653.

[19] B.K. Marsh, R.L. Day, D.G. Bonner, Pore structure characteristics affecting the permeability of cement paste containing fly ash, Cement and Concrete Research, 15 (1985) 1027-1038.

[20] D. McPolin, P. Basheer, A. Long, K. Grattan, T. Sun, New Test Method to Obtain pH Profiles due to Carbonation of Concretes Containing Supplementary Cementitious Materials, J. Mater. Civ. Eng., 19 (2007) 936-946.

[21] J. Khunthongkeaw, S. Tangtermsirikul, T. Leelawat, A study on carbonation depth prediction for fly ash concrete, Construction and Building Materials, 20 (2006) 744-753.

[22] V.G. Papadakis, Effect of supplementary cementing materials on concrete resistance against carbonation and chloride ingress, Cement and Concrete Research, 30 (2000) 291-299.

[23] X.-Y. Wang, H.-S. Lee, A model for predicting the carbonation depth of concrete containing low-calcium fly ash, Construction and Building Materials, 23 (2009) 725-733.

[24] J. Khunthongkeaw, S. Tangtermsirikul, Model for simulating carbonation of fly ash concrete, Journal of materials in civil engineering, 17 (2005) 570-578.

[25] D.S. Kosson, F. Sanchez, P. Kariher, L.H. Turner, R. Delapp, P. Seignette, Characterization of Coal Combustion Residues from Electric Utilities – Leaching and Characterization Data, USEPA, 2009.

[26] J.L. Branch, K.G. Brown, J.R. Arnold, H.A. van der Sloot, D.S. Kosson, Reactive Transport Modeling and Characterization of Concrete Materials with Fly Ash Replacement under Carbonation Attack- #15477, Waste Management SymposiaTempe, AZ, March 2015.

[27] U.S. EPA, Liquid–solid partitioning as a function of extract pH using a parallel batch extraction procedure (EPA-600/R-09/151), http://www3.epa.gov/epawaste/hazard/testmethods/sw846/pdfs/1313.pdf, October 2012.

[28] A. Garrabrants, D. Kosson, L. Stefanski, R. DeLapp, P. Seignette, H. Van der Sloot, P. Kariher, M. Baldwin, Interlaboratory validation of the leaching environmental assessment framework (LEAF) method 1313 and method 1316, EPA-600/R-12/623, September, 2012.

[29] A.C. Garrabrants, D.S. Kosson, H.A. van der Sloot, F. Sanchez, O. Hjelmar, Background information for the Leaching Enviornmental Assessment Framework (LEAF) Test Methods, EPA-600/R-10/170, U.S. Environmental Protection Agency, Air Pollution Prevention and Control Division, (November 2010).

[30] U.S. EPA, Method 6010C (SW-846): Inductively Coupled Plasma-Atomic Emission Spectrometry. Revision 3., 2007.

[31] L.S. Clesceri, Greenberg, A.E., Eaton, A.D., Standard Methods for the Examination of Water and Wastewater, American Public Health Association, American Water Works Association, and Water Environment Federation, Washington, DC, 1998, pp. 2-26- 22-29 & 22-75 - 22-78.

[32] K.L. Scrivener, T. Füllmann, E. Gallucci, G. Walenta, E. Bermejo, Quantitative study of Portland cement hydration by X-ray diffraction/Rietveld analysis and independent methods, Cement and Concrete Research, 34 (2004) 1541-1547.

[33] G. Villain, M. Thiery, G. Platret, Measurement methods of carbonation profiles in concrete: Thermogravimetry, chemical analysis and gammadensimetry, Cement and Concrete Research, 37 (2007) 1182-1192.

[34] L. Alarcon-Ruiz, G. Platret, E. Massieu, A. Ehrlacher, The use of thermal analysis in assessing the effect of temperature on a cement paste, Cement and Concrete Research, 35 (2005) 609-613.

[35] G. Villain, G. Platret, Two experimental methods to determine carbonation profiles in concrete, ACI Materials Journal, 103 (2006) 265-271.

[36] D. Li, Y. Chen, J. Shen, J. Su, X. Wu, The influence of alkalinity on activation and microstructure of fly ash, Cement and Concrete Research, 30 (2000) 881-886.

[37] J. Jain, N. Neithalath, Analysis of calcium leaching behavior of plain and modified cement pastes in pure water, Cement and Concrete Composites, 31 (2009) 176-185.

[38] L. Haselbach, Potential for Carbon Dioxide Absorption in Concrete, Journal of Environmental Engineering, 135 (2009) 465-472.

[39] L. Black, C. Breen, J. Yarwood, K. Garbev, P. Stemmermann, B. Gasharova, Structural Features of C–S–H(I) and Its Carbonation in Air—A Raman Spectroscopic Study. Part II: Carbonated Phases, Journal of the American Ceramic Society, 90 (2007) 908-917.

[40] Z. Šauman, Carbonization of porous concrete and its main binding components, Cement and Concrete Research, 1 (1971) 645-662.

[41] P.H.R. Borges, J.O. Costa, N.B. Milestone, C.J. Lynsdale, R.E. Streatfield, Carbonation of CH and C–S–H in composite cement pastes containing high amounts of BFS, Cement and Concrete Research, 40 (2010) 284-292.

[42] P.A. Slegers, P.G. Rouxhet, Carbonation of the hydration products of tricalcium silicate, Cement and Concrete Research, 6 (1976) 381-388.

[43] J. Payá, J. Monzó, M.V. Borrachero, E. Perris, F. Amahjour, Thermogravimetric Methods for Determining Carbon Content in Fly Ashes, Cement and Concrete Research, 28 (1998) 675-686.

[44] A. Medina, P. Gamero, X. Querol, N. Moreno, B. De León, M. Almanza, G. Vargas, M. Izquierdo, O. Font, Fly ash from a Mexican mineral coal I: Mineralogical and chemical characterization, Journal of Hazardous Materials, 181 (2010) 82-90.

[45] K.L. Scrivener, Backscattered electron imaging of cementitious microstructures: understanding and quantification, Cement and Concrete Composites, 26 (2004) 935-945.

[46] T. Bakharev, J.G. Sanjayan, Y.B. Cheng, Resistance of alkali-activated slag concrete to carbonation, Cement and Concrete Research, 31 (2001) 1277-1283.

[47] V.G. Papadakis, Effect of fly ash on Portland cement systems: Part I. Low-calcium fly ash, Cement and Concrete Research, 29 (1999) 1727-1736.

[48] S. Li, D.M. Roy, Investigation of relations between porosity, pore structure, and C1− diffusion of fly ash and blended cement pastes, Cement and Concrete Research, 16 (1986) 749-759.

[49] I.G. Richardson, The calcium silicate hydrates, Cement and Concrete Research, 38 (2008) 137-158.

[50] V.W.Y. Tam, X.F. Gao, C.M. Tam, Carbonation around near aggregate regions of old hardened concrete cement paste, Cement and Concrete Research, 35 (2005) 1180-1186.

[51] A. Schwartzentruber, C. Catherine, Method of the concrete equivalent mortar (CEM)—a new tool to design concrete containing admixture, Materials and structures, 33 (2000) 475-482.

[52] H.S. Wong, M.K. Head, N.R. Buenfeld, Pore segmentation of cement-based materials from backscattered electron images, Cement and Concrete Research, 36 (2006) 1083-1090.

[53] D.P. Bentz, P.E. Stutzman, SEM analysis and computer modelling of hydration of Portland cement particles, Petrography of Cementitious Materials, ASTM International1994.

[54] L. Zhang, F.P. Glasser, Investigation of the microstructure and carbonation of $C\bar{S}A$-based concretes removed from service, Cement and Concrete Research, 35 (2005) 2252-2260.

[55] V.T. Ngala, C.L. Page, Effects of carbonation on pore structure and diffusional properties of hydrated cement pastes, Cement and Concrete Research, 27 (1997) 995-1007.

[56] C.S. Poon, L. Lam, Y.L. Wong, Effects of Fly Ash and Silica Fume on Interfacial Porosity of Concrete, Journal of Materials in Civil Engineering, 11 (1999) 197-205.

[57] H.S. Wong, N.R. Buenfeld, Euclidean Distance Mapping for computing microstructural gradients at interfaces in composite materials, Cement and Concrete Research, 36 (2006) 1091-1097.

[58] K. Scrivener, A. Crumbie, P. Laugesen, The Interfacial Transition Zone (ITZ) Between Cement Paste and Aggregate in Concrete, Interface Science, 12 (2004) 411-421.

[59] A.C. Garrabrants, F. Sanchez, D.S. Kosson, Changes in constituent equilibrium leaching and pore water characteristics of a Portland cement mortar as a result of carbonation, Waste Management, 24 (2004) 19-36.

[60] C. Gervais, A.C. Garrabrants, F. Sanchez, R. Barna, P. Moszkowicz, D.S. Kosson, The effects of carbonation and drying during intermittent leaching on the release of inorganic constituents from a cement-based matrix, Cement and Concrete Research, 34 (2004) 119-131.

[61] H.A. van der Sloot, D.S. Kosson, A.C. Garrabrants, J.R. Arnold, The Impact of Coal Combustion Fly Ash Used as a Supplemental Cementitious Material on the Leaching of Constituents from Cements and Concretes, USEPA Office of Research and Development, Research Triangle Park, NC.

[62] M.S.B. Shafique, J.C. Walton, N. Gutierrez, R.W. Smith, A.J. Tarquin, Influence of carbonation on leaching of cementitious wasteforms, Journal of Environmental Engineering, 124 (1998) 463-467.

[63] H.S. Wong, N.R. Buenfeld, M.K. Head, Estimating transport properties of mortars using image analysis on backscattered electron images, Cement and Concrete Research, 36 (2006) 1556-1566.

[64] S. Diamond, Mercury porosimetry: An inappropriate method for the measurement of pore size distributions in cement-based materials, Cement and Concrete Research, 30 (2000) 1517-1525.

[65] A. El-Dieb, R. Hooton, Evaluation of the Katz-Thompson model for estimating the water permeability of cement-based materials from mercury intrusion porosimetry data, Cement and Concrete Research, 24 (1994) 443-455.

[66] M. Safiuddin, N. Hearn, Comparison of ASTM saturation techniques for measuring the permeable porosity of concrete, Cement and Concrete Research, 35 (2005) 1008-1013.

[67] K.K. Aligizaki, Pore structure of cement-based materials: testing, interpretation and requirements, CRC Press2005.

[68] K.L. Scrivener, H.H. Patel, P.L. Pratt, L.J. Parrott, Analysis of Phases in Cement Paste using Backscattered Electron Images, Methanol Adsorption and Thermogravimetric Analysis, MRS Online Proceedings Library Archive, 85 (1986) 67 (10 pages).

[69] Y. Wang, S. Diamond, An Approach to Quantitative Image Analysis for Cement Pastes, MRS Online Proceedings Library Archive, 370 (1994) 23.

[70] R. Yang, N.R. Buenfeld, Binary segmentation of aggregate in SEM image analysis of concrete, Cement and Concrete Research, 31 (2001) 437-441.

[71] B. MÜNch, L.H.J. Martin, A. Leemann, Segmentation of elemental EDS maps by means of multiple clustering combined with phase identification, Journal of Microscopy, 260 (2015) 411-426.

[72] L. Basheer, P.A.M. Basheer, A.E. Long, Influence of coarse aggregate on the permeation, durability and the microstructure characteristics of ordinary Portland cement concrete, Construction and Building Materials, 19 (2005) 682-690.

[73] C.A. Rigo da Silva, R.J.P. Reis, F.S. Lameiras, W.L. Vasconcelos, Carbonation-Related Microstructural Changesin Long-Term Durability Concrete, Materials Research, 5 (2002) 287-293.

[74] H.W. Song, S.J. Kwon, Permeability characteristics of carbonated concrete considering capillary pore structure, Cement and Concrete Research, 37 (2007) 909-915.

[75] K.G. Brown, J. Arnold, S. Sarkar, G. Flach, H. van der Sloot, J.C.L. Meeussen, D.S. Kosson, Modeling Carbonation of High-Level Waste Tank Integrity and Closure, EPJ Web of Conferences, 56 (2013).

[76] J. Ollivier, J. Maso, B. Bourdette, Interfacial transition zone in concrete, Advanced Cement Based Materials, 2 (1995) 30-38.

[77] K.L. Scrivener, K.M. Nemati, The percolation of pore space in the cement paste aggregate interfacial zone of concrete, Cem. Concr. Res., 26 (1996) 35.

[78] A. Delagrave, J.P. Bigas, J.P. Ollivier, J.P. Marchand, M. Pigeon, Influence of the interfacial zone on the chloride diffusivity of mortars, Adv. Cem. Based Mater., 5 (1997) 86.

[79] C.C. Yang, J.K. Su., Approximate migration coefficient of interfacial transition zone and the effect of aggregate content on the migration coefficient of mortar, Cem. Concr. Res., 32 (2002) 1559.

[80] R.A. Patel, Q.T. Phung, S.C. Seetharam, J. Perko, D. Jacques, N. Maes, G. De Schutter, G. Ye, K. Van Breugel, Diffusivity of saturated ordinary Portland cement-based materials: A critical review of experimental and analytical modelling approaches, Cement and Concrete Research, 90 (2016) 52-72.

[81] D.N. Winslow, M.D. Cohen, D.P. Bentz, K.A. Snyder, E.J. Garboczi, Percolation and pore structure in mortars and concrete, Cement and concrete research, 24 (1994) 25-37.

[82] P. Chindaprasirt, C. Jaturapitakkul, T. Sinsiri, Effect of fly ash fineness on compressive strength and pore size of blended cement paste, Cement and Concrete Composites, 27 (2005) 425-428.

[83] V.G. Papadakis, Effect of fly ash on Portland cement systems: Part II. High-calcium fly ash, Cement and Concrete Research, 30 (2000) 1647-1654.

[84] K.H. Suchomel, D.K. Kreamer, A. Long, Production and transport of carbon dioxide in a contaminated vadose zone: a stable and radioactive carbon isotope study, Environmental science & technology, 24 (1990) 1824-1831.

[85] I. Vadillo, J. Benavente, F. Carrasco, A. Soler, C. Liñán, Isotopic (13C) Signature of CO2 Sources in the Vadose Zone of a Mediterranean Karst (Nerja Cave Site, Southern Spain), in: B. Andreo, F. Carrasco, J.J. Durán, J.W. LaMoreaux (Eds.) Advances in Research in Karst Media, Springer Berlin Heidelberg, Berlin, Heidelberg, 2010, pp. 463-468.

[86] Q.T. Phung, N. Maes, D. Jacques, E. Bruneel, I. Van Driessche, G. Ye, G. De Schutter, Effect of limestone fillers on microstructure and permeability due to carbonation of cement pastes under controlled CO2 pressure conditions, Construction and Building Materials, 82 (2015) 376-390.

[87] N. Hyvert, A. Sellier, F. Duprat, P. Rougeau, P. Francisco, Dependency of C–S–H carbonation rate on CO2 pressure to explain transition from accelerated tests to natural carbonation, Cement and Concrete Research, 40 (2010) 1582-1589.

[88] M. Thiery, P. Dangla, P. Belin, G. Habert, N. Roussel, Carbonation kinetics of a bed of recycled concrete aggregates: A laboratory study on model materials, Cement and Concrete Research, 46 (2013) 50-65.

[89] M. Thiéry, V. Baroghel-Bouny, A. Morandeau, P. Dangla, Impact of carbonation on the microstructure and transfer properties of cement-based materials, Transfert, Lille, (2012).

[90] M. Thiéry, P. Faure, A. Morandeau, G. Platret, J.-F. Bouteloup, P. Dangla, V. Baroghel-Bouny, Effect of carbonation on the microstructure and moisture properties of cement-based materials, XII DBMC (12th International Conference on Building Materials and Components, 2011, pp. 1-8.

[91] J.L. Branch, D.S. Kosson, A.C. Garrabrants, P.J. He, The impact of carbonation on the microstructure and solubility of major constituents in microconcrete materials with varying

alkalinities due to fly ash replacement of ordinary Portland cement, Cement and Concrete Research, 89 (2016) 297-309.

[92] M.H.N. Yio, H.S. Wong, N.R. Buenfeld, 3D Monte Carlo simulation of backscattered electron signal variation across pore-solid boundaries in cement-based materials, Cement and Concrete Research, 89 (2016) 320-331.

[93] Y.F. Houst, F.H. Wittmann, Influence of porosity and water content on the diffusivity of CO2 and O2 through hydrated cement paste, Cement and Concrete Research, 24 (1994) 1165-1176.

[94] A. Elsharief, M.D. Cohen, J. Olek, Influence of aggregate size, water cement ratio and age on the microstructure of the interfacial transition zone, Cement and Concrete Research, 33 (2003) 1837-1849.

[95] Y. Gao, G. De Schutter, G. Ye, Micro- and meso-scale pore structure in mortar in relation to aggregate content, Cement and Concrete Research, 52 (2013) 149-160.

[96] Z. Jiang, Q. Huang, Y. Xi, X. Gu, W. Zhang, Experimental Study of Diffusivity of the Interfacial Transition Zone between Cement Paste and Aggregate, Journal of Materials in Civil Engineering, 28 (2016).

[97] L. Jiang, The interfacial zone and bond strength between aggregates and cement pastes incorporating high volumes of fly ash, Cement and Concrete Composites, 21 (1999) 313-316.

[98] M. Kuroda, T. Watanabe, N. Terashi, Increase of bond strength at interfacial transition zone by the use of fly ash, Cement and Concrete Research, 30 (2000) 253-258.

[99] Y.L. Wong, L. Lam, C.S. Poon, F.P. Zhou, Properties of fly ash-modified cement mortar-aggregate interfaces, Cement and Concrete Research, 29 (1999) 1905-1913.

[100] S. Diamond, J. Huang, The ITZ in concrete – a different view based on image analysis and SEM observations, Cement and Concrete Composites, 23 (2001) 179-188.

[101] W.A. Tasong, C.J. Lynsdale, J.C. Cripps, Aggregate-cement paste interface: Part I. Influence of aggregate geochemistry, Cement and Concrete Research, 29 (1999) 1019-1025.

[102] R. Dodd, J. Cammann, Progress in Retrieval and Closure of First High-Level Waste Tank at Hanford: Single-Shell Tank C-106, Waste Management Symposium 2005, Tucson, AZ, February 27-March 3, 2005.

[103] R.E. Gephart, R.E. Lundgren, Hanford tank clean up: A guide to understanding the technical issues, 1995.

[104] Hanford Tank Waste Retrieval, Treatment, and Disposition Framework, U.S. Department of Energy, Washington, D.C., 2013.

[105] J.H. Westsik, G.F. Piepel, M.J. Lindberg, P.G. Heasler, T.M. Mercier, R.L. Russell, A. Cozzi, W.E. Daniel, R.E. Eibling, E.K. Hansen, M.M. Reigel, D.J. Swanberg, Supplemental Immobilization of Hanford Low-Activity Waste: Cast Stone Screening Tests, 2013.

[106] K. Dixon, Harbour, J., and Phifer, M., Hydraulic and Physical Properties of Saltstone Grouts and Vault Concretes, Savannah River National Laboratory, November 2008.

[107] C.A. Langton, Almond, P.M., Cast Stone Oxidation Front Evaluation: Preliminary Results for Samples Exposed to Moist Air, Savannah River National Laboratory, November 2013.

[108] J.L. Branch, R. Epps, D.S. Kosson, The impact of carbonation on bulk and ITZ porosity in microconcrete materials with fly ash replacement, Cement and Concrete Research, 103 (2018) 170-178.

[109] J.L. Branch, D.S. Kosson, K.G. Brown, A.C. Garrabrants, H.A.v.d. Sloot, Evaluating the impacts of reactive gas (carbon dioxide and oxygen) ingress on leaching from cementitious waste forms, Waste Management Symposia 2017, Phoenix, AZ, USA, March 5-9, 2017.

[110] R. Russell, J. JH Westsik, D. Swanberg, R. Eibling, A. Cozzi, M. Lindberg, G. Josephson, D. Rinehart, Letter Report: LAW Simulant Development for Cast Stone Screening Tests, Pacific Northwest National Laboratory, Richland, WA, 2013.

[111] S. Rassat, L. Mahoney, R. Russell, S. Bryan, R. Sell, Cold Dissolved Saltcake Waste Simulant Development, Preparation, and Analysis, Pacific Northwest National Laboratory, Richland, WA, 2003.

[112] W. Um, J.-S. Yang, R.J. Serne, J.H. Westsik, Reductive capacity measurement of waste forms for secondary radioactive wastes, Journal of Nuclear Materials, 467 (2015) 251-259.

[113] A. International, ASTM C305-14, Standard Practice for Mechanical Mixing of Hydraulic Cement Pastes and MortarsWest Conshohocken, PA, 2014, pp. 3 pp.

[114] D. Russell, P.A.M. Basheer, G.I.B. Rankin, A.E. Long, Effect of relative humidity and air permeability on prediction of the rate of carbonation of concrete, Proceedings of the Institution of Civil Engineers - Structures and Buildings, 146 (2001) 319-326.

[115] I. Galan, C. Andrade, M. Castellote, Natural and accelerated CO2 binding kinetics in cement paste at different relative humidities, Cement and Concrete Research, 49 (2013) 21-28.

[116] C. Langton, D. Missimer, X-ray Diffraction of Slag-based Sodium Salt Waste Forms, CBP-TR-2014-004, SRS, 2014.

[117] C.-W. Chung, W. Um, M.M. Valenta, S.K. Sundaram, J. Chun, K.E. Parker, M.L. Kimura, J.H. Westsik Jr, Characteristics of Cast Stone cementitious waste form for immobilization of secondary wastes from vitrification process, Journal of Nuclear Materials, 420 (2012) 164-174.

[118] K.A. Snyder, P.E. Stutzman, Hydrated Phases in Blended Cement Systems and Synthetic Saltstone Grouts, National Institute of Standards and Technology, http://dx.doi.org/10.6028/NIST.IR.7947, June 2013.

[119] T. Degen, M. Sadki, E. Bron, U. König, G. Nénert, The HighScore Suite, Powder Diffraction, 29 S13-S18.

[120] R.T. Downs, M. Hall-Wallace, The American Mineralogist crystal structure database, American Mineralogist, 88 (2003) 247-250.

[121] S. Grazulis, Chateigner, D., Downs, R. T., Yokochi, A. T., Quiros, M., Lutterotti, L., Manakova, E., Butkus, J., Moeck, P. & Le Bail, A., Crystallography Open Database – an open-access collection of crystal structures, J. Appl. Cryst., 42 (2009) 726-729.

[122] A.C. Garrabrants, R.C. DeLapp, J.L. Branch, K.G. Brown, D.S. Kosson, Cast Stone Materials: Porosity Determination and Relative Humidity-Saturation Relationships, Rev. 0, Vanderbilt University and Consortium for Risk Evaluation with Stakeholder Participation (CRESP), June 2016.

[123] Standard Test Method for Dry and Wet Bulk Density, Water Absorption, and Apparent Porosity of Thin Sections of Glass-Fiber Reinforced Concrete, 2009.

[124] US EPA, Method 1316, Liquid-solid partitioning as a function of liquid-to-solid ratio in solid materials using a parallel batch procedure, https://www.epa.gov/sites/production/files/2015-12/documents/1316.pdf, July 2017.

[125] US EPA, Method 1313, Liquid-solid partitioning as a function of extract pH using a parallel batch extraction procedure, https://www.epa.gov/sites/production/files/2017-10/documents/method_1313_-_final_8-3-17.pdf, July 2017.

[126] US EPA, Method 1315, Mass transfer rates of constituents in monolith or compacted granular materials using a semi-dynamic tank leaching procedure, https://www.epa.gov/sites/production/files/2017-10/documents/method_1315_-_final_8-3-17.pdf, July 2017.

[127] R. Berger, J. Young, K. Leung, Accleration of hydration of calcium silicates by carbon dioxide treatment, Nature Nanotechnology, 97 (1972) 16-18.

[128] D. Zhang, Z. Ghouleh, Y. Shao, Review on carbonation curing of cement-based materials, Journal of CO2 Utilization, 21 (2017) 119-131.

[129] B. Lothenbach, P.T. Durdziński, K.D. Weerdt, Chapter 5: Thermogravimetric analysis, in: K. Scrivener, R. Snellings, B. Lothenbach (Eds.) A Practical Guide to Microstructural Analysis of Cementitious Materials, CRC Press, Boca Raton, FL, 2016.

[130] K.H. Stern, High Temperature Properties and Thermal Decomposition of Inorganic Salts and Oxyanions, CRC Press, Boca Raton, 2001.

[131] D.A. Lange, H.M. Jennings, S.P. Shah, Image analysis techniques for characterization of pore structure of cement-based materials, Cement and Concrete Research, 24 (1994) 841-853.

[132] S.T. Pham, W. Prince, The Carbonation of Calcium-Silicate-Hydrate C-S-H in Cement Mortar Studied Using Thermal Analysis and Gas Pycnometer: Determination of the Quantity of Calcium Carbonate Produced and the Increase in Molar Volume, Advanced Materials Research, 931-932 (2014) 411-415.

[133] T. Grounds, H. G Midgley, D. V Novell, Carbonation of ettringite by atmospheric carbon dioxide, Thermochimica Acta, 135 (1988) 347-352.

[134] D.S. Kosson, A.C. Garrabrants, R. DeLapp, H.A. van der Sloot, pH-dependent leaching of constituents of potential concern from concrete materials containing coal combustion fly ash, Chemosphere, 103 (2014) 140-147.

[135] A.C. Garrabrants, D.S. Kosson, R. DeLapp, H.A. van der Sloot, Effect of coal combustion fly ash use in concrete on the mass transport release of constituents of potential concern, Chemosphere, 103 (2014) 131-139.

[136] E. Martens, D. Jacques, T. Van Gerven, L. Wang, D. Mallants, Geochemical modeling of leaching of Ca, Mg, Al, and Pb from cementitious waste forms, Cement and Concrete Research, 40 (2010) 1298-1305.

[137] C.J. Engelsen, H.A. van der Sloot, G. Wibetoe, G. Petkovic, E. Stoltenberg-Hansson, W. Lund, Release of major elements from recycled concrete aggregates and geochemical modelling, Cement and Concrete Research, 39 (2009) 446-459.

[138] S. Sarkar, D.S. Kosson, S. Mahadevan, J.C.L. Meeussen, H.v. der Sloot, J.R. Arnold, K.G. Brown, Bayesian calibration of thermodynamic parameters for geochemical speciation modeling of cementitious materials, Cement and Concrete Research, 42 (2012) 889-902.

[139] H.A. van der Sloot, Comparison of the characteristic leaching behavior of cements using standard (EN 196-1) cement mortar and an assessment of their long-term environmental behavior in construction products during service life and recycling, Cement and Concrete Research, 30 (2000) 1079-1096.

[140] N. Schiopu, L. Tiruta-Barna, E. Jayr, J. Méhu, P. Moszkowicz, Modelling and simulation of concrete leaching under outdoor exposure conditions, Science of The Total Environment, 407 (2009) 1613-1630.

[141] G. Cornelis, B. Etschmann, T. Van Gerven, C. Vandecasteele, Mechanisms and modelling of antimonate leaching in hydrated cement paste suspensions, Cement and Concrete Research, 42 (2012) 1307-1316.

[142] L. Tiruta-Barna, Using PHREEQC for modelling and simulation of dynamic leaching tests and scenarios, Journal of Hazardous Materials, 157 (2008) 525-533.

[143] L. De Windt, R. Badreddine, Modelling of long-term dynamic leaching tests applied to solidified/stabilised waste, Waste Management, 27 (2007) 1638-1647.

[144] D.O. McPolin, P.A. Basheer, A.E. Long, K.T. Grattan, T. Sun, New Test Method to Obtain pH Profiles due to Carbonation of Concretes Containing Supplementary Cementitious Materials, Journal of Materials in Civil Engineering, 19 (2007) 936-946.

[145] L. De Ceukelaire, D. Van Nieuwenburg, Accelerated carbonation of a blast-furnace cement concrete, Cement and Concrete Research, 23 (1993) 442-452.

[146] D.J. Anstice, C.L. Page, M.M. Page, The pore solution phase of carbonated cement pastes, Cement and Concrete Research, 35 (2005) 377-383.

[147] A. Garrabrants, D. Kosson, R. DeLapp, P. Kariher, P. Seignette, H. Van der Sloot, L. Stefanski, M. Baldwin, Interlaboratory validation of the leaching environmental assessment framework (LEAF) method 1314 and method 1315, US Environmental Protection Agency, Office of Research and Development, Research Triangle Park, NC, (2012).

[148] J.C.L. Meeussen, ORCHESTRA: An Object-Oriented Framework for Implementing Chemical Equilibrium Models, Environmental Science & Technology, 37 (2003) 1175-1182.

[149] H. Van der Sloot, P. Seignette, J. Meeussen, O. Hjelmar, D. Kosson, A database, speciation modelling and decision support tool for soil, sludge, sediments, wastes and construction products: LeachXS™-Orchestra, Second international symposium on energy from biomass and waste, Venice, 2008.

[150] Thermodynamic Database for MINTEQA2 V4.0 in ORCHESTRA format, Available at http://www.meeussen.nl/orchestra/minteqv4.txt.

[151] MINTEQA2/PRODEFA2, A Geochemical Assessment Model for Environmental Systems: User Manual Supplement for Version 4.0, U.S. Environmental Protection Agency National Exposure Research Division, Athens, Georgia, June 1998.

[152] P. Seignette, LeachXS QA Documentation, DRAFT ECN-X-15-123, Version 2.0.x DRAFT, Energy Research Centre of The Netherlands, Petten, The Netherlands, 2015.

[153] J.C.L. Meeussen, K.G. Brown, ORCHESTRA Software Quality Assurance (SQA) Documentation, U.S. Department of Energy, Washington, D.C., December 2015.

[154] J.C.L. Meeussen, K.G. Brown, ORCHESTRA Manual and Documentation, CBP-TR-2015-00X-Y, Rev. C (DRAFT for CBP review, in: NRG (Ed.)Petten, The Netherlands, December 2015.

[155] E. Samson, J. Marchand, Modeling the transport of ions in unsaturated cement-based materials, Computers & Structures, 85 (2007) 1740-1756.

[156] H. Van der Sloot, D. Kosson, Use of characterisation leaching tests and associated modelling tools in assessing the hazardous nature of wastes, Journal of hazardous materials, 207 (2012) 36-43.

[157] Version cemdata14, release date 07.05.2014 during the 4th GEMS Workshop, EMPA, Switzerland (2014), Available at http://www.empa.ch/cemdata.

[158] Personal communication with Hans A. van der Sloot, 2017.

[159] ASTM C33/C33M-16 Standard Specification for Concrete Aggregates, ASTM International, West Conshohocken, PA, 2016.

[160] A.C. Garrabrants, D.S. Kosson, Modeling Moisture Transport from a Portland Cement-Based Material During Storage in Reactive and Inert Atmospheres, Drying Technology, 21 (2003) 775-805.

[161] Ionic Conductivity and Diffusion at Infinite Dilution, in: J.R. Rumble (Ed.) CRC Handbook of Chemistry and Physics, 98th Edition, CRC Press/Taylor & Francis, Boca Raton, FL, Internet Version 2018.

[162] J.E. Mackin, R.C. Aller, The infinite dilution diffusion coefficient for A1(OH)4− at 25°C, Geochimica et Cosmochimica Acta, 47 (1983) 959-961.

[163] J. Arnold, R. Duddu, K. Brown, D.S. Kosson, Influence of multi-species solute transport on modeling of hydrated Portland cement leaching in strong nitrate solutions, Cement and Concrete Research, 100 (2017) 227-244.

[164] R. Mills, Self-diffusion in normal and heavy water in the range 1-45.deg, The Journal of Physical Chemistry, 77 (1973) 685-688.

[165] L. Yuan-Hui, S. Gregory, Diffusion of ions in sea water and in deep-sea sediments, Geochimica et Cosmochimica Acta, 38 (1974) 703-714.